Studies on Biopolymer based Solid Electrolyte Membrane and Electro-catalysts for Direct Methanol Fuel Cells

Submitted in Partial Fulfilment of the Requirements

for the Degree of

DOCTOR OF PHILOSOPHY

By

SURENDRA SINGH GAUR

DEPARTMENT OF CHEMICAL ENGINEERING

INDIAN INSTITUTE OF TECHNOLOGY GUWAHATI

May, 2021.

TH-2592_156107017

TH-2592_156107017

Dedicated to

My Beloved Parents, Wife and Teachers

for their

Support and Encouragement

TH-2592_156107017

Department of Chemical Engineering
Indian Institute of Technology Guwahati

CERTIFICATE

This is to certify that the research work in the thesis entitled **"Studies on Biopolymer based Solid Electrolyte Membrane and Electro-catalysts for Direct Methanol Fuel Cells"**, is carried out by me at Department of Chemical Engineering, Indian Institute of Technology Guwahati, under the supervision of Prof. Vimal Katiyar and Dr. Amit Kumar. The results documented in this thesis are achieved by me and has not been submitted to any other University or Institute for the award of any degree or diploma.

Date:

Surendra Singh Gaur
Roll No: 156107017
Department of Chemical Engineering
Indian Institute of Technology Guwahati
Guwahati - 781 039, India.

TH-2592_156107017

Department of Chemical Engineering
Indian Institute of Technology Guwahati

CERTIFICATE

This is to certify that the thesis entitled **"Studies on Biopolymer based Solid Electrolyte Membrane and Electro-catalysts for Direct Methanol Fuel Cells"**, being submitted by **Surendra Singh Gaur** for the award of Ph.D. Degree has been carried out by him at Department of Chemical Engineering, Indian Institute of Technology Guwahati, under our guidance and supervision. The work documented in this thesis has not been submitted to any other University or Institute for the award of any degree or diploma.

Date:

Dr. Vimal Katiyar
Professor
Department of Chemical Engineering
Indian Institute of Technology Guwahati
Guwahati - 781 039, India.

Dr. Amit Kumar
Associate Professor
Department of Chemical Engineering
Indian Institute of Technology Guwahati
Guwahati - 781 039, India.

TH-2592_156107017

Acknowledgement

I owe a debt of gratitude to all the people who have helped me in completing this research work directly or indirectly, I would like to acknowledge them all. At foremost, I would like to express my sincere and profound sense of gratitude, to both of my learned supervisors Prof. Vimal Katiyar and Dr. Amit Kumar, for their valuable guidance and encouragement provided during the course of my PhD work. Their constant teachings, learnings and support, have helped me in making this dissertation possible. I have been fortunate to have advisors who gave me the freedom to explore a different area of research and helped me every time when I struggled in the research. I would like to acknowledge my Doctoral Committee members Prof. Pranab Goswami (Department of Biosciences and Bio-Engineering), Prof. Ashok Kumar Dasmahapatra and Dr. Anki Reddy Katha (Department of Chemical Engineering) for their insightful comments and encouragement. I would like to sincerely thank Dr. Prodyut Dhar, who initiated and worked intensively in the area of biopolymers and created a path for my PhD research work and several times guided me in my research work. I would like to thank Prof. Shinichi Sakurai, KIT Japan, for providing me opportunity to carry out part of my research work in his laboratory as well as guiding me during my stay in his lab. I would like to express my gratitude to my bachelor's degree mentor and Guru Dr. Murali Rangrajan, Amrita Vishwa Vidyapeetham, Coimbatore, for motivating me to move towards research. I would like to acknowledge Dr. G. Velayutham, Anabond Sainergy Fuel Cell Private Limited for providing me the opportunity to visit his laboratory and teaching me the various electrochemical techniques which were helpful in my entire research work. I would like to acknowledge Centre of Excellence for Sustainable Polymers (CoE-SusPol), DBT Centre of Excellence on BioFuels and Biocomodities,

TH-2592_156107017

Central Instruments Facilities (CIF), IIT Guwahati, Analytical lab of Department of Chemical Engineering for providing the sophisticated instrumentation facility to carry out analysis part of my work. I would like to thank KIT Global Human Resource Department, KIT Japan for providing me scholarship during my stay in Japan to carry out part of my research work. I would also like to thank Head, Department of Chemical Engineering, Faculty members and Staffs for their constant support during my stay at IIT Guwahati.

I would like to sincerely thank my friends and colleagues Dr. Narendren, Mr. Umesh Bhardwaj, Sourav, Dr. Arvind, Dr. Melaku, Dr. Rahul Saha, Khalid, Kiran, Dr. Purabi, and Dr. Riddhi for technical help and discussions, which helped me in my research work a lot. I am also thankful to all my other co-research fellows and lab colleagues: Debashish, Dr. Sidhhartha, Dr. Gourhari, Dr. Shasanka, Dr. Monika, Dr. Akhilesh, Dr. Rahul, Neha, Bhanupriya, Tabli, Durluv, Pankaj, Sayan, Naba, Modu, Chetna, Kona, Munmi, Doli, Deepshikha, Lakhiya and Diganta for all kinds of help and morale support made available to me in the lab and making my stay at IIT Guwahati cheerful and memorable. I am blessed to have wonderful parents and wife who are really supportive, encouraging and their countless sacrifices, have made it possible for me to reach this stage in my life. In the end I owe it all to the Almighty for enabling me to reach to completion of the doctoral work.

TH-2592_156107017

Abstract

Direct methanol fuel cell (DMFC) has been viewed as one of the emerging technologies and it can play vital role in future for cleaner and greener energy conversion. In DMFCs methanol is used as fuel, which can be produced from agricultural waste and other waste biomass, making it a sustainable source of energy. At the same time DMFC only produces CO_2 as byproduct, maintaining the carbon cycle without increasing the carbon footprint. Existing problems of high methanol crossover, slower reaction kinetics, high cost of electro-catalyst and solid electrolyte materials and catalyst poisoning in acidic type of DMFCs have made researchers to focus on its alternatives. Alkaline type DMFCs have shown to be best alternative of it by addressing several of these issues. Possibility to utilize low cost non-noble metal catalyst, low corrosive environment, faster electrochemical reaction kinetics, lower methanol permeation, lower flooding problem and less impact of poisoning species on electrocatalysts are the major advantages of the alkaline type DMFCs. The roadblock for alkaline type DMFCs is that a suitable commercial polymer electrolyte membranes for alkaline medium is still not developed. While, if DMFCs based technology is successfully commercialized, synthetic polymer based membranes can cause a lot of environmental issues. Biopolymers such as such as cellulose and cellulose nanocrystals (CNCs), chitosan, proteins like keratein and carrageenan, which are abundant and renewable in nature can be derived from waste materials, are one of the suitable candidates for fabrication of anion exchange membranes (AEMs). Due to availability of different functional groups, their properties can be tuned, according to AEM's requirements and their use as AEM can make already deemed green fuel cell technology greener, cheaper and sustainable. The commercial Pt/C and Pd/C based electrocatalysts materials used in

TH-2592_156107017

alkaline DMFCs have also been found to suffer from several issues including catalyst leaching, agglomeration of metal nanoparticles and degradation of carbon based catalysts supports due to attack of hydrogen peroxide, hydroxyl radicals and carbonates formed in presence of CO_2. So, suitable electrocatalyst materials have to be develop which can provide the stability for longer runs to the DMFCs. Clay based biomaterials such as montmorillonite, which are formed in the presence of extremely corrosive and chemically reactive environment can be suitable candidates as electrocatalyst support to be utilized in alkaline DMFCs.

In the current work with motivation to utilize biomaterials, biopolymers and biodegradable polymers, we have developed a new set of materials for alkaline DMFCs. Cellulose rich source was utilized to derive different acidic moieties contained CNCs with different morphologies, as well as human hair bio-waste was utilized to derive hair hydrolysate, containing different amino acid as basic structural unit. Both of these biopolymeric materials were utilized as ion conduction source to prepare polymer electrolyte membranes. CNCs with different morphologies showed their possible application as ion conductive source in electrolyte membrane and their morphologies had impact on membrane properties such as water uptake, swelling behavior and ion conductivity. While, human hair hydrolysate based ion conductive material showed promising results for AEMs. Hair hydrolysate having hydrophilic and hydrophobic part contained peptide/ small protein chains created different type of self-assembly crystalline structures in PVA matrix, which subsequently created a channel network, providing direct path for charge transfer in the water saturated membranes. Presence of 70 wt.% proteinaceous material, out of which 27 wt.% was charged amino acids and 19 wt.% was polarizable amino acids, provided charge transfer sites to the membrane. Presence of 7 wt.% of arginine in hair hydrolysate, having

TH-2592_156107017

continuous delocalized net positive charge, which makes it stable even in highly alkaline conditions, played a positive role in anion transfer and provided stability to the membranes in alkaline conditions. Annealing of the membranes further improved its properties with slight reduction in ionic conductivity. The selectivity of the membrane was increased to almost a decimal place and was in the range of some of the commercially used membranes, making it suitable for alkaline DMFCs. The charge transfer mechanism was investigated through molecular dynamics (MD) simulation studies, having a model human hair peptide, containing the different charge transfer functional groups present in the hair hydrolysate with PVA matrix. The MD simulation studies showed the impact of water in ion conductivity of the membranes, which is very much dependent on the presence of water. The methanol permeability was found to be controlled by electro-osmotic drag, which is positive sign for the hair hydrolysate based membranes, as it would decrease the methanol permeation from anode to cathode. A Grotthuss type of charge transfer mechanism was proposed for the system, based on the MD simulation studies, where three different sites followed two different ways of charge transfer. Around PVA chains which forms a channel of water molecules around it, as well as around the ammonium cation charge transfer site present in the peptide, hydroxyl ion transport takes place by continuous formation ($H_3O_2^-$) and breaking ($OH^- + H_2O$) of H-bonds with water molecule. Around the guanidino cation present in the system, the charge transfer follows a little different mechanism, where OH^- ion from the bulk jumps on guanidino cation in its original form, which can jump on to another guanidino cationic sites without formation of intermediate species or can move to bulk system by forming $H_3O_2^-$ intermediate species through H-bonding with water. Thus, having guanidino cation as charge transfer functional group in AEMs can enhance the conductivity of OH^- ions significantly as it does not require formation of intermediate species like $H_3O_2^-$ for charge transfer. As an alternative to commercially available carbon

TH-2592_156107017

supported Pt/Pd electrocatalyst, which has low stability in alkaline medium, we developed a clay-CNC supported Pt/Pd electrocatalyst and the calcined material showed good performance for methanol oxidation with highly stable nature. The clay based support having metal oxides in its structural unit enhanced the chemical stability of the Pt/Pd electrocatalyst. Further, investigations on the formation and removal of intermediates species during the electrochemical oxidation of methanol through cyclic voltammetry and impedance spectroscopy showed that that reaction intermediates formed during oxidation are being removed in the forward CV scan, as opposed to the many reports on Pt catalyst, which assume it to happen during reverse scan. The range of potential for the removal of the reaction intermediates was found to be 0.1V–0.2V through impedance spectroscopy. Similarly, to have a stable electrocatalyst for H_2O_2 oxidation in cathode side and prevent the leaching of catalytic nanoparticles, we developed Pd-Fe encapsulated clay-CNC based nanoscorlls, having significantly low amount of palladium in it. In the novel technique we were able to synthesize clay nanscrolls from the 2:1 type montmorillonite clay for the first time, which showed good electrochemical perofrmencve for H_2O_2 reduction in alkaline medium with lower palladium content. The current density obtained by clay nanoscrolls for H_2O_2 reduction was in the same range with significantly high Pd loaded commercial Pd/C catalyst. Thus, the clay nanoscrolls are found to be suitable electrocatalyst for H_2O_2 reduction in alkaline medium. In the parallel reaction of clay nanscrolls formation, during the thermal treatment through changing the environment from normal atmosphere to nitrogen, resulted in the formation of highly stable zero-valent iron (ZVI), which showed the stable nature in normal atmosphere even up to 130 days. Thus, overall in the current doctoral thesis a different set of bio-based novel materials were developed with promising results and with further research on these materials to enhance their properties can make them commercially viable candidates for alkaline DMFCs.

TH-2592_156107017

Graphical Abstract of the PhD Thesis

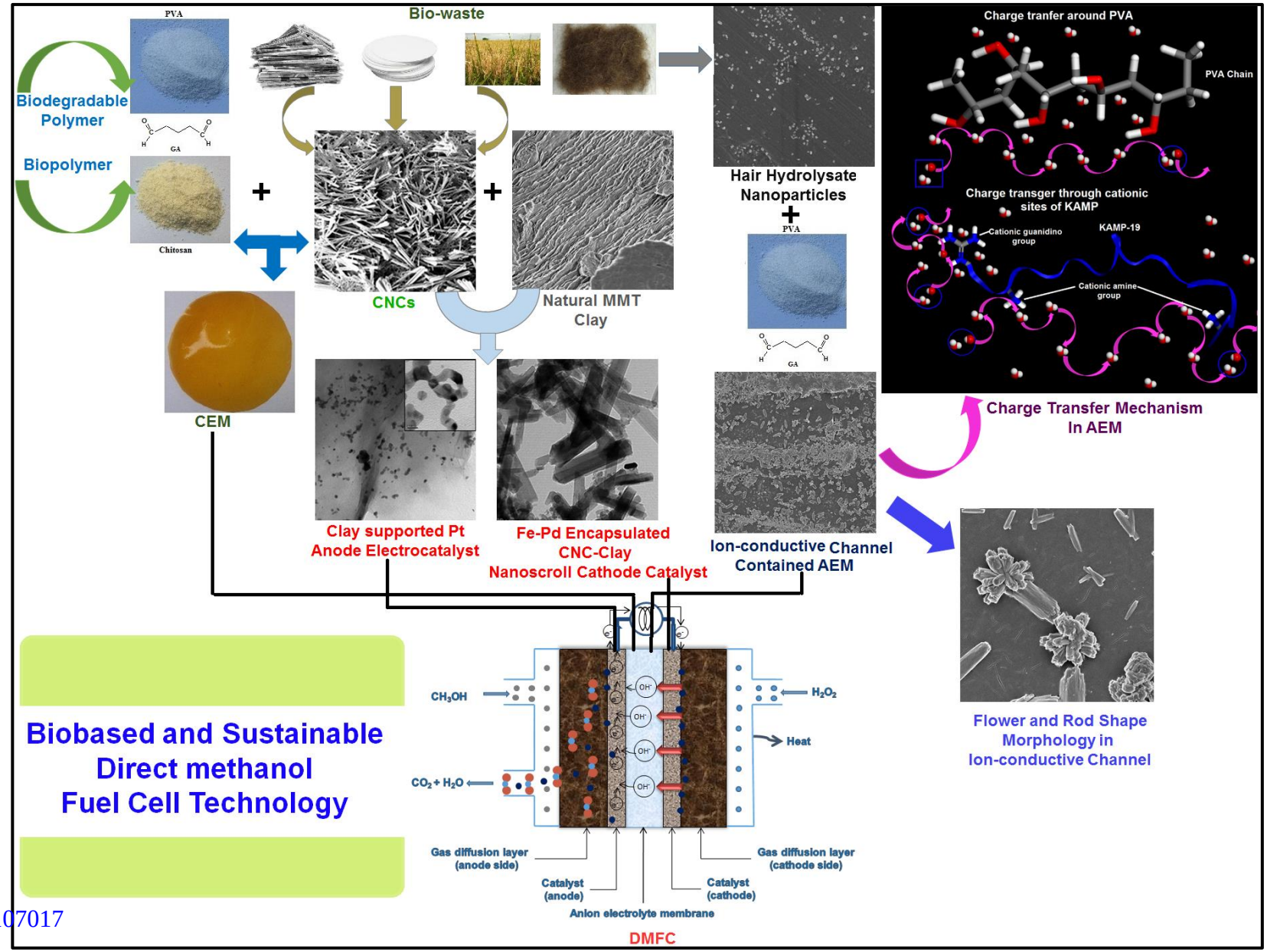

TH-2592_156107017

Contents

Acknowledgment iv

Abstract vi

PhD Thesis Graphical Abstract x

Contents xi

List of Figures xvi

List of Tables xxiii

Abbreviations xxiv

Chapter 1:

Introduction and Literature Review 1

1.1 Introduction 2

1.1.1 Fuel Cells 2

1.1.1.1 Solid Oxide Fuel Cells (SOFCs) 4

1.1.1.2 Molten Carbonate Fuel Cells (MCFCs) 5

1.1.1.3 Phosphoric Acid Fuel Cells (PAFCs) 6

1.1.1.4 Alkaline Fuel Cells (AFCs) 6

1.1.1.5 Polymer Electrolyte Membrane Fuel Cells (PEMFCs) 8

1.2 Acidic type Direct Methanol Fuel Cells (DMFCs) 12

1.2.1 Properties Required for Polymer Electrolyte Membrane (PEM) 13

1.2.1.1 Ionic Conductivity 14

1.2.1.2 Methanol Permeability 15

1.2.1.3 Water Management 16

1.2.1.4 Chemical and Mechanical Stability 17

1.2.2 Polymer Membrane Materials for Acidic type DMFCs 17

1.2.2.1 Perflourinated Ionomeric Membranes: 17

1.2.2.2 Partially Fluorinated Membrane: 18

1.2.2.3 Non-fluorinated Hydrocarbon Membranes: 18

1.2.2.4 Non-fluorinated Aromatic Membranes: 18

1.2.2.5 Acid–base Blend Membranes: 18

1.2.3 Electrocatalyst for Acidic type DMFCs 19

1.2.3.1 Impregnation Method 20

TH-2592_156107017

1.2.3.2 Colloidal Method 20
1.2.3.3 Microemulsion Method 21
1.2.3.4 Sol-gel Method 21
1.2.4 Issues with Acidic type DMFCs 22
1.2.4.1 Issues Associated with the Cation Exchange Membranes 22
1.2.4.2 Issues Associated with Electrocatalysts 23
1.3 Alkaline type DMFCs 24
1.3.1 Membrane Materials for Alkaline type DMFCs 26
1.3.1.1 Membrane Fabrication Techniques 27
1.3.1.2 Non-commercial and Commercial AEMs 28
1.3.2 Ion Transport Mechanism in AEMs 31
1.3.3 Electrocatalysts for Alkaline type DMFCs 32
1.3.3.1 Electrocatalyst for Oxygen Reduction Reaction 32
1.3.3.2 Electrocatalyst for Hydrogen Peroxide Reduction Reaction 34
1.3.3.3 Electrocatalyst for Methanol Oxidation Reaction 36
1.3.4 Issues with Alkaline type DMFCs 39
1.3.4.1 Issues Associated with the AEMs 39
1.3.4.2 Solution for the Issues Associated with the AEMs 42
1.3.4.3 Issues Associated with the Electrocatalysts 44
1.3.4.4 Solution for the Issues Associated with the Electrocatalysts 48
1.3.5 Biopolymers–Biodegradable Polymers as Electrolyte Material 50
1.4 Knowledge Gap and Hypotesis 56
1.5 Proposed Objectives and Organization of the Research Work 58
Chapter 2:
Primary Investigation on Cellulose Nanocrystals based Ion Conductive Materials .61
2.1 Introduction 62
2.2 Experimental Section 65
2.2.1 Materials 65
2.2.2 Fabrication of Cellulose Nanocrystals (CNCs) 65
2.2.3 Membrane Preparation 66
2.2.4 Methanol Permeability Experiment 67
2.3 Characterization 67
2.3.1 Thermal and Thermo-mechanical Analysis: 67
2.3.2 Surface Morphology, Crystal Structure and FTIR Studies 68

TH-2592_156107017

2.3.3 Water Uptake and Swelling Behavior: 68
2.3.4 Ionic Conductivity: 69
2.3.5 Methanol Permeability and Selectivity 69
2.4 Results and Discussions 70
2.4.1 Thermal and Thermo-mechanical Analysis: 70
2.4.2 Surface Morphology, Crystal Structure and FTIR Studies 75
2.4.3 Water Uptake and Swelling Behavior 78
2.4.4 Ionic Conductivity, Methanol Permeability and Selectivity 79
2.5 Conclusions 81
Chapter 3:
Human Hairs based Anion Exchange Membrane for Alkaline DMFCs 82
3.1 Introduction 84
3.2 Material and Methods 87
3.2.1 Materials 87
3.2.2 Green Thermal Hydrolysis of Hairs 87
3.2.3 Modification of CNCs by Hair Hydrolysate 88
3.2.4 Fabrication of CS and Modified CNCs based AEMs 89
3.2.5 Fabrication of PVA-Hair Hydrolysate based Composite AEMs 90
3.3 Characterization 90
3.4 Results and Discussion 95
3.4.1 Confirmation of Presence Amino Acids/ Peptides in Hair Hydrolysate (HH) by XPS and FTIR 95
3.4.2 Molecular Weight Analysis of Hair Hydrolysate 97
3.4.3 Amino Acid Composition of Hair Hydrolysate 98
3.4.4 Crystallinity Analysis and Thermal Stability of Hair Hydrolysate 102
3.4.5 Morphology of Hair Hydrolysate 107
3.4.6 Confirmation of CNCs Modification by XPS Analyses 107
3.4.7 Morphology of Modified CNCs and Modified CNC-CS Membrane 108
3.4.8 Ionic Conductivity, Water Uptake and % Swelling 108
3.4.9 Morphology of PVA-Hair Hydrolysate Membranes 114
3.4.10 Thermal Stability of PVA-Hair Hydrolysate Membranes 116
3.4.11 Ionic Conductivity, Methanol Permeability and Selectivity of the PVA-Hair Hydrolysate Membranes 118
3.4.12 Water Uptake and %swelling of PVA-Hair Hydrolysate Membranes 120

TH-2592_156107017

3.4.13 Effect of Annealing on the Properties of PVA-5wt.% Hair Hydrolysate Membrane and its Alkaline Stability 121

3.5 Conclusions 125

Chapter 4:

Anion Transport in Human Hair Peptide-based System by Molecular Dynamics Simulation 128

4.1 Introduction 129

4.2 Theory and Simulation Details 132

4.2.1 Molecular Dynamics Simulation 132

4.2.2 Details of the Simualtion 135

4.2.3 Calculation of the Diffusivity and Ionic Conductivity 141

4.3 Results and Discussion 141

4.3.1 Mechanism of OH^- Transport 150

4.4 Conclusion 174

Chapter 5:

Stable CNC-Clay Supported Pt/Pd Catalyst for Methanol Oxidation in Alkaline Medium 176

5.1 Introduction 177

5.2 Materials and Methods 180

5.2.1 Materials 180

5.2.2 Formation of Macroion-nanogel Complex between the CNCs and CNa^+ clay 181

5.2.3 Fabrication of the Platinum/ Palladium Nanoparticles Encapsulated Macrion-nanogels 181

5.3 Characterization 182

5.3.1 FTIR Spectroscopy, Crystal Structure and Surface Morphology 182

5.3.2 Surface Area, XPS and Compositional Analysis of Pt/Pd in Calcined Electrocatalysts 183

5.3.3 Electrochemical Performance, Methanol Oxidation Studies, Linear Sweep Voltammetry (LSV) and Electrochemical Impedance Spectroscopy (EIS) Analysis 183

5.4 Results and Discussion 184

5.4.1 Physico-Chemical Properties of the Fabricated Macro-Ion Nanogels 184

5.4.2 Surface Morphology 188

5.4.3 XPS and Compositional Analysis of Pt/Pd in the Calcined Electrocatalysts 190

5.4.4 Electrochemical Performance and Methanol Oxidation Studies 191

TH-2592_156107017

5.4.5 LSV Investigation for the Role of –OH and Reaction Intermediates in Methanol Oxidation 197
5.4.6 Electrochemical Impedance Spectroscopy (EIS) Analysis 203
5.4.7 Surface Area Analysis and Hydrogen Adsorption Studies 205
5.5 Conclusions 206
Chapter 6:
CNC-Clay based Cathode Electrocatalyst for H_2O_2 Reduction in Alkaline medium 208
6.1 Introduction 209
6.2 Materials and Methods 214
6.2.1 Materials 214
6.2.2 Fabrication of Iron-Palladium Loaded CNCs (Fe-Pd-CNC) 215
6.2.3 Fabrication of Clay Nanoscrolls and ZVI 215
6.3 Characterization 216
6.4 Results and Discussion 218
6.4.1 Crosslinking of Fe-Pd-CNCs to Clay Sheets 218
6.4.2 Morphology 219
6.4.3 X-ray Diffraction Analysis and Magnetic Properties 225
6.4.4 Composition Analysis 232
6.4.5 Mechanism of Scroll Formation 233
6.4.6 Hydrogen Peroxide Reduction on Clay Nanoscroll in Alkaline Medium 237
6.4.7 Fuel Cell Performance 239
6.4.8 Hydrogen Adsorption Study 240
6.5 Conclusions 242
Chapter 7:
Conclusions and Future Scope 244
7.1 Conclusions 244
7.2 Novelty or Technical Problems Addressed 249
7.3 Future Scope 249
Appendix 251
Lennard-Jones Potential Parameter for MD Simulation 251
Research Outcome 254
Research articles published/ under publication/ under preparation: 254
References 259

TH-2592_156107017

List of Figures

Fig. 1.1 Schematic representation of a fuel cell. 3

Fig. 1.2 Schematic of polymer electrolyte membrane fuel cell. 7

Fig. 1.3 Applications of PEM Fuel Cells. 10

Fig. 1.4 Nafion chemical structure. 13

Fig. 1.5 Proton transfer mechanism in sulfonic acid containing PEMs, where the sulfonic acid works as driver and water work as charge carrier (Jiao & Li, 2011; Zhai et al., 2019). 15

Fig. 1.6 Schematic of alkaline type DMFC. 25

Fig. 1.7 Hydroxyl ion transport in water by formation of $(H_9O_5)^-$ and $(H_7O_4)^-$ complexes (Tuckerman et al., 1995). 32

Fig. 1.8 Chemical degradation mechanism of quaternary ammonium cations by (a) nucleophilic substitution attack (b) Hofmann degradation reaction (c) nucleophilic elimination reaction (Wang et al., 2013). 41

Fig. 1.9 Chemical structure of (a) guanidino cation (b) imidazolium cation. 43

Fig. 2.1 TGA thermograph of PVA and PVA-CS-CNC samples. 72

Fig. 2.2 DSC thermograph of PVA and PVA-CS-CNC samples. 72

Fig. 2.3 Possible network formation (A) H-bonding between PVA, CS, CNC (B) crosslinking of chitosan with GA and (C) crosslinking of PVA with GA. 73

Fig. 2.4 Storage modulus vs temperature curves of PVA and PVA-CS-CNC samples. 73

Fig. 2.5 Tan(δ) vs temperature curves of PVA and PVA-CS-CNC samples. 74

Fig. 2.6 FESEM images of the CNCs hydrolyzed from the different acid sources (a) Sulfuric acid, (b) Hydrochloric acid and (c) Nitric acid. 77

Fig. 2.7 XRD patterns of PVA and PVA-CS-CNC sample. 77

Fig. 2.8 FTIR spectra of PVA and PVA-CS-CNC films. 78

TH-2592_156107017

Fig. 3.1 CNCs oxidation by $NaIO_4$ and subsequently modification by hair hydrolysate. 88

Fig. 3.2 CS and modified CNCs crosslinking by epichlorohydrin. 89

Fig. 3.3 XPS spectra of hair hydrolysate for (a) C1s (b) N1s. 96

Fig. 3.4 FTIR spectra of hair hydrolysate. 97

Fig. 3.5 MALDI-TOF-MS of three different batches of hair hydrolysate. 98

Fig. 3.6 Hopping mechanism of OH− ion through charge transfer sites. 102

Fig. 3.7 XRD curve of hair hydrolysate. 103

Fig. 3.8 (a) TGA and DTG thermograph (b) DSC thermograph of hair hydrolysate. 104

Fig. 3.9 FESEM images of (a) Hair hydrolysate (b) Partially crosslinked hair hydrolysate. 105

Fig. 3.10 XPS spectra of carbon 1s (a) CNCs (b) hair extract (c) modified CNCs and nitrogen 1s spectra of (d) hair extract (e) modified CNCs. 106

Fig. 3.11 FESEM images of (a) CNC (b) hair extract modified CNC (c) & (d) chitosan-hair extract modified CNC based AEM cross-section. 109

Fig. 3.12 FESEM imges of (a) & (b) PVA-1wt.% hair hydrolysate membrane. 110

Fig. 3.13 FESEM images of (a) & (b) PVA-5wt.% hair hydrolysate membrane. 111

Fig. 3.14 FESEM images of (a) & (b) PVA-10wt.% hair hydrolysate membrane. 112

Fig. 3.15 FESEM images (a) & (b) magnified flower morphology of present in 5wt.% and 10wt.% hair hydrolysate based PVA membranes. 113

Fig. 3.16 Mechanism of different types of morphologies formation in PVA-hair hydrolysate membranes 114

Fig. 3.17 (a) TGA (b) DTG thermograph of PVA-hair hydrolysate (HH) membranes. 117

Fig. 3.18 XRD spectra of PVA-5wt.% hair hydrolysate membrane before and after annealing. 122

Fig. 3.19 DMA analysis of PVA-5wt.% hair hydrolysate membrane before and after annealing. 123

TH-2592_156107017

Fig. 3.20 (a) TGA (b) DTG thermographs of PVA-5wt.% hair hydrolysate membrane before and after annealing. 124

Fig. 4.1 Structure of a representative simulation box with all the components. 137

Fig. 4.2 Schematic of simulation box and LAMPPS input preparation. 138

Fig. 4.3 Schematic of MD simulation run procedure for LAMPPS. 138

Fig. 4.4 MSD curves of (a) OH^- (b) methanol for all the systems obtained from MD simulation. 144

Fig. 4.5 Low water zone boxes in the snapshots at 10 ns for KAMP loading of (a) 2.6wt.% (b) 5.1 wt.%, (c) 7.4 wt.%, (d) 9.6 wt.% (e) Increased number of charge transfer sites in hydrophobic zone in 9.6wt.%. 146

Fig. 4.6 Snapshots of 8 pairs of hydroxyl ion-methanol moving together during MD simulation, showing the effect of electro-osmotic drag of OH^- on methanol. 147

Fig. 4.7 Snapshots of a pair of OH^- ion (O-tagged) and methanol molecules (C-tagged) moving together during the entire duration of the MD simulation run, showing the effect of electro-osmotic drag of OH^- ion on methanol. 148

Fig. 4.8 Different functional sites of KAMP-19 considered for RDF calculation with oxygen of OH− and H2O. The atoms names correspond to the CVFF force field and details of each atom type is given in appendix. 151

Fig. 4.9 (a) RDF of $O_{OH^-} - O_{H_2O}$ and (b) CN of O_{H_2O} around O_{OH^-} for samples with different KAMP loadings. 152

Fig. 4.10 OH^- ion transfer through formation and breaking of H-bond with water. 153

Fig. 4.11 (a) RDF of $O_{OH} - O_{OH^-}$ (b) CN of O_{OH^-} around O_{OH} for samples with different KAMP loadings. 154

Fig. 4.12 (a) RDF of $O_{OH} - O_{H_2O}$ (b) CN of O_{H_2O} around O_{OH} for samples with different KAMP loadings. 155

Fig. 4.13 (a) RDF of $N4 - O_{OH^-}$ (b) CN of O_{OH^-} around N4 for samples with different KAMP loadings. 156

TH-2592_156107017

Fig. 4.14 (a) RDF of $N4 - O_{H_2O}$ (b) CN of O_{H_2O} around N4 for samples with different KAMP loadings. 157

Fig. 4.15 OH^- transfer mechanism at ammonium cation site of peptide..... 158

Fig. 4.16 (a) RDF of $N1 - O_{OH^-}$ (b) CN of O_{OH^-} around N1 for samples with different KAMP loadings. 162

Fig. 4.17 (a) RDF of $N1 - O_{H_2O}$ (b) CN of O_{H_2O} around N1 for samples with different KAMP loadings. 163

Fig. 4.18 Charge transfer mechanism at guanidino cation site of peptide observed during the MD simulation. The blue circle shows the motion of OH^- ion with increasing time steps. The pink arrows shows the H-bonding interaction between H_2O and OH^- suggesting the formation of $H_3O_2^-$ H-bonded species and its motion. The square box in the final snapshot shows that OH^- ion has completely moved away from the guanidino cation. 164

Fig. 4.19 (a) RDF of $Cr - O_{OH^-}$ (b) CN of O_{OH^-} around Cr for samples with different KAMP loadings. 165

Fig. 4.20 (a) RDF of $Cr - O_{H_2O}$ (b) CN of O_{H_2O} around Cr for samples with different KAMP loadings. 166

Fig. 4.21 (a) RDF of $N2 - O_{OH^-}$ (b) CN of O_{OH^-} around N2 for samples with different KAMP loadings. 167

Fig. 4.22 (a) RDF of $N2 - O_{H_2O}$ (b) CN of O_{H_2O} around N2 for samples with different KAMP loadings. 168

Fig. 4.23 (a) RDF of $N - O_{OH^-}$ (b) CN of O_{OH^-} around N for d samples with different KAMP loadings. 169

Fig. 4.24 (a) RDF of $O' - O_{OH^-}$ (b) CN of O_{OH^-} around O' for samples with different KAMP loadings. 170

Fig. 4.25 Schematic representation of the proposed OH^- transfer mechanism in the PVA-KAMP system (a) around PVA chains, and (b) around cationic sites of KAMP. 173

Fig. 5.1 FTIR spectra of CNC, CNa^+ clay and gel formed by CNa-CNC. 185

TH-2592_156107017

Fig. 5.2 XRD spectra of CNC, CNa^+ clay and gel formed by CNa-CNC. 186

Fig. 5.3 XRD spectra of (a) calcined Pt-CNa-CNC and (b) calcined Pd-CNa-CNC..187

Fig. 5.4 FESEM images of (a) CNa^+ clay, (b) sonicated CNa^+ clay film surface, (c) CNa-CNC gel film surface and (d) CNa-CNC gel film crosssection. 188

Fig. 5.5 FESEM images of (a) un-calcined Pt-CNa-CNC, (b) un-calcined Pd-CNa-CNC, (c) calcined Pt-CNa-CNC (d) calcined Pd-CNa-CNC catalyst. 189

Fig. 5.6 TEM images of calcined (a) Pt-CNa-CNC and (b) Pd-CNa-CNC (in inset magnified images of carbon covered Pt/Pd nanoparticles).....190

Fig. 5.7 XPS carbon 1s spectra of (a) Pt-CNa-CNC (b) Pd-CNa-CNC.....192

Fig. 5.8 Cyclic voltammograms of calcined (a) Pt-CNa-CNC (b) Pd-CNa-CNC in 0.5M KOH solution at 100mV/s scan rate. 193

Fig. 5.9 Cyclic voltammogram of the prepared calcined Pt-CNa-CNC catalyst in 0.5M KOH and 0.5M methanol at 100mV/s scan rate (a) for initial 50 cycles (b) after 1000 cycles. 194

Fig. 5.10 CV of the prepared calcined Pt-CNa-CNC catalyst in 0.5M KOH and 0.5M methanol at 100mV/s scan rate (a) for initial 50 cycles (b) after 1000 cycles. ... .195

Fig. 5.11 Linear scan voltammetry (LSV) scans of calcined Pt-CNa-CNC in 0.5M KOH and 0.5M methanol solution at 100mV/s scan rate and their comparison with cyclic voltammetry of it in 0.5M KOH solution.....199

Fig. 5.12 After running 10 LSV scans, two CV cycles of calcined Pt-CNa-CNC catalyst in 0.5M KOH and 0.5M methanol at 100mV/s scan rate, starting the cycle from 0.3 V to reverse direction.....200

Fig. 5.13 Linear scan voltammetry scans with platinum wire as working electrode in 0.5M KOH and 0.5M methanol solution at 100mV/s scan rate. 201

Fig. 5.14 After running 10 LSV scans, three CV cycles of Pt wire in 0.5M KOH and 0.5M methanol at 100mV/s scan rate, starting the cycle from 0.4V to reverse direction. 202

TH-2592_156107017

Fig. 5.15 Nyquist plots of calcined Pt-CNa-CNC catalyst at different applied potential in 0.5M KOH and 0.5M methanol. 203

Fig. 5.16 Hydrogen adsorption isotherms for Pt-CNa-CNC and Pd-CNa-CNC. 204

Fig. 6.1 XPS spectra of (a) CNCs (b) C30B clay (c) uncalcined Fe-Pd-CNC grafted C30B. 219

Fig. 6.2 FESEM images of (a) Fe-Pd-CNC (b) Fe-Pd-CNC grafted on C30B clay (c) pristine C30B clay before sonication and any modification (d) nanoscrolls formed by the calcination of Fe-Pd-CNC grafted C30B clay (in inset: enlarged porous morphology of clay scrolls) and TEM images of (e) & (f) C30B clay nanoscrolls. 220

Fig. 6.3 XRD curve of C30B clay before and after sonication. 221

Fig. 6.4 Structure of cloisite-Na^{+}clay. 221

Fig. 6.5 (a) & (b) FESEM images and (c) TEM image of caterpillar shape nanoscrolls. 223

Fig. 6.6 (a) FESEM micrograph of improper scrolls formed due to low sonication time (b) TEM micrograph of tampered type scrolls formed due to more sonication time. 224

Fig. 6.7 (a) & (b) FESEM images, (c) TEM image and (d) SAED pattern of ZVI containing clay sheets. 225

Fig. 6.8 Small amount of non-uniform scrolls formed during the nitrogen atmosphere calcination of Fe-Pd-CNC grafted C30B clay material due to low content of γ - Fe_2O_3 226

Fig. 6.9 Image of calcined Fe-Pd-CNC grafted clay (a) in normal (oxygen contained) atmosphere (b) in nitrogen atmosphere. 228

Fig. 6.10 XRD curve of (a) C30B clay nanoscrolls and (b) clay supported Pd and stable ZVI nanoparticles. 229

Fig. 6.11 XRD curves of Pd and stable ZVI on clay after specific number of days of synthesis. 230

TH-2592_156107017

Fig. 6.12 XRD micrographs of C30B scrolls, prepared from Fe-CNC (without palladium loading) by calcination (Fe-C30B cal.) and Fe-CNC graft C30B clay before calcination (Fe-C30B un-calcination).....231

Fig. 6.13 Magnetic hysteresis loops of C30B clay nanoscrolls and C30B supported ZVI. 231

Fig. 6.14 Time-temperature curve for the induction heating of clay nanscroll and ZVI samples. 232

Fig. 6.15 EDX spectra of C30B clay. 234

Fig. 6.16 EDX spectra and elemental mapping of clay nanoscrolls. 235

Fig. 6.17 EDX spectra and mapping of Fe, Pd and O on clay nanoscrolls. 236

Fig. 6.18 (a) Current density potential curve for H_2O_2 reduction in 0.5M KOH solution with different H_2O_2 concentrations on clay nanoscrolls (b) comparison of current density of clay scrolls with commercial Pd-C catalyst in 0.5M KOH and 0.5 M H_2O_2 solution.....238

Fig. 6.19 Alkaline DMFC performance of the clay nanoscorlls by polarization curve and power density curve. 239

Fig. 6.19 Hydrogen adsorption isotherm of clay nanoscrolls. 240

TH-2592_156107017

List of Tables

Table: 1.1 Ion conductivity data of some of the membrane materials reported in literature. 29

Table: 1.2 Stability data of Pt and Pd catalysts reported in the literature. 46

Table: 1.3 Ion conductivity and fuel permeability results reported in literature for some of the biopolymer-biodegradable polymer based membranes. 52

Table: 2.1 Water uptake and %swelling of PVA and PVA-CS-CNC membranes. 79

Table: 2.2 Ionic conductivity, methanol permeability and selectivity of the PVA and PVA-CS-CNC membranes. 80

Table: 3.1 Amino acid composition in g/ 100g of dry sample. 99

Table: 3.2 Ionic conductivity, water uptake and %swelling of CS-modified CNC membrane. 109

Table: 3.3 Ion conductivity data of PVA based membranes with increasing temperature. 119

Table: 3.4 Methanol permeability and selectivity data of PVA based membranes at 30°C temperature. 119

Table: 3.5 Water uptake and % swelling in 0.5 M KOH solution of PVA based membranes. 119

Table: 3.6 Properties of PVA-5wt.% hair hydrolysate membrane sample before and after annealing. 123

Table: 4.1 Compositions of simulation cells prepared for different systems. 135

Table: 4.2 Density, diffusivity and conductivity of OH^-, MSD and diffusivity of methanol for each system. 143

Table: 5.1 Stability of the various electrocatalysts in alkaline medium reported in literature. 196

Table: 6.1 Hydrogen adsorption capacity of various clay based materials. 241

TH-2592_156107017

Abbreviations

AEM	Anion exchange membrane
AFC	Alkaline fuel cell
BC	Bacterial cellulose
BET	Brunauer-Emmett-Teller
C-30B	Closite-30B
CEM	Cation exchange membrane
CN	Coordination number
CNa^+	Closite-Na^+
CNC	Cellulose nanocrystals
CNF	Cellulose nanofibrils
CS	Chitosan
CV	Cyclic voltammetry
CVFF	Consistent-valence forcefield
DMA	Dynamic mechanical analyzer
DMFC	Direct methanol fuel cell
DSC	Differential scanning calorimetry
ECH	Epichlorohydrin
EDX	Energy dispersive X-ray analysis
EIS	Electrochemical impedance spectroscopy
FESEM	Field emission scanning electron microscope
FTIR	Fourier transform infrared spectroscopy
GA	Glutaraldehyde
GC	Gas chromatography
HH	Hair hydrolysate
HRTEM	High-resolution transmission electron microscopy
KAMP	Keratein derived antimicrobial peptide

TH-2592_156107017

LAMMPS	Large-scale Atomic/Molecular Massively Parallel Simulator
LDH	Layered double hydroxide
LJ	Lennard–Jones
LSV	Linear sweep voltammetry
MALDI-TOF-MS	Matrix assisted laser desorption/ionization-time of flight mass spectrometry
MCFC	Molten carbonate fuel cell
MOR	Methanol oxidation reaction
MSD	Mean square displacement
Mt	Montmorillonite
ORR	Oxygen reduction reaction
PAFC	Phosphoric acid fuel cell
PEM	Polymer electrolyte membrane
PEMFC	Polymer electrolyte membrane fuel cells
POM	Polarizing optical microscope
PPPM	Particle-particle particle-mesh
PTFE	Polytetrafluoroethylene
PVA	Poly(vinyl alcohol)
RDF	Radial distribution function
SAED	Selected area electron diffraction
SOFC	Solid oxide fuel cell
TEM	Transmission electron microscopy
TGA	Thermogravimetric analysis
TOT	Tetrahedral-octahedral-tetrahedral
VMD	Visual molecular dynamics
VSM	Vibrating sample magnetometer
XPS	X-ray photoelectron spectroscopy
XRD	X-ray Diffraction
ZVI	Zero-valent iron

TH-2592_156107017

TH-2592_156107017

Chapter 1:
Introduction and Literature Review

Fuel cells are electrochemical devices that convert chemical energy of fuels to electrical energy with low emission and high efficiency. Fuel cells have long history as their working principal was first discovered in 1839 by William Grove. Fuel cells consists three main components which are an electrolyte, cathode electrocatalyst and anode electrocatalyst. Based on the electrolyte used in the fuel cells, they have been divided in different types. Solid polymer membrane electrolyte based low operating temperature fuel cells have been in the focus due to their easy handling and possible application in different areas including household portable devices to transport systems and many more. Based on the fuel used they produce low to no pollutant during energy conversion reaction. These polymer electrolyte membrane fuel cells (PEMFCs) work in both acidic and alkaline environment based on the electrolyte membrane used. Acidic type of PEMFCs have been studied in detailed from last few decades. They have several drawbacks and some of them can be overcome by utilizing alkaline type PEMFCs, thus the fuel cell research in last few years have been increased in the area of alkaline PEMFCs. These fuel cells require an anion exchange membrane (AEM) as electrolyte and unavailability of suitable alkaline medium stable commercial membrane as well as unstable nature of electrocatalysts are some of the issues with these type of fuel cells. At the same time, the PEMFC technology has been deemed to be green, but use of the synthetic polymer electrolytes will create environmental issues. The chapter provides an introduction on the different types of fuel cells, their working principle, working conditions, advantages and disadvantages. The main focus of the research work of this thesis is on methanol fuel based PEMFCs, which are known as direct methanol fuel cells (DMFCs). In the initial part, advantages and -

TH-2592_156107017

applications of PEMFCs have been described. In the next part, introduction to DMFCs, the drawbacks of acidic DMFCs and advantages of alkaline DMFCs over acidic type have been described. The issues associated with membranes investigated in past and possible solutions to overcome them and how the biopolymer based materials can play their role have been discussed next. Different biopolymers and biodegradable polymers based membranes investigated in the past for the alkaline PEMFCs and the results described in literature for them have been reviewed. The final section of the chapter is focused on the stability issues of the commercial electrocatalysts used in the alkaline DMFCs and the possible methods described in the literature to solve the same. On the basis of different issues described in the literature for electrolyte membrane and electrocatalysts and with the motive to develop a new set of materials for alkaline DMFCs by using biomaterials to make the green fuel cell technology cheaper, greener and sustainable, the objectives for the current research work were set.

1.1 Introduction

1.1.1 Fuel Cells

Fuel cells, as mentioned earlier, are electrochemical devices that convert the chemical energy through an electrochemical reaction to directly in electrical energy and heat with low emission and high efficiency. Fuel cells have long history as their working principal was first discovered in 1839 by William Grove. The principle of fuel cells is same as that of batteries, but here fuel and oxidant are continuously consumed, so they can be used for longer run. The electrochemical reaction in fuel cells is not reversible, thus recharging is not possible. As shown in Fig. 1.1, the basic design of fuel cell comprises of electrolyte layer which is in contact with anode and cathode on either side. In a fuel cell gaseous or liquid fuels are fed continuously to the anode and an oxidant is fed continuously to the

TH-2592_156107017

cathode and electrochemical reactions take place on the electrode surface to produce electric current. During the electrochemical reaction electrons are produced on anode side, which passes through the external circuit to reach on cathode side to react with oxidant. Depending upon the charge carrier and electrolyte used the ion generated during the electrochemical reaction moves from anode to cathode or cathode to anode side. Unlike thermal engines which are limited by Carnot efficiency, fuel cells does not have any such limitations and if the heat released during the cell reactions can be utilized, the efficiency of fuel cells can be much higher compared to the thermal engines. Another advantages of fuel cells is there low emission and if hydrogen is used as fuel, it will only generate power and water without any emission. According to electrolytes used, fuel cells are divided in five different categories.

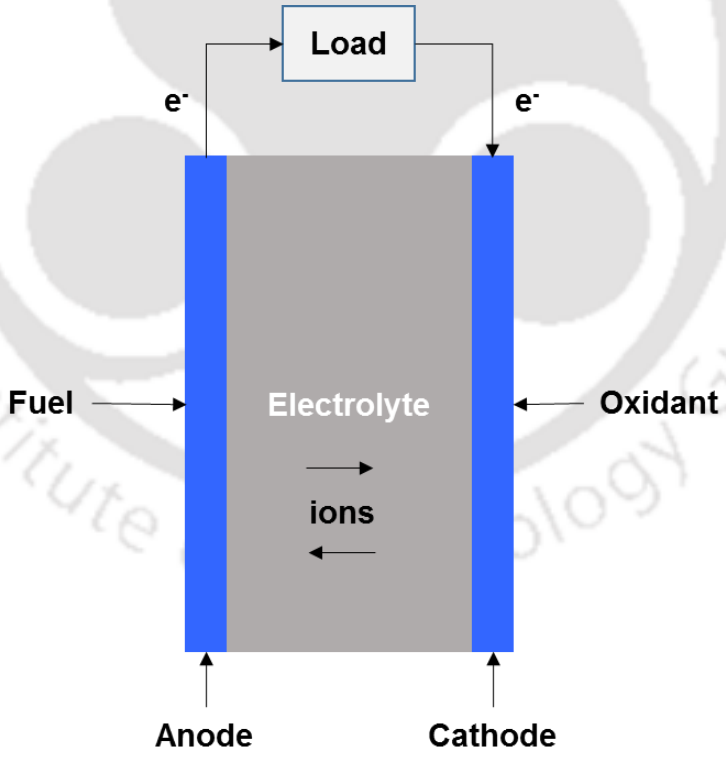

Fig. 1.1 Schematic representation of a fuel cell.

TH-2592_156107017

1.1.1.1 Solid Oxide Fuel Cells (SOFCs)

SOFCs are used for large scale power requirements such as stationary power generation units. The SOFCs which uses solid electrolyte works in the temperature range of 700–1000 °C, where the oxidic electrolyte becomes oxygen ion (O^{2-}) conducting material (Shekhawat et al., 2011). Yttria-stabilized zirconia (YSZ) is the best known candidate for the solid electrolyte used in the SOFCs (Bagotsky, 2009). The operating temperature of SOFCs depends on the conductivity of the solid electrolyte. While lower ion conductive electrolyte requires higher operating temperatures, modern thin electrolyte cell based SOFCs have reduced the operating temperature. The cell components of the SOFCs are mostly ceramic based. The anodes of these type of fuel cells consists of cermet (ceramic–metal composite) of nickel and the zirconia and the cathode consist of manganites or cobaltites of lanthanum doped with divalent metal ions, such as Sr-doped $LaMnO_3$ (Bagotsky, 2009). When hydrogen is used as fuel and oxygen is used as oxidant following are the simple reactions takes place in a SOFC:

Anode: $H_2 + O^{2-} \rightarrow H_2O + 2e^-$ (1.1)

Cathode: $\frac{1}{2}O_2 + 2e^- \rightarrow O^{2-}$ (1.2)

Overall: $H_2 + \frac{1}{2}O_2 \rightarrow H_2O$ (1.3)

The electron produced in anode side reaches to cathode through external circuit, reducing the oxygen to produce O^{2-} ions, which transfer through the electrolyte to anode side to complete the circuit. The advantages of the SOFCs includes its high efficiency (55-65%), all solid material based design allows the flexibility of engineer it, faster reaction kinetics, modest cost of materials used, possible direct use of CO as fuel and higher operating

TH-2592_156107017

temperature makes viable to use hydrocarbon based fuel via internal reforming. There are several problems associated with the SOFCs, which are complex cell and stack fabrication, high operational temperature making the start-shut down process slow, issues of safety with regard to handling of gases, electrode sintering, thermal and mechanical instability due to thermal stresses, catalyst poisoning and limited diffusion between electrode and electrolyte materials (Mahato et al., 2015) .

1.1.1.2 Molten Carbonate Fuel Cells (MCFCs)

The electrolyte used for such kind of fuel cells is molten carbonate (Li_2CO_3 and K_2CO_3) retained in a ceramic matrix of $LiA1O_2$. The operating temperature of MCFCs is in the range of 600–700 °C (Basu, 2007). Thus, similar to SOFCs, it is also lies in the category of high temperature fuel cells and the high temperature is used to have highly conductive molten salt, where ionic conduction is provided by carbonate ions. High temperature used in such type of fuel cells helps in avoiding noble metal catalysts. Nickel and nickel oxide are used as anode and cathode electrocatalyst, respectively. Following are the reactions which takes place inside a MCFC (Hoogers, 2003):

Anode: $H_2 + CO_3^{2-} \rightarrow H_2O + CO_2 + 2e^-$ (1.4)

Cathode: $\frac{1}{2}O_2 + CO_2 + 2e^- \rightarrow CO_3^{2-}$ (1.5)

Overall: $H_2 + \frac{1}{2}O_2 \rightarrow H_2O$ (1.6)

The advantages of the MCFCs include overall improved efficiency (55-65%) (Basu, 2007) by utilizing the reaction heat, noble metal catalysts are not required, possibility to utilize carbon monoxide, natural gas and various hydrocarbons directly by internal conversion to hydrogen and improved reaction kinetics. The disadvantages include difficulty in material

TH-2592_156107017

development for corrosive and mobile electrolyte, mechanical stability and cell life issues and additional source of CO_2 is required at the cathode to form the carbonate ions (Shekhawat et al., 2011; Bagotsky, 2009).

1.1.1.3 Phosphoric Acid Fuel Cells (PAFCs)

The PAFCs uses 100% concentrated phosphoric acid as electrolyte, which operates in the temperature range of 150 to 220 °C. Use of concentrated acid reduces the water vapor pressure, making water management easier in the PAFCs (Bagotsky, 2009). The catalyst used in PAFCs is platinum for both anode and cathode side. Due to lower ionic conductivity of phosphoric acid and risk of CO poisoning of Pt electrocatalyst on anode side at lower temperature, high temperature operations are preferred. The electrolyte is used in silicon carbide matrix with PTFE binder. The efficiency of PAFCs can reach up to 55% (Basu, 2007). The advantages of the PAFCs are their low sensitivity towards CO, much lower operational temperature compared to SOFCs and MCFCs allows the use of common materials to be utilized for construction and thermal management is little easier to achieve better efficiency. The disadvantages of PAFCs are slower cathode reaction kinetics making the use of platinum catalyst compulsory and highly corrosive nature of phosphoric acid.

1.1.1.4 Alkaline Fuel Cells (AFCs)

As name suggests, the AFCs uses alkaline electrolyte and KOH due to better conductivity, is generally used as electrolyte at different concentrations. Highly concentrated (85 wt.%) electrolyte solution is used for higher operational temperatures (≈250 °C), while lower concentration (35-50 wt.%) KOH electrolyte is used for lower operation temperature (Bagotsky, 2009). The alkaline environment is less corrosive compare to the acidic conditions used in PAFCs, giving opportunity to utilize a range of low cost catalyst

TH-2592_156107017

materials as well as nickel and iron alloys based structural materials. In a simple hydrogen-oxygen based AFC following reactions takes place inside the cell:

Anode: $2H_2 + 4OH^- \rightarrow 4H_2O + 4e^-$ (1.7)

Cathode: $O_2 + 2H_2O + 4e^- \rightarrow 4OH^-$ (1.8)

Overall: $2H_2 + O_2 \rightarrow 2H_2O$ (1.9)

The AFCs have advantages of possibility to utilize low cost metal catalyst, low corrosive environment increases the feasibility to utilize wide range of material for fabrication and oxygen reduction reaction kinetics is faster, which obtains higher voltage, the major drawbacks of AFCs is its high sensitivity of electrolyte towards CO_2, which requires the use of highly purified hydrogen fuel as well as highly purified oxidant (Basu, 2007).

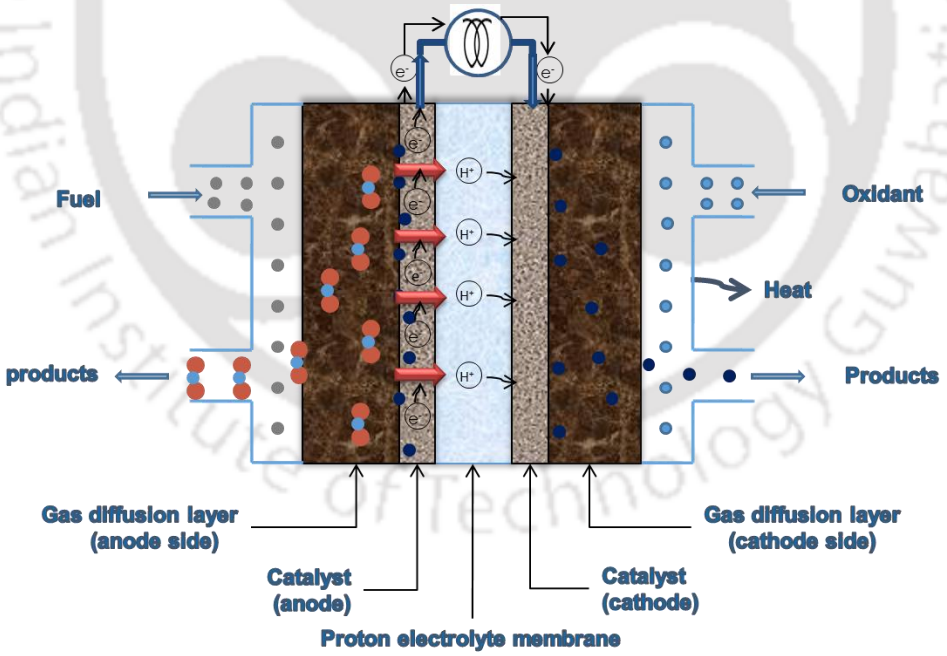

Fig. 1.2 Schematic of polymer electrolyte membrane fuel cell.

TH-2592_156107017

1.1.1.5 Polymer Electrolyte Membrane Fuel Cells (PEMFCs)

Polymer electrolyte membranes (PEMs) are used as electrolyte material in PEMFCs. Fig. 1.2 shows the schematic of basic components and working principal of PEMFCs. Solid polymer electrolyte membrane, anode and cathode side electrodes, which plays the role of electrocatalyst also and gas diffusion layers are the major components of a single cell. Perfluorosulfonated polymer membranes are commonly used as electrolyte, while platinum or its alloys supported on carbon are used as electrocatalyst. In the PEMFCs, a range of fuels can be used such as hydrogen, methanol, ethanol, formic acid and several other low molecular weight hydrocarbons and oxygen and air are the most common oxidants utilized in it. The typical reactions which take place on anode and cathode electrodes for most common fuels, hydrogen, methanol and ethanol used in PEMFCs are as follows:

Hydrogen as fuel:

Anode: $H_2 \rightarrow 2H^+ + 2e^-$ (1.10)

Cathode: $\frac{1}{2}O_2 + 2H^+ + 2e^- \rightarrow H_2O$ (1.11)

Overall: $H_2 + \frac{1}{2}O_2 \rightarrow H_2O$ (1.12)

Methanol as fuel:

Anode: $CH_3OH + H_2O \rightarrow CO_2 + 6H^+ + 6e^-$ (1.13)

Cathode: $\frac{3}{2}O_2 + 6H^+ + 6e^- \rightarrow 3H_2O$ (1.14)

Overall: $CH_3OH + \frac{3}{2}O_2 \rightarrow CO_2 + 2H_2O$ (1.15)

TH-2592_156107017

Ethanol as fuel:

Anode: $C_2H_5OH + 3H_2O \rightarrow 2CO_2 + 12H^+ + 12e^-$ (1.16)

Cathode: $3O_2 + 12H^+ + 12e^- \rightarrow 6H_2O$ (1.17)

Overall: $C_2H_5OH + 3O_2 \rightarrow 2CO_2 + 3H_2O$ (1.18)

Hydrogen is a gaseous fuel and handling it is very difficult. Especially if the fuel cells are utilized for transport applications, the hydrogen storage will take more space in vehicles. For applications where continuous electricity is required a reformer is needed to continuously generate H_2. Methanol and ethanol have been explored as alternative for H_2 fuel in PEMFCs due to their high energy density and easy handling at ambient conditions. The disadvantage of these liquid fuel based fuel cells is low power density, due to which cell voltage is generally in the range 0.25 to 0.4 V compared to ≈0.7V in case of H_2 fuel based fuel cells (EG&G, 2004). The reason for lower voltage is partial decomposition of fuels and absorption of partially decomposed products such as CO. Another reason is crossover of the liquid fuel from anode side to cathode side and their decomposition on cathode. The working temperature for PEMFCs is below 100°C, which makes them suitable for various application including automobile, stationary power generation and portable devices (Wang et al., 2011). Scheme shown in Fig. 1.3 summarizes the main applications of PEMFCs.

TH-2592_156107017

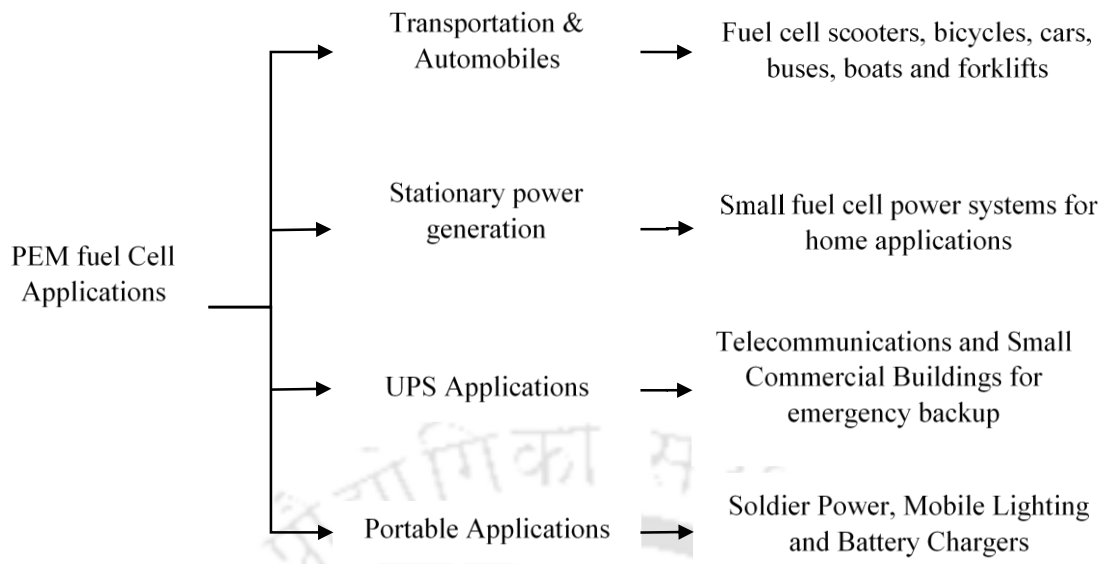

Fig. 1.3 Applications of PEM Fuel Cells.

The efficiency of PEMFCs is calculated by electric energy generated (output) and the total heat of combustion of fuel (considered as input). Total available energy for use from chemical reaction is given by Gibbs free energy:

$$\Delta G = \Delta H - T\Delta S \tag{1.19}$$

The total electric work achievable from fuel cell is given by Gibbs free energy and for electrochemical reactions it is written as:

$$\Delta G = W_{el} = -nFE \tag{1.20}$$

where n is the number of electron taking part in electrochemical reaction, F is Faraday's constant and E is the ideal potential of fuel cell. E value at a given temperature T can be calculated from the general form of Nernst equation.

$$E = E^o + \frac{RT}{nF} ln \frac{\prod(reactant\ fugacity)}{\prod(products\ fugacity)} \tag{1.21}$$

TH-2592_156107017

where E^o is the cell potential at standard temperature and pressure. As mentioned earlier in ideal fuel cell case the chemical energy converted to electric energy is given by Gibbs free energy and energy input can be taken as the enthalpy of heat of fuel. So for ideal case of fuel cell, efficiency can be calculated as:

$$\eta_{ideal} = \frac{\Delta G}{\Delta H} \tag{1.22}$$

For H_2 fuel at standard temperature 25°C and pressure 1 atmosphere, heat generated in H_2 combustion is 285.8 kJ/mole and available free energy for work is 237.1 kJ/mole (Frano, 2005). Therefore, the ideal efficiency for H_2 based fuel cells is:

$$\eta_{ideal} = \frac{237.1}{285.8} = 0.83 \tag{1.23}$$

For better understanding, generally the efficiency is calculated by using the cell operating voltage and ideal cell voltage (E_{ideal}). E_{ideal} is equal to the ΔH, total heat of combustion of fuel. Operating cell voltage is always lower than the ideal one due to various losses during the cell operations, which includes ohmic and polarization losses. The general efficiency of fuel cells can be written as (Frano, 2005):

$$\eta = \frac{Useful\ energy}{(\Delta G/0.83)} = \frac{V_{actual} \times I}{(V_{ideal} \times I)/0.83} = \frac{0.83 \times V_{actual}}{E_{ideal}} \tag{1.24}$$

Fuel cell working with H_2 fuel and O_2 oxidant, at standard temperature and pressure the E_{ideal} is 1.229. So the efficiency of H_2 fuel cells (η):

$$\eta = \frac{0.83 \times V_{actual}}{1.229} = 0.675 V_{actual} \tag{1.25}$$

This efficiency calculation considers complete conversion of fuel to final products, but in real scenario it is not the case. Fuel utilization is also be needed to include in the calculation. Efficiency in the range 50–60% can be achieved in the PEMFCs in real conditions (Basu,

TH-2592_156107017

2007). Performance of the PEMFCs are affected by the losses that happen during operation. Three major losses, which happen during operation are activation losses, ohmic losses and mass transfer losses. Activation losses occurs due to activation energy required for the electrochemical reactions on electrodes surface. Ohmic losses occur due to the ionic resistance of electrolyte and ohmic resistances of the components of cell. Similarly, mass transfer losses occur due to mass transfer restriction of fuel from bulk to electrode surface and back diffusion of products from electrode surface to bulk. These losses depends on the fuel used and their concentration, properties of electrode and electrolyte material and fuel cell operating conditions. Fuel used has huge impact on the performance of fuel cells, its selection is a critical tasks. The current study is focused on the methanol based PEMFCs, thus the same has been discussed in detailed manner in next section.

1.2 Acidic type Direct Methanol Fuel Cells (DMFCs)

The PEMFCs which instead of using methanol reformer to produce hydrogen as fuel, utilizes methanol directly as fuel are called direct methanol fuel cells (DMFCs) and the proton is charge carrier produced during the reaction are called acidic type of DMFCs. Such type of DMFCs utilize cation exchange membranes as electrolyte, where strong anion functionalities such as sulfonic acid groups, work as charge transfer site. Methanol can be produced from agricultural waste and other waste biomass, making it a sustainable source of energy. As shown in overall reaction (1.15), DMFCs only produces CO_2, along with water as byproduct, maintaining the carbon cycle without increasing the carbon footprint. DMFCs have advantages of easy to handle liquid fuel, high energy density of methanol, reformer is not required as well as membrane humidification is not required and quick start-up. This type of fuel cells suffer from low power density due to slow reaction kinetics at anode side and high fuel crossover. As represented in the Fig. 1.2, the membrane and

TH-2592_156107017

electrocatalysts work as heart and brain of the fuel cell, respectively, where electrocatalysts perform the electrochemical reactions, membrane selectively allows the proton to pass through it to make the fuel cell functional. So, the subsequent sections are focused on the membrane and electrocatalyst properties required to be utilized in DMFCs.

1.2.1 Properties Required for Polymer Electrolyte Membrane (PEM)

The major features required for polymer electrolyte membranes to be utilized in DMFCs are high ionic conductivity, low permeability to fuels, chemical stability, low electron conductivity, and good mechanical properties. For an operating system, properties such as water transport by diffusion and electro-osmosis and water uptake are important for better performance. Currently, for acidic type PEMFCs and DMFCs, expensive perfluorocarbon-sulfonic acid ionomers based membranes are utilized as PEM and Nafion® is the most common commercial membrane used. The Nafion as shown in Fig. 1.4 is the polymer of sulfonated tetrafluoroethylene, perfluorovinyl ether incorporated in it.

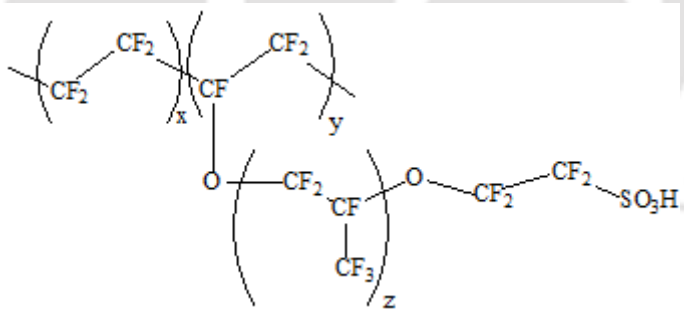

Fig. 1.4 Nafion chemical structure.

In the cation exchange type (acidic type) DMFCs, during the electrochemical reactions proton (H^+) and electrons are produced. The proton transfer in Nafion takes place through hoping on acidic ($–SO_3H$) sites. The same principal has been followed to develop different

TH-2592_156107017

electrolyte membranes for DMFCs. Following are the parameters need to be monitored for a polymer electrolyte membrane (PEM):

1.2.1.1 Ionic Conductivity

The key property of a PEM is its capability to conduct ions through the ion exchange membrane. As shown in Fig. 1.5, in an acidic DMFC membrane, proton conduction is dependent on both water content in the membrane as well as acid strength. Other parameters such as temperature, chemical structure and morphology of the membrane also have effect on proton conduction (Jiao & Li, 2011). In this type of fuel cells, the protons transfer through the membrane from anode to cathode by forming several intermediate species (H_3O^+, $H_9O_4^+$, $H_5O_2^+$) through hydrogen bonding with water molecule to diffuse through it. Here, in the proton conduction process, while acidic (anionic) sites work as driver, the water molecules work as the proton carrier. Similar kind of mechanism is considered for hydroxyl ion conduction in alkaline type DMFCs. The membrane must be non-conductive for electrons and electrons take external circuit path to reach the cathode side. Increase in the temperature creates flexibility in the membrane by reorganizing the structure, favoring faster proton transfer. If the operational temperature crosses the dew point of membranes, conductivity drops drastically due to the evaporation of water molecules. So maintaining optimum temperature is necessary for efficient operation of fuel cells (Zhang et al., 2006).

TH-2592_156107017

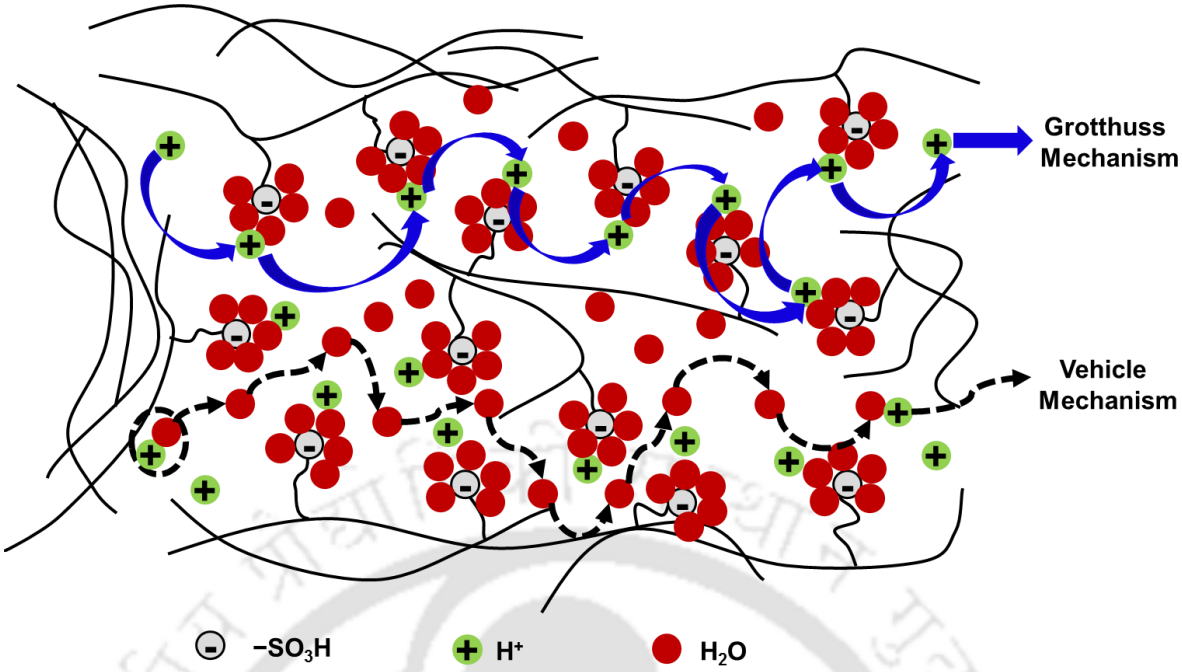

Fig. 1.5 Proton transfer mechanism in sulfonic acid containing PEMs, where the sulfonic acid works as driver and water work as charge carrier (Jiao & Li, 2011; Zhai et al., 2019).

1.2.1.2 Methanol Permeability

Methanol permeability is one of the key parameter to be taken care of in DMFC, because methanol crossover is directly related to the performance of the fuel cell. Membrane should be impermeable to reactant species, to avoid there mixing before there electrochemical reaction. But due to the membrane's porous structure, some amount of reactants does pass through the membrane. At the same time, the liquid methanol used is similar to water molecules and by electro-osmotic drag carried to cathode side. The issue of methanol crossover in DMFCs would result not only in fuel loss, but also air demand will increase, resulting in the decrease of the fuel cell efficiency due to the parallel oxidation and reduction reactions on the cathode (Zaidi and Matsuura, 2009). So, crossover of methanol through the membrane is one of the major technical hurdles in case of liquid methanol

TH-2592_156107017

based DMFCs. The factors on which methanol permeability depends are morphology and structure of membrane, its thickness and acid content, and the operating parameters of the fuel cells including temperature and fuel feed concentration. The crossover of fuel decreases with increase in the membrane thickness. So, it is advantageous to use thicker or high equivalent weight membrane to reduce methanol crossover rate. But, as the thickness increases the resistance increases, which results in high voltage lose. Moreover, a thicker membrane increases the cost of material (Liu et al., 2006). Thus, a trade-off needs to be achieved between methanol permeability and membrane resistance through optimizing the membrane thickness.

1.2.1.3 Water Management

During the electrochemical reactions in fuel cells, water is produced as byproduct in cathode side. Water content is an important parameter for operation in case of PEMFCs and for DMFCs, when methanol is supplied in vapor form. Water is compulsory for proton transfer, so maintaining optimum water content in PEMs is compulsory. But at the same time excessive water in cathode side which is result of electrochemical reaction as well as transported through membrane to cathode by electro-osmotic drag and diffusion, creates flooding problem, which slows down the oxidation reaction (Bagotsky, 2009). Similarly, the water can diffuse in the same direction as well as back diffusion to the anode side is also occurs due to the concentration gradient that happens with buildup of water at the cathode and dehydration at the anode (Jiao & Li, 2011). Water content of the membranes is affected by these processes, subsequently affecting the proton conductivity, which depends on water content. Water transport is dependent on chemical acid content of the membranes, nature of the membrane and operating temperature.

TH-2592_156107017

1.2.1.4 Chemical and Mechanical Stability

The membranes has to handle continuous varying chemical and physical environment. When the membrane comes in contact with the fuels, particularly to the liquid fuels like methanol, ethanol etc., membrane swelling increases which reduces the mechanical stability. Similarly, during the operations the membranes work under acidic or basic environment, as per the type of DMFC, which requires chemical inertness of the membrane. Diffusion of oxygen to anode side results in formation of peroxyl and hydroxyl radicals and causes chemical degradation of the membrane. Other possible mechanisms of membrane degradation are hydrolysis, oxidative attack and depolymerisation (Wilkinson et al., 2010). So, the membranes have to be stable in such harsh chemical environments and mechanically need to be strong to withstand high pressures of gaseous oxidants as well as stresses generated during shutdown process.

1.2.2 Polymer Membrane Materials for Acidic type DMFCs

As per literature, there are five different types of polymeric materials which have been utilized for cation exchange membrane (Smitha et al., 2005):

1.2.2.1 Perflourinated Ionomeric Membranes:

High electronegativity of fluorine in such polymers makes C-F strong, which gives these membrane high thermal stability and chemical inert nature. While, the present sulfonic acid groups have enhanced acidity, making these polymer materials suitable for fabrication of cation exchange membrane (Souzy & Ameduri, 2005). Nafion® membrane comes under this category.

TH-2592_156107017

1.2.2.2 Partially Fluorinated Membrane:

These membranes have fluorocarbon base and aromatic or hydrocarbon based side chain. They have lower chemical stability compared to the Perflourinated polymeric membranes, but higher mechanical strength.

1.2.2.3 Non-fluorinated Hydrocarbon Membranes:

These are the hydrocarbon polymer based membranes having polar functional groups. They have advantages of low cost, commercial availability and easy modification to add polar pendent groups. But, at the same time, they have poor chemical and thermal stability, lower ion conductivity, and high swelling problem (Peighambardoust et al., 2010).

1.2.2.4 Non-fluorinated Aromatic Membranes:

This kind of membrane have aromatic repeat unit in main chain and generally have polar side group. Such kind of membrane show good thermal, mechanical and chemical stability even at higher temperatures. They have good water adsorption as well as better proton conductivity compared to the previous case.

1.2.2.5 Acid–base Blend Membranes:

In such kind of membranes alkaline polymer base membrane is modified by incorporating acidic functionality. These membrane are shows good chemical stability in oxidative, reducing and acidic environment with good thermal and dimensional stability. These kind of membranes have shown their proton conductivity in the range of Nafion® membrane.

Other than these five major categories, several composite membranes also have been studied, which have been prepared by incorporation of various nanofillers to the polymer matrix.

TH-2592_156107017

1.2.3 Electrocatalyst for Acidic type DMFCs

Platinum based electrocatalysts are found to be suitable candidates for both anode and cathode electrocatalysts. There are several processes occur on electrocatalyst layer, which includes mass transport of reactant and products, electrochemical reaction at active sites, ion transport from the active reaction site to electrolyte membrane and electron conduction through external circuit (Basri et al., 2010). To successfully conduct these process parallelly, the electrocatalyst material requires several properties, which include highly porous nature for better mass transfer, high active surface area for faster electrochemical reaction and high electron conductivity. Carbon based supports have been utilized for Pt-catalyst to fulfill these properties requirement of electrocatalyst, where they not only provide the nano-porous structure, but also provide high active surface area for nano-electrocatalysts material with high electric conductivity. Carbon black (Vulcan XC-72R) support has been utilized in the commercial Pt-catalysts, but the carbon supports such as mesoporous carbon, carbon nanotubes, carbon nanofibers, carbon aero and xerogels with high surface area have shown better performance with lower Pt-loading (Basri et al., 2010). During the electrochemical oxidation of methanol, CO is produced as reaction intermediate, which acts as catalyst poisoning agent. To overcome this problem, Pt-based binary and ternary electrocatalysts have been investigated and Pt-Ru binary electrocatalyst has been found to be most suitable for methanol oxidation (Watanabe & Motoo, 1975; Andrew et al., 1977; Ladewig et al., 2015). Ladewig et al. (2015) and Zhang (2008) have described the different synthesis methods of metal electrocatalysts, which are detailed in brief below.

TH-2592_156107017

1.2.3.1 Impregnation Method

In this method, the metal precursors are dissolved, which are absorbed in porous carbon and then a reducing agent is used to convert the metal precursor to metal nanoparticles at optimized conditions (Goodenough et al., 1990; Román-Martínez et al, 2000). Since, the nanoparticle nucleation and growth takes place inside the support, its wetting behavior, porous morphology and pore size distribution are important for the process. This process is simple and easy to scale-up, thus it is one of the most common methods which has been utilized for electrocatalyst synthesis. The main drawback of the process is non-uniform particle size distribution and it is hard to control the shape and structure of catalyst.

1.2.3.2 Colloidal Method

Colloidal method provides precise size, shape and structural control of the prepared electrocatalyst. In this method metal colloids are prepared initially and then deposited on the carbon support (Ahmadi et al., 1996; Toshima and Yonezawa, 1998). Agglomeration of metal colloid is prevented by using stabilizing agents. These stabilizing or capping agents allows the effective size and shape control by controlling the nucleation and particle growth steps. Steric hindrance by organic compounds is used for controlling narrow size distribution. Polyol method is a sub-category of colloidal method which is used for synthesis of monometallic and multimetallic colloids in polyol or diol solvent. The solvent also works as temperature dependent reducing. In this method the precursor is reduced at higher temperatures (near to boiling point of solvent). High temperature are used for the synthesis of thermodynamically favored shapes. Preparation of nanodendrites, nanorods and nanobars of Pt with precise control, is carried out by this method (Lim et al., 2009; Xiong et al., 2002). Organic-phase method, which is also another sub-category of colloidal method, is mostly used for homogenous and controlled bimetallic nanoparticles formation

TH-2592_156107017

(Wang et al., 2007). In this method nonpolar organic solvents are used, which provide more intimate contacts to the precious metal precursors. Use of organic reducing agent in this method can reduce the transitional metal precursor completely.

1.2.3.3 Microemulsion Method

This method is used for simultaneous control on size and composition of metal nanoparticles (Shinoda & Friberg, 1975; Bommarius et al., 1990). The microemulsion is prepared by two immiscible liquids, metal precursor and a reducing agent. Reduction of metal precursor takes place only inside the small drops of precursor in liquid formed by surfactant. The microemulsion droplets having size of few hundred nanometer, works as nano reactor, giving control to the size of nanoparticles. This method cannot be used for shape control as it requires costly surfactants and multiple steps of cleaning, which is not suitable for large scale production.

1.2.3.4 Sol-gel Method

The sol-gel process requires a suspended particles liquid solution, which is aged and dried to form suspension of semi-solid material and it is finally calcined to form mesoporous powder. Pore size and pore volume are controlled by aging and calcination parameters such as time, heating rate and temperature. The metal nanoparticles are incorporated in the mesoporous structure by different methods, which includes direct inclusion of nanoparticles to sol-gel, adding the microemulsion of nanoparticles to mesoporous structure, adding of metal salts during the gel formation or after the mesoporous structure formation and subsequent reduction. The problem connected to this method is that the adsorption of nanoparticles may happen deep inside the pores and may not be accessible to

TH-2592_156107017

reactants. Thus, adding metal catalyst nanoparticles after formation of mesoporous material is a better method for electrocatalyst formation by sol-gel method.

There are several other techniques such as electrochemical deposition, spray pyrolysis, chemical vapor deposition, physical and thermal vapor deposition, which have been utilized for the electrocatalysts fabrication and reported in the literature. Large scale production by these techniques is quite difficult.

1.2.4 Issues with Acidic type DMFCs

DMFCs have advantages such as methanol is cheap fuel alternative to the hydrogen used in PEMFCs, it can be synthesized from natural and sustainable sources of biomass, it can be easily distributed by utilizing current liquid fuel distribution system and it has advantage over ethanol for low amount of intermediate formation and high probability to complete conversion to CO_2 (Wasmus & Küver, 1999; Arico et al., 2001). Along with durability and material cost, there are several issues related to materials used in acidic type DMFCs as well as its working environment, causing the overall reduction in efficiency, due to which the commercialization of acidic type DMFCs is still not possible. Issues related to the polymer membrane and electrocatalysts are discussed here.

1.2.4.1 Issues Associated with the Cation Exchange Membranes

The first and foremost problem associated with the commercially available perfluorosulfonated membranes is their high cost and no other suitable replacement with similar properties to replace them at commercial level. The commercial Nafion® membranes are chemically stable, but due to formation of highly reactive free oxygen radicals in the cathode side, causes the slow degradation of the membrane, which results in the increase of resistance, increase in the brittleness and mechanical defects in the

TH-2592_156107017

membrane (Bagotsky, 2009). The major drawback of the cation exchange membranes used in acidic DMFCs is gradual permeation of methanol fuel through the membrane. This results not only loss of methanol fuel, but resulting in the reduction of overall reaction potential due to mixed oxygen-methanol reaction taking part in the cathode side electrocatalyst. The parameters which affects the methanol permeation has already been discussed in section 1.2.1.2, which includes nature and morphology of the membrane, its thickness, temperature and fuel concentration used. As mentioned earlier the electro-osmotic drag also adds to the worries by dragging the methanol molecules along the protons to cathode side, increasing the methanol permeation. Further, the Nafion® membranes have limited working temperature range as they have several issues at higher temperatures, which includes higher methanol permeation, dehydration of the membrane resulting in the decrease in ion conductivity and humidity-induced stresses resulting in membrane failure.

1.2.4.2 Issues Associated with Electrocatalysts

Similar to the electrolyte membrane, cost of noble metal based electrocatalysts used in anode and cathode side is the major problem associated with catalyst materials. The other major problem is poor reaction kinetics of platinum towards methanol oxidation compared to the hydrogen used in PEMFCs. The poor reaction kinetics results in incomplete oxidation of methanol, which does not produce six electron transfer reaction. The poor reaction kinetic restricts the performance of DMFCs (Mallick et al., 2016). The incomplete oxidation of methanol also produces intermediates like CO, which are undesirable for Pt electrocatalyst. In the acidic medium Pt adsorbed CO is quite stable and works as catalyst poison by reducing the active surface area for electrochemical reaction (Liu et al., 2006). Pt-Ru alloy has been a good option to overcome the CO problem with acceptable catalytic activity. But, Pt-Ru alloy also has stability issues in longer run as well as when the working

TH-2592_156107017

potential is slightly shifted towards positive. It was found that, in these condition ruthenium dissolves selectively from the catalyst material in solution and penetrates in the membrane in the form of ruthenium ion, resulting in the decrease of catalyst activity (Piela et al., 2004; Sarma et al. 2007). Degradation of catalyst layers during long run also creates durability issues. The main degradation happens due to agglomeration of Pt-nanoparticles. There are reports which showed that Pt particles are dissolved in ionomer and formed bigger size particles, which happens by removal of Pt particle anchoring from the carbon support (Ferreira et al., 2005; Borup et al., 2006). Studies even found that during the cell operation Pt moved from catalyst layer to membrane, reducing the available catalyst surface area for reaction (Yasuda et al., 2006; Kim et al., 2008). The removal of Pt anchors from carbon support surface happens due the corrosive acidic environment and formation of highly active free radicals in the cathode side oxygen reaction. Other than this, impurities such as NO_x, SO_2, NH_3, H_2S and CO causes the reduction in catalyst activity by blocking the active surface area.

1.3 Alkaline type DMFCs

Alkaline type DMFCs have shown to be the best alternative of acidic type DMFCs by addressing several of the issues related to it. As per the literature costly noble metal based electrocatalysts can be replaced by low cost metal catalysts (Ryu et al., 2019). There are several other advantages of alkaline medium in DMFCs. The first one is, superior corrosion resistance of DMFC materials in alkaline medium compare to that in acidic medium. Second is, during OH^- transport via electro-osmotic drag, water is dragged away from cathode side, preventing the flooding problem. Third one is, transport of OH^- from cathode to anode will reduce the methanol crossover, which in case of acidic medium generally gets

TH-2592_156107017

dragged with H^+ ions (Scott et al., 2008). Another major advantage of alkaline medium is lower impact of electrode poisoning by intermediates formed during reaction (Basu, 2007).

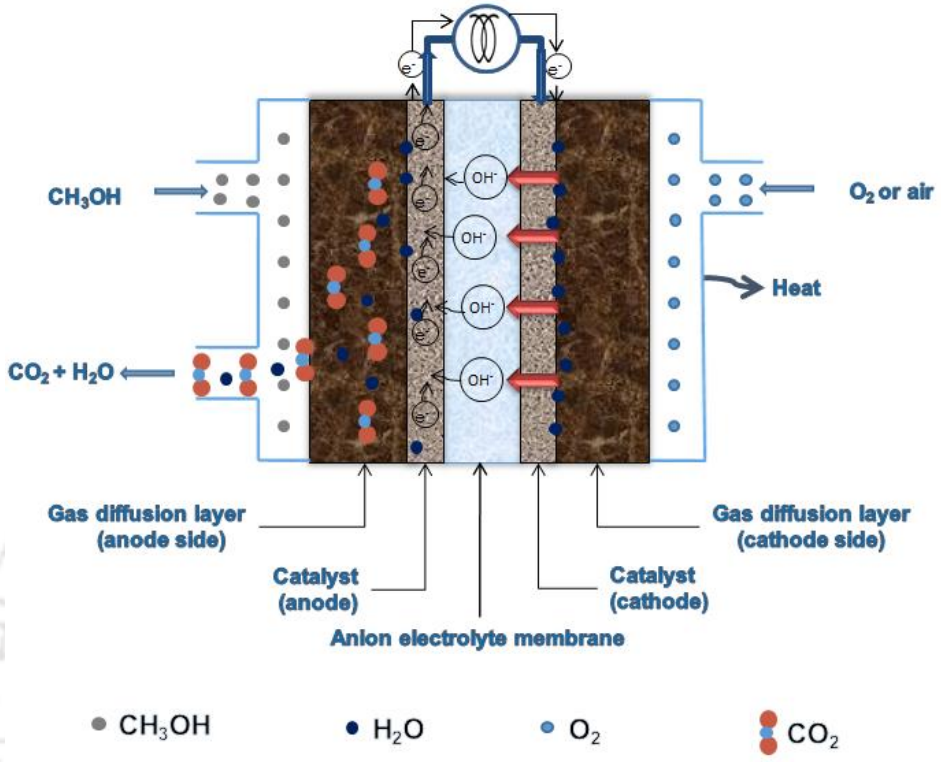

Fig. 1.6 Schematic of alkaline type DMFC.

Anode: $CH_3OH + 6OH^- \rightarrow CO_2 + 5H_2O + 6e^-$ (1.26)

Cathode: $\frac{3}{2}O_2 + 3H_2O + 6e^- \rightarrow 6OH^-$ (1.27)

Overall: $CH_3OH + \frac{3}{2}O_2 \rightarrow CO_2 + 2H_2O$ (1.28)

Fig. 1.6 is the schematic representation of single alkaline DMFC. In alkaline DMFCs the membrane used is an anion exchange membrane (AEM), which allows OH^- to pass through it. Reactions shown from (1.26) to (1.28) are the general reactions, which take place at anode and cathode in alkaline DMFC with methanol as fuel and O_2 as oxidant. The alkaline medium used in this fuel cells provides enhanced reaction kinetics for both at anode side

TH-2592_156107017

and at cathode side (Burchardt et al., 2002; Rahim et al., 2004). Basically, alkaline type DMFCs are simple AFCs where the liquid KOH electrolyte solution has been replaced by a solid polymer electrolyte AEM to overcome the issue of carbonate formation in electrolyte. Thus, alkaline type DMFCs have all the advantages of AFCs minus the carbonate formation drawback in electrolyte.

1.3.1 Membrane Materials for Alkaline type DMFCs

The ionic diffusion of H^+ in acidic type DMFCs is four time faster than the OH^- diffusion in alkaline type DMFCs. Thus, the AEMs mostly suffer from high ionic resistivity and the membrane materials have to be designed accordingly (Agel et al., 2001). For alkaline type of DMFCs, there is no equivalent suitable commercial candidate of Nafion® which is used in acidic type DMFCs (Merle et al., 2011). The same properties which required of acidic DMFC membranes are required for AEMs that includes high chemical, mechanical and thermal stability, high ionic conductivity, low electric conductivity, low methanol permeation, low thickness and high durability in alkaline medium. Similar to cationic exchange membrane which contains anions to conduct proton, the anion exchange membranes must contain strong cations to conduct the OH^- ions. In general, quaternary ammonium, quaternary phosphonium, imidazolium, guanidinium and piperazinium cations based AEMs are the common membranes which have been investigated for alkaline type DMFCs (Cheng et al., 2015). The most common membranes which are reported in literature are based on quaternary ammonium cation (R_4N^+), which are formed by radiation grafting of the cation in polymer backbone or by chemical modification of different polymers (Varcoe & Slade, 2006; Hong et al., 2008; Kostalik et al., 2010). Membranes produced by Tokuyama Corporation are one of the best known membranes having quaternary ammonium ions. They have demonstrated very good hydroxyl ion conductivity

TH-2592_156107017

at room temperature. There are several techniques which have been utilized to produce AEMs and Ladewig et al. (2015) have summarized some of these methods.

1.3.1.1 Membrane Fabrication Techniques

Polymer Functionalization: It has been one of the most frequent method utilized in literature to prepare AEMs. This method follows two steps, first is halogenation of the starting polymer material and the second is quaternization to add the quaternary ammonium or quaternary phosphonium type functional groups to the polymer chains to replace the haloalkyl groups. The method is quite simple and different choices of polymer backbone and cationic functionality can be made independently. The problem with this method is, it is hard to control the degree of functionalization.

Monomer Polymerization: It is the basic method to start the fabrication of AEMs from a monomer unit which contains the cationic functionality or works as precursor. The monomer is polymerized by ring opening or nucleophilic condensation reaction (Clark et al., 2009; Zhou et al., 2009). The method has advantage of flexibility of designing the chemical structure as well as control over degree of functionalization. The drawback is complex procedure of polymerization and several intermediate steps may require to get the purified polymeric material.

Radiation Grafting: This method utilizes non-functionalized membranes as precursor. The membranes are initially radiated with gamma rays or electron beams which creates radicals on polymer chain. Then grafting of the polymer radicals with haloalkyl-containing unsaturated monomer units is done. In the final step the polymer functionalization is done in the same way, which is followed in polymer functionalization method. The advantage of this method is that, an already prepared membrane material can be directly utilized. The

TH-2592_156107017

drawbacks of this method are stability of the prepared membranes due to radiation damage and uncontrolled grafting.

Reinforcement or Blending Method: This method has also been very common where different organic and inorganic additives have been added to the polymer matrix or two or more polymers have been mixed together to form a blend which gives overall improved properties to the final membrane. Thus, prepared polymer composites or blends are generally crosslinked to each other to provide better chemical, mechanical and thermal stability. This method is generally used where one of the component has better barrier properties and stability, but does not have good ionic conductivity, so the other is added to improve the conductivity of the membrane.

1.3.1.2 Non-commercial and Commercial AEMs

Table-1.1 summarizes the ionic conductivity data of some of the commercial and non-commercial membranes. Merle et al. (2011) have categorized the non-commercial AEMs in three categories: homogenous membranes, heterogeneous membranes and interpenetrating polymer network membranes.

Homogenous Membranes: This type of membrane are consist of single phase system, which have covalently bonded cationic charges in the polymer backbone. The cationic sites on the backbone of polymer chains are charged balanced by mobile counter ions. Based on the preparation methods, these membranes are further have three different categories. In the first category, monomer having cationic functionality or can be modified to have cationic functionality are copolymerized with non-functionalized monomers to form AEM. In the second category, cationic functionalities are introduced on an already prepared film by-grafting of functionalized monomer or grafting of non-functionalized monomer and -

TH-2592_156107017

Table: 1.1 Ion conductivity data of some of the membrane materials reported in literature.

Membrane material	Temp (°C)	Ionic conductivity (mS/cm)	Reference
PEO/KOH	25	1	Fauvarque et al., 1995
PBI/KOH	90	100	Xing & Savadogo, 2000
PEO–$[Si(OCH_3)_3]^{2+}$	25	3	Wu et al., 2008
Quaternized-Ech/PAN/DABCO	25	2	Altmeier, 1998
Quaternized/cross-linked PCMS	25	9.2	Danks et al., 2002
Norbonene/DCPD	25	28	Clark et al., 2009
PS-poly(ethylene-ran-butylene)-PS/TMA	80	9.3	Zeng et al., 2010
PMMA-co-butyl-acrylate-co-vinyl benzyl	80	8.2	Luo et al., 2010
Tetraalkylammonium functionalized PE	20	48	Kostalik et al, 2010
ETFE-FEP/PVB trimethylammonium	30	30	Varcoe, 2007
Epichlorohydrin/DABCO /TEA	25	10	Agel et al., 2001
Quaternary ammonia polysulfone	65	20	Pan et al., 2010
Tokuyama-A 201	25	29	www.tokuyama.co.jp
Tokuyama-A 901	25	11.4	www.tokuyama.co.jp

TH-2592_156107017

subsequently its functionalization. The third category consists of modification of polymer or polymer blends by introducing cationic functionalities and then dissolve to cast the film.

Heterogeneous Membranes: This kind of membranes are prepared by incorporation of cationic functional group containing material into an inert compound. Based on the nature of inert compound, these type of membranes are further divided in two categories: ion solvating polymer membranes and hybrid membranes. Ion solvating polymer membranes consist of a water soluble polymer matrix and a hydroxide salt. Potassium hydroxide is mostly used as salt in the membrane. The salt used in the matrix provides the ion conductive nature to the membrane, while the membrane works as mechanical support and fuel separator. Electronegative atoms are present in the polymer chains, which interacts with the cations of the salt. Hydroxyl ion hops through the cations present on the interactive sites. PEO based membranes which provides better interaction with salt cation are one of the example of such type of membranes. Ion conductivity of such type of membranes depends on the amount of hydroxide salt added and water content. Thus, the same membrane material with different concentration of salt shows different range of ion conductivity values. PBI based membrane prepared by ion solvating method showed extraordinary results, where the ion conductivity was improved from 0.05 mS/cm to 100 mS/cm by addition of KOH (Xing & Savadogo, 2000), which is in the same range of Nafion® membrane used for acidic DMFCs. The second category of heterogeneous membranes, which is hybrid membranes are composed of organic polymer matrix and inorganic filler. The polymer matrix provides ion exchange sites, while the inorganic filler helps in improving mechanical properties and sometime ion transport properties of the matrix. Silane and siloxane are the most common example of inorganic materials used in hybrid membranes (Wu et al., 2008).

TH-2592_156107017

Interpenetrating Polymer Network Membranes: This type of membranes have two different polymer as matrix, which are interconnected by a network formation, but do not form covalent bond with each other. They are similar to polymer blends having intertwined network of polymer chains. Due to the network structure they show good electrochemical and mechanical properties.

1.3.2 Ion Transport Mechanism in AEMs

Understanding the ion transfer mechanism is quite crucial to optimize the membrane properties. There is very low clarity on the charge transfer mechanism through AEMs, as there is little literature available. But, several studies which have been carried out in this area have proposed the similar kind of charge transfer mechanism, which is followed by protons in cation exchange membranes (Grew & Chiu, 2010; Barbir, 2005) (Fig. 1.5). It includes the hopping of OH^- ions, which is known as Grotthuss mechanism, vehicular mechanism and charge transfer by diffusion and convection. Vehicular mechanism is a simple diffusion of OH^- ions in the form of $H_3O_2^-$ which is continuously formed and cleave back to H_2O and OH^- ions by proton exchange (Takaba et al, 2017). Grotthuss mechanism involves two types of hopping of OH^-, one within water and other through surface charged sites present in polymer matrix used in AEMs. In hopping within water, oxygen of OH^- forms hydrogen bond with four coplanar water molecules and OH^- takes near perpendicular position to form $(H_9O_5)^-$ complex, which converts to $(H_7O_4)^-$ intermediate complex and reverts back to $(H_9O_5)^-$ (Tuckerman et al., 1995[a,b]) (Fig. 1.7). Hopping of OH^- is rather simpler in case of polymer matrix, where OH^- simply hops from one cationic site to another cationic site present in the polymer matrix due to ionic interaction (Chen et al., 2016). Several molecular dynamics (MD) simulation studies on OH^- transfer in AEMs have considered Grotthuss to be main mechanism for charge transfer.

TH-2592_156107017

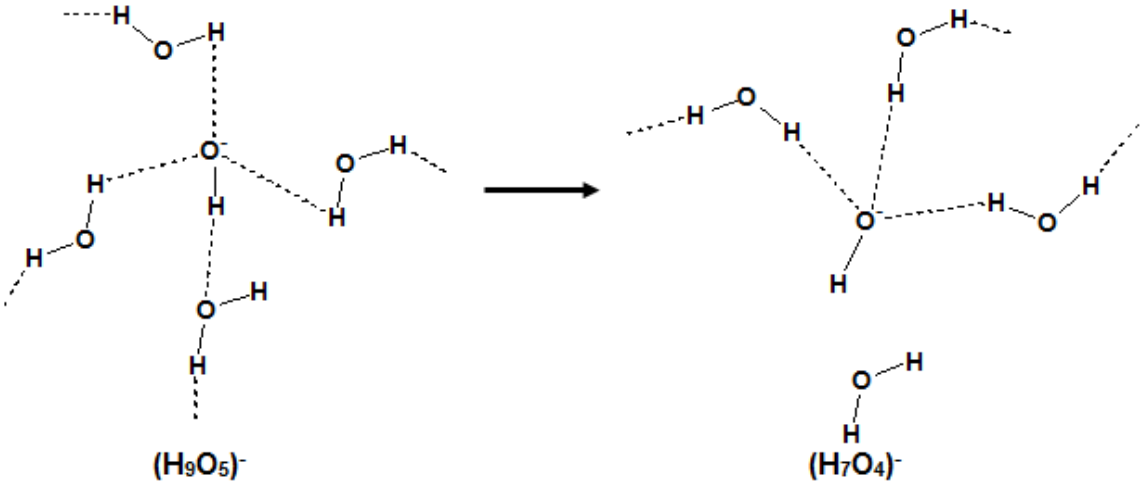

Fig. 1.7 Hydroxyl ion transport in water by formation of $(H_9O_5)^-$ and $(H_7O_4)^-$ complexes (Tuckerman et al., 1995).

Wang et al. (2018) in their MD simulation studies on OH^- transfer in amorphous polynorbornen, considered Grotthuss mechanism and mass diffusion as combined mechanism for charge transfer. Takaba et al. (2017) used poly(arylene ether sulfone ketone)s containing quaternized ammonio-substitutedfluorenyl groups (QPE) as anion exchange polymers to study OH^- transfer by MD simulation and they also observed that the hydroxide ion diffuses by hopping between ammonium groups present. Similarly, Chen et al. (2016) also evaluated hydroxide ion transport in AEMs and found significant contribution of both Grotthuss and vehicular mechanism in charge transfer. Zhang et al. (2019) also showed the importance of Grotthuss mechanism for OH^- diffusion in AEMs by atomistic-scale simulations.

1.3.3 Electrocatalysts for Alkaline type DMFCs

1.3.3.1 Electrocatalyst for Oxygen Reduction Reaction

There are two reaction paths for oxygen reduction which are followed. In the one direct 4-electron reduction takes place (1.29). In the second path 2-electron transfer reduction

TH-2592_156107017

converts oxygen to dioxidanide ions, which further goes under 2-electron transfer reduction to form hydroxyl ion (Zhang, 2008). In the alkaline DMFCs, the 4-electron reduction path is the suitable one.

$$O_2 + 2H_2O + 4e^- \rightarrow 4OH^- \quad (1.29)$$

$$O_2 + H_2O + 2e^- \rightarrow HO_2^- + OH^- \quad (1.30)$$

$$HO_2^- + H_2O + 2e^- \rightarrow 3OH^- \quad (1.31)$$

Platinum is considered as suitable candidate for oxygen reduction reaction (ORR) for both acidic and alkaline type DMFCs. But, due to faster ORR kinetics in alkaline medium, there is possibility to utilize other low cost metal catalysts. Even all carbon material show slight activity towards ORR in alkaline medium and there are several reports available for ORR activity of different carbon materials including graphite, glassy carbon, active carbon and carbon nanotubes (Yeager, 1986; Taylor & Humffray, 1975; Paliteiro et al., 1987; Zhang et al., 2004). As per the carbon type used, the reaction mechanism of ORR is also varies. Glassy carbon and pyrolytic graphite takes 2-electron reduction path to produce hydrogen peroxide, while on oxidized glassy carbon and oxidized graphite electrodes hydrogen peroxide can be further reduced to water (Taylor & Humffray, 1975; Paliteiro et al., 1987). Carbon nanotubes follows mix of 2-electron and 4-electron path to produce mixture of hydrogen peroxide and hydroxyl ions (Zhang et al., 2004). The quinone group present in the carbon materials is considered to be active catalyst site for ORR (Yeager, 1986), which led to several investigations on quinone compounds such as anthraquinone or similar kind of chemicals (Huissoud & Tissot, 1999; Gyenge & Oloman, 2003). But degradation of anthraquinone during the process makes it unsuitable for the long term application.

TH-2592_156107017

Metal catalysts are the preferred electrocatalysts utilized for ORR in alkaline DMFCs. On Pt electrocatalyst 4-electron reduction is the main ORR process considered in both acidic and alkaline medium, in which hydrogen peroxide is formed as intermediate and converted to water as final product (Marković & Ross, 2002). Due to direct 4-electrone transfer ORR reaction, Pt is preferred as electrocatalyst material and research work is mainly focused on reducing its loading. The other metal catalyst which have been considered for ORR in alkaline conditions includes Pd, Ru, Ni, Au, Ag, Co, iron-porphyrin, cobalt oxides, titanium oxide and manganese oxides (Karim & Kamarudin, 2013). While some of these non-Pt catalysts have advantage of low or no activity towards methanol in alkaline medium, preventing the occurrence of mixed potential of methanol-oxygen due to methanol diffusion, most of these catalysts follow the 2-electrone ORR or they have several other drawbacks, hindering their application in alkaline type DMFCs. Pd based electrocatalysts show the similar 4-electron ORR mechanism as shown by Pt catalysts (Ramos Sánchez & Solorza-Feria, 2010). Transition metal macrocyclic complexes also have shown promising results. These macrocyclic catalysts are mainly based on transition metals Fe, Co, Ni and Cu and sequence of their activity is Fe>Co>Ni>Cu (Zhang, 2008). Iron-porphyrin complex, iron (III) tetramethoxyphenylporphyrins (Fe-TMMP) chloride on black pearl carbon formed by heat treatment at 1000 °C have shown good ORR activity and stability in alkaline medium. The onset potential for oxygen is equivalent to the Pt and the electrocatalyst follows 4-electron ORR, similar to Pt in alkaline medium, which is remains un-affected by the presence of methanol (Gojković et al., 1999).

1.3.3.2 Electrocatalyst for Hydrogen Peroxide Reduction Reaction

Oxygen as an oxidant is supplied through open air cathode, the impurities hinders the performance of fuel cells, while pure oxygen requires compressed storage tanks reducing

TH-2592_156107017

the energy density and at the same time it has slow reaction kinetics, hindering the use of non-noble metal electrocatalysts. Due to faster reaction kinetics, liquid phase and easy handling made the H_2O_2 as alternative and attractive oxidant in fuel cells. In the alkaline medium H_2O_2 reacts with OH^- ions and forms HO_2^- ions and then it follows the reaction shown in (1.31) for electrochemical reduction. Fuel cells with H_2O_2 gives high performance and uses more compact design and thus, they have been utilized in various types of fuels cells including direct methanol–H_2O_2 fuel cell, borohydride–H_2O_2 fuel cell, metal–hydrogen peroxide semi-fuel cell, hydrazine–H_2O_2 fuel cell and biofuel–H_2O_2 fuel cell (Wang et al., 2010). Different types of catalysts have been studied for H_2O_2 reduction in alkaline medium which includes platinum, palladium, iridium, gold, silver, metal complexes such transition metal macrocycle complexes of Fe, Co, Cu and transition metal oxides (Wang et al., 2010). Pt and Pd based catalysts show high activity towards H_2O_2 reduction, but due to high cost there loading has to be significantly need to be reduced. Transition metal oxides, especially cobalt oxides have shown good performance for H_2O_2 reduction in alkaline medium (Cao et al., 2008). Perovskite materials such as $La_{0.4}Sr_{0.6}MnO_3$ (Wang et al., 2010), $Pr_{0.2}Ba_{0.8}CoO_{3-\delta}$ (PBCO), $Ba_{0.5}Sr_{0.5}Co_{0.5}Fe_{0.5}O_{3-\delta}$ (BSCF) (Bick et al., 2016), $LaCoO_3$, $LaMnO_3$ and $La_{0.8}Sr_{0.2}MnO_3$ (Poux et al., 2014), $La_{0.6}Ca_{0.4}CoO_3$ (Zhuang et al., 2012) have also shown very good activity towards H_2O_2 reduction in alkaline medium. These non-noble metal catalysts may have higher overpotential compared to the Pt-based electrocatalysts, but their low cost and insensitive nature towards methanol makes them suitable for the H_2O_2 reduction catalysts in alkaline medium (Tulloch & Donne, 2009; Miyazaki et al., 2008). Iron based electrocatalyst supported on mesoporous carbon have also shown good results for H_2O_2 reduction (Fort et al., 2013).

TH-2592_156107017

1.3.3.3 Electrocatalyst for Methanol Oxidation Reaction

Methanol crossover from anode to cathode and low activity of electrocatalysts for methanol oxidation has created the major roadblock for acidic type DMFC, which cannot compete with hydrogen based acidic fuel cell in area of electrochemical performance. While the hydrogen based fuel cells have their own issues to overcome. But, there are electrocatalysts which performs much better in alkaline medium for electrochemical oxidation of methanol. It was found that electro-oxidation of methanol is insensitive to structure in alkaline medium (Adžić et al., 1984) and the increased activity in alkaline medium provides the opportunity to utilize non-Pt based cheaper electrocatalysts such as Pd, Ag, and Ni etc. (Taraszewska & Rosłonek, 1994). The other major advantage, which is discussed earlier is, in alkaline medium the poisoning effect of methanol oxidation intermediates is not observed on electrocatalyst. The poisoning is not observed in alkaline medium due to weak bonding of intermediates on the catalysts surface and at the certain potentials alkaline medium showed a decimal magnitude higher current density compared to the acidic medium (Liu & Zhang, 2009). Similar to acidic type DMFCs, Pt-based electrocatalysts are the most investigated for methanol oxidation in alkaline medium. Liu & Zhang (2009) in their detailed review, have provided the reaction mechanism of methanol oxidation on the Pt electrocatalyst surface.

$$Pt + OH^- \rightarrow Pt - (OH)_{ads} + e^- \quad (1.32)$$

$$Pt + (CH_3OH)_{sol} \rightarrow Pt - (CH_3OH)_{ads} \quad (1.33)$$

$$Pt - (CH_3OH)_{ads} + OH^- \rightarrow Pt - (CH_3O)_{ads} + H_2O + e^- \quad (1.34)$$

$$Pt - (CH_3O)_{ads} + OH^- \rightarrow Pt - (CH_2O)_{ads} + H_2O + e^- \quad (1.35)$$

TH-2592_156107017

$$Pt-(CH_2O)_{ads} + OH^- \rightarrow Pt-(CHO)_{ads} + H_2O + e^- \quad (1.36)$$

$$Pt-(CHO)_{ads} + OH^- \rightarrow Pt-(CO)_{ads} + H_2O + e^- \quad (1.37)$$

$$Pt-(CHO)_{ads} + Pt-(OH)_{ads} + 2OH^- \rightarrow 2Pt + CO_2 + 2H_2O + 2e^- \quad (1.38)$$

$$Pt-(CHO)_{ads} + Pt-(OH)_{ads} + OH^- \rightarrow Pt + Pt-(COOH)_{ads} + 2H_2O + e^- \quad (1.39)$$

$$Pt-(CO)_{ads} + Pt-(OH)_{ads} + OH^- \rightarrow 2Pt + CO_2 + H_2O + e^- \quad (1.40)$$

$$Pt-(CO)_{ads} + Pt-(OH)_{ads} \rightarrow Pt + Pt-(COOH)_{ads} \quad (1.41)$$

$$Pt-(COOH)_{ads} + OH^- \rightarrow Pt-(OH)_{ads} + HCOO \quad (1.42)$$

$$Pt-(COOH)_{ads} + Pt-(OH)_{ads} \rightarrow 2Pt + CO_2 + H_2O \quad (1.43)$$

The reaction mechanism of methanol oxidation is quite complex and having different Pt-alloys or other metal electrocatalysts in the system also has its own effect on the reaction mechanism. The Pt-Ru alloy which helps to prevent CO poisoning and enhances the methanol oxidation kinetics in acidic medium also has positive effect in alkaline medium, but it is not as pronounce as in acidic medium (Lović, 2007). Lović (2007) proposed that for Pt-Ru electrocatalyst both in acidic and alkaline medium reaction between CO_{ads} and OH_{ads} step is the rate determining step. Here, Ru specifically forms the OH_{ads} species and selectively reacts with CO_{ads} on the Pt surface to remove adsorbed CO and thus preventing the CO poisoning. In the alkaline medium the effect of CO poisoning is may be less pronounce, but whatever small adsorbed CO amount is present, gets removed faster by the help of Ru. In the presence of Ru with Pt, the purposed reaction mechanism for methanol oxidation is as follows (Tripković et al., 2002):

$$Pt + (CH_3OH)_{sol} \rightarrow Pt-(CH_3OH)_{ads} \quad (1.44)$$

TH-2592_156107017

$$Ru + OH^- \rightarrow Ru - (OH)_{ads} + e^- \quad (1.45)$$

$$Pt + OH^- \rightarrow Pt - (OH)_{ads} + e^- \quad (1.46)$$

$$Pt - (CO)_{ads} + Ru - (OH)_{ads} \rightarrow Ru + Pt - (COOH)_{ads} \quad (1.47)$$

$$Pt - (CO)_{ads} + Pt - (OH)_{ads} \rightarrow Pt + Pt - (COOH)_{ads} \quad (1.48)$$

$$Pt - (COOH)_{ads} + Pt - (OH)_{ads} \rightarrow 2Pt + CO_2 + H_2O \quad (1.49)$$

Tripković et al. (2007) have investigated the dependence of kinetics on pH and temperature and found that the methanol oxidation activity was five time higher at 333 K than at 295 K and it was much better in alkaline medium than in acidic. They contributed the high activity in alkaline medium to pH supportive adsorption of oxygenated species. While, they found that there is not significant difference between Pt and Pt-Ru alloy in methanol oxidation reaction kinetics in alkaline medium due to slow oxidation of methanol on Ru rich surface and low amount of Pt surface available for methanol adsorption.

In non-noble metal catalysts, nickel has been most promising one due to its surface oxidation properties and it has been used in both anodic and cathodic electrochemical reactions (Liu & Zhang, 2009). There are several studies reported the use of nickel based electrocatalyst for alcohol oxidation in alkaline medium (Wang et al., 2011; El-Shafei, 1999; Wang et al., 2017; Amin et al., 2014; Tehrani & Ghani, 2009). Taraszewska & Rosłonek (1994) and El-Shafei (1999) found that modified glassy carbon-$Ni(OH)_2$ can effectively oxidized methanol in alkaline medium. El-Shafei (1999) explained that nickel oxyhydroxide (NiOOH) formed by oxidation of $Ni(OH)_2$ was acting as electrocatalyst for methanol oxidation and for low concentration of methanol reaction was diffusion controlled, while at higher concentration it was controlled by the reaction between

TH-2592_156107017

NiOOH and methanol. The methanol oxidation begins only when NiOOH has been formed. Similar kind of observation was made by Van Effen and Evans (1979), where they found that generation of a higher valence nickel oxide was acting as the oxidizing catalyst. Other than nickel, cobalt (Shobba et al., 2002) and gold (Borkowska et al., 2004) based electrocatalysts have shown methanol oxidation activity in alkaline medium. Studies on other metals and their oxides such as V, Fe, Ni, In, Sn, La and Pb did not show high enough activity for methanol oxidation in alkaline medium to be utilized (Ohmori, 1990). Some studies on perovskite materials also showed promising results (Deshpande et al., 2006; Lan & Mukasyan, 2007).

1.3.4 Issues with Alkaline type DMFCs

There are several advantages of alkaline type DMFCs over acidic type, but still there are many issues which are hindering their commercialization. The major roadblock for alkaline type DMFCs is that the commercial polymer electrolyte membranes are still under development (Merle et al., 2011). Other than that low hydroxyl ion conductivity, low chemical stability of AEMs, methanol crossover through the membrane and carbonation are also big problems for alkaline DMFC utilization (Maurya et al., 2015).

1.3.4.1 Issues Associated with the AEMs

As mentioned earlier, the ionic diffusion of H^+ in acidic type DMFCs is four time faster than the OH^- diffusion in alkaline type DMFCs. At the same time the cationic functionalities which are used in AEMs are weaker ion exchanger (weaker base) compared to its counterpart anionic functionalities in cation exchange membranes (Varcoe et al, 2014). Further, the use of electrolyte solution such as KOH is mandatory for serval membranes to have good ionic conductivity (Agel et al., 2001). Thus, the formation of carbonates which are known to create problem in AFCs, will create the same issue in case

TH-2592_156107017

of alkaline DMFCs. This includes the blocking of porous ion conductive channels of the electrolyte membrane by the formation of carbonates through reaction with hydroxyl ions, thus, reducing the ion conductivity and formation of metal carbonate crystals on gas diffusion layer, reducing the overall performance of the DMFCs (Merle et al., 2011; Watanabe et al., 2010). The carbonate formation happens due to CO_2 impurities introduced with gaseous oxidant which reacts with hydroxyl ions and KOH as shown in reaction (1.50), (1.51) and (1.52) (Varcoe et al., 2014; Gülzow, E., & Schulze).

$$CO_2 + OH^- \rightarrow HCO_3^- \quad (1.50)$$

$$HCO_3^- + OH^- \rightarrow CO_3^{2-} + H_2O \quad (1.51)$$

$$CO_2 + 2KOH \rightarrow K_2CO_3 + H_2O \quad (1.52)$$

While formation of carbonates creates above mentioned problems, formation of carbonate ions shown in reactions (1.50) and (1.51) further reduces the ion conductivity of the membrane due to slow diffusion.

Another big problem for the AEMs is their degradation in alkaline medium due to hydroxyl ion attack on the cationic functional sites, resulting in the reduction of ionic conductivity and mechanical properties (Sata et al., 1996). The most commonly used quaternary ammonium based membranes are prone to be at higher risk of hydroxyl ion attack compared to the phosphonium based membranes (Gu et al., 2009). The quaternary ammonium groups present in the AEMs are susceptible to degradation by nucleophilic attack of hydroxyl ion, as shown in Fig. 1.8 (a). In the nucleophilic substitution hydroxyl ion attacks on α-hydrogen of the ammonium cation to form alcohol and amine.

TH-2592_156107017

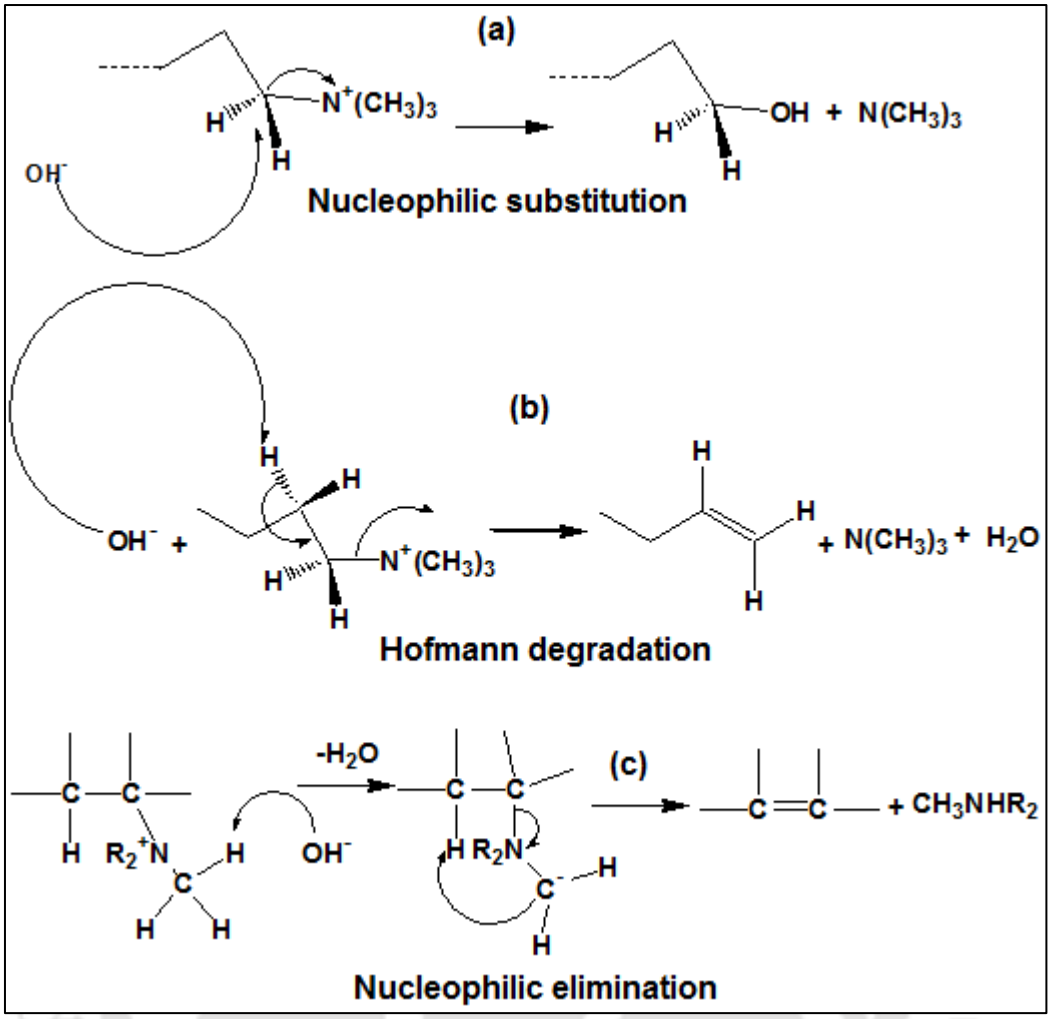

Fig. 1.8 Chemical degradation mechanism of quaternary ammonium cations by (a) nucleophilic substitution attack (b) Hofmann degradation reaction (c) nucleophilic elimination reaction (Wang et al., 2013).

The second mechanism of membrane degradation, which is known as Hofmann degradation, occurs by attack of hydroxyl ion on β-hydrogen of ammonium cation, resulting in the formation of alkene, amine and water (Cope & Trumbull, 1975) (Fig. 1.8 (b)). Hofmann degradation is temperature dependent reaction, which occurs slowly at temperature below 60 °C, but temperature around 100 °C or above it takes place at faster rate (Chempath et al., 2010). Another mechanism of degradation occurs rather rarely, in which hydroxyl ion attacks on the hydrogen of α-carbon of quaternary ammonium

TH-2592_156107017

cation, forming an alkene and an amine after rearrangement (Cope & Mehta, 1963) (Fig. 1.8 (c)). This kind of mechanism occurs when there is a bulky group attached to the cation. Other than these major problems, methanol crossover is still a problem in AEMs, which may not be as severe as in the case of acidic type DMFCs, but it still causes mixed potential at cathode and has to be avoided by using AEMs with significantly reduced methanol permeation. Several membranes which have been reported to demonstrate high ion conductivity in alkaline medium are based on ion solvating method (Xing & Savadogo, 2000; Yang & Lin, 2002; Yang, 2006). These membranes may have high ion conductivity initially, but with time KOH (or the other salt used) will leak out, reducing the conductivity of the membranes. Problems of carbonate formation, which have been discussed earlier will also increase significantly, reducing the overall performance of the membranes drastically.

1.3.4.2 Solution for the Issues Associated with the AEMs

Issue of carbonate formation in the electrolyte and electrocatalysts surface is a big issue for alkaline type DMFCs. The issue can be overcome to a large extent by utilizing a liquid fuel and oxidant. In DMFCs, mostly the methanol solution is supplied in liquid phase, but to reduce the cost, oxygen present in the air is used as oxidant, which contains the CO_2 impurity. The problem of impurities can be solved by utilizing a liquid oxidant, which will not have CO_2 impurities present. At the same time the continuous flow of liquid methanol fuel in anode side will help in the removal of CO_2 produced. Thus, system having liquid based fuel and oxidant will solve the problem of carbonate formation, the handling of the system will be easy, a more compact system can be designed and energy density can be improved. Hydrogen peroxide which is a cheap material can be used as the liquid oxidant, which will not increase the cost significantly when it is used as replacement of oxidant

TH-2592_156107017

supplied through air. Further, H_2O_2 has advantage over oxygen as oxidant, as the theoretical voltage is higher for H_2O_2 based alkaline fuel cells, compared the oxygen based alkaline fuel cells (An & Zhao, 2011), as shown below by reactions (1.53) to (1.59). Along with it, the activation energy required for two electron transfer reduction reaction of H_2O_2 is low, reducing the activation losses in the fuel cell (Miley et al., 2007).

Electrochemical reactions for the methanol-oxygen based alkaline DMFCs:

Anode: $CH_3OH + 6OH^- \rightarrow CO_2 + 5H_2O + 6e^- \quad E^0 = -0.81\,V\ vs\ SHE$ (1.53)

Cathode: $\frac{3}{2}O_2 + 3H_2O + 6e^- \rightarrow 6OH^- \quad E^0 = 0.40\,V\ vs\ SHE$ (1.54)

Overall: $CH_3OH + \frac{3}{2}O_2 \rightarrow CO_2 + 2H_2O \quad E^0 = 1.21\,V\ vs\ SHE$ (1.55)

Electrochemical reactions for the methanol-H_2O_2 based alkaline DMFCs:

Anode: $CH_3OH + 6OH^- \rightarrow CO_2 + 5H_2O + 6e^- \quad E^0 = -0.81\,V\ vs\ SHE$ (1.56)

Cathode: $H_2O_2 + OH^- \rightarrow HO_2^- + H_2O$ (1.57)

$HO_2^- + H_2O + 2e^- \rightarrow 3OH^- \quad E^0 = 0.87\,V\ vs\ SHE$ (1.58)

Overall: $CH_3OH + H_2O_2 + 4OH^- \rightarrow CO_2 + 5H_2O + 4e^- \quad E^0 = 1.68\,V\ vs\ SHE$ (1.59)

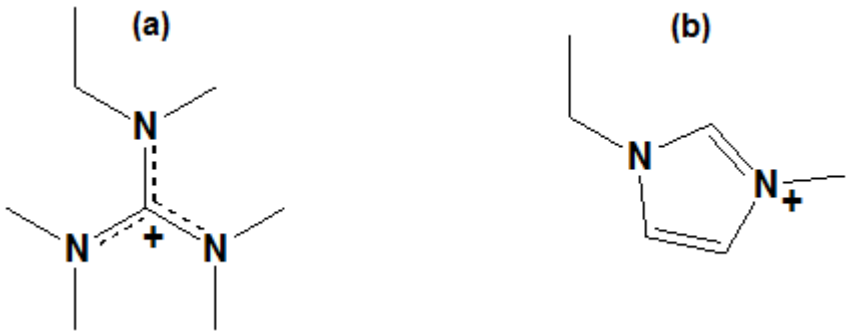

Fig. 1.9 Chemical structure of (a) guanidino cation (b) imidazolium cation.

TH-2592_156107017

To have alkaline medium stable membranes researchers are trying to utilize the cationic functionalities having mobile charge, where the cationic site is not fixed, thus site of hydroxyl ion attack is not fixed, can help in improved stability. Cationic functional groups such as guanidino cations (Fig. 1.9 (a)) having charge delocalization between one carbon and three nitrogen or imidazolium group (Fig. 1.9 (b))having conjugated π-bonds in the heterocyclic system, can be utilized for the membranes preparation to have stable AEMs (Maurya et al., 2015; Vijayakumar & Nam, 2019). Due to strong basic nature and charge delocalization guanidino cations have been reported to avoid the Hoffman degradation reaction (Liu et al., 2014). Sajjad et al. (2013) have prepared guanidinium-based anion exchange membranes by incorporating guanidinium-based polymer in to porous polytetrafluoroethylene (PTFE) and found the ion conductivity of the membrane to be around 80 mS/cm at 20°C. They also investigated the stability of the membranes in 5 M KOH solution at 55°C for 50 h and found that the prepared membranes have superior stability compared to the commercial quaternary ammonium AEMs. In another investigation by the same group (Sajjad et al., 2015), guanidinium-based polymer and chitosan blend membranes were prepared, which showed the ion conductivity of 21 mS/cm at 20°C, proving that guanidino cation is a suitable alternative of quaternary ammonium cation based membranes.

1.3.4.3 Issues Associated with the Electrocatalysts

The issues of methanol crossover and lower activity for oxygen reduction in acidic medium which requires methanol tolerant and Pt-based electrocatalyst for the respective problems can be overcome in alkaline medium up to large extent. Similarly, there is possibility even to address the lower methanol oxidation activity in acidic medium with non-noble metal catalysts, when alkaline medium is used. But, alkaline medium also has several issues

TH-2592_156107017

which need to be overcome to have better catalytic performance in alkaline DMFCs. The issue of carbonate crystal formation in membrane and electrocatalyst layer has already been discussed with possible solution to utilize liquid based fuel and oxidants. The major concern for electrocatalysts in both acidic and alkaline medium is the low stability and durability of the commercial Pt-C and Pd-C electrocatalysts in long fuel cell runs (Xu et. al., 2007). Other non-precious metal catalysts suffer from this problem even more severely. Pd-C based catalyst have been reported to be more stable in alkaline medium than the Pt-C catalyst, but Pt-C catalyst shows better activity for methanol oxidation than the Pd-C catalyst (Xu et. al., 2007). So, even Pd has much lower cost and better stability, its activity makes it slightly unsuitable for methanol oxidation. Nickel based catalysts, which have been most studied non-noble metal catalysts for methanol oxidation, requires activation of catalysts by formation of oxides prior to start of methanol oxidation. Thus, it is activation limited process and at the same time formation of excess nickel oxides inhibits its activity of electron transfer and requires reactivation (Liu & Zhang, 2009). Schulze & Gülzow (2004) tested the stability of nickel anodes in AFCs for long term use and found the decrease in electrochemical performance due to decomposition of PTFE binder and disintegration of nickel catalyst.

Au based electrocatalysts have high affinity towards hydroxyl ions and methanol has to react with the hydroxyl ion chemisorbed Au catalysts, which becomes rate limiting (Borkowska et al. 2004). For oxygen reduction reaction, Pd catalyst initially produce water as main product, but at lower potentials H_2O_2 becomes main product (Yang et al., 1995). Similar to nickel catalyst for methanol oxidation, ruthenium based catalysts suffer the reduction in activity for oxygen reduction reaction due to oxide formation on catalyst surface (Prakash & Joachin, 2000). Banham et al. (2015) have described the various-

TH-2592_156107017

Table: 1.2 Stability data of Pt and Pd catalysts reported in the literature.

Catalyst	Fuel	%Reduction Property	Reference
Pt-C	CO stripping	57% (in ECSA) After accelerated test 150 CV cycles at 100 mV/sec in alkaline sol	Zadick et al., 2015
Pd-C	CO stripping	35% (in ECSA) After accelerated test and 150 CV cycles at 100 mV/sec in alkaline sol	Zadick et al., 2015
Pd	2-propanol	≈90% CD after chronoamperometry test for 1800 s at a constant potential of at−0.4 V	Ye et al., 2007
Pd-C	Ethanol	≈27% CD after 3000 CV cycles	Xu et al., 2010
Pd_3Au-C	Ethanol	≈26% CD after 3000 CV cycles	Xu et al., 2010
PdAu-C 90:10	Ethanol	≈70% CD after chronoamperometry test for 1200 s at a constant potential of−0.2 V	Zhao et al., 2011
Pd_1Nb_1-C	Ethanol	≈45% CD after 1000 CV cycles	Souza et al., 2018
Ni–Al LDHf/G	Methanol	≈60% CD after chronoamperometry test for 1000 s at a constant potential of at 0.55 V	Wang et al., 2011

mechanism of the reduction in stability and durability of non-precious metal catalysts for ORR. Leaching of metal catalysts is the most common reason for the degradation in the performance of the metal catalysts. Fe and CO based electrocatalysts which have thermodynamic instability, suffer from this problem a lot (Schulenburg et al., 2003;

TH-2592_156107017

Van Der Putten et al., 1986). To protect the non-precious metal catalyst from leaching a protective coating has to be utilized. Another reason for the performance loss and the main reason for corrosion of carbon based support at the active sites is H_2O_2. The attack of H_2O_2 and oxidation of carbon support is proposed to happen mainly by two pathways: first is by direct oxidation by H_2O_2 and second is formation of highly active hydroxyl radicals and its attack on carbon support (Schulenburg et al., 2003; Lefèvre & Dodelet, 2003). The third reason for the performance loss which only occurs in acidic medium is by protonation of the active catalysts site on the carbon support and subsequent binding of anions (Liu et al., 2009; Herranz et al., 2011). Due to chemical instability of the carbon materials in alkaline medium due to H_2O_2 attack, they are not suitable electrocatalyst material for ORR and they cannot be used as support material for metal anode and cathode electrocatalysts for long term stability in alkaline medium. So, researchers have to be find an alternative of the carbon based support material, especially for the ORR reaction, where H_2O_2 attack is more prominent.

Pt and Pd based electrocatalyst are the only promising industrially available candidates till date for anode and cathode electrocatalysts for alkaline DMFCs due to several issues related to non-precious metal catalysts. Thus, most of the investigation are focused on to design Pt/ Pd based electrocatalysts such that there loading is reduced significantly. As mentioned earlier in this section that Pt/ Pd based electrocatalysts also suffer the instability issue in both acidic and alkaline medium. Table 1.2 shows the low stability of some of the Pt, Pd and Ni based electrocatalysts in alkaline medium, reported in literature. Zadick et al. (2015) found that the degradation of Vulcan XC-72-supported platinum nanoparticles (Pt/C) is three time faster in alkaline medium compared to the degradation in acidic medium. They observed that carbon corrosion is not the reason for the degradation of the catalyst, as severe corrosion was not seen by Raman spectroscopy. The degradation was mainly happened due

TH-2592_156107017

to loss of nanoparticles and they hypothesize that the detachment of Pt nanoparticles is happened due to change in the surface chemistry of carbon support at the anchoring site in alkaline medium, which has to be proven with further studies. As per Lafforgue et al. (2018) detachment of Pt/Pd catalyst and local corrosion of the carbon supports happens due to attack of metal carbonates formed by CO_2 on the anchoring site of catalyst. They explained that the active site for electrochemical reaction is the anchoring site of metal catalyst to the support and the reaction intermediates and final products are formed at the same site. When CO_2 is formed at the anchoring site, the Na^+ or K^+ ions present in the surrounding will react with it to form metal carbonate, subsequently breaking the anchor of metal catalyst from the carbon support. This shows that carbonates not only covers the catalyst surface by formation of metal carbonate crystal on it, they also removes it from the support, causing the leaching of catalyst nanoparticles.

1.3.4.4 Solution for the Issues Associated with the Electrocatalysts

From the discussion in the previous section, it can be concluded that leaching of metal catalyst nanoparticles can be prevented if Pt/Pd nanoparticles are supported on different nanoparticle support which is supported on the carbon. The active site has to be the Pt and intermediate nanoparticles anchoring site. At the same time the intermediate nanoparticles have to play a role in electrochemical reaction to help in removal of reaction intermediates from the catalyst surface faster, which will prevent the formation of carbonates on the Pt-intermediate nanoparticle anchoring site. Several reports have confirmed the enhancement in the catalyst stability by incorporation of different metal oxide nanoparticles with Pd/Pt catalyst (Shen & Xu, 2006; Xu et al., 2007; Xu et al., 2008; An et al., 2013). Here the metal oxides play the same role as the Ru in PtRu alloy catalyst, helping in the reaction kinetics

TH-2592_156107017

of the Pt/Pd catalysts, as shown below by reactions (1.60) to (1.65) (M=metal oxide) (Ozoemena, 2016).

$$Pd/Pt + CH_3OH \rightarrow Pd/Pt - (CH_3OH)_{ads} \quad (1.60)$$

$$Pd/Pt - (CH_3OH)_{ads} + 4OH^- \rightarrow Pd/Pt - (CO)_{ads} + 4H_2O + 4e^- \quad (1.61)$$

$$M + OH^- \rightarrow M - OH_{ads} + e^- \quad (1.62)$$

$$Pd/Pt - (CO)_{ads} + M - OH_{ads} \rightarrow Pd/Pt - (COOH) + M \quad (1.63)$$

$$Pd/Pt - (COOH) + M - OH_{ads} \rightarrow Pd/pt + M + CO_2 + H_2O \quad (1.64)$$

$$Pd/Pt - (COOH) + Pt/Pd - OH_{ads} \rightarrow 2Pd/Pt + CO_2 + H_2O \quad (1.65)$$

The metal oxides improve the reaction kinetics and help in faster removal of reaction intermediates to provide the safety to electrocatalyst from carbonate formation and subsequent activity reduction. Xu & Shen (2006) showed the improvement in the electro-kinetics by using the nanocrystalline oxide (CeO_2, Co_3O_4, Mn_3O_4 and NiO) in combination with Pd/C electrocatalyst to have a low cost electrocatalyst with better performance in comparison to the Pt/C catalyst. Further, the same group (Xu et al., 2007) investigated the effect of metal oxides on both Pd/C and Pt/C to compare the results for ethanol oxidation and they found that metal oxide promoted Pd/C electrocatalyst still out performs the metal oxide promoted Pt/C catalysts and even the PtRu/C catalyst. An et al. (2013) confirmed the mechanism earlier hypothesize in the beginning of this section, where Pt/Pd is supported on intermediate nanoparticles which are supported on carbon to have stable electrocatalyst. They used two different oxides (SnO_2 and TiO_2) with Pd on multiwall carbon nanotube (MWCNT) support. Through different analysis they found that Pd nanoparticles are uniformly distributed onto the SnO_2–TiO_2 surface which is anchored onto the MWCNT.

TH-2592_156107017

They found that the metal oxides promoted Pd electrocatalyst showed superior performance in terms of activity of electrocatalyst, electrochemically active surface area of catalyst, carbon monoxide tolerance and stability in alkaline medium for methanol as well as ethanol oxidation in comparison to the Pd/MWCNT electrocatalyst.

The problem of attack of H_2O_2 or the hydroxyl radical to corrode the carbon support will still be present even after using the metal oxide promotor, hindering the long term stability and use of carbon supported metal electrocatalysts. In such case a more stable catalyst support which can work as both, Pt/Pd catalyst promotor and stable support to the attack of H_2O_2 and hydroxyl ions can be a better option. Aluminosilicate based montmorillonite (Mt) clays having silica and alumina in the structural unit in form of tetrahedral-octahedral-tetrahedral layered structure can play the role of such metal oxides in catalysts. If the metal nanoparticles of Pt/Pd can be captured in the TOT structure of the Mt clay and carbon can be used to only enhance the conductivity of the Mt support, such combination can be a promising candidate for electrocatalysts in alkaline DMFCs.

1.3.5 Biopolymers–Biodegradable Polymers as Electrolyte Material

Most of the polymeric materials used in membrane preparation for fuel cells are based on the synthetic polymers, which are not easy to degrade. Membrane electrolyte based fuel cell technology is deemed to be green energy conversion technology, but if commercialized, it will increase the consumption of synthetic polymers, increasing the carbon footprint. So, the development of natural and bio-based sustainable polymer or biodegradable polymer based membranes will have advantage to make the green fuel cell technology greener and sustainable. In 1960 E. J. Murphy found that, cellulose, silk and wool contains ion generating sites, which when connected with water can conduct ions. Thus, these biopolymeric materials can be investigated as ion conductive material in fuel

TH-2592_156107017

cell membranes. Chitosan (CS) and cellulose are biodegradable biopolymer and poly(vinyl alcohol) is one of the synthetic polymers which is well known for its biodegradability in the presence of suitable microorganisms, under both aerobic and anaerobic conditions (Chiellini et al., 2003; Halima et al., 2016). These materials have been investigated as direct electrolyte membrane material or in combination with other polymers. CS and PVA have been used in both acidic and alkaline type of fuel cells. CS has amine group which upon protonation can form an ammonium cation, which can help in ion conduction in anionic membrane. But presence of amine group depends on degree of deacetylation of chitin and crystallinity of CS also reduces the ion conductivity of the CS membranes. Similarly, problem with PVA is that it does not contain strong cations for hydroxyl ion transport and its hydroxyl ion conductivity is not sufficient enough. Moreover, their water solvency nature creates mechanical stability issues, creating the need for addition of another component in the CS and PVA based matrixes to improve the ion conductivity and mechanical stability. There is a lot of work reported on the biopolymers and biodegradable polymers mostly focused around CS and PVA and some amount of work has been reported on cellulose, starch and alginate biopolymers. Table 1.3 summarizes some of the work reported in the literature on biopolymer-biodegradable polymer based alkaline fuel cell membranes.

Xiong et al. (2008) synthesized different combinations of cross-linked quaternized PVA and quaternized CS composite AEMs for which the maximum ionic conductivity observed was 12.5 mS/cm and methanol permeability observed was 4.42×10^{-6} cm^2/s. Feketeföldi et al. (2016) have used the same combination of quaternized PVA and quaternized CS with different crosslinking agents to form a series of membranes. The ion conductivity of such membrane was reached to 16 mS/cm, while it showed the ethanol permeability in the range of 10^{-7} $cm^2/$ s.

TH-2592_156107017

Table: 1.3 Ion conductivity and fuel permeability results reported in literature for some of the biopolymer-biodegradable polymer based membranes.

Membrane	Ionic conductivity (mS cm^{-1})	Fuel permeability (cm^2/s)	Reference
PVA/KOH PVA/glass-fiber-cloth mat/KOH	1 (30°C)	-	Lewandowski et al., 2000
	47 (25°C)	-	Yang & Lin, 2002
Crosslinked PVA/TiO_2	13.4 (70°C)	-	Yang, 2007
PVA–TiO_2–KOH	17.1 (20°C)	-	Wu et al., 2008
Quaternized-cross-linked PVA-CS	12.5 (60°C)	Methanol 4.42×10^{-6}	Xiong et al., 2008
Quaternized CS and quaternized PVA	16 (60°C)	Ethanol 3.30×10^{-7}	Feketeföldi et al., 2016
Quaternized PVA/CS/MoS_2	31.5 (30°C)	Methanol 3.37×10^{-6}	Jiang et al., 2018
CS NPs/ Quaternized PVA	40 (70°C)	Methanol 8.16×10^{-6}	Li et al., 2016
Crosslinked CS	1	-	Wan et. al., 2003
Quaternary Ammonium Modified CS	7.1 (30°C)	-	Wan et. al., 2008
CS/KOH	15.4 (30°C)	-	Wan et al., 2005
	31.4 (30°C)	-	Wan et al., 2006

TH-2592_156107017

Quaternized CS-silicatrimethyl ammonium	18.9 (80°C)	Methanol 1.5×10^{-6}	Wang & Wang., 2014
Quaternized CS/ poly (diallyldimethylammonium chloride)	37.9 (80°C)	-	Yuan et al., 2018
Quaternized CS/ functionalized carbon nanotubes	42.7 (80°C)	-	Jang et al., 2019
(BC/TiO_2/CHPTAC) Bacterial cellulose	9.3 (80°C)	-	Zeng et al.,2017
PVA-Silica gel-CNC	65 (60°C)	-	Lu et al., 2015
Quaternized CS/bi-imidazolium	41.9 (80°C)	-	Wang et al., 2015
Guanidinium/CS	21 (22°C)	Methanol $\approx7.5\times10^{-7}$	Sajjad et al., 2015

Yuan et al. (2018) studied cross-linked quaternized CS/ poly(diallyldimethylammonium chloride) blend AEMs, which showed the hydroxyl ion conductivity of 37.9 mS/cm at 80°C. More than 50% decrease in ionic conductivity was observed for the membranes in alkaline solution after 350 h, at elevated temperature of 60°C. Wang & Wang (2014) studied a series of organic–inorganic alkaline hybrid membranes using crosslinked quaternized CS as matrix and tetraethoxysilanes as inorganic filler. The methanol permeability of the membranes was in the range of 10^{-6} cm^2/s and maximum anion conductivity achieved was 18.9 mS/cm. The inorganic filler formed a network structure helping in the formation of mechanically and chemically stable membranes with low swelling. There are several other studies which have utilized quaternized CS and

TH-2592_156107017

quaternized PVA based membrane showing the ion conductivity in the same range (Wan et al., 2008; Li et al., 2016; Jiang et al., 2018; Jang et al., 2019).

García-Cruz et al. (2015) investigated mixed matrix membranes with CS matrix and different fillers including room temperature ionic liquid, metallic Sn powder, layered titanosilicate and layered stannosilicate. They achieved the maximum ionic conductivity of 12.6 mS/cm with Sn filler based CS membranes. Similar to the synthetic membranes, hydroxide salt based ion solvating technique has also been utilized with biopolymer-biodegradable polymer based membranes. In one of the earliest studies on PVA based ion solvating membranes, Lewandowski et al. (2000) have reported the use KOH to improve the ionic conductivity of PVA. The membranes having best ion conductivity were composed of 40 wt.% of PVA, 25–30 wt.% of KOH, and 30–35 wt.% of water and the conductivity was reached to 10^{-3} mS/cm range. Yang & Lin (2002) improved the ion conductivity of PVA-KOH membranes by adding glass fiber cloth mat in it, which was reached to 47 mS/cm at room temperature. Wan et al. (2006) did preliminary investigations on Cs matrix with incorporation of KOH to have good ionic conductivity. The membranes were prepared with three layers, central porous layer and two crosslinked solid surface layers on the both side of porous layer. The ion conductivity of the thus obtained membranes was reached to 31.4 mS/cm at 30°C. Yang (2007) used TiO_2 to improve the properties of PVA membrane and prepared crosslinked PVA-TiO_2 AEMs, which showed the ionic conductivity of 13.4 mS/cm at 70°C. Wu et al. (2008) prepared AEMs by utilizing KOH in PVA matrix along with TiO_2 filler. The conductivity values varied in the range of 10.2 to 17.1 mS/cm for the different combinations of the PVA, KOH and TiO_2.

Cellulose based membranes have not been much studied for the alkaline DMFC application. In one of the investigation bacterial cellulose (BC) was used in combination

TH-2592_156107017

TiO_2 and CHPTAC (3-chloro-2-hydroxypropyl trimethyl ammonium chloride) to prepare composite membranes (Zeng et al., 2017). The membrane demonstrated the ion conductivity around 9.3 mS/cm at 80°C. Lu et al. (2015) used cellulose derived cellulose nanocrystal (CNCs) as main material (60 wt.%) and PVA-silica gel as binder to prepare CNC based AEM, which showed improved ionic conductivity which was around 65 mS/cm at 60°C. Shaari & Kamarudin (2015) provided a review on alginate types of biopolymer membranes and most of them are not very promising.

As discussed above and detailed in some of the review articles (Merle et al., 2011; Maiti et al., 2012), different organic and inorganic materials have been investigated to improve these properties of PVA membranes. In organic materials, mainly polymers are used to prepare a blend with CS and PVA, which brings the environmental concerns back. Other organic materials include carbon-based nanofillers such as carbon nanotubes (Gong et al., 2019), graphene (Ye et al., 2013), graphene oxide (Lin et al., 2017) etc., cost of production of which is high and large scale production is still an issue for them. Inorganic fillers include metals, metal oxide and different metal alloy nanoparticles, different type of clays and zeolites. Some of these require pre-processing, which will increase the cost and some are less efficient in terms of ion conductivity (Merle et al., 2011). Several studies have also utilized the basic materials such as KOH by incorporating it in the membrane (Lewandowski et al., 2000; Yang & Lin, 2002; Wu et al., 2008; Yang, 2002). Such membranes have shown good conductivity, but their stability is under question as discussed in the issues with AEM section. Some of the membranes reported in the literature utilizing the guanidino cation and imidazolium cation functional groups have shown quite good stability in the alkaline medium due to the charge delocalization. Wang et al. (2015) fabricated a bi-imidazolium (N-dodecyl-imidazole and 1,4-dibromobutane) based ionic liquid which was used with quaternized CS to synthesize a novel AEM. The membrane

TH-2592_156107017

showed the ionic conductivity of 41.9 mS/cm at 80°C and long-term stability for 300 h in 1 mol/ dm^3 KOH methanol solution. Similarly, Sajjad et al. (2015) reported high chemical stability against hydroxyl group attack for Guanidinium-CS based membrane.

1.4 Knowledge Gap and Hypothesis

As discussed in the previous section, there has been already research work going to bring sustainability in the area of alkaline fuel cells through utilization of biopolymers and biomaterials, but it has not been in major focus. At the same time, the stability issues and production cost of biopolymers are other issues which may need to be considered. Use of biopolymers and bio-nanofillers produced from waste, along with the CS and PVA matrixes for the preparation of AEMs, is a good option to convert waste into wealth. Proteins and their derivatives are another categories of biopolymers, which can be extracted from plants and waste animal biomass. Proteins are well known for their charge transferability and photosynthesis is one such example. There are several reports which have described the charge transfer mechanisms for different types of proteins (Khoshtariya et al., 2003; Ahn et al., 2008; Bradley et al., 2004; Stuchebrukhov, 2009). There are few other reports as well, where amino acids are directly used to modify the nanofillers and incorporated in different polymer matrixes to prepare proton conductive membrane for acidic type fuel cells (Leem et al., 2008; Wu et al., 2012; Xu et al., 2019; Zhao et al., 2019). For the alkaline type of fuel cell membranes, it is hard to find any such report where proteins or its derivatives (amino acids, peptides) have been utilized as electrolyte. Another issue with proteins or their derivatives is their preparation and purification process, which may enhance the cost of electrolyte membrane. To overcome this issue, use of the crude proteins from waste biomass without purification and with minor thermo-chemical treatment to prepare electrolyte can be a good alternative. Some of the amino acids derived from

TH-2592_156107017

proteins have the cationic functional groups which can provide the stability to the AEMs in alkaline medium. For example, arginine has a guanidine group and histidine bears an imidazolium moiety. Thus, these amino acids or proteins rich in these amino acids can be good option for bio-based AEM. So, here we are hypothesizing that the membranes fabricated through use of various biopolymers and biodegradables polymers with incorporation of different bio-nanofillers as ion conductive source can work as suitable polyelectrolyte membrane for fuel cell application. Cellulose nanocrystals (CNCs) derived by acid hydrolysis of cellulose can work as ion conductive source as during the hydrolysis process the hydroxyl functionalities of cellulose are modified to acidic moieties. So, here in the current thesis utilization of various acid hydrolyzed CNCs in combination with PVA and CS matrix to investigate their suitability for acidic type of PEMFCs has been proposed. The focus of current thesis is on alkaline type PEMFCs, so derivation of cost effective ion conductive amino acid/ proteinic source from human hair waste and its utilization to modify the CNCs to prepare hydroxyl ion conductive fillers as well as its direct use as hydroxyl ion conductive source with PVA matrix is proposed. Investigation to understand the charge transfer mechanism through theoretical studies can further provide the mechanistic understanding of ion transfer in such protein/ amino acid based electrolyte membranes. So, to establish the possible charge transfer mechanism in such membranes, MD simulation studies are also proposed in the current thesis work.

The stability issues of electrocatalysts applied in alkaline fuel cells is another area which needs to be addressed to enhance the performance of alkaline PEMFCs. As discussed in section 1.3.4.4, the leaching of metal catalyst nanoparticles can be prevented if Pt/Pd nanoparticles are supported on different nanoparticle support which is supported on the carbon and metal oxide nanoparticles have been found to enhance the catalyst stability when incorporated with the Pd/Pt catalyst. Aluminosilicate based montmorillonite (Mt)

TH-2592_156107017

clays having silica and alumina in the structural unit in form of tetrahedral-octahedral-tetrahedral layered structure can play the role of such metal oxides in catalysts. If the metal nanoparticles of Pt/Pd can be captured in the TOT structure of the Mt clay and carbon can be used to only enhance the conductivity of the Mt support, such combination can be a promising candidate for electrocatalysts in alkaline DMFCs. Based on this hypothesis, investigation to fabricate Mt clay based support material for both anode and cathode catalysts for alkaline PEMFCs and studies to find out their performance has been also proposed in the current thesis.

1.5 Proposed Objectives and Organization of the Research Work

There are several problems associated with the membrane and electrocatalyst materials used for alkaline DMFCs, which have been discussed in this chapter. At the same time there are large number of bio-based sustainable materials which are available in the surrounding as waste or cheap resource and can be utilized to develop a new set of materials for alkaline DMFCs. With motivation to utilize these cheap bio-based materials to address the issues related membrane and electrocatalysts for alkaline type DMFCs and make the already deemed green fuel cell technology cheaper, greener and sustainable, the following objectives were formulated for the current research:

- Synthesis and characterization of cheaper bio-based ion-conductive materials focused on alkaline anion exchange membrane fuel cells.
- Fabrication of polymer electrolyte membrane with bio-based ion conductors and its characterization for direct methanol fuel cells.
- Molecular dynamics simulation studies on the possible charge transfer mechanism in the fabricated polymer electrolyte membrane.

TH-2592_156107017

- Study the possible application of montmorillonite clays to fabricate Pt/Pd based stable anode electrocatalyst for methanol oxidation in alkaline medium.
- Fabrication of significantly low Pd based cathode electrocatalyst for electrochemical reduction of hydrogen peroxide in alkaline medium.

These objectives have been addressed and the outcome has been discussed in the subsequent chapters which are organized in the following manner:

Chapter-2: **Primary Investigation on Cellulose Nanocrystals based Ion Conductive Materials**

The chapter details about the use of CNCs produced from different acid hydrolysis in the PVA-CS matrix to prepare a proton exchange membrane. Further, the effect of CNCs different morphologies arriving from different acid hydrolysis on membrane properties related to DMFCs have been investigated. The chapter explains the fabrication and characterization of bio-based ionic conductive materials, the polymer electrolyte membranes prepared by it.

Chapter-3: **Human Hairs based Anion Exchange Membrane for Alkaline DMFCs**

The chapter is focused on the synthesis of human hair derived ion conductive material by simple and green thermal hydrolysis process and its application in PVA matrix to prepare an AEM is discussed.

Chapter-4: **Anion Transport in Human Hair Peptide-based System by Molecular Dynamics Simulation**

This chapter reports the investigations on the possible charge transfer mechanism in the system similar to one that has been studied experimentally in previous chapter by MD

TH-2592_156107017

simulation. Here a model human hair derived peptide has been used with PVA matrix, which has the cationic functional group, that are present in hair hydrolysate obtained from human hair in previous chapter.

Chapter-5: **Stable CNC-Clay Supported Pt/Pd Catalyst for Methanol Oxidation in Alkaline Medium**

The chapter is focused on development of clay based support for Pt/Pd electrocatalyst as an alternative to commercially available electrocatalysts which are unstable in alkaline medium.

Chapter-6: **CNC-Clay based Cathode Electrocatalyst for H_2O_2 Reduction in Alkaline medium**

This chapter discusses synthesis process for CNC-clay nanoscrolls, which are used for cathode side electrocatalyst for H_2O_2 reduction in alkaline medium. Further, the use of prepared nanscrolls in hydrogen adsorption has been shown. In similar method by altering the calcination environment production of highly stable ZVI is discussed and its possible application in biomedical area by induction heating has been shown.

Chapter-7: **Conclusions**

This section summarizes the key results, discuss the fundamental issues and technological problems addressed related to DMFCs. It also discusses the encouraging results obtained by using bio-based and sustainable materials for the DMFC applications and how the properties obtained by these materials can be further improved to make them usable in commercial level.

TH-2592_156107017

Chapter 2:

Primary Investigation on Cellulose Nanocrystals based Ion Conductive Materials

Graphical Overview

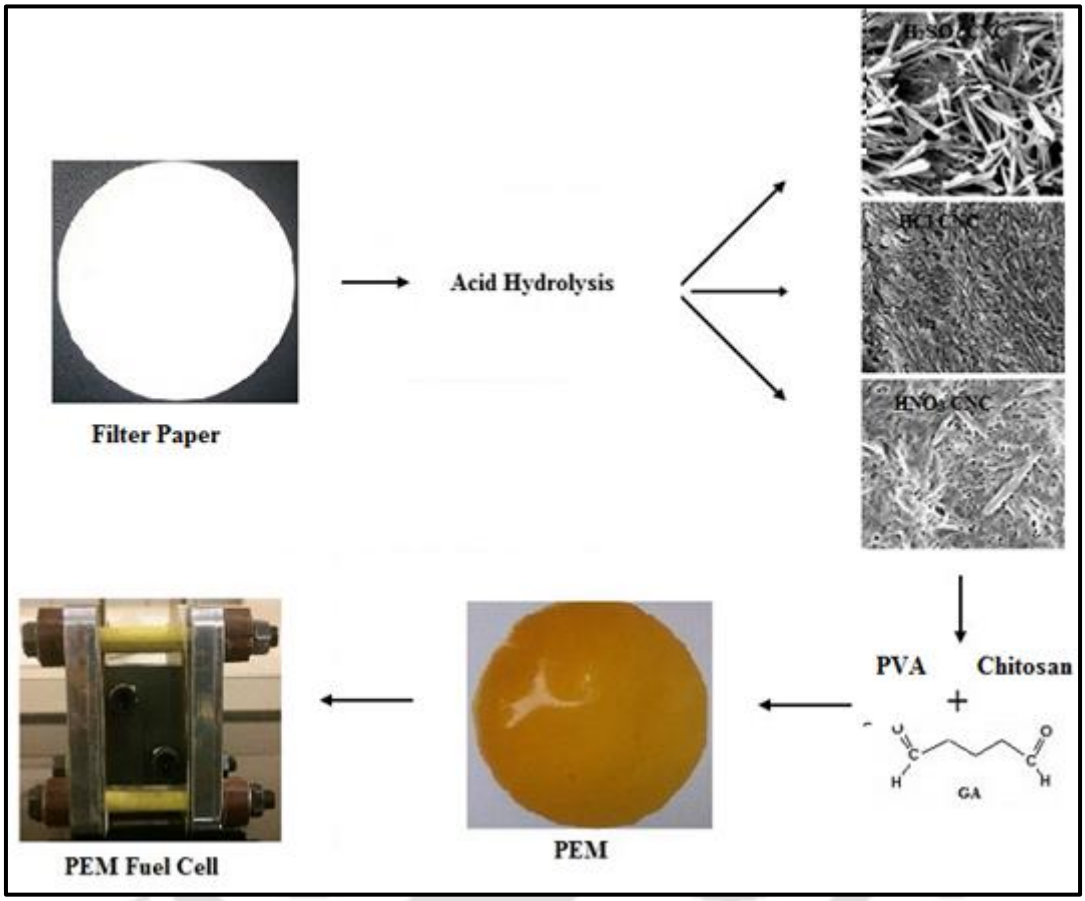

Cellulose is one of the most abundant renewable biopolymer available in nature. Cellulose nanocrystals (CNCs) are the crystalline domain of the cellulose having one of its dimension in nanosize, generally produced by acid hydrolysis. Use of different types of acids for cellulose hydrolysis gives different type of morphology. At the same time CNCs have different functionalities and are hydrophilic in nature. Possibility of large scale production due to abundant availability and its properties makes CNCs attractive material to be studied for its application in fabrication of polymer electrolyte membrane (PEM)-

Publication:

- Gaur, S. S., Dhar, P., Sonowal, A., Sharma, A., Kumar, A., & Katiyar, V. (2017). Thermo-mechanically stable sustainable polymer based solid electrolyte membranes for direct methanol fuel cell applications. *Journal of Membrane Science*, 526, 348-354.

TH-2592_156107017

for fuel cell. Keeping it in mind, in this study we have utilized CNCs having different morphologies due to production by different acid hydrolysis, to fabricate a PEM for cationic direct methanol fuel cell (DMFC). The objective of the study is to check the possible use of CNCs as ion conductive material and effect of different morphologies of CNCs on the properties of the poly(vinyl alcohol)-chitosan matrix based PEM. Membranes fabricated as part of this work are eco-friendly in nature and also broaden the scope for using biodegradable poly(vinyl alcohol) (PVA) with biopolymer materials such as chitosan (CS) and CNCs based technologies for future direct methanol fuel cell applications. The different acid functionality (due to different acid hydrolysis) and morphological dimensions of CNCs have an impact on water uptake (varying in the range: 68%–253%), swelling behavior (varying in the range: 5%–50%) and ion conductivity (varying in the range: 3.58×10^{-5} – 6.42×10^{-4} $S.cm^{-1}$) of the prepared membranes. Dynamic mechanical behavior analyses confirms that the PVA-CS-CNC membranes are found thermo-mechanically stable under dynamic load up to 120°C which is well above the required fuel cell operating temperature. Although, crosslinking of the membranes have adversely converted crystalline phase of the membranes into amorphous, however the incorporation of CNCs, a crystalline nano-fillers in PVA matrix created tortuous path which suppressed the methanol permeability to 3.12×10^{-8} cm^2 s^{-1} that is significantly lower than that for the base PVA membrane methanol permeability $4.19\times10^{-7}cm^2$ s^{-1}.

2.1 Introduction

Although the perfluorinated ionomer membranes used in DMFCs have high proton conductivity, good chemical and mechanical stability, they suffer from the issues of high methanol permeability, high cost and environmental inadaptability (Wang et al, 2008). So there is a need for developing low cost alternative membranes with improved properties,

TH-2592_156107017

which can serve the purpose of solid electrolyte membranes and provide better environmental sustainability. Significant research effort has been devoted to this area for the last few years. Modification of perfluorinated ionomer membranes, functionalized non-fluorinated membranes and their composites and acid–base composite membranes are the several alternatives reported in literature reviews (Peighambardoust et al., 2010; Mehta & Cooper, 2003; Smitha et al., 2005). One of the polymeric materials, which has been studied extensively for PEM applications is poly(vinyl alcohol) (PVA). PVA has good chemical resistance, mechanical stability, low cost and after crosslinking, it is stable in aqueous phase at high temperature (Kim et al., 2006). But PVA is poor ionic conductor as it does not contain ionic conduction sites. So incorporation of groups like amine, carboxylate, sulfonate, phenolic, and quaternary ammonium salts is necessary to enhance the ionic conductivity (Sahu et al., 2008). Poly styrene sulfonic acid, phosphotungstic acid, sulfosuccinic acid, poly(acrylic acid), sulfonated poly(ether ether ketone) (SPEEK) and many other combinations have been tried with PVA to prepare ion conductive PVA composite PEMs (Yang et al., 2014; Bhat et al., 2009; Yang, 2011; Rhim et al., 2014; Yang, 2008; Li et al., 2003; Wu et al., 2006).

Chitosan (CS) is a biopolymer which has also been used with PVA to investigate the combination for PEM application. CS is an easily available material, which is produced from deacetylation of chitin and known for its good barrier properties (Caner et al., 1998). Along with this, it contains amine group in the backbone, which makes it ion conductive. PVA-CS based membranes have been reported to have good ion conductivity and methanol barrier properties (Danwanichakul & Sirikhajornnam, 2012; Palani et al., 2014; Meenakshi et al., 2012). The problem with PVA and CS based membranes is their stability at higher temperatures in the presence of moisture, which can be solved by crosslinking (Torres et al., 2007). Glutaraldehyde (GA) has been used as crosslinking agents for both

TH-2592_156107017

PVA and CS (Filipkowska & Jóźwiak, 2013; Bhat et al., 2009). However, crosslinking using GA causes the amino groups of CS to get crosslinked, which results in reduction of ionic conductivity of the membranes. To improve the ion conductivity, addition of a material containing ion-conductive functional groups is required. In 1960, Murphy (Murphy, 1960) reported that biopolymers such as cellulose, silk and wool contains ion generating sites, which when connected with water can conduct ions. So, here CNCs have been used as conductive material with PVA-CS matrix, which also have ability to provide excellent dimensional stability to the membrane. Other than that, we have used CNCs in PVA along with CS with an aim to improve the thermo-mechanical, methanol barrier properties, swelling characteristics and ion conductivity of the base PVA membrane, so that the prepared membrane can be utilized for DMFC applications. CNCs are bio-fillers with high aspect ratio and abundant hydroxyl functional groups, which improves the filler-matrix interaction. After protonation, the CNC containing nanocomposite membranes will have improved ionic conductivity due to the acquired cationic moieties during protonation. To investigate the effect of CNCs produced by hydrolysis using different acids, on the properties of base PVA membrane, we have conducted the study with three types of CNCs produced by using H_2SO_4, HCl and HNO_3 acids. Use of these acids results in CNCs having different size and aspect ratio, which are expected to interact differently with the polymer matrix when used as filler material. The prepared membranes have been characterized by using thermogravimetric analysis (TGA), differential scanning calorimetry (DSC), Fourier transform infrared spectroscopy (FTIR), field emission scanning electron microscopy (FESEM) and X-ray diffraction spectroscopy (XRD). Ion conductivity is measured by impedance spectroscopy. Methanol permeability experiment has been carried out in a double cell diffusion setup and permeability is quantified by gas chromatography (GC).

TH-2592_156107017

2.2 Experimental Section

2.2.1 Materials

PVA (99% hydrolyzed and M_w in the range 89000–98000 Da), CS (medium molecular weight), whatman filter paper (grade 1) and dialysis tubing cellulose membrane were purchased from Sigma-Aldrich, India. Sulfuric acid (H_2SO_4), hydrochloric acid (HCl) and nitric acid (HNO_3) were obtained from HiMedia Laboratories, India. Acetic acid (glacial) was procured from SISCO Research Laboratories, India and glutaraldehyde (GA) was purchased from Rankem, India.

2.2.2 Fabrication of Cellulose Nanocrystals (CNCs)

CNCs were synthesized by acid hydrolysis of whatman filter paper (grade 1) as reported in earlier studies (Dhar et al., 2016[a]; Dhar et al. 2016[b]). In each case of CNC preparation, 2 gm of filter paper was initially chopped into small pieces and sonicated at 20% amplitude to form a cellulosic slurry. In the case of hydrolysis with hydrochloric acid, HCl (6 M, 120 ml) was taken and the sonicated pulp was mixed in it. The mixture was stirred for 6 h at a temperature of 110°C. For H_2SO_4 acid hydrolysis 1:1 volume ratio of acid and water was taken to make a final concentration of 64 wt.% of H_2SO_4 and the chopped filter paper was mixed under stirring for 2 hours at room temperature. Similarly in the case of acid hydrolysis with HNO_3, the cellulosic slurry was reacted with the nitric acid (6 M, 50 ml) under vigorous stirring for ≈4 hours. After preparation of CNCs, the excess acid has to be removed to bring the CNC suspension at a pH of ≈7. For this purpose dialysis process was used. The acidic solution containing the CNCs was taken in a dialysis tubing cellulose membrane (cut of molar mass ≈14,000 Da, Sigma Aldrich, India) and kept in a water bath. The neutralized CNC solution was centrifuged and excess water was removed from the

TH-2592_156107017

solution and the thick precipitate was freeze dried to get the CNCs in powdered form. The CNCs thus prepared were used for further characterization and nanocomposite PEM formation. The CNCs prepared by H_2SO_4, HCl and HNO_3 hydrolysis are hereinafter represented as H_2SO_4-CNCs, HCl-CNCs and HNO_3-CNCs respectively.

2.2.3 Membrane Preparation

The membranes were prepared by solution casting method. The same weight percentages of the different components were maintained in each case, namely 46.5 wt.% PVA, 46.5 wt.% CS, 5 wt.% CNCs (fabricated using different acids) and 2 wt.% GA. PVA was dissolved in water at 85°C under stirring and CS was dissolved in 2 vol.% glacial acetic acid solution at the same condition. Each type of acid-derived CNCs was taken in 10 ml glass vial with water and sonicated for 1 hour for proper dispersion. After dispersing CNCs in water, PVA, CS and CNCs were mixed at room temperature at high stirring speed (1000 rpm) for 30 minutes, which was followed by addition of GA in the solution and further stirring for 15 minutes. GA was added to crosslink the PVA-CS matrix as it is unstable in water at higher temperatures. The resulting final solution was poured in Teflon petri dishes and dried at room temperature in fumehood to get the dried membranes. All the membranes were prepared under identical conditions. The membranes were further dried in hot air oven at 50°C overnight to remove the remaining moisture before further characterization. On the basis of type of CNCs added in the membranes, here onwards they are represented as PVA-CS-H_2SO_4 CNC, PVA-CS-HCl CNC and PVA-CS-HNO_3 CNC membranes for H_2SO_4-CNCs, HCl-CNCs and HNO_3-CNCs respectively. The term PVA-CS-CNC is used to represent all the CNC based membranes in general.

TH-2592_156107017

2.2.4 Methanol Permeability Experiment

Methanol permeability experiment was carried out in a double cell diffusion system reported by Gaur et al. (2014), in which membrane was sandwiched between two cells. One cell contained deionized water and the other cell contained 5 mol. % methanol–water solution. Liquids in both the cells were kept under stirring to maintain the concentration uniform within the cell. The experiments were carried out for 24 hours and samples were taken out from the water side at regular time intervals to determine the amount of methanol permeated from methanol side to water side. Variation in concentration of methanol on the water side was measured by gas chromatography (GC). The permeability of each combination was calculated by taking average of 3 samples.

2.3 Characterization

2.3.1 Thermal and Thermo-mechanical Analysis:

Thermal stability of the membrane samples was analyzed by TGA. TGA analysis was done with a PerkinElmer Thermogravimetric Analyzer TGA 4000 system in the temperature range 30°C–700°C at heating rate of 10°C/ min. under N_2 atmosphere. DSC analysis was utilized to investigate the variation in properties such as morphology and melting or degradation temperatures of the membrane samples. DSC was done in a NETZSCH DSC 204 F1 Phoenix system in heating-cooling-heating cycle under N_2 atmosphere. First heating cycle was run in the temperature range 20°C–100°C at 10°C/ min. heating rate, to remove the physically or chemically bound moisture. The samples were maintained at 100°C for 3 min. and then cooling was done at 20°C/ min cooling rate to bring the sample back to 20°C temperature. Second heating cycle was run in the temperature range 20°C–250°C at 10°C/ min heating rate. To check the mechanical

TH-2592_156107017

stability of the membranes at higher temperatures with dynamic force application, thermo-mechanical studies were carried out using DMA (NETZSCH DMA 242 E model) in the temperature range 25°C–140°C at 3°C/ min. heating rate, 1 Hz frequency and 10 μm displacement amplitude.

2.3.2 Surface Morphology, Crystal Structure and FTIR Studies

Surface morphology, shape and size of the prepared CNCs were investigated by FESEM, a SUPRA ultra-high resolution FESEM system from Carl Zeiss. The crystallography study of the PEMs was conducted using a Bruker D8 advance system for 2θ angles in the range of 5–50° with Cu-K alpha electron source. Structural differences between different CNCs, chemical changes in the PVA matrix due to addition of CS and crosslinking agent GA, along with the interaction of the added CNCs with the polymer matrix were analyzed by FTIR (a PerkinElmer Frontier FT-IR Spectrometer system). The scanning wavenumber range was kept in the range 4000cm^{-1}–500cm^{-1}.

2.3.3 Water Uptake and Swelling Behavior:

Water uptake of the dried solid electrolyte membranes was measured by immersing 3 stes of each sample in water for 24 hours and after that excess surface water were removed using tissue paper and thereafter checking the water absorbed by the samples. Equation-2.1 was used for the water uptake calculation by taking averahe of three samples:

$$Water\ uptake\ (\%) = \frac{W_{wet} - W_{dry}}{W_{dry}} \times 100\% \qquad (2.1)$$

where W_{dry} is the dry membrane weight and W_{wet} is the weight of wet membrane. % swelling of the membranes was calculated by the same experiment, where changes in the membrane dimensions after taking out the samples from water after 24 hours were

TH-2592_156107017

measured for the calculation. Equation-2.2 was used for the calculation of the % swelling and average of 3-samples was taken as result.

$$\%\ swelling\ = \frac{L_{wet} - L_{dry}}{L_{dry}} \times 100\% \quad (2.2)$$

where L_{dry} is the length of the sample in a particular direction in dry state and L_{wet} is the length of the sample in the same direction after taking out from water.

2.3.4 Ionic Conductivity:

Ionic conductivity measurement of the PEM samples was carried out using impedance spectroscopy (Autolab PGSTAT204 system from Metrohm). Protonation of PEMs was done by immersing them in 2M H_2SO_4 solution for 24 hours. The membranes were then washed with deionized water three times. A single cell system of 5cm×5cm size, procured from Anabond Sainergy Fuel Cell India Pvt. Ltd., Chennai, India was used for ion conductivity measurement. The membranes of 25 cm^2 area were soaked in water for 24 h and fitted in between copper electrodes of single cell. The impedance measurements were carried out in the frequency range 1 Hz–1 MHz at room temperature. The ion conductivity (σ) was calculated by equation-2.3 using the resistance of the membranes (R) obtained from impedance data, membrane area (A) and thickness of the membranes (L) and taking average of 3-samples.

$$\sigma = \frac{L}{R \times A}\ (S\ cm^{-1}) \quad (2.3)$$

2.3.5 Methanol Permeability and Selectivity

The samples collected from methanol permeability experiment were analyzed by GC (a Bruker 450–GC system) in CP-Chirasil-Dex CB column from Agilent Technologies and

TH-2592_156107017

flame ionization detector (FID) was used for detection of methanol. The temperature at injection, column and detection point were kept 120°C, 85°C and 150°C respectively and 2µl of the samples was injected in GC for methanol detection. A calibration curve of the known concentrations of methanol was used to determine the unknown concentration of the samples collected during methanol permeability experiment. Methanol permeability (P) was calculated by using the slope of curve (k) plotted between concentration of methanol on the water side and corresponding permeation time, initial volume of deionized water (V), membrane thickness (L), area of permeation (A) and initial concentration of methanol (C_A), from equation-2.4.

$$P = \frac{k \times V \times L}{A \times C_A} \ (cm^2\ s^{-1}) \qquad (2.4)$$

Selectivity of the samples is the ratio of ionic conductivity (σ) and methanol permeability (P), higher the selectivity, more suitable is the membrane for DMFC application.

2.4 Results and Discussions

2.4.1 Thermal and Thermo-mechanical Analysis:

Thermal degradation studies shown by TGA thermograph in Fig. 2.1 suggest that, there are three main weight loss regions in each type of membrane. The first weight loss region in each case is due to the removal of physically and chemically bound water, which contributed to 10–20% weight loss. Difference in the %weight loss due to physically and chemically bound water in different CNCs based membranes is due to variation in affinity of different anions attached to CNCs by substituting hydroxyl group during acid hydrolysis. The influence of crosslinking and filler incorporation can be seen from second weight loss region. In the case of PVA there is a sharp weight loss in the temperature range 250°C–

TH-2592_156107017

500°C, but in the other three cases of PVA-CS-CNC films the weight loss is gradual due to crosslinking and filler matrix interaction. In case of PVA, second weight loss occurs due to the degradation of the PVA side chains whereas in other three cases, it is a combined effect of the degradation of PVA side chains, CS and CNC. The third weight loss region in PVA starts after 500°C, which is delayed in the case of nanocomposite membranes by around 50°C. Different morphologies of CNCs do not significantly affect the thermal stability of the samples. DSC thermograph shown in Fig. 2.2 highlights the changes in morphology of the base material PVA due to addition of CNCs and crosslinking. PVA is a semicrystalline material, the glass transition (T_g) of which is around 90°C and melting temperature (T_m) is around 230°C. There is no significant variation in the onset of T_g of PVA-CS-CNC membranes compared to that of the PVA membrane, but the DSC curves of PVA-CS-CNC membranes in the glass transition region have been stretched to broader temperature range, which signifies the increase in amorphous region. Stretching of glass transition region can also be verified by the tan(δ) vs temperature curve shown in Fig. 2.5, obtained by DMA analysis. The curve clearly shows that neat PVA membrane has T_g in the range of 30–70°C, while for all the other CNC based membranes the T_g range stretches more than 100°C. The CNCs prepared by using HCl and H_2SO_4 have more pronounced effect on the T_g compared to the HNO_3 CNCs. This could be explained by the morphology of different acid hydrolyzed CNCs (shown by FESEM images in next section), where H_2SO_4 and HCl hydrolyzed CNCs have rod like structure, but HNO_3 acid hydrolyzed CNCs have fiber like network structure. This network structure provides better interaction with polymer matrix, thus there is less impact of amorphous region on T_g of HNO_3 CNC based membrane.

TH-2592_156107017

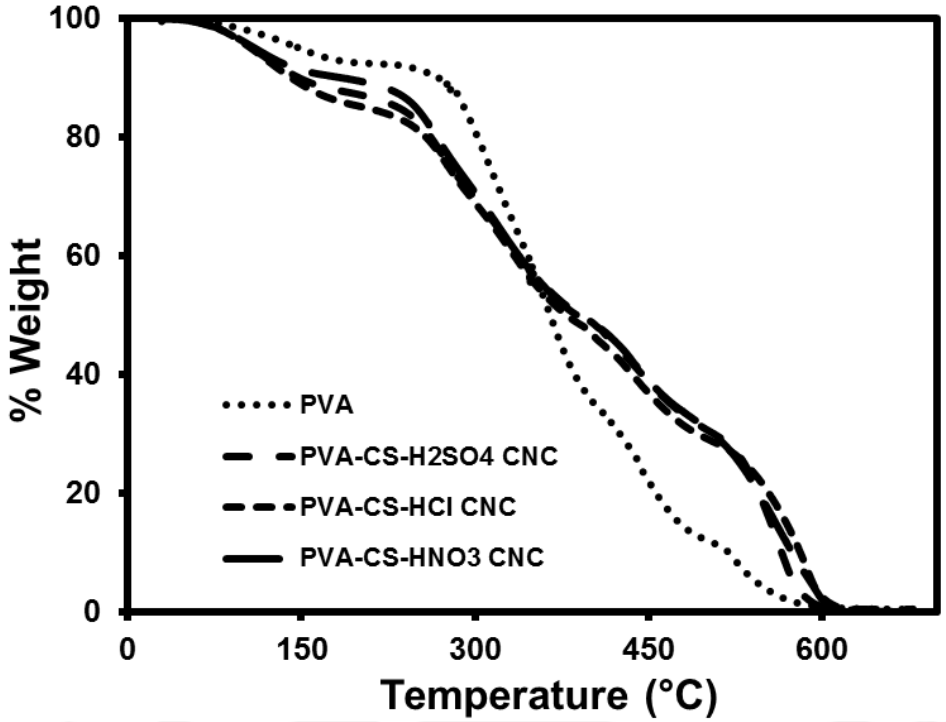

Fig. 2.1 TGA thermograph of PVA and PVA-CS-CNC samples.

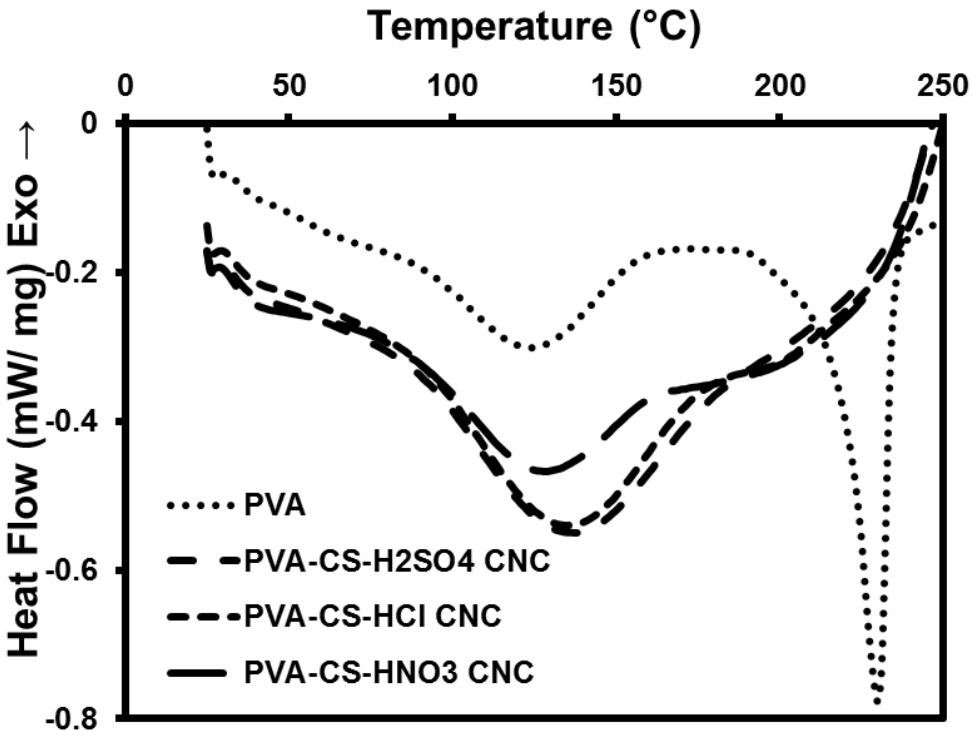

Fig. 2.2 DSC thermograph of PVA and PVA-CS-CNC samples.

TH-2592_156107017

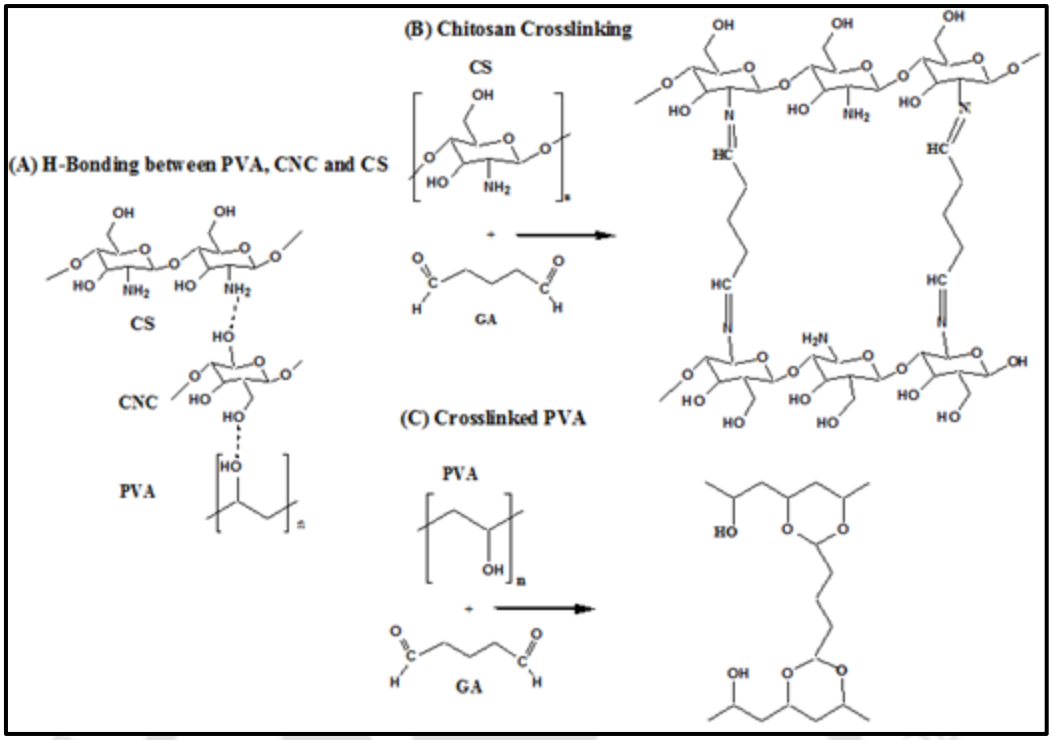

Fig. 2.3 Possible network formation (A) H-bonding between PVA, CS, CNC (B) crosslinking of chitosan with GA and (C) crosslinking of PVA with GA.

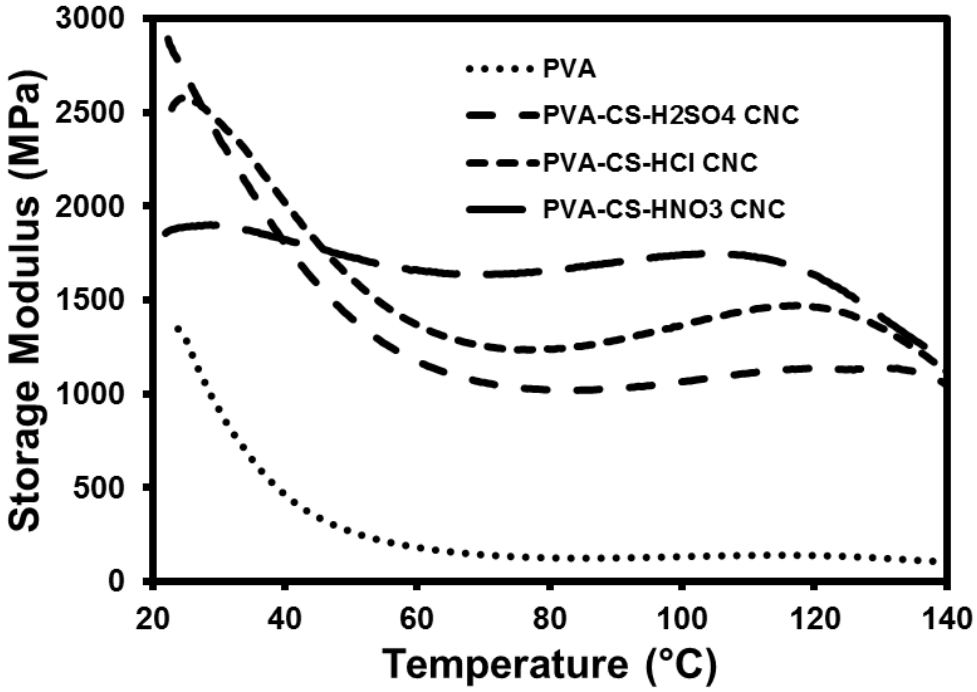

Fig. 2.4 Storage modulus vs temperature curves of PVA and PVA-CS-CNC samples.

TH-2592_156107017

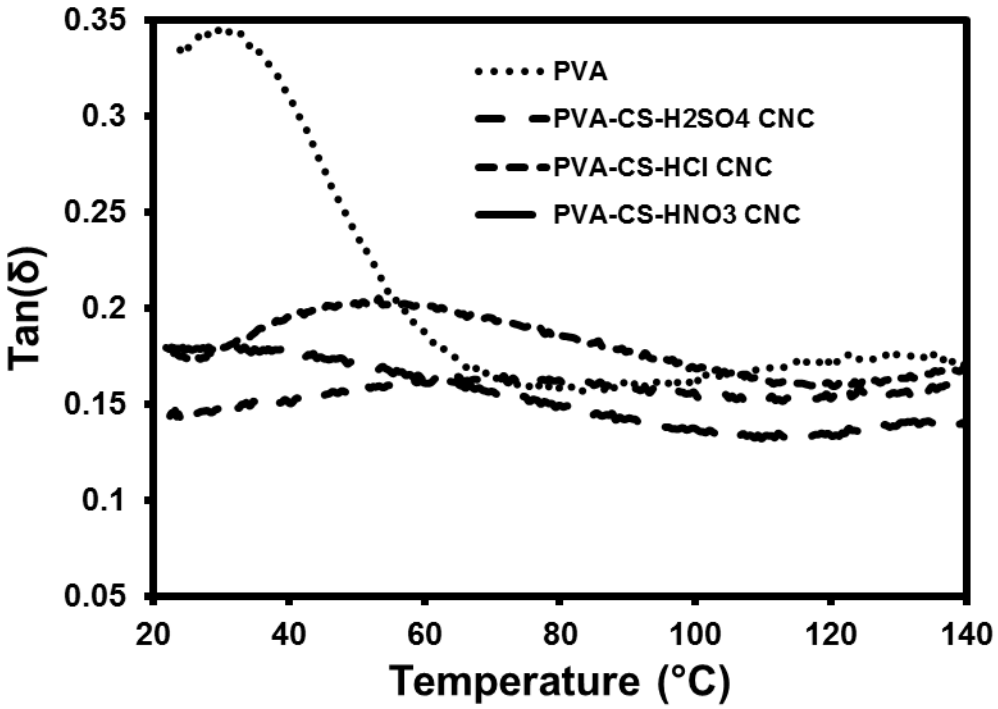

Fig. 2.5 Tan(δ) vs temperature curves of PVA and PVA-CS-CNC samples.

Due to crosslinking (Fig. 2.3) and incorporation of CNCs, polymer matrix has become almost amorphous and the melting peak of PVA has disappeared in the case of HCl and H_2SO_4-CNC based PVA-CS-CNC membranes. HNO_3-CNC based membrane shows very small melting hump.

Effect of crosslinking and filler-matrix interaction (Fig. 2.3) on thermo-mechanical properties can be visualized from Fig. 2.4. Storage modulus (E′) of the PVA-CS-CNC samples improved significantly compared to the un-crosslinked PVA membrane. The important point here to notice is that E′ in all the three CNC based membrane samples is above 1000 MPa up to 140°C, which is quite high from the working temperature range of the DMFCs (≈80°C) and shows the good mechanical stability of the samples even at high temperatures. At low temperatures, the value of E′ for PVA-CS-HNO_3-CNC nanocomposite is lower compared to the other two CNC nanocomposite membranes. However, the E′ value for the PVA-CS-HNO_3-CNC nanocomposite remains almost

TH-2592_156107017

constant up to around 120°C and is higher than that for the other two at temperatures above 50°C. It is due to the fiber like network morphology of HNO_3-CNCs (Fig. 2.5(c)), which provides good filler matrix interaction and the membrane is stable up to higher temperatures. This indicates that among the three types of CNCs, HNO_3-CNC has better filler-polymer matrix interaction.

2.4.2 Surface Morphology, Crystal Structure and FTIR Studies

The cellulose nanocrystals (CNCs) fabricated through various acids using hydrolysis approach shows significant variation in both the morphological as well as physicochemical properties. CNCs obtained from hydrolysis with sulfuric acid show distinct rod-like morphology with high aspect ratio of ≈50 (length ≈1100±150 nm and width ≈30±15 nm) (Fig. 2.6 (a)). CNCs fabricated using hydrochloric acid also show rod-like morphology, with comparatively lower aspect ratio of ≈15 (length ≈210 ± 25 nm and width ≈10±7 nm) (Fig. 2.6 (b)). Similarly, the nitric acid derived CNCs show fibril-like network kind of structure and have higher aspect ratio with width of ≈25±12 nm (Fig. 2.6 (c)). The difference in the morphologies of different acid hydrolyzed CNCs shows the effect of acid strength to remove the amorphous sections from precursor cellulosic material. Crystal structure analysis of the membrane samples from XRD patterns as shown in Fig. 2.7, provides clear picture of changes in crystallinity of the PVA-CS-CNC films due to incorporation of CNCs and crosslinking agent. The XRD results are in agreement with DSC data as semicrystalline PVA membrane has been converted completely into amorphous phase in case of HCl and H_2SO_4 CNCs based membranes, while in the case of HNO_3 CNC based membrane, small crystalline phase is still present in the sample.

FTIR spectra of all the three types of CNCs, CS, PVA and PVA-CS-CNC films are presented in Fig. 2.8. All CNCs show the characteristic peaks at 2904, 1432, 1314, 1201,

TH-2592_156107017

1166, 1031 and 897 cm^{-1}, which represents the stretching of –CH, bending and vibration of $–CH_2$, bending of C(6)–OH, asymmetric stretching of –C–O–C– (glycosidic linkages) and in-plane C–OH bending respectively. The characteristic peaks of PVA at 3248, 1082 and 1414 cm^{-1}, which represent the –OH stretching, and –CO group stretching and bending are present in FTIR spectra. Characteristic absorption peaks of CS are observed at 1554, 1334, 2927, 896, 1154 and 1080 cm^{-1} which represent the stretching vibration of amino group, – CH vibration, amine –NH symmetric vibration, typical –CH vibration, and saccharide structure vibrations and –CO stretching vibrations. With the addition of crosslinking agent GA, it is expected that the free hydroxyl group of PVA and amine group of chitosan will crosslink due to which corresponding peak shifts may be observed for the FTIR of PVA-CS-CNC film samples. Similarly due to hydrogen bonding between PVA, CS and CNC peak shifts can be observed in FTIR spectra (Fig 2.8) (Miri et al., 2015). In the FTIR spectra of PVA-CS-CNC films, peak at 1548 cm^{-1} corresponds to $–NH_2$ group (shifted to lower wavenumber) of chitosan (Nasef et al., 2011). The peak around 1648 cm^{-1} is for the N=C bond, which appears due to crosslinking between chitosan chains by GA (Fig. 2.8) (Ingole et al., 2013). The free –OH bending peak of CNC has shifted from 1651 to 1668 cm^{-1} in the case of PVA-CS-CNC films due to hydrogen bonding with the PVA matrix. Similarly, the peak of O–C–O stretching which is observed around 1031 cm^{-1} in CNCs has shifted to 1026 cm^{-1} and the intensity of this peak is increased in the case of PVA-CS-CNC films, as crosslinking of PVA (Fig. 2.8) produces more number of O–C–O linkage (Anicuta et al., 2010; Abitbol et al., 2011).

TH-2592_156107017

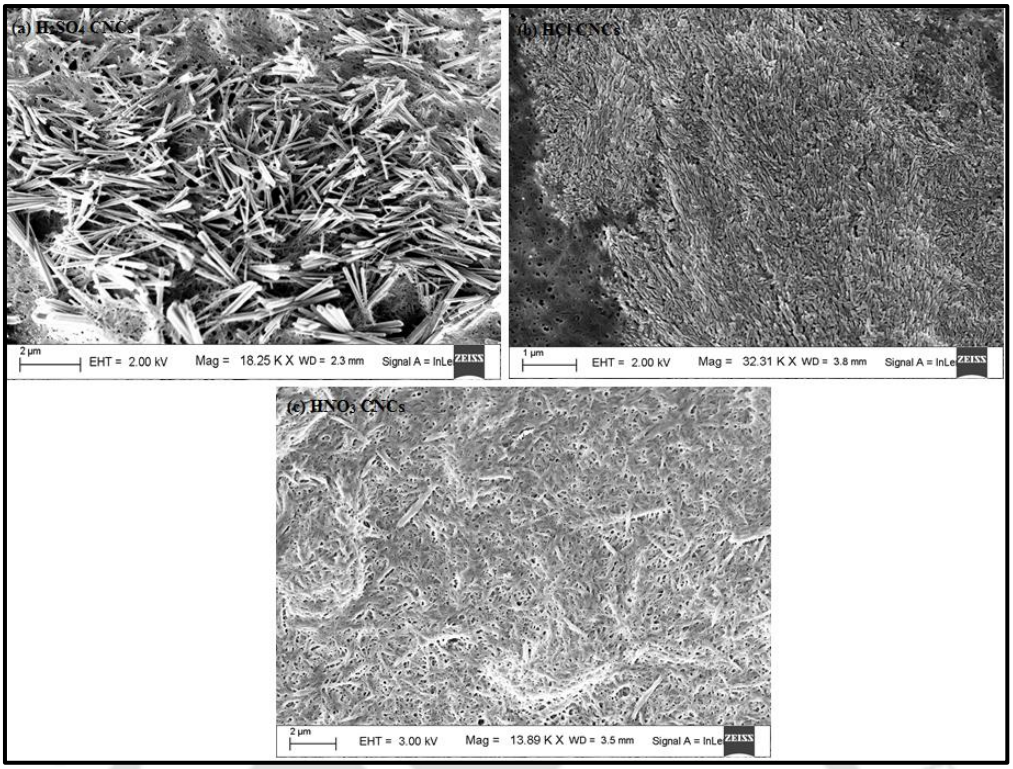

Fig. 2.6 FESEM images of the CNCs hydrolyzed from the different acid sources (a) Sulfuric acid, (b) Hydrochloric acid and (c) Nitric acid.

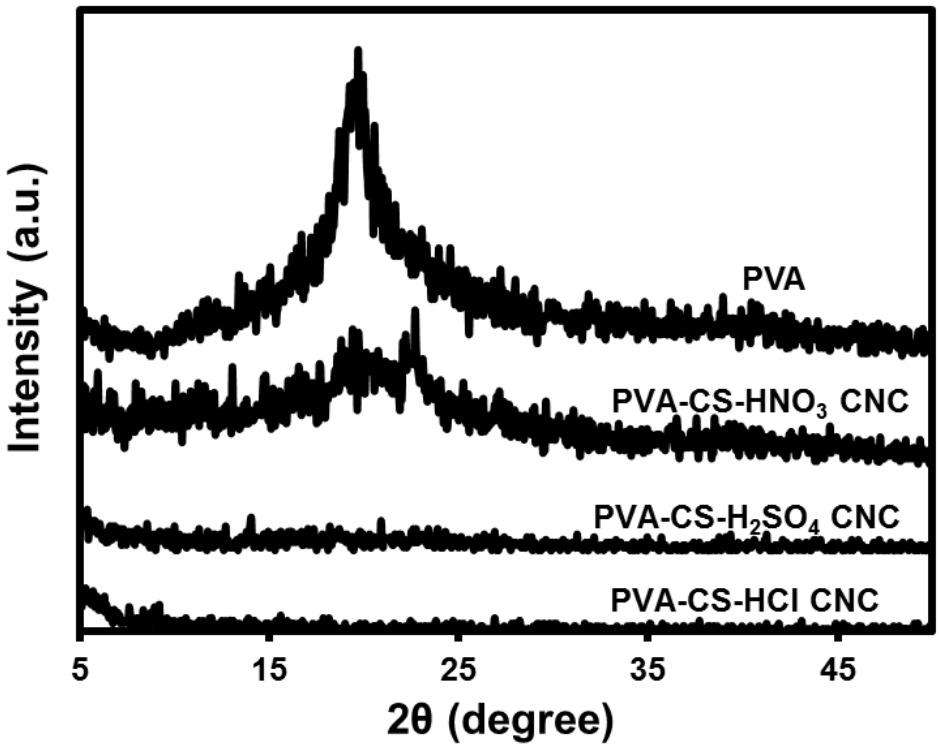

Fig. 2.7 XRD patterns of PVA and PVA-CS-CNC sample.

TH-2592_156107017

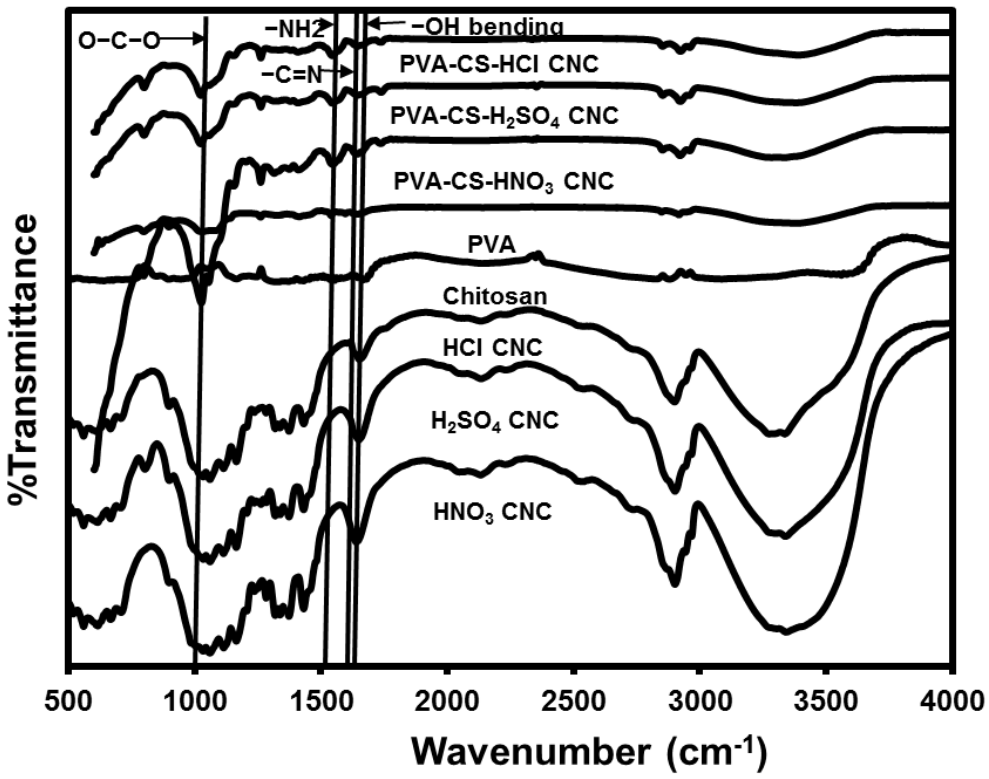

Fig. 2.8 FTIR spectra of PVA and PVA-CS-CNC films.

2.4.3 Water Uptake and Swelling Behavior

Water uptake and %swelling of PVA and PVA-CS-CNC PEMs are tabulated in Table 2.1. PVA is hydrophilic polymer and has very high water uptake (around 250%), along with high swelling properties, which makes it unstable during fuel cell operations. Crosslinking of PVA and CS has reduced the water uptake capacity drastically in PVA-CS-CNC membranes, which signifies the improvement in the membrane stability. At the same time presence of sufficient water helps in ion conduction. Parallely, the swelling of membranes reduced significantly to make these membranes highly suitable for fuel cell operation in moisture containing environment. The nature of different CNCs has effect on water uptake and %swelling. As it would be expected that H_2SO_4 CNCs based membrane should have highest water uptake due to presence of sulfonic acid groups, which have higher affinity to water compared to other two anions (chloride and nitrate). But it is very interesting that

TH-2592_156107017

HNO_3-CNC membrane has higher water uptake compare to HCl and H_2SO_4-CNC membranes and at the same time exhibits the lowest swelling. It is the result of special fiber like network structure of HNO_3-CNCs. On the one hand the network structure avoids the problem of agglomeration of filler and provides voids to retain higher amount of water, at the same time this network structure does not allow the membrane to deform (swell) much.

Table: 2.1 Water uptake and %swelling of PVA and PVA-CS-CNC membranes.

Sample	**≈Water uptake (%)**	**≈%swelling**
PVA	253.0±0.4	50.0±0.5
PVA-CS-H_2SO_4-CNC	68.0±0.4	15.0±0.2
PVA-CS-HCl-CNC	71.0±0.2	10.0±0.5
PVA-CS-HNO_3-CNC	78±0.3	5.0±0.2

2.4.4 Ionic Conductivity, Methanol Permeability and Selectivity

Ionic conductivities of the CNC based PEM samples, reported in Table 2.2 are in the range of 10^{-4} S cm^{-1} at room temperature. Ion conductivity of the polymer electrolytes depend on the water uptake as well as charge transfer groups present in the membrane. The dependency of samples on water uptake is evident from Tables 2.1 and 2.2, where the conductivity is observed to follow the same trend as that of the water uptake of PVA-CS-CNC films. HNO_3-CNC based nanocomposite membrane has higher water uptake compared to the HCl and H_2SO_4-CNC based membranes, and thus has higher ion conductivity as well. The dependency on charge transfer groups can be understand by comparing the ion conductivity of CNCs based membrane with Nafion 117. As mentioned in Table 2.2, Nafion 117 has higher ion conductivity due to presence of ion conductive pendent groups present in the polymer. Therefore, similar ion conductive functional groups

TH-2592_156107017

($-SO_4^{-2}$) have been introduced on the CNCs during sulphuric acid hydrolysis. The performance of this conductive group was also compared with other acidic moieties such as $-Cl$ or $-NO_3^{-}$. Ion conductivity of the membranes can be further improved by controlling the crosslinking of chitosan and optimizing the CNC content in the membrane, which has not been considered in this work.

Methanol permeability data tabulated in Table 2.2 show significant improvement in the methanol barrier property of the membranes compared to both Nafion 117 and base PVA membrane. HCl CNCs based membrane has the lowest methanol permeation compared to the other three samples. The reduction in methanol permeation in PVA-CS-CNC membranes is result of crosslinking and better filler-matrix interaction, which creates tortuous path for methanol permeation. According to the selectivity data of membranes, HCl-CNCs and HNO_3-CNC based nanocomposite membranes have better selectivity compared to the other membranes including Nafion 117.

Table: 2.2 Ionic conductivity, methanol permeability and selectivity of the PVA and PVA-CS-CNC membranes.

Sample	**Ion conductivity (S cm^{-1})**	**Methanol permeability (cm^2 s^{-1})**	**Selectivity (S s cm^{-3})**
PVA	$(3.58\pm0.10) \times 10^{-5}$	$(3.97\pm0.17) \times 10^{-7}$	8.54×10^{1}
PVA-CS-H_2SO_4-CNC	$(4.65\pm0.02) \times 10^{-4}$	$(5.10\pm0.21) \times 10^{-8}$	8.66×10^{3}
PVA-CS-HCl-CNC	$(5.85\pm0.07) \times 10^{-4}$	$(2.98\pm0.10) \times 10^{-8}$	1.89×10^{4}
PVA-CS-HNO_3-CNC	$(6.31\pm0.12) \times 10^{-4}$	$(3.36\pm0.14) \times 10^{-8}$	1.81×10^{4}
Nafion 117	$(8.45\pm0.05) \times 10^{-3}$	2.07×10^{-6}	4.08×10^{3}

TH-2592_156107017

2.5 Conclusions

Demonstrated CNCs based solid polymer electrolyte membranes for DMFCs are capable to have good thermo-mechanical stability and very low swelling characteristics. Incorporation of CNCs in PVA-CS matrix has improved the methanol barrier properties by creating tortuous path for methanol permeation. The comparative study made here with different CNCs as ion conductive nanofiller have shown that the properties such as water uptake, swelling behavior and ionic conductivity of the base PVA membrane are positively impacted by CNCs. The water uptake of PVA-CS-CNC membranes has come down from ≈250% in case of pure PVA membrane to ≈70% and %swelling has come down to ≈5% from ≈50%. The morphology of CNCs has also played a role in the controlling these properties. PVA-CS-HNO_3 CNC nanocomposite membrane has superior thermo-mechanical stability, higher water uptake, very low swelling in moisture environment and higher ionic conductivity compared to the PVA-CS-HCl-CNC and PVA-CS-H_2SO_4-CNC nanocomposite membranes. HCl-CNC based nanocomposite membrane shows better performance in the case of methanol permeability and selectivity; however, the performance of HNO_3-CNC based membrane is also in the same range. Ionic conductivity of the CNC based PEMs is lower than that of Nafion 117, but it is in the range suitable for DMFC applications and at the same time lower methanol permeability and better selectivity makes these membranes better than Nafion 117. Ionic conductivity of the membranes can be further improved by controlling the crosslinking of chitosan and optimizing the CNC content in the membrane samples. So, it can be concluded by this work that the biodegradable PVA-CS-CNC based nanocomposite PEMs can be good candidate for DMFCs and HNO_3-CNC based nanocomposite membranes are the better option among three PEMs discussed.

TH-2592_156107017

Chapter 3:

Human Hairs based Anion Exchange Membrane for Alkaline DMFCs

Graphical Overview

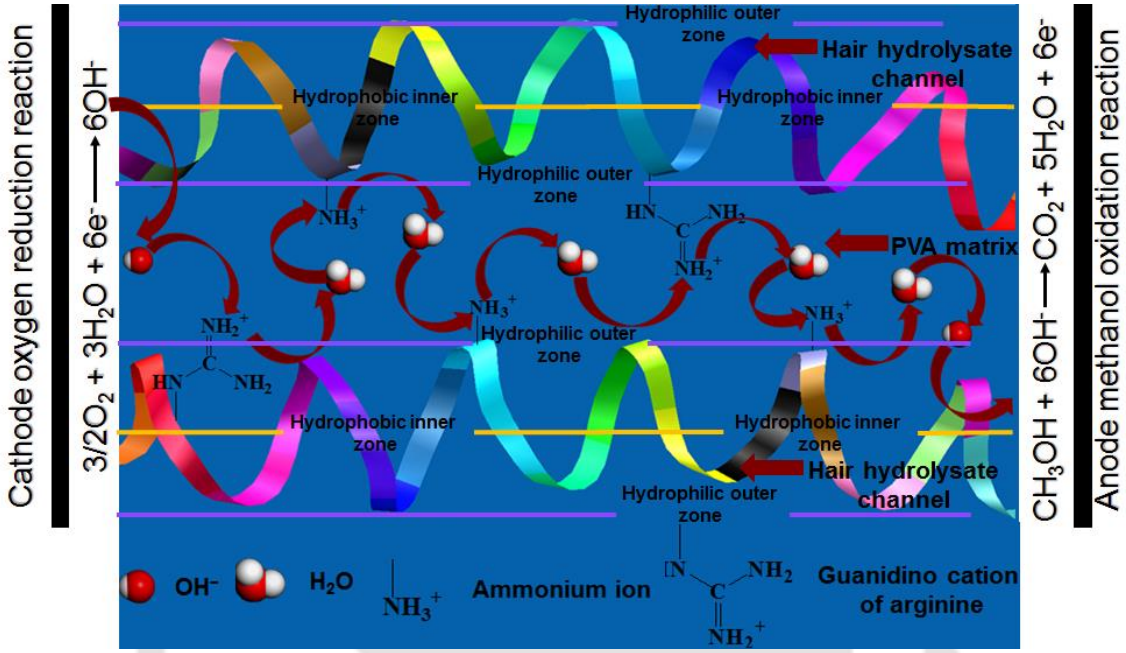

Ion transfer phenomenon occurring in nature are known to be most efficient. Many efforts have been made to bio-mimic such phenomena, especially in the area of energy transfer. Proteins consisting of various amino acids are known to be the fundamental materials behind these phenomenon. In this study, we have extracted proteinaceous material from human hair bio-waste by green chemical-free thermal hydrolysis process. A simple heat treatment of human hairs in presence of water led to the formation of water soluble material, which is called hair hydrolysate here, contains 70 wt.% proteinaceous material. In the current work we have utilized the hair hydrolysate for the fabrication of two different types of AEMs. As we have seen from the previous investigation reported in -

Publication:

- Gaur, S. S., Dhar, P., Wani, K. M., Srivastava, M., Sakurai, S., Kumar, A., & Katiyar, V. (2021). Ion transfer channel network formed by flower and rod shape crystals of hair hydrolysate in poly (vinyl alcohol) matrix and its application as anion exchange membrane in fuel cells. Journal of Colloid and Interface Science, *587*, 214-228.

TH-2592_156107037

chapter-2, CNC can be utilized as ion conductive material and due to availability of different functionalities, it can be modified easily, so in the first type, hair hydrolysate modified CNCs have been utilized with CS matrix to fabricate a biopolymer based AEM. The epichlorohydrin crosslinked 5wt.% modified CNC-CS based membrane was investigated for its ion conductivity, which was found to be around 1 mS/cm. The ion conductivity results for the current membrane are better than the conductivity results in acidic conditions for CNC based membrane reported in the previous chapter. For the second type of membrane, PVA matrix-based AEM was fabricated by using hair hydrolysate as ion conductive material directly. It was observed that the hair hydrolysate contains 27 wt.% charged amino acids and 19 wt.% polarizable amino acids, which provided effective charge transfer sites under alkaline conditions with potential hopping kind of mechanism for charge transfer. Presence of 7 wt.% of arginine in hair hydrolysate, having continuous delocalized net positive charge, which makes it stable even in highly alkaline conditions and can provide stability to the AEMs, which was confirmed by an indirect alkaline stability analysis. The hair hydrolysate formed rod and flower shape crystal morphology in glutaraldehyde crosslinked PVA matrix, which created a continuous channel network at higher loading (5 wt.%). In the presence of water, the channel network provided a simple path for ion transfer, which achieved hydroxyl ion conductivity of 7.46 mS/cm at 70°C for 5 wt.% hair hydrolysate loading. Further increase in the loading created higher amount of crystals, subsequently blocking the channels and reducing the ion conductivity. Annealing of 5 wt.% hair hydrolysate loaded sample minimized the PVA matrix swelling. A reduction in ionic conductivity to 6.16 mS/cm (at 70°C) was observed, at the same time it improved other properties related to anion exchange membrane, such as increase in mechanical, thermal and thermo-mechanical stability, reduction in water uptake (≈100% reduction), %swelling (from 30% to 15%) and methanol permeability (by

TH-2592_156107017

ten orders of magnitude). The selectivity of the membrane was increased to almost a decimal place at 30°C. Thus, the hair hydrolysate-PVA membrane showed good prospects to fabricate an anion conductive membrane for alkaline fuel cells.

3.1 Introduction

As mentioned in the chapter-1, there are several advantages of alkaline medium in DMFCs over acidic medium. Some of which includes, costly noble metal based electrocatalysts can be replaced by low cost metal catalysts (Ryu et al., 2019), superior corrosion resistance of DMFC materials in alkaline medium compare to that in acidic medium, during OH^- transport via electro-osmotic drag, water is dragged away from cathode side, preventing the flooding problem and transport of OH^- from cathode to anode will reduce the methanol crossover, which in case of acidic medium generally gets dragged with H^+ ions (Scott et al., 2008). The roadblock for alkaline type DMFCs is that the commercial polymer electrolyte membranes are still under development (Merle et al., 2011). A recent review on the development of AEMs used in fuel cells shows that quaternary ammonium, quaternary phosphonium, imidazolium, guanidinium and piperazinium cations based AEMs have been investigated for this application (Cheng et al., 2015). Most of the polymeric materials used are based on the synthetic polymers, which are not easy to degrade and if used in large amounts, will create environmental issues. As discussed in introduction chapter, CS is a biodegradable biopolymer and PVA is one of the synthetic polymers which is well known for its biodegradability in the presence of suitable microorganisms, under both aerobic and anaerobic conditions (Chiellini et al., 2003; Halima et al., 2016). CS and PVA have been used in both acidic and alkaline type of fuel cells. The CS and PVA based matrixes need another component to improve the ion conductivity and mechanical stability. Different issues related to the organic and inorganic materials used to improve the properties of CS

TH-2592_156107017

and PVA membranes are discussed in introduction, which hinders the application of these membranes.

Use of biopolymers and bio-nanofillers produced from waste, along with the CS and PVA matrixes for the preparation of AEMs, is a good option to convert waste into wealth. In our previous study, we have shown the use of cellulose derived CNCs in PVA-CS matrix for potential application as ion conductive membranes for acidic type DMFCs (Gaur et al., 2017). Proteins and their derivatives are another categories of biopolymers, which can be extracted from plants and waste animal biomass. Proteins are well known for their charge transferability and photosynthesis is one such example. As discussed in introduction chapter, there are several reports which have described the charge transfer mechanisms for different types of proteins (Khoshtariya et al., 2003; Ahn et al., 2008; Bradley et al., 2004; Stuchebrukhov, 2009). Bradley et al., (2004), in their study have shown the charge transfer between protein and carbon nanotubes. Similarly, Dhar et al., (2019) have prepared protein based genetically modified nacre-like material with superior electrochemical performance, showing the ability of proteins to be utilized for the fabrication of bioengineered devices. Use of protein in biofuel cells as substrate and bioelectrocatalyst is also well stablished (Liu et al., 2009; Minteer et al., 2012; Willner, 2002). Amino acids are the building blocks of proteins, which contains both acidic and basic functionality. Upon deprotonation amino acids form carboxylate anion and upon protonation they form ammonium cation. Thus, there is a possibility to utilize proteins in the both acidic and alkaline type of polymer electrolyte membranes. Ho et al., (2004) have fabricated ion transport proteins based block copolymer membrane and suggested its possible application to prevent leaking of protons in Nafion® as well as production of current driven by protein, across these membranes in acidic type fuel cells. There are few other reports as well, where amino acids are directly used to modify the nanofillers and

TH-2592_156107017

incorporated in different polymer matrixes to prepare proton conductive membrane for acidic type fuel cells (Leem et al., 2008; Wu et al., 2012; Xu et al., 2019; Zhao et al., 2019). For the alkaline type of fuel cell membranes, it is hard to find any such report where proteins or its derivatives (amino acids, peptides) have been utilized as electrolyte. Another issue with proteins or their derivatives is their preparation and purification process, which may enhance the cost of electrolyte membrane. To overcome this issue, use of the crude proteins from waste biomass without purification and with minor thermo-chemical treatment to prepare electrolyte can be a good alternative.

In the current investigation, we have used human hair waste biomass as a source of protein-based electrolyte and fabricated two different kind of AEMs. For the first type, we have modified the CNCs with hair hydrolysate and incorporated it in CS matrix. For the second type, we have directly incorporated the hair hydrolysate in PVA matrix to prepare the AEM for alkaline DMFC. Human hairs are composed of proteins and α-keratin is the major component. Twisted coil structure with hydrogen bonding and disulfide linkage between keratin strands gives it high chemical and mechanical stability (Menefee, 1977) and makes it insoluble in water. Enzymatic and thermo-chemical hydrolysis processes can be used for disintegration of keratin strands by breaking the disulfide bonds. Hydrolysis process results in the formation of water soluble amino acids, peptides and lower molecular weight keratin (Bertini et al., 2013; Villa et al., 2013), which makes it easy to utilize and process for the fabrication of electrolyte membrane. Further, there are reports on chemical-free green hydrolysis of keratin in microwave reactor through thermal treatment (Bertini et al., 2013; Zoccola et al., 2012). So, a thermal treatment based green approach has been utilized here to prepare hair protein-based electrolyte, which is further characterized and used. Properties of the thus prepared environment-friendly electrolyte based AEMs are discussed in the subsequent sections.

TH-2592_156107017

3.2 Material and Methods

3.2.1 Materials

Poly (vinyl-alcohol) (99% hydrolyzed and M_w-89000-98000 Da) (PVA) and chitosan (CS) (medium molecular weight) were purchased from Sigma-Aldrich India. 25% v/v glutaraldehyde (GA) solution was used as crosslinking agent in PVA based AEM and it was purchased from Rankem, India. Epichlorohydrin (ECH), which was used as crosllinker for CS based AEM and rest of the solvents needed for analysis and washing purpose were purchased from HiMedia laboratories private limited, India.

3.2.2 Green Thermal Hydrolysis of Hairs

Human hairs were collected from local barbershop and washed multiple times with industrial soap solution, and after that with acetone to remove oil and dust. The cleaned hairs were dried in hot air oven at 60°C overnight. For thermal hydrolysis a sealed steel vessel with 200 ml capacity was used. Around 500 mg of dried hairs were taken in the vessel and 50 ml water is added into it. The vessel was sealed and kept on a heating plate at 200°C for 7 hours. After 7 hours of thermal hydrolysis, the solution was centrifuged and the supernatant was taken out in separate beaker. As per water-vapor pressure-temperature correlation at 200°C, water-vapors can build pressure up to 15 bar. Thus, high temperature and pressure resulted in the digestion of hairs during hydrolysis and most parts of the hairs was dissolved in water, so the resulted supernatant was black-brownish in color. The supernatant was dried in a hot air oven at 100°C and the dried material which may consist of mixture of amino acids, peptides and low molecular weight proteins of hair keratein was used for further analysis as well as ion conductive material in PVA to prepare anion exchange membranes (AEMs) with different weight ratios.

TH-2592_156107017

3.2.3 Modification of CNCs by Hair Hydrolysate

The objective of the modification was to have functionalities on CNCs which can provide CNCs anion exchange sites. The hair hydrolysate is mix of amino acids, peptides and low molecular weight keratinic protein. Thus it has lot of amine groups available and it can be used to modify the CNCs. To create a site to bind the hair hydrolysate to CNCs, very well-known technique: periodate oxidation of polysaccharides (Kristiansen et al., 2010) is used, which breaks the cellulosic ring from the part where two hydroxyl groups are on neighboring carbon to form aldehyde. We have used CNC and sodium periodate in 1:1 ration for the CNC oxidation reaction. CNCs were dispersed in Millipore water by sonication and later the sodium periodate was added and the mixture was stirred around 70°C for three hours in dark. After the reaction the CNC dispersed solution was washed with water three times and centrifuged and subsequently freeze dried. Thus oxidized CNCs were modified by dispersing it in hair hydrolysate solution and stirring at 80°C around 6 h.

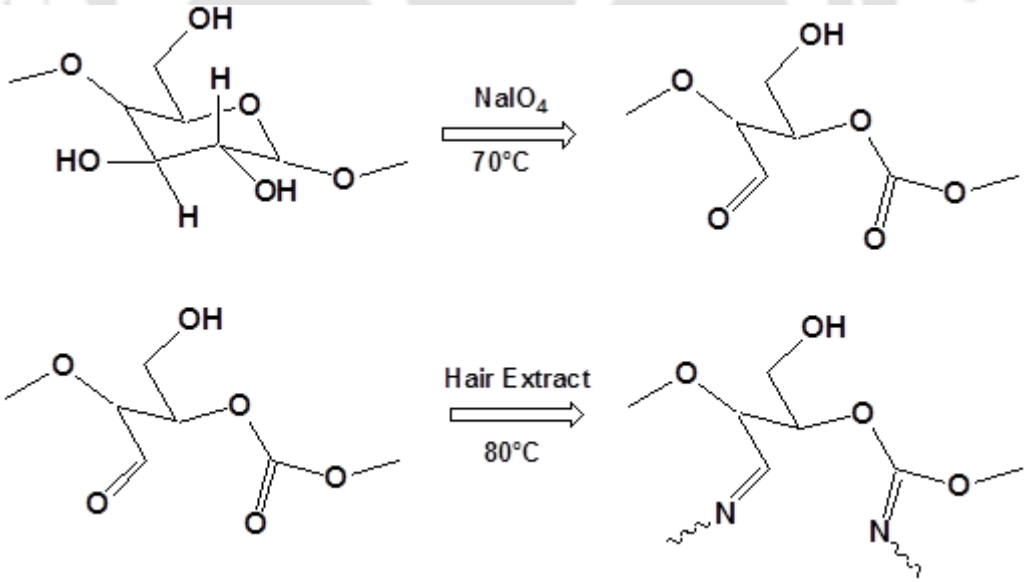

Fig. 3.1 CNCs oxidation by $NaIO_4$ and subsequently modification by hair hydrolysate.

TH-2592_156107017

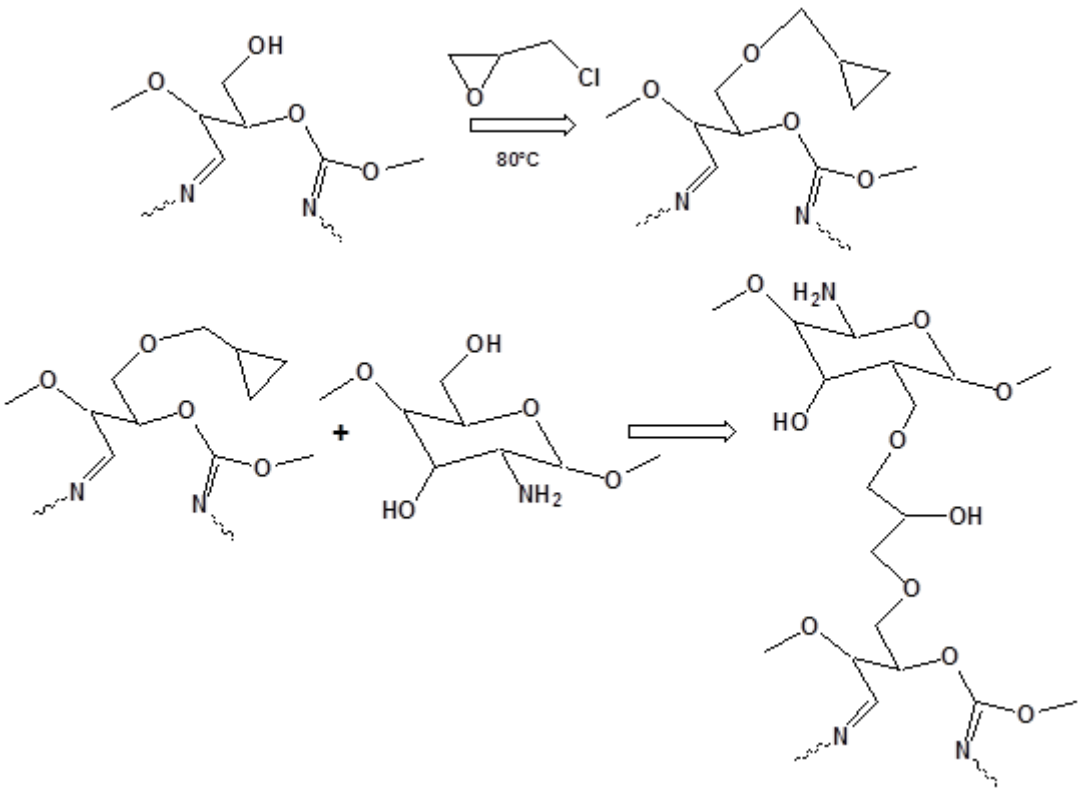

Fig. 3.2 CS and modified CNCs crosslinking by epichlorohydrin.

During this reaction the aldehyde groups of oxidized CNCs crosslinked with the amine group present in hair hydrolysate (as shown in Fig. 3.1). After the reaction the CNCs were centrifuged and washed multiple times with water and after that with acetone, methanol and chloroform to remove the unbound hair hydrolysate. Thus prepared material was freeze dried and used for further characterization and CS based biopolymer AEM preparation.

3.2.4 Fabrication of CS and Modified CNCs based AEMs

To prepare CS-modified CNCs based membrane, first modified CNCs (5wt% of total weight) were epoxidized by reacting it with epichlorohydrine (ECH) solution (5 ml ECH + 5ml water) at 80°C for 6 hours. As shown in Fig. 3.2, epichlorohydrine was used as cross-linker between chitosan and modified CNCs. After 6 h epoxidized CNCs mixture was added to the CS solution (prepared by dissolving in water by using 0.1 ml of 35wt.% HCl

TH-2592_156107017

solution) and both the solution were mixed properly by stirring for another 30 min at 80°C. The final solution was dried in Teflon petri dishes to prepare AEM.

3.2.5 Fabrication of PVA-Hair Hydrolysate based Composite AEMs

AEMs with different weight% loadings (1 wt%, 5 wt% and 10 wt%) of hair hydrolysate in PVA matrix were investigated to find the optimum loading for alkaline fuel cell application. 2 wt% GA was used as a crosslinking agent to provide the PVA matrix mechanical stability in presence of water. To prepare the AEMs, total 2 gm of material was taken for single AEM, in which PVA and hair hydrolysate content was varied as per weight % of hydrolysate. PVA was dissolved in 50 ml of water by stirring at 85°C and hair hydrolysate was dissolved in 10 ml of water at room temperature. Both the solutions were mixed along with GA and stirred for 30 minutes at 85°C. Later the solution was poured in 15 cm dia. petri dish and dried at room temperature to prepare the AEMs. For all the wt% loadings several samples were prepared to carry out different analyses and check the repeatability of the performance of the AEMs. For comparison of results with base matrix, PVA membranes were prepared by using PVA solution and 2 wt% GA in similar way.

3.3 Characterization

The Presence of proteinaceous material in hair hydrolysate was confirmed through X-ray photoelectron spectroscopy (XPS) in which nitrogen elemental analysis was done in a JEOL-JPS-9010MC/SP system with a MgK_{α} X-ray source. Carbon C1s peak at 285.0 eV was taken as the reference. The hair hydrolysate was characterized by FTIR (in a PerkinElmer Frontier FT-IR Spectrometer system) for its structural analysis. Molecular weight distribution of the proteinaceous material present in hair hydrolsate was analyzed by MALDI-TOF-MS (matrix assisted laser desorption/ionization - time-of-flight - mass

TH-2592_156107017

spectrometry) analysis by using α-Cyano-4-hydroxycinnamic acid matrix in an Autoflex Speed, Bruker system. The amino acid profile of hair hydrolysate sample was carried out at Aqua Research Laboratory, Department of Zoology, University of Delhi, Delhi, India using automated L-8900 Amino Acid Analyzer (Hitachi Co. Ltd., Tokyo, Japan). Initially, hydrolysis of the powdered sample was carried out with 6N HCl for 22 h at 110°C. Nitrogen evaporator (PCI Analytics Pvt. Ltd., Maharashtra, India) was used for drying the hydrolyzed sample. In the 0.5 mg/mL concentration of the protein sample, 0.02 N HCl was added. Autosampler was used for injecting the 20 µL of sample volume. Since hydrolysis of sample with 6 N HCl destroys methionine, cysteine and tryptophan, these are estimated using specific reagents. Performic acid and hydrobromic acid (48%) were used for methionine and cysteine. Hydrolysis of the sample was carried out with 4 N methane sulfonic acid and 3-(2-aminoethyl) indole for tryptophan. The rest of the methodology was same for all amino acids. The ninhydrin derivative of proline and hydroxyproline was observed at 440 nm, and monitoring of all the other amino acids was done at 570 nm. Quantification of the amino acids was done based on respective peak area in comparison to the amino acids mixture standard solutions. Wako Pure Chemical Industries Limited, Japan provided the Type B and Type AN-2 standards. Sigma-Aldrich, USA supplied standard solutions for glutamine and tryptophan. Morphological analyses were carried out using field emission scanning electron microscope (FESEM) (a SUPRA Ultra-high resolution FESEM system from Carl Zeiss, India). The crystalline nature of dried hydrolysate powder and membrane composites was investigated by XRD (a Rigaku TTRAX, Seifert XRD 3003 T/T model) with Cu-K_α radiation (λ= 0.1541 nm) as X-ray source. Thermal stability analysis of hydrolysate and composite membranes was done by thermogravimetric analysis (TGA) (in a PerkinElmer Thermogravimetric Analyzer TGA

TH-2592_156107017

4000 system), while crystallization and melting behavior of hair hydrolysate was observed by differential scanning calorimetry (DSC) (in a NETZSCH DSC 204 F1 Phoenix system).

Water uptake and %swelling of the membranes was checked by using 5 cm^2 dried membrane samples. For each wt% composite membrane, three dried samples (for average value) were taken after noting down their initial weight and dipped in a solution of 0.5 M KOH for 24 hours. Then the samples were taken out and their final weight, as well as their dimensions were measured. Water uptake was calculated by taking the difference of the initial and final weight of the samples and dividing it by initial weight, which was converted to percentage by multiplying by 100. Similarly, %swelling was calculated by taking the difference of the initial and average final length of the sample and dividing it by initial length and then multiplying the result with 100. The usefulness of the composite membranes for an alkaline fuel cell was checked by ionic conductivity analysis. The ionic conductivity analysis was carried out by using 5 cm^2 size three samples of each wt.% membrane in a single cell assembly. Prior to analysis each sample was kept in 0.1 M HCl solution overnight for formation of cations and after that rinsed multiple time with water to remove the excessive acid. The samples were sandwiched between graphite plates with channels for liquid flow. The outer side of each graphite plate was covered by copper plate electrodes and the cell was closed. 0.5 M solution of KOH was prepared and a constant flow of the same solution was maintained in both the sides of the membrane through graphite plate flow channels. Impedance spectroscopy measurements (in an Autolab PGSTAT204 system from Metrohm, India) were carried out after 1 h (after reaching the saturation state of the membrane by KOH solution) in the frequency range of 0.1 Hz – 1 MHz at 0.1V. The impedance measurements were carried out at different cell temperatures between 30-70 °C with 10 °C gap and the cell temperatures were maintained within $\pm$2 °C range. Ionic conductivities of the samples were calculated by using

TH-2592_156107017

equation (3.1). Methanol permeability of the samples was analyzed by cyclic voltammetry in the -1.0 – 0.4V range at 100mV/s scan rate. Platinum wire (10 mm length) was used as a working electrode and a 3 mm diameter platinum electrode was used for counter electrode, while Ag/ AgCl was used as a reference electrode for cyclic voltammetry (All the electrodes purchased from Metrohm, India). A calibration curve was prepared for known concentrations of methanol in 0.5 M KOH solution through cyclic voltammetry by plotting the methanol oxidation peak intensity vs concentration. To keep the condition near to real alkaline fuel cell testing conditions, methanol permeability of the samples was carried out in the single cell, similar to ion conductivity analysis. On one side of the membrane 0.5 M methanol and 0.5 M KOH solution was used and the other side of the membrane only 0.5 M KOH solution was used. The methanol permeability tests were carried out for 6 h for each sample and it was run for three samples for each type of membrane. The methanol crossover through the membrane from methanol and KOH solution side to only KOH solution side was monitored by cyclic voltammetry analysis by measuring the methanol oxidation peak at different time intervals. The unknown concentration of the methanol that reached the pure KOH solution at different time intervals was calculated by interpolation, using a calibration curve and calculation of methanol permeation was done by using equation (3.2). In the case of hair hydrolysate modified CNC-CS based membrane, where ion conductivity was found to be lower than the PVA based membrane, where hair hydrolysate is directly used in matrix, thus only ion conductivity, water uptake and %swelling analysis related to DMFCs were carried out. Further detailed investigation were carried out only for PVA-hair hydrolysate based AEMs due to better ion conductive properties.

$$\sigma = \frac{L}{RA} (s.cm^{-1}) \quad (3.1)$$

TH-2592_156107017

$$P = \frac{kVL}{AC_a}\ (cm^2 s^{-1}) \quad (3.2)$$

Where σ: Ion conductivity

R: Membrane resistance (calculated by impedance spectroscopy)

A: Area of the membrane

L: Thickness of the membrane

k: Slope of the time vs methanol concentration in the pure KOH solution curve

V: Initial volume of the Pure KOH solution

C_a: Initial concentration of methanol in methanol + KOH solution

Swelling is one of the major issues with PVA based membranes, so to further enhance the crosslinking and crystallinity, annealing of the membrane samples was done at 120°C temperature for 3 hours. The hair hydrolysate wt.% sample, which showed the best results among the all wt.% samples for ionic conductivity was chosen for annealing and properties like %swelling, water uptake, mechanical stability, thermal stability, thermo-mechanical stability, methanol permeability and ionic conductivity were compared with the sample before annealing. The changes in thermo-mechanical stability of the composite membrane were investigated by dynamic mechanical analyzer (DMA) (a NETZSCH DMA 242 E model). To check the stability of the annealed PVA-hair hydrolysate based membrane in alkaline medium, an indirect method was used, where the ionic conductivity of the fresh annealed sample was calculated and later the sample was dipped in 0.5 M KOH solution for 10 days. After 10 days the membrane sample was again used to check the ionic conductivity and the decrease in the ionic conductivity was used as indirect measure of decrease in stability of the membrane in alkaline medium.

TH-2592_156107017

3.4 Results and Discussion

3.4.1 Confirmation of Presence Amino Acids/ Peptides in Hair Hydrolysate (HH) by XPS and FTIR

Binding energy peaks corresponding to different bonds in amino acids/ peptides are present in the XPS spectra of the hair hydrolysate (shown in Fig. 3.3) and verified from literature (Roguska et al., 2011). The carbon 1s spectra (Fig. 3.3(a)) includes the peak for C-C and C-H bonds at binding energy 285 eV, peak for C-O and C-N bonds is observed at 286.3 eV and N-C=O amide carbon bond peak is observed at 288.2 eV. The presence of nitrogen peaks in nitrogen 1s spectra (Fig. 3.3(b)) confirms the existence of amino acids/ peptides in hair hydrolysate, where peaks at 398.8 eV, 400.2 eV and 401.8 eV corresponds to N-C, N-C=O and N-H binding energies respectively. Amide A, amide I, amide II and amide III peaks present in the FTIR spectra (Fig. 3.4) certifies the presence of protein/ peptides in the hair hydrolysate. All the characteristic bands of peptides as indicated in literature are present in the FTIR spectra of hair hydrolysate (Ma et al., 2016; Dinesh et al., 2015; Sharma et al., 2017; Zhang et al, 2013). The band at 3286 cm^{-1} is the result of combination of N-H (amide A) stretching and O-H stretching, while the transmission bands at 1658 cm^{-1} and 1538 cm^{-1} are for C=O stretching (amide I) and N-H bending (amide II) respectively. The band at 1238 cm^{-1} is attributed to amide III (a combination of C-N stretching and N-H in-plane bending) and C-C stretching and C=O bending vibration. According to Dinesh et al., (2015) the band at 1452 cm^{-1} corresponds to the π–π interactions in peptide. The higher energy band at 618 cm^{-1} is resulted due to the presence of C-S bond, while a clear band around 470 cm^{-1}, reported in literature[41] for undigested keratin contained material for disulfide bond (S-S) is missing from the FTIR spectra shown in Fig. 3.4 -

TH-2592_156107017

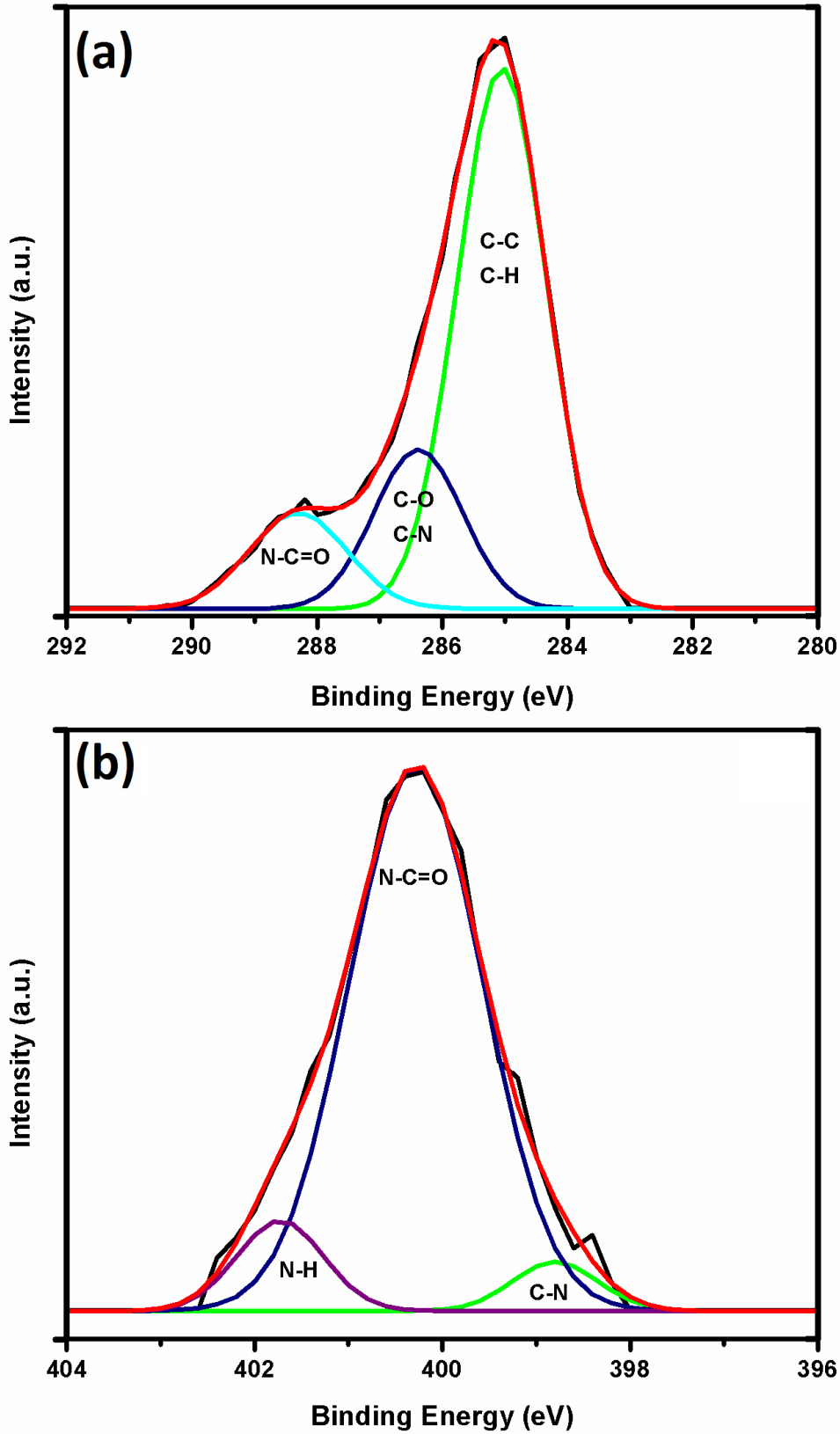

Fig. 3.3 XPS spectra of hair hydrolysate for (a) C1s (b) N1s.

TH-2592_156107017

indicating the complete cleavage of disulfide bonds. The presence of small bands at 1080 cm^{-1} and 1042 cm^{-1} is due to sulfate oxides, which formed during cleavage of disulfide bonds in keratin and subsequent oxidation during thermal hydrolysis. The band at 2962 cm^{-1} corresponds to the C-H stretching vibration.

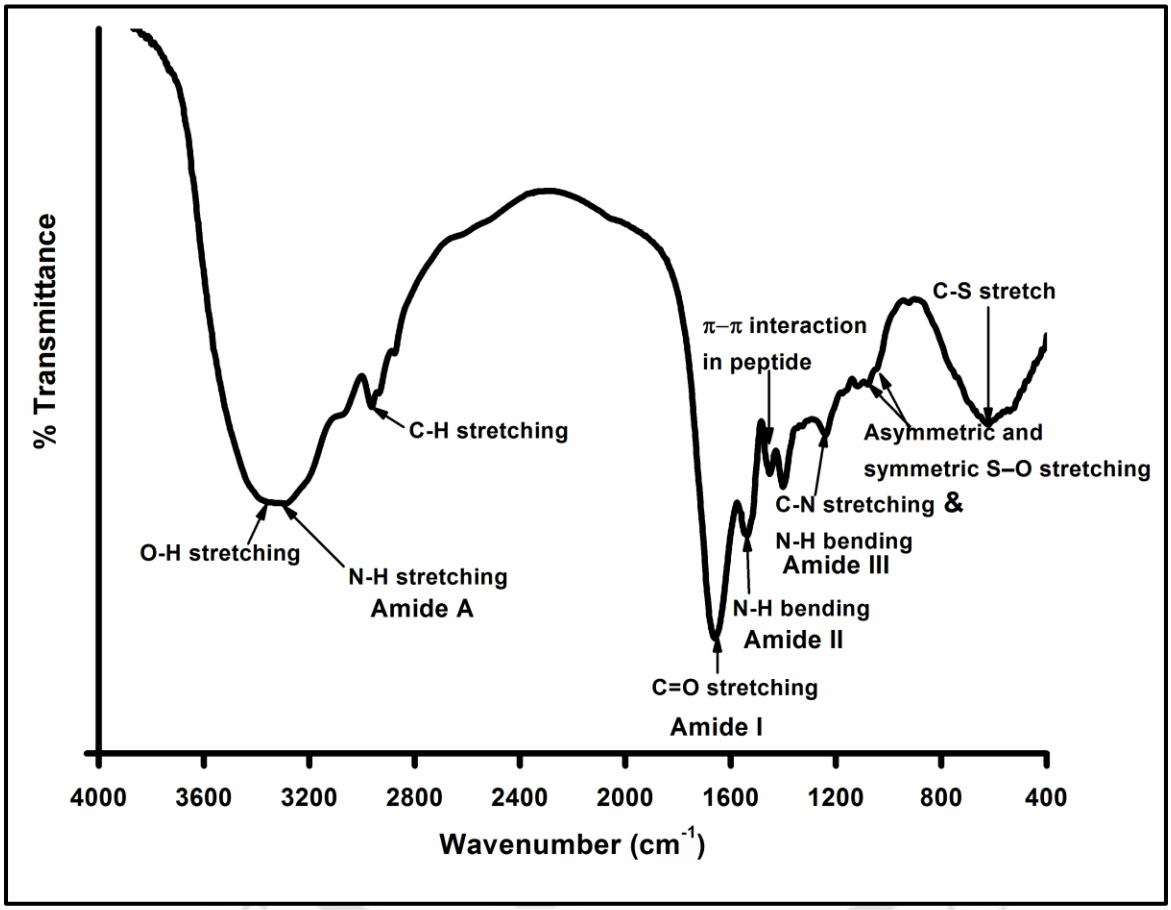

Fig. 3.4 FTIR spectra of hair hydrolysate.

3.4.2 Molecular Weight Analysis of Hair Hydrolysate

Molecular weight of hair hydrolysate calculated by MALDI-TOF-MS (as shown in Fig. 3.5 for three different batches of hair hydrolysate) displayed two different ranges of mass distribution, one is from lower molecular weight below 1 KDa to 7.5 KDa and the other is from 7.9 KDa to 15 KDa. The peak position for lower side molecular weight distribution varied between 1–2 KDa, while for the higher side molecular weight distribution, it is fixed

TH-2592_156107017

around 7.9 KDa. Thus, it is clear that the human keratins which generally have molecular weight in the range ≈44–66 KDa (Moll et al., 2008) and hair keratin is one of them, has been decomposed by thermal hydrolysis process and reduced to lower molecular weight range hydrolysate that can be easily dissolved in water.

3.4.3 Amino Acid Composition of Hair Hydrolysate

The results for amino acid composition shown in Table 3.1 indicates that in the hair hydrolysate approximately 70 wt.% part is keratin protein. Around 27 wt.% part of hair hydrolysate consists of charged amino acids (arginine, histidine, lysine, aspartate and glutamic acid) and approximately 19wt.% part consists of polar amino acids (Fischer et al., 2002). The presence of charged and ionizable hydrogen donor and acceptor species in amino acids helps in the ion conduction. Recently, Liu et al., (2020) reported that

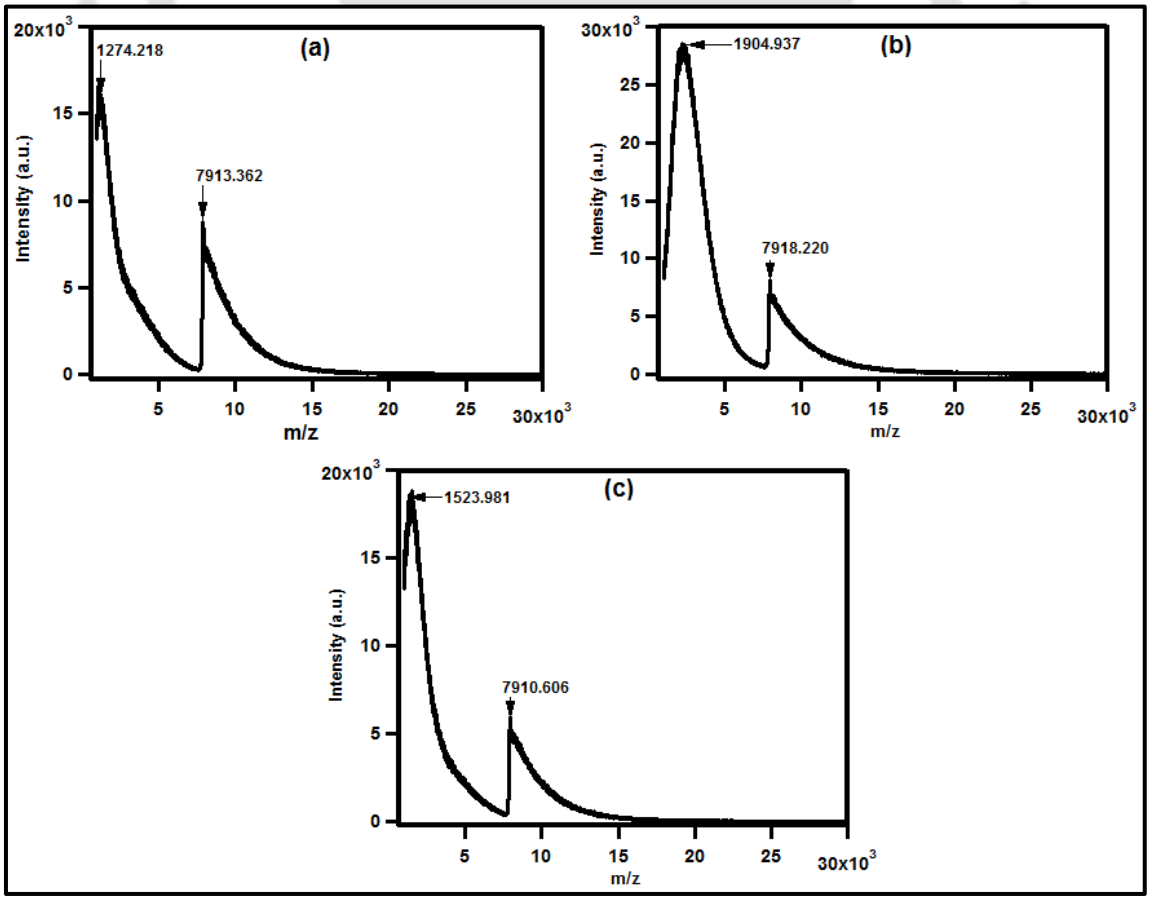

Fig. 3.5 MALDI-TOF-MS of three different batches of hair hydrolysate.

TH-2592_156107017

layer of protein nanowires worked as power generation unit by using only ambient moisture gradient across the layer as driving force, where layers accept the charge from ionized water ($H(H_2O)_n^+$ /$HO(H_2O)_n^-$) which results in closed-loop current flow. Charged amino acids consists of both acidic and basic type and polar amino acids can be polarized by changing the pH, which indicates that proteins are capable of transferring both cationic and anionic species. Transfer of protons through proteins in biological systems (such as photosynthesis) is well known. While proton transport in processes like photosynthesis follows a very rigorous mechanism, where else the proton transport in enzymes involved for energy generation, as reported by Stuchebrukhov, (2009) occurs through special proton conducting channels consisting of protonable groups of protein connected by water. He further described the proton transfer mechanism for three possible cases along the channel. In the first case where deficiency of water is observed in the channel, the proton transfer happens through localized charge, where water molecules carry the charges in the H_3O^+ or OH^- form

Table: 3.1 Amino acid composition in g/ 100g of dry sample.

Amino acid	Amount in gm	Amino acid	Amount in gm
Arginine	7.170±0.330	Valine	5.396±0.326
Histidine	0.645±0.030	Alanine	5.516±0.046
Isoleucine	2.171±0.106	Aspartate	2.018±0.332
Leucine	6.066±0.279	Glutamic acid	14.780±0.376
Lysine	2.279±0.104	Glycine	5.179±0.098
Methionine	0.650±0.055	Proline	7.217±0.310
Phenylalanine	1.711±0.063	Serine	3.668±0.491
Threonine	2.975±0.335	Tyrosine	2.199±0.385
Total		**69.64g/ 100g**	

TH-2592_156107017

between hydrogen donor and acceptor groups of protein. In the second case where a continuous chain is formed by water molecules inside the channel, the transfer occurs via hopping of charge and partial hydrogen bonding, which is activated by thermal changes and localized solvation reduces the activation barrier. In the third case where water molecules form a chain of hydrogen bonds with strong pairing, the proton transfer becomes delocalized between donor and acceptor and transfer becomes much faster compare to other two cases. Similar kind of mechanism has been proposed by Chen et al., (2009) for proton transfer in guanine-cytosine base pair. During high energy radiation positive holes and electrons are formed within the DNA. The holes transfer to guanine, while electron shifts to cytosine. To charge balance, one proton transfers from other site of guanine to cytosine. This proton transfer in the absence of water is difficult resulting in the damage of DNA strand due to excess of electron cytosine, while the slight hydration allows the transfer of proton. In the event of bulk hydration charge transfer takes place by delocalization and base pair captures extra electron due to ease of charge transfer, which can again results in DNA damage.

Anion transport through protein is well known in red blood cell protein called erythrocyte which facilitates the exchange of Cl^- for HCO_3^- across the plasma membrane of the cell (Sterling & Casey, 1999). The red cell membrane shows quite high selectivity for anions in comparison to cations. It was assumed by Mond, (1927) that fixed positive charges lined in water filled channel in the membrane are the reason for the high selectivity of the red blood cell membrane. Selectivity of the anion permeability is regained by loading of OH^- ions. Knauf, (1979) has provided a detailed review chapter on erythrocyte in which he has mentioned that a large number of substrates can be transported through the membrane which includes some exotic compounds such as spin labels, superoxide radical, cyclic nucleotides, carboxylic and sulfonic acids. So, such protein compounds can be used for

TH-2592_156107017

OH^- anion transport. Further, he has detailed the mechanism of anion transport which mainly includes simultaneous and ping-pong models. In the simultaneous model the anions combine with the system and then translocated simultaneously, while in ping-pong model one anion is combined and translocated before the other. These mechanisms are similar to currently known as surface hopping mechanism for H^+ and OH^- ions transport, which is site dependent and where charges hop through certain functional groups present in the ion conductive membranes by converting water in certain intermediate species and then translocating (Grew & Chiu, 2010). Knauf, (1979) also provided review on the nature of sites responsible for anion transfer in erythrocyte and concluded that guanidino group is the most probable site of anion binding compare to other amine sites present in the protein. In general the presence of quaternary ammonium derived functional groups in the polymer chains is well known for its use in alkaline anion exchange membrane for fuel cells (Grew & Chiu, 2010). But presence of guanidino group in anion transport will be an added advantage as they provide preferable anion binding sites. Here, as shown in amino acid analysis approximate 7 wt.% of hair hydrolysate contains arginine which is having guanidino functional group. Arginine as an anion transfer unit has advantages of two positive charge sites, one in form of guanidino group and other is amino group cation. The charge delocalization in guanidino group will also further help in charge transfer and in the acidic medium as explained by Henry & Sykes, (1995) it gets easily protonated and deprotonated in water, making it very suitable for proton transport in the cationic fuel cell membrane as well. The most important advantage of arginine is the stability of guanidino group in the charged (protonated) form in strong basic medium (Xu et al., 2017), which is known to be low for organic cations of the anionic fuel cell membranes in alkaline medium (Sun et al., 2018; Miyanishi et al., 2017; Mahmoud et al., 2016). Thus, as an overall inclusion of hair hydrolysate in membrane will provide anion transfer capability to the

TH-2592_156107017

matrix through different cationic functionalities of the charged and polarizable amino acids present in the hair hydrolysate by following a hopping kind of mechanism as shown in Fig. 3.6, where hairs hydrolysate is used in PVA matrix as AEM.

3.4.4 Crystallinity Analysis and Thermal Stability of Hair Hydrolysate

The crystal structure analysis of hair hydrolysate powder through X-ray diffraction spectroscopy showed its crystalline nature. There are two crystalline peaks, one is around 2θ value 9.7° for α-helix structure, which is very small and hardly recognizable and the second is around 2θ value 20° for β-sheet structure of peptides present in the hair hydrolysate (wang et al., 2018) (Fig. 3.7). The presence of amide I band around 1658 cm^{-1} indicates the presence of α-helix structure in hair hydrolysate (Kong & Yu, 2007), which

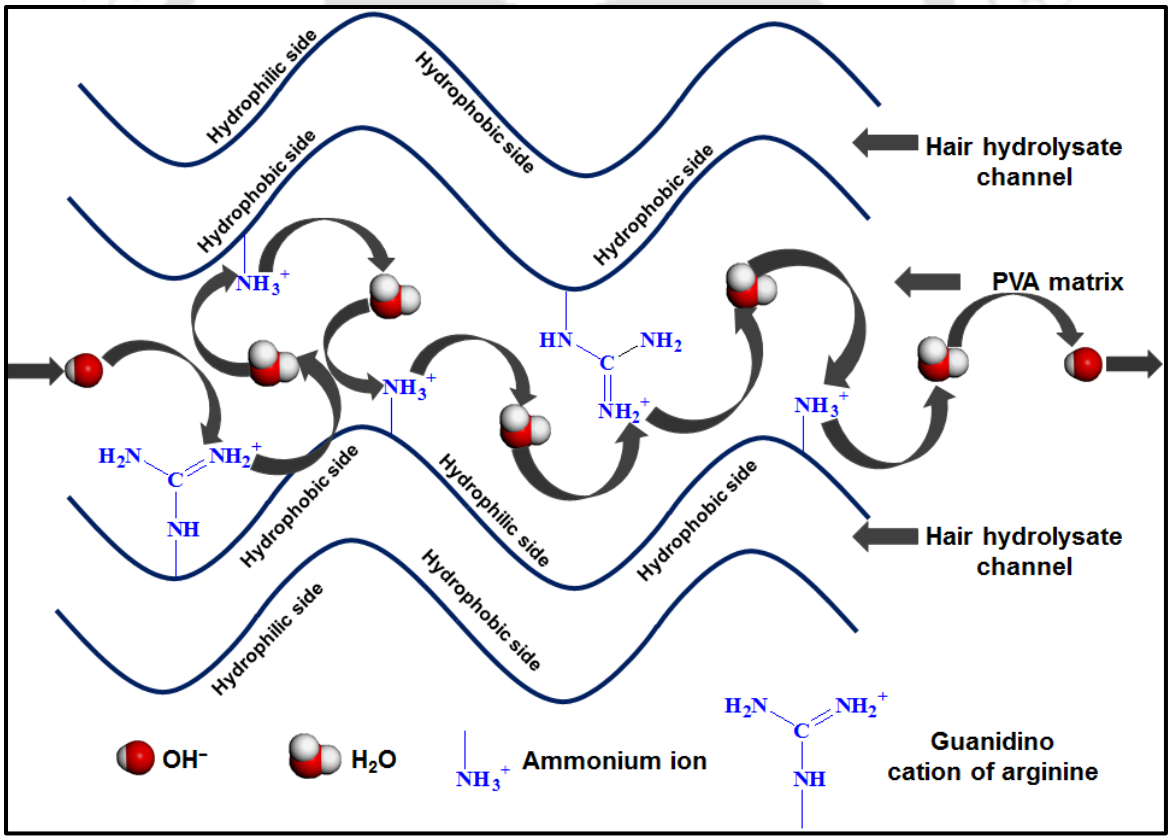

Fig. 3.6 Hopping mechanism of OH− ion through charge transfer sites.

TH-2592_156107017

has been further supported by XRD results. Thermal stability of hair hydrolysate can be observed from Fig. 3.8(a). From the differential thermogravimetric graph (DTG) shown in Fig. 3.8(a), we can observe four major weight loss zones. The weight loss below 150°C can be attributed to removal of physically bound moisture to the sample. Second weight loss region in the temperature range 150°C to 350°C is observed due decomposition of β-sheet structure of hair hydrolysate and a sharp weight loss peak just adjacent to the second weight loss peak is due to decomposition of α-helix structure. The final weight loss beyond 380°C represents the pyrolysis of remaining material in the N_2 atmosphere. With increasing temperature, there is hardly any crystallization and melting behavior was observed by DSC analysis for hair hydrolysate (Fig. 3.8(b)), only a very small endothermic peak can be observed around 200°C due to slight melting of crystals present. Beyond 200°C, the material simply degrades, leaving behind around 10 wt.% ash content.

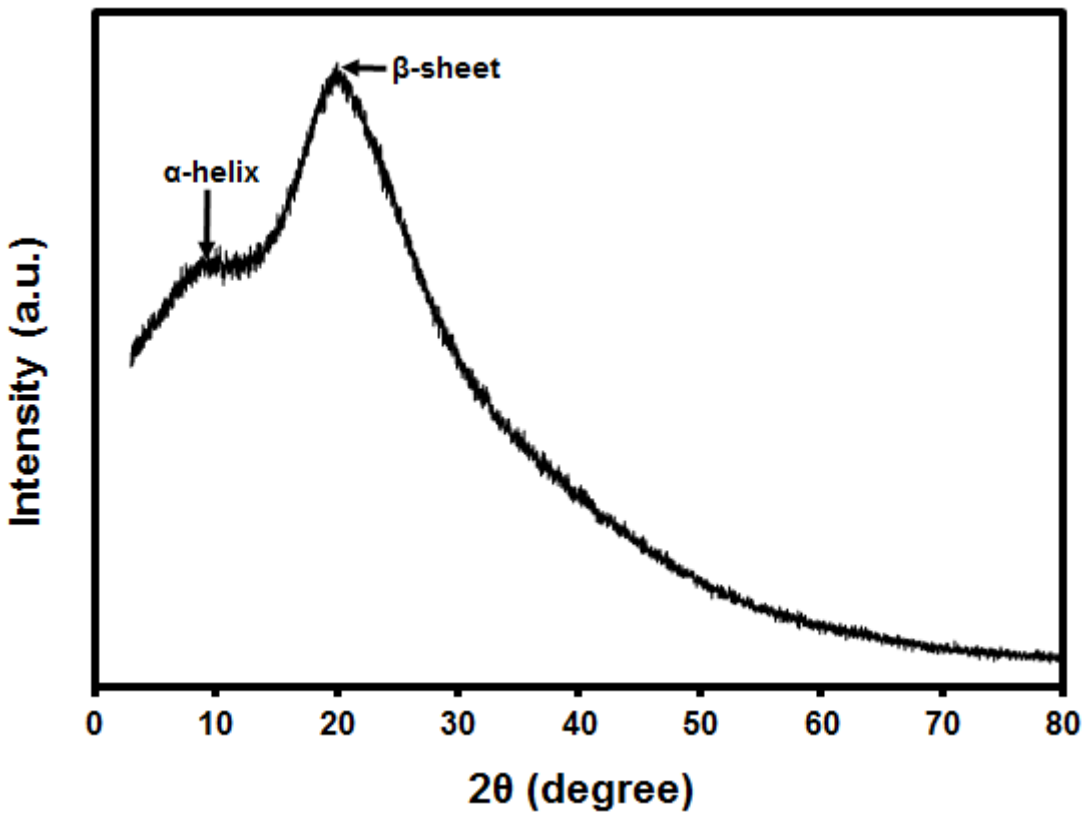

Fig. 3.7 XRD curve of hair hydrolysate.

TH-2592_156107017

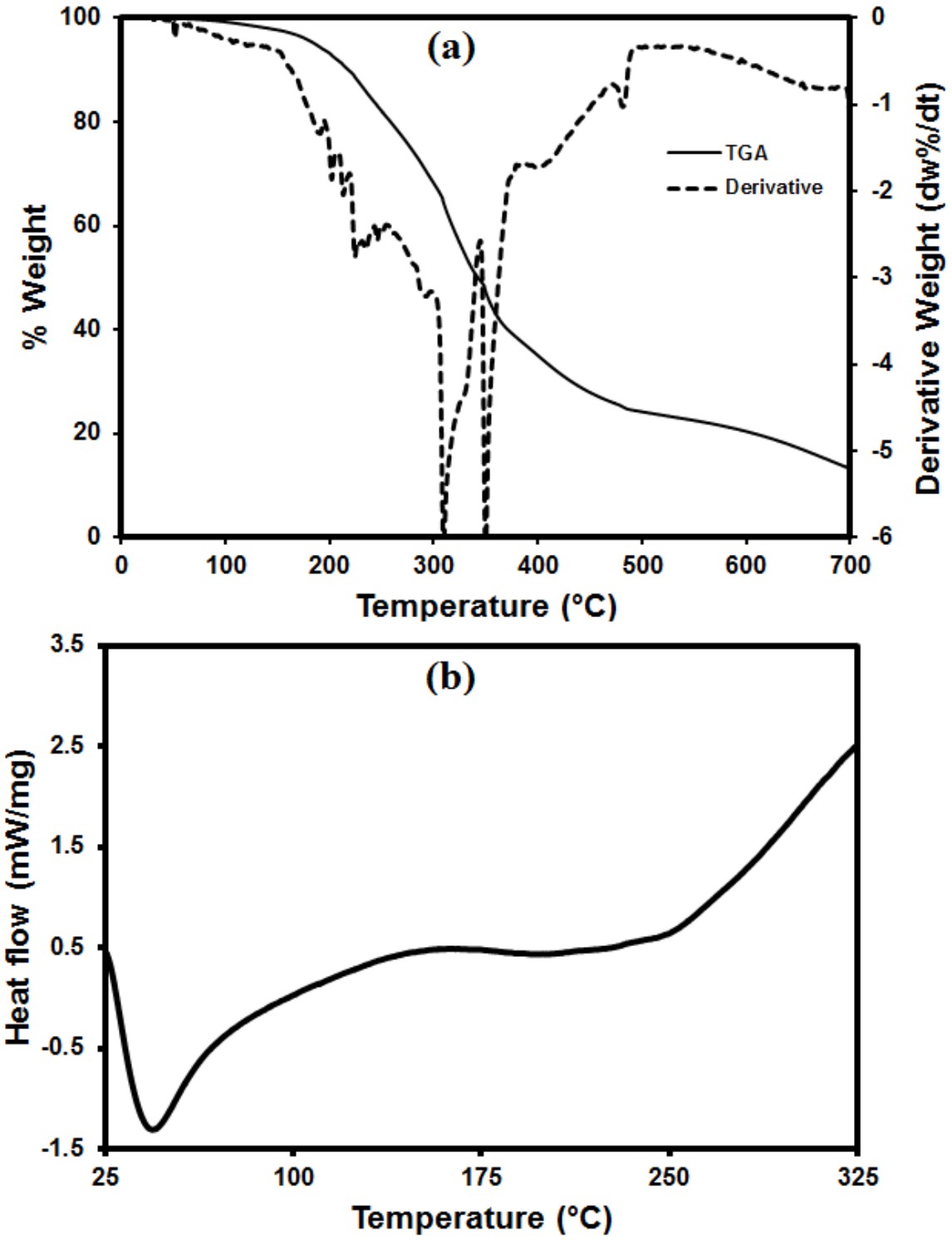

Fig. 3.8 (a) TGA and DTG thermograph (b) DSC thermograph of hair hydrolysate.

TH-2592_156107017

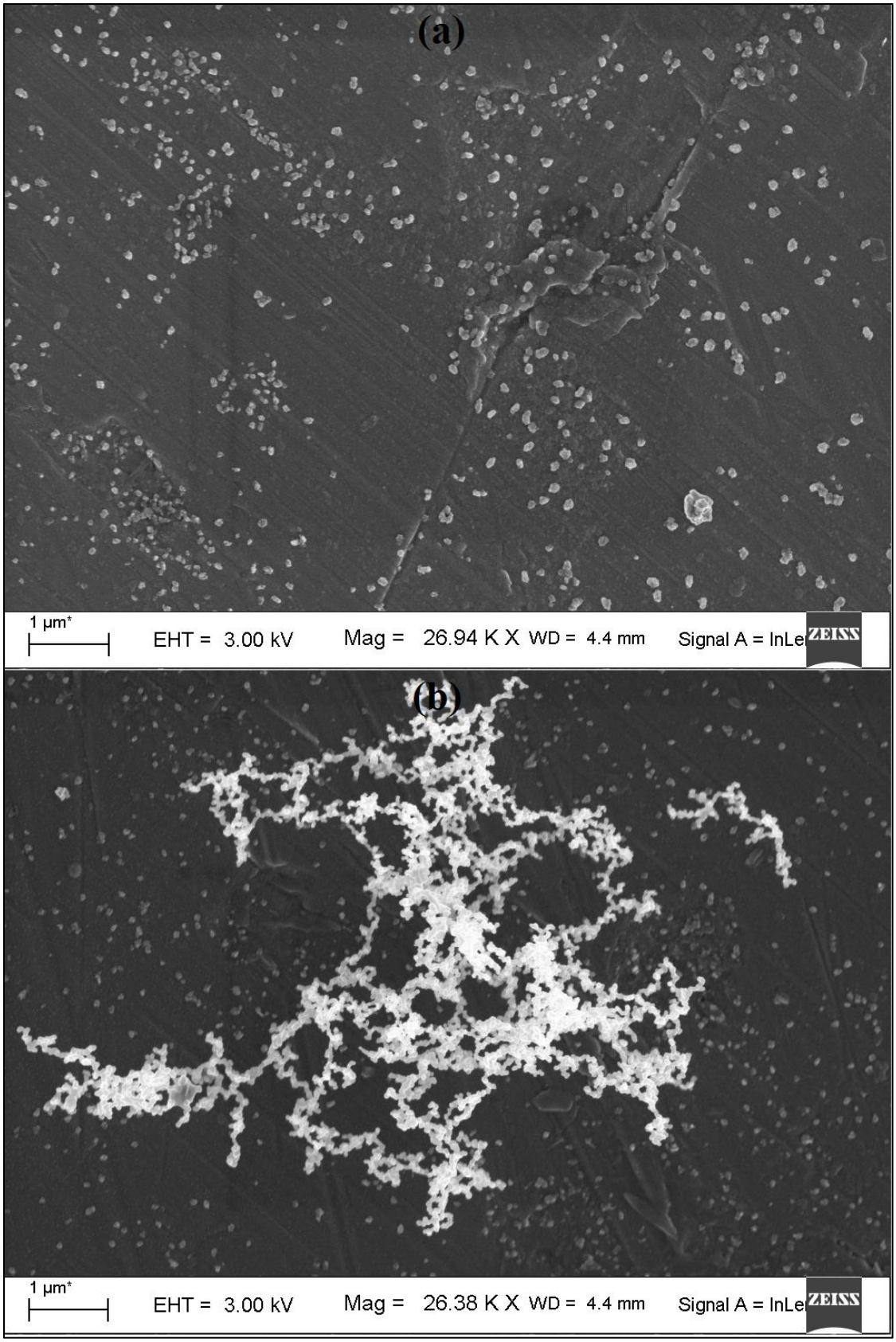

Fig. 3.9 FESEM images of (a) Hair hydrolysate (b) Partially crosslinked hair hydrolysate.

TH-2592_156107017

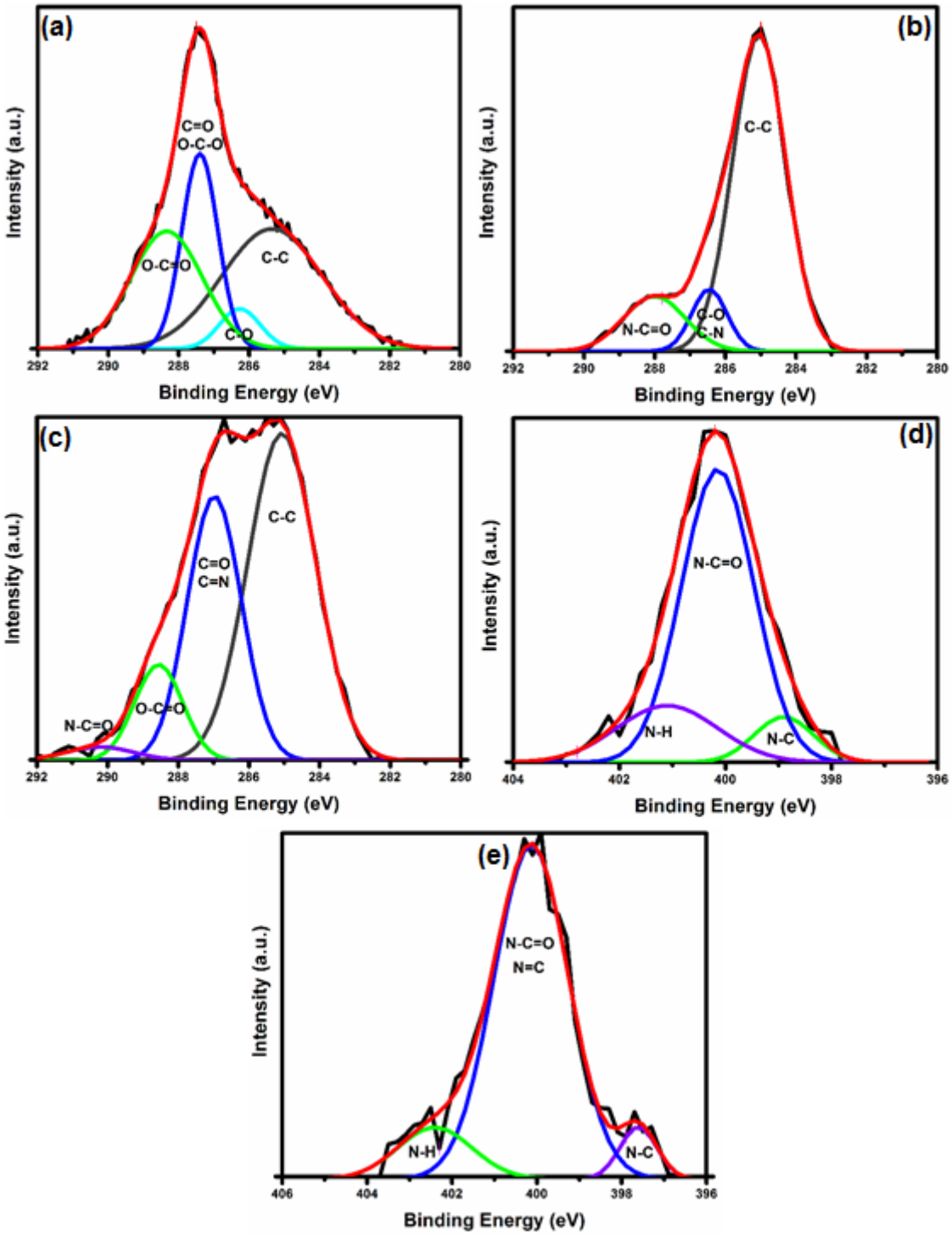

Fig. 3.10 XPS spectra of carbon 1s (a) CNCs (b) hair extract (c) modified CNCs and nitrogen 1s spectra of (d) hair extract (e) modified CNCs.

TH-2592_156107017

3.4.5 Morphology of Hair Hydrolysate

The spherical shape nanoparticle morphology of hair hydrolysate as shown in Fig. 3.9 (a) matches with the morphology of keratein micro and nanoparticles reported in the literature (Ma et al., 2016; Sharma et al., 2017; Zhang et al., 2013). To check the effect of crosslinker GA on hair hydrolysate, 10 mg of hair hydrolysate was dissolved in 1.5 ml of water and 100 µl of GA solution was added into it. One drop of the solution was taken on aluminum foil and drop casted by drying at 100°C for 10 minutes and FESEM images were taken. Fig. 3.9(b) shows that GA can crosslink the spherical hair hydrolysate particles to form a random chain morphology. In the background of random chain morphology in Fig. 3.9(b), we can see the rest of un-crosslinked hair hydrolysate particles.

3.4.6 Confirmation of CNCs Modification by XPS Analyses

Fig. 3.1 showed the possible reaction mechanism of CNC modification by hair hydrolysate. To prove the modification of CNCs XPS analysis was carried out. As shown in Fig. 3.10, carbon 1s spectra of CNCs shows four peaks for C-C at 285 eV, C-O at 286.2 eV, C=O and O-C-O at 287.3 eV and O-C=O at 288 eV, while hair extract shows three peaks of C-C at 285 eV, C-O and C-N at 286.3 eV and O-C=O at 288.3 eV. The effect of modification of oxidized CNCs by hair extract is clearly visible from the carbon 1s spectra of modified CNCs. It has major peak of C-C due to attached keratinic protein/peptide chains of hair extract, while the high intensity of the second peak is result of formation of C=N bond along with the presence C=O from non-crosslinked aldehyde groups. The modification of oxidized CNCs was further confirmed by the presence of nitrogen in nitrogen 1s spectra of modified CNCs.

TH-2592_156107017

3.4.7 Morphology of Modified CNCs and Modified CNC-CS Membrane

As shown in the Fig. 3.11 (a), CNCs have road like morphology. The $NaIO_4$ oxidized CNCs after reacting with low molecular weight hair hydrolysate forms network like structure (Fig 3.11 (b)), where the CNC are connected by network of the chains of it. The cross-sectional image of CS-hair extract modified CNC film shows CS matrix bounded by CNCs via epichlorohydrin crosslinking agent (Fig. 3.11 (c) and (d)).

3.4.8 Ionic Conductivity, Water Uptake and % Swelling

Table 3.2 shows the results of ion conductivity, water uptake and %swelling for the CS-5 wt.% hair hydrolysate modified CNCs. The ion conductivity of the sample at room temperature was observed to be around 1 mS/cm. Improvement in the ion conductivity was observed for modified CNC based membrane, compared to CS membrane. The ion conductivity data also showed the improvement in the ionic conductivity of modified CNC based membrane compared to the CNCs based membranes studied for acidic type DMFCs in the previous chapter. Water uptake was increased slightly due to hydrophilic network formed by hair hydrolysate modified CNCs in CS matrix, as shown in Fig. 3.11 (c) and at the same time this network formation enhanced the matrix to filler interaction resulting in the reduction of %swelling in comparison to ECH crosslinked CS membrane. The membrane prepared here had long term mechanical stability issues and failed several time during methanol permeability analysis. At the same time PVA based membrane with hair hydrolysate showed better ionic conductivity and good thermo-mechanical stability, the CS-modified CNC based membranes were not pursued for further investigations.

TH-2592_156107017

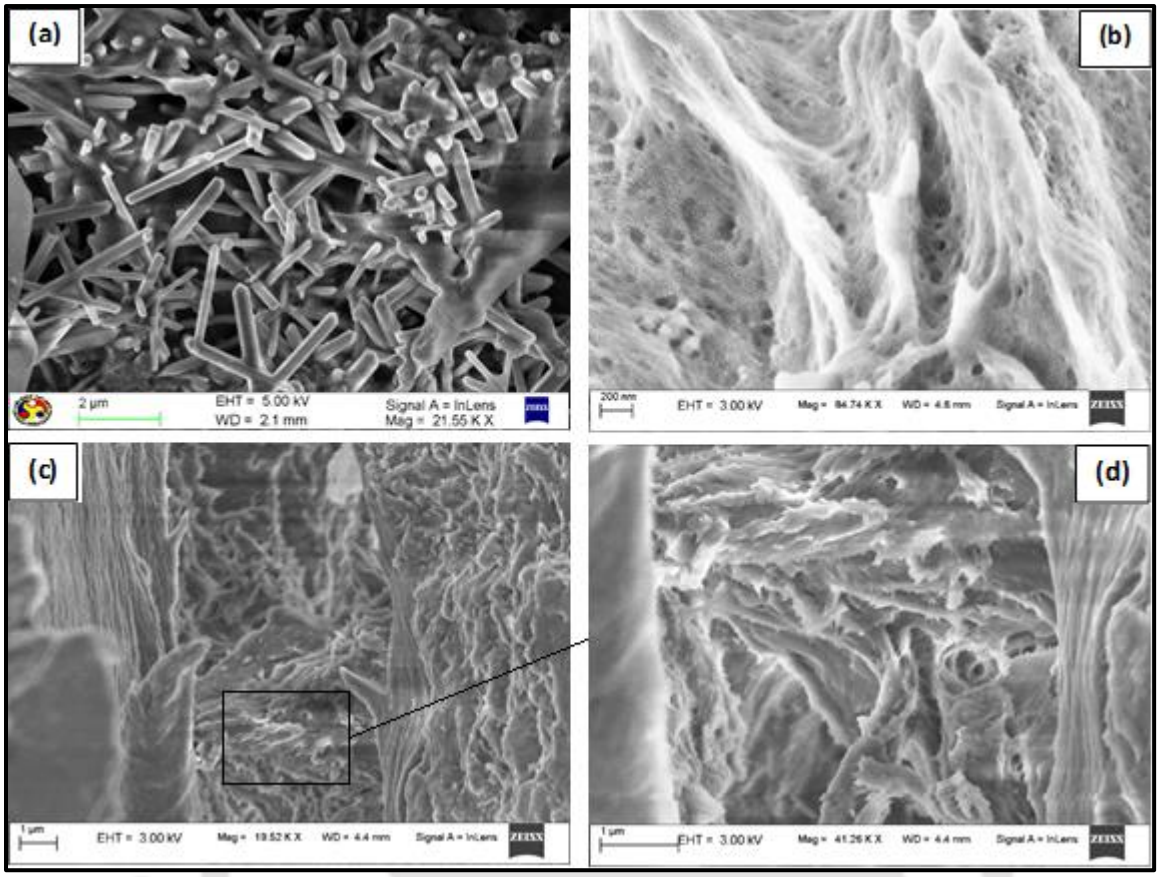

Fig. 3.11 FESEM images of (a) CNC (b) hair extract modified CNC (c) & (d) chitosan-hair extract modified CNC based AEM cross-section.

Table: 3.2 Ionic conductivity, water uptake and %swelling of CS-modified CNC membrane.

Property	**ECH crosslinked chitosan film**	**ECH crosslinked-5wt.% HH modified CNC film**
Ionic Conductivity (mS/cm)	0.25±0.02	1.04±0.02
Water Uptake (%)	48±5	60±2
%Swelling	38±4	26±2

TH-2592_156107017

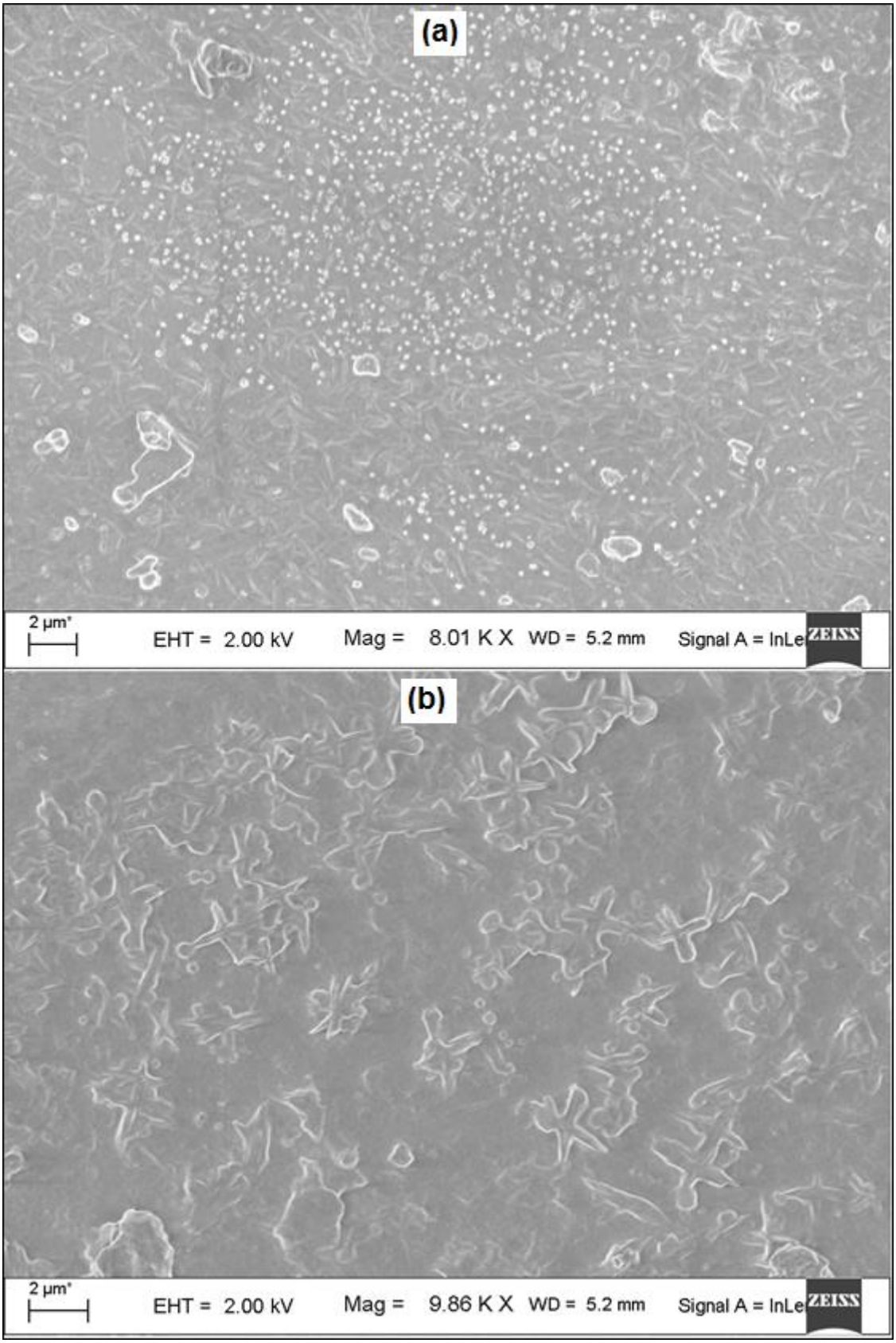

Fig. 3.12 FESEM imges of (a) & (b) PVA-1wt.% hair hydrolysate membrane.

TH-2592_156107017

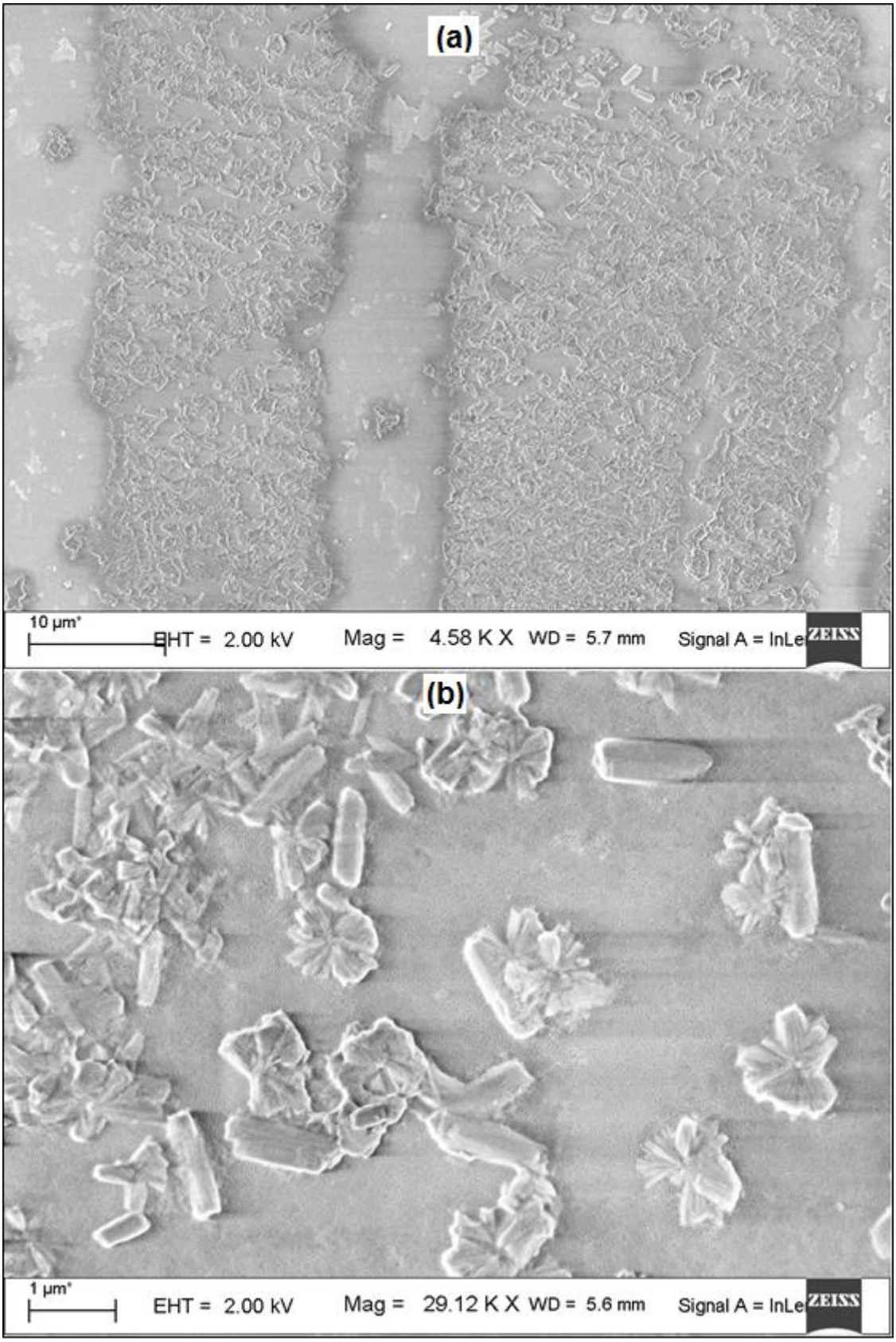

Fig. 3.13 FESEM images of (a) & (b) PVA-5wt.% hair hydrolysate membrane.

TH-2592_156107017

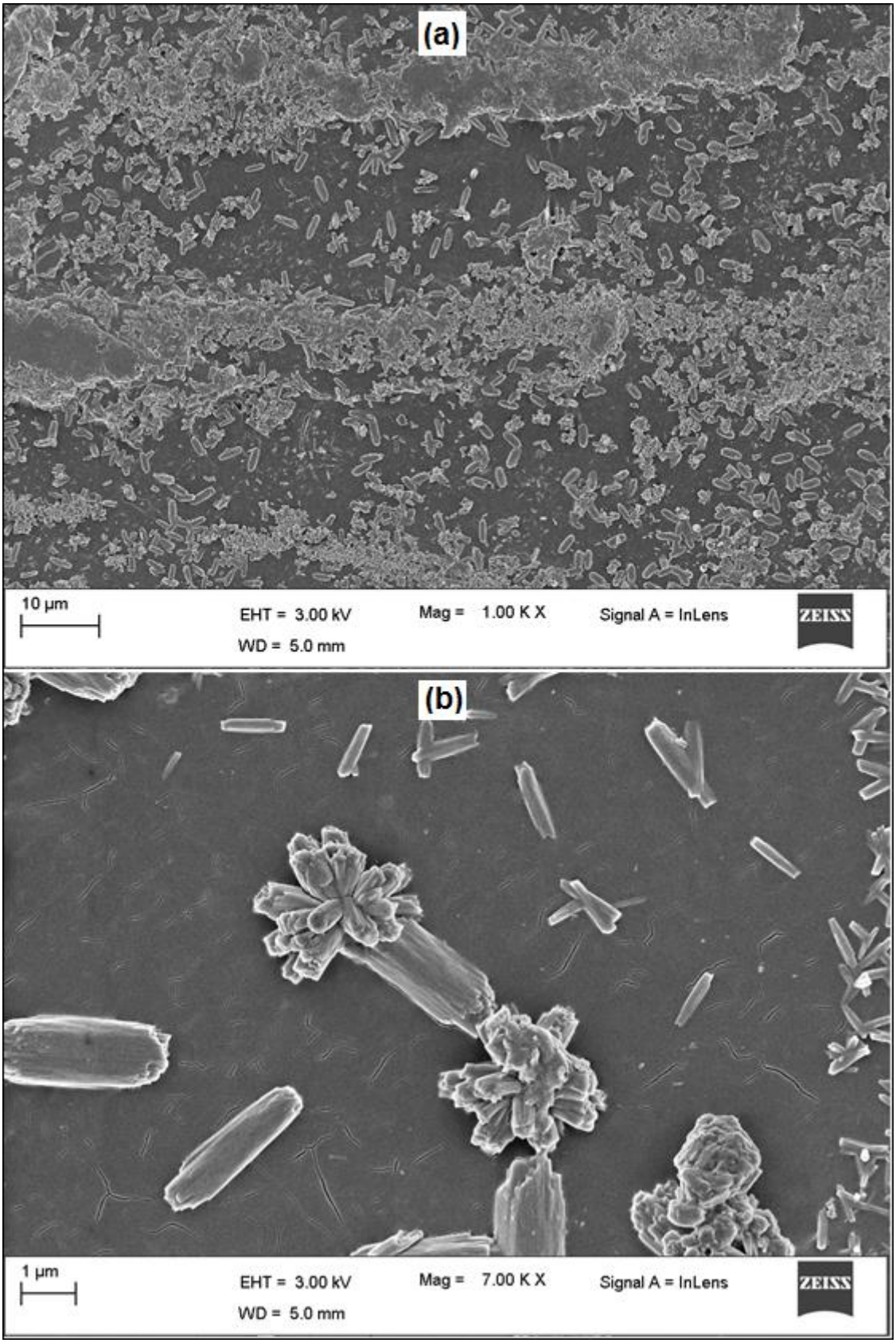

Fig. 3.14 FESEM images of (a) & (b) PVA-10wt.% hair hydrolysate membrane.

TH-2592_156107017

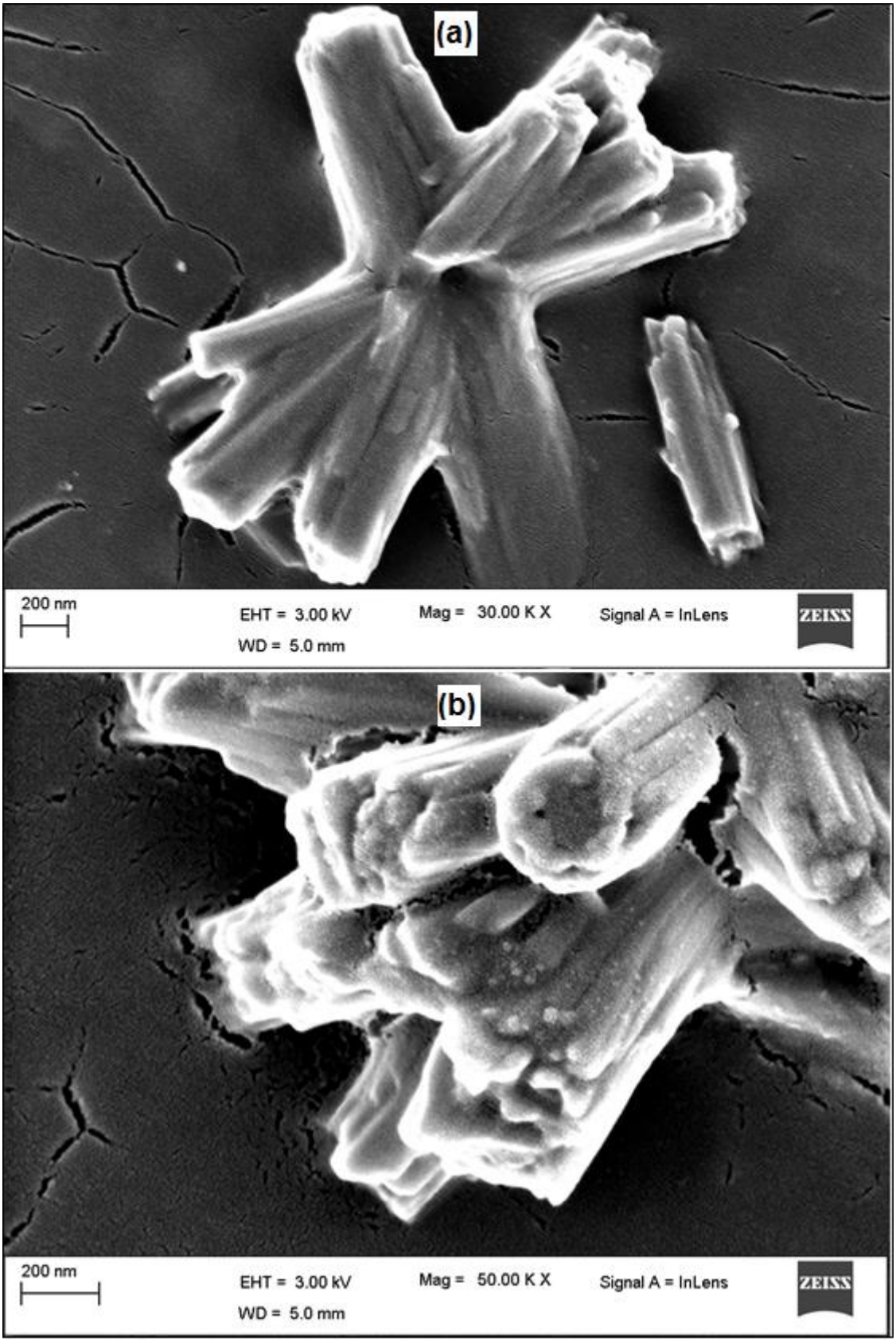

Fig. 3.15 FESEM images (a) & (b) magnified flower morphology of present in 5wt.% and 10wt.% hair hydrolysate based PVA membranes.

TH-2592_156107017

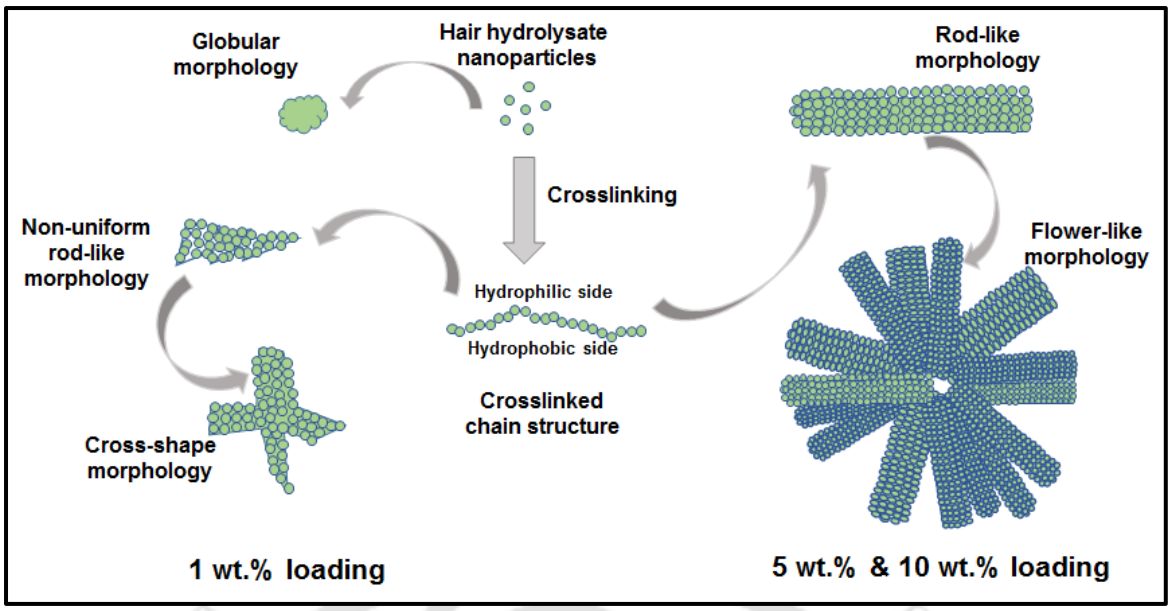

Fig. 3.16 Mechanism of different types of morphologies formation in PVA-hair hydrolysate membranes

3.4.9 Morphology of PVA-Hair Hydrolysate Membranes

PVA-1wt.% hair hydrolysate GA crosslinked membranes showed random morphology. As shown in Fig. 3.12 (a), in one part of the membrane, it shows the presence of hair hydrolysate nanoparticles, globular shape bigger particles and in background rod shape morphology can be observed. In another part of the membrane (Fig. 3.12 (b)) we can observe the globular and cross shape morphologies of hair hydrolysate in the PVA matrix. While the globular morphology may be observed due to combining of several hair hydrolysate nanoparticles, the rod-shape morphology may be present due to combined effect of crosslinking and alignment of hydrophobic-hydrophilic sections of hair hydrolysate. The crosslinking gives hair hydrolysate chain-like structure, at the same time hydrophobic zones of chains may align inwards as PVA is hydrophilic, forming a rod-like crystal morphology. The cross-shape morphology is formed by joining of hydrophilic ends of four such rods. The effect of alignment of hydrophobic-hydrophilic sections of hair

TH-2592_156107017

hydrolysate is clearly visible in the higher concentration (5 wt.% and 10 wt.%) of hair hydrolysate. In case of PVA-5 wt.% hair hydrolysate membrane, we can see channels formation (Fig. 3.13 (a)) in the membrane by hair hydrolysate.

Due to increased concentration, hair hydrolysate forms separate channel like sections, where it tries to bring hydrophobic parts together and align them inwards side of the channels, while keeping the hydrophilic sections outwards and in between two channels is the PVA matrix. Such micron size channels in the presence of water will provide a continuous path for charge transfer, reducing the charge transfer barrier. The magnified image (Fig. 3.13 (b)) of the channels shows the presence of rod-like and flower-like morphology. As explained for PVA-1wt.% hair hydrolysate membrane, the rods are crystals formed by alignment of the hydrophilic and hydrophobic parts of the crosslinked hair hydrolysate chains. Due to higher concentration the rod-shape morphology is clearly visible in PVA-5wt.% hair hydrolysate membrane. While the flower shape morphology also can be contributed to increased concentration, where the hydrophilic ends of multiple small rods combined to form the flower morphology, similar to the formation of cross shape in previous case. This can be further verified from Fig. 3.15(a) where we can see that multiple rods are combining together to form the flower shape and as edges of the rods touches each other, they are creating a hollow section in the center of the flower. The assumption of formation of rods by crystal formation through arrangement of hair hydrolysate nanoparticles can also be verified through Fig. 3.15(b) in which we can see the very small to bigger size nanoparticles in the magnified image of flower shape morphology. As the concentration of hair hydrolysate is further increased to 10 wt.% in PVA matrix, we can see the formation of even bigger rods and 3D flowers formation by smaller rods (Fig. 3.14(b)). But higher concentration also results in the formation of multiple flat agglomerated phase sections in the channels, as shown in parts of Fig. 3.14(a), as well as it

TH-2592_156107017

blocks the gap between two channels, subsequently blocking the continuous path of charge transfer and resulting in higher resistance to charge transfer. The ion conductivity results agree with the morphological analysis results and will be discussed in the subsequent section. Overall mechanism of formation of different types of morphologies in different wt.% hair hydrolysate loadings with PVA matrix membranes is explained in Fig. 3.16.

3.4.10 Thermal Stability of PVA-Hair Hydrolysate Membranes

The thermal stability of base PVA-GA and its composite membrane with hair hydrolysate (denoted by HH) is shown in Fig. 3.17. The base membrane shows four weight loss regions in the DTG curve. The first weight loss region below 200°C is common in all the membranes, which is observed due to evaporation of physically bound water to samples. The second region between 230°C to 330°C is degradation region of amorphous part of PVA and the third region from 330°C to 420°C is observed due to decomposition of crystalline PVA. The final weight loss region beyond 420°C is simple pyrolysis of remaining sample. After inclusion of hair hydrolysate in the PVA matrix there is not much change found in first and final weight loss regions, only the final weight loss started from a little lower temperature (400°C-410°C) for the composite membranes. The noticeable changes were observed in the second weight loss region, as the peak of second weight loss in DTG curve slowly disappeared with increasing the concentration of hair hydrolysate in the PVA matrix. It indicates that the hair hydrolysate crystals during formation of particular type of morphology such as rod shape and cross shape in 1 wt.% hair hydrolysate loading and rod shape and flower shape in case of 5 wt.% and 10 wt.% hair hydrolysate loading, tries to arrange the PVA chains along with them by interaction of their exterior hydrophilic sites with hydrophilic PVA chains to form a single phase. So, as the concentration of hair hydrolysate goes up the weight loss peak due to amorphous section is reduced continuously

TH-2592_156107017

and it is completely merged to the third weight loss peak in 10 wt.% hair hydrolysate loading showing single weight loss zone in the temperature range 230°C to 420°C. Thus, we can conclude that interaction between hair hydrolysate and PVA matrix improved the thermal stability of composite membranes in comparison to base PVA-GA membrane.

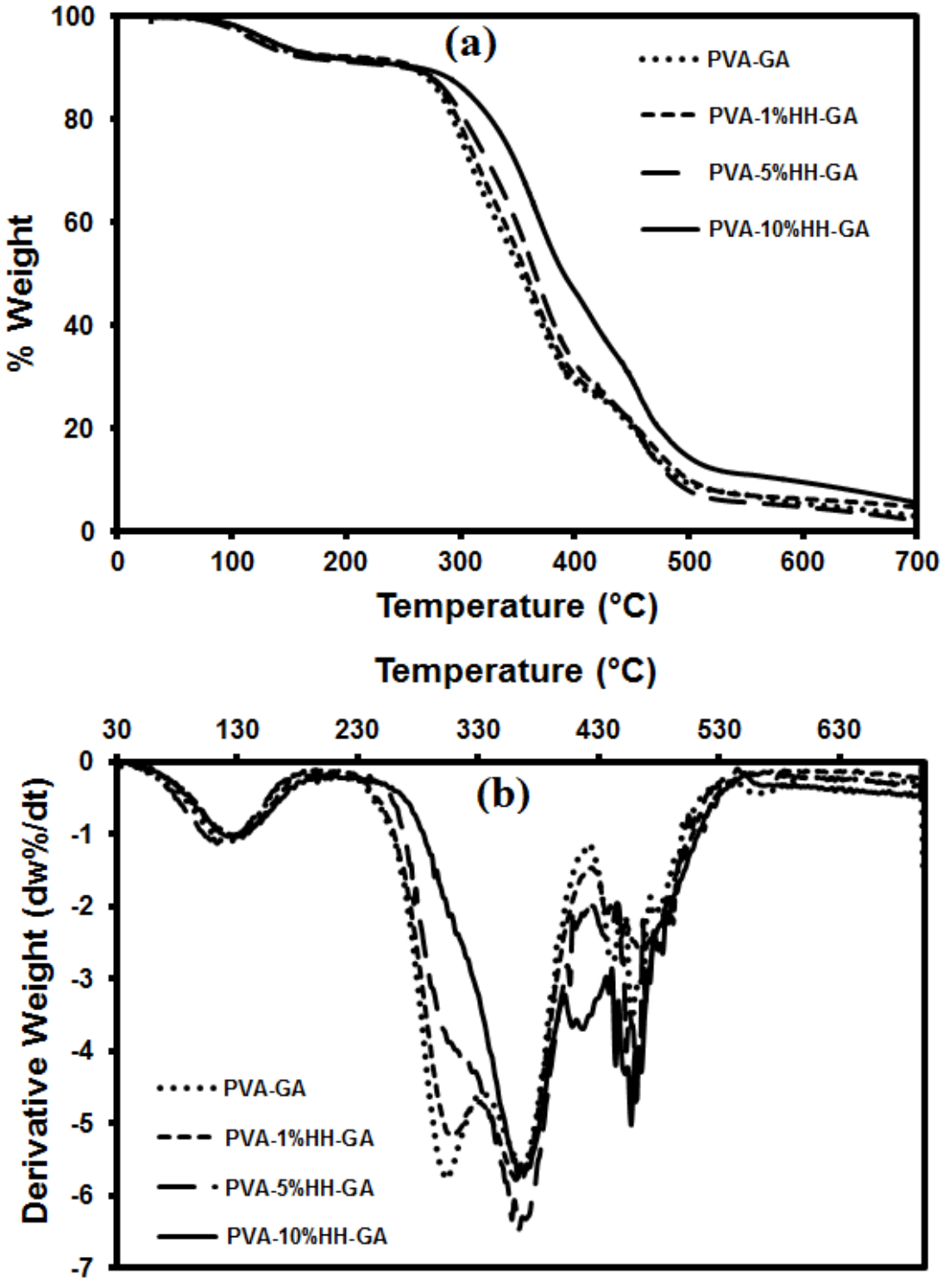

Fig. 3.17 (a) TGA (b) DTG thermograph of PVA-hair hydrolysate (HH) membranes.

TH-2592_156107017

3.4.11 Ionic Conductivity, Methanol Permeability and Selectivity of the PVA-Hair Hydrolysate Membranes

Hydroxyl ion conductivity was analyzed in the alkaline medium for the PVA-hair hydrolysate samples and the results are listed in Table-3.3 and a comparison was made with the base PVA membrane. The ionic conductivities of all the samples were increased with increase in the temperature. All the hair hydrolysate based samples showed at least a decimal order of magnitude higher ionic conductivity at all the temperatures, compared to the base membrane. As expected through morphological analysis, the best results for ionic conductivity (7.46 mS/cm at 70°C) were observed for 5 wt.% hair hydrolysate loading, where we could observe clear channel network for ion conduction in the membrane. While introduction of hair hydrolysate by adding 1 wt.% into the PVA matrix improved the ionic conductivity, adding higher amount (10 wt.%) resulted in the blocking of channel network as well as the increased crystal network increased the resistance to ion permeation, resulting in the reduction of ionic conductivity. Effect of interaction between hydrophilic PVA matrix and hair hydrolysate (observed through TGA analysis) as well as increased crystal network content can be observed through methanol permeability data (Table-3.4). Increasing the content of hair hydrolysate resulted in the improvement of methanol barrier properties and 10 wt.% hair hydrolysate loading sample showed lowest methanol diffusion coefficient (4.14×10^{-7} cm^2/s). As per selectivity data, which is ration of ion conductivity to methanol permeability, 5 wt.% hair hydrolysate loading sample showed the best results with a selectivity value of 6.14×10^3 $S.s/cm^3$.

TH-2592_156107017

Table: 3.3 Ion conductivity data of PVA based membranes with increasing temperature.

Sample	**Ionic conductivity (mS/cm)**				
Temperature (°C)	30	40	50	60	70
PVA-GA	0.08±0.01	0.09±0.01	0.11±0.02	0.12±0.01	0.16±0.04
PVA-1wt.%HH-GA	2.13±0.22	2.46±0.24	2.65±0.12	2.85±0.07	3.10±0.05
PVA-5wt.%HH-GA	4.48±0.45	4.58±0.17	5.35±0.76	7.31±0.95	7.46±0.57
PVA-10wt.%HH-GA	2.05±0.26	2.39±0.12	2.45±0.35	2.55±0.23	2.93±0.20

Table: 3.4 Methanol permeability and selectivity data of PVA based membranes at 30°C temperature.

Sample	Methanol permeability (cm^2/s)	Selectivity ($S.s/cm^3$)
PVA-GA	$(1.39\pm0.09)\times10^{-6}$	0.06×10^3
PVA-1wt.%HH-GA	$(1.05\pm0.10)\times10^{-6}$	2.02×10^3
PVA-5wt.%HH-GA	$(7.29\pm0.87)\times10^{-7}$	6.14×10^3
PVA-10wt.%HH-GA	$(4.14\pm0.24)\times10^{-7}$	4.95×10^3

Table: 3.5 Water uptake and % swelling in 0.5 M KOH solution of PVA based membranes.

Sample	Water uptake (%)	% Swelling
PVA-GA	165±5	60±6
PVA-1wt.%HH-GA	130±3	34±2
PVA-5wt.%HH-GA	144±6	30±1
PVA-10wt.%HH-GA	150±8	30±1

TH-2592_156107017

3.4.12 Water Uptake and %swelling of PVA-Hair Hydrolysate Membranes

Presence of water is important for the ionic conductivity of the membranes as it works as ion carrier and a continuous water channel helps in ion transport. But excessive water uptake is a problem for PVA based membranes as it creates excessive swelling, reducing the stability of the membranes. At the same time during cell reaction production of water will create a flooding problem. As we can observe from Table-3.5, the water uptake for PVA-GA membrane is quite high, which results in the high swelling %. Inclusion of hair hydrolysate introduced crystalline network in the PVA matrix, resulting in a reduction of %swelling with increasing hair hydrolysate content. At the same time, hair hydrolysate contains more hydrophilic functional groups, resulting in again increasing trend for water uptake. %swelling has reduced to 30% in comparison to 50% for base PVA membrane, but 30% swelling is still high. To reduce the %swelling further annealing was done for the 5 wt.% hair hydrolysate loaded membrane samples at 120°C. Annealing of polymers is well known process to improve the crystallinity, at the same time, as reported in literature (Rynkowska et al., 2019) annealing of PVA improves the crosslinking. Both of these processes decrease the free volume available in membrane. Reduced free volume will reduce the water uptake as well as %swelling and increased crosslinking will improve the thermal and mechanical properties. 5 wt.% hair hydrolysate loaded PVA membrane sample was chosen based on its better ion conductivity and selectivity. The changes in various properties of the 5 wt.% hair hydrolysate loaded PVA membrane sample due to annealing are discussed in the subsequent section.

TH-2592_156107017

3.4.13 Effect of Annealing on the Properties of PVA-5wt.% Hair Hydrolysate Membrane and its Alkaline Stability

Annealing of the membrane results in the crystallization of PVA matrix as well as improvement in the crosslinking which affects all the properties of membrane related to an AEM. Increasing in the crystallinity of the membrane due to annealing can be observed through XRD spectra shown in Fig. 3.18. As we can see from the spectra, the peak around 2θ value 20° had drastic increase in the intensity which is combined peak of β-sheet structure of peptides present in the hair hydrolysate and PVA (101) crystal plane. The other PVA peaks around 2θ value 23° and 41° for crystal planes (200) and (102) did not change much, indicating that (101) is the main crystal plane formed in the matrix. Slight improvement in the crystallinity was also happened by hair hydrolysate, which is visible from slight increased intensity of α-helix band around 9.7°. Crystallization of the membrane had very significant effect on the thermo-mechanical stability. Thermo-mechanical stability showed drastic improvement as storage modulus (E′) was increased from around 1800 MPa for before annealed sample to around 6800 MPa for annealed sample at 25°C and it remain around 950 MPa at 100°C for the annealed sample, while for before annealed sample it reduced to around 100 MPa (Fig. 3.19), showing the impact of increased crosslinking. Reduction in elongation due to increased crystallinity can also be detected through DMA analysis, as shown in Fig. 3.19, where under continuous force of 1 N during sample run the total elongation observed for before annealed sample having initial sample length of 10 mm, is around 2.70 mm, while after annealing it is observed to be around 1.45 mm. Thermal stability of the base matrix did not change much by annealing, only the small peak for degradation of amorphous part of PVA present before annealing in the temperature range 230°C-330°C, completely merged in the thermal degradation peak of crystalline PVA (Fig. 3.20). The noticeable change was found in the weight loss region due to evaporation

TH-2592_156107017

of bound moisture, where weight loss started around 30°C in the membrane sample before annealing, while after annealing it delayed and started around 85°C. It shows the increased capability of the membrane sample to trap the water molecules in between crystals and keep it bound tightly till 85°C. Another noticeable thing is weight loss due to evaporation of trapped water, which is around 10 wt.% before annealing and after annealing it is reduced to 4 wt.%, confirming the reduction in water uptake of membrane and the same has also been supported by water uptake data shown in Table-3.6. Increment in crystallinity improves the barrier properties, which is quite indicative by both methanol permeability as well as ionic conductivity data shown in the Table-3.6.

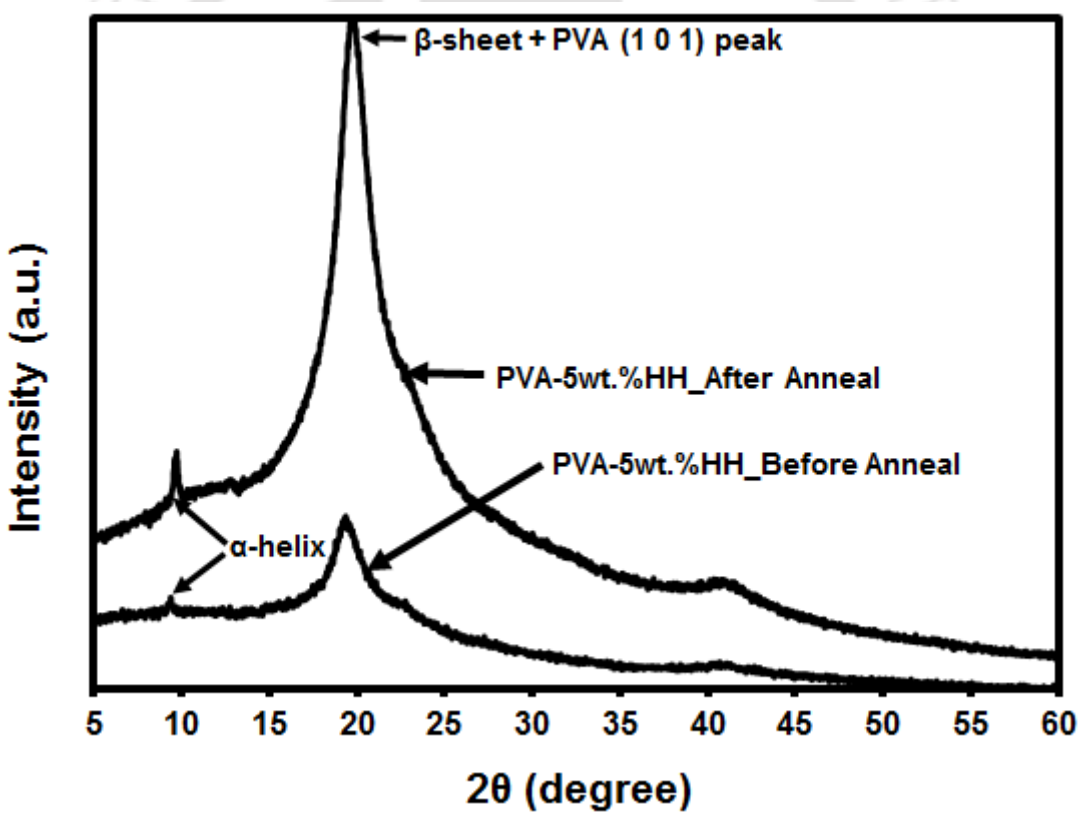

Fig. 3.18 XRD spectra of PVA-5wt.% hair hydrolysate membrane before and after annealing.

TH-2592_156107017

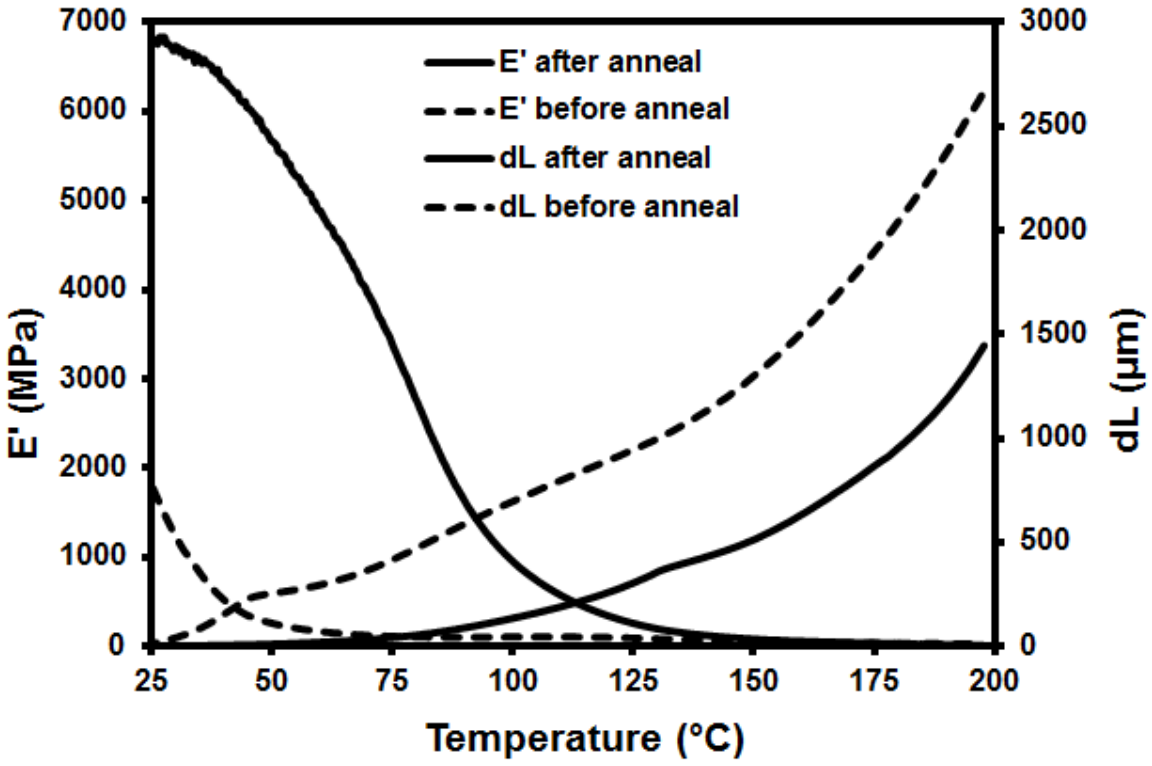

Fig. 3.19 DMA analysis of PVA-5wt.% hair hydrolysate membrane before and after annealing.

Table: 3.6 Properties of PVA-5wt.% hair hydrolysate membrane sample before and after annealing.

Sample	PVA-5wt.%HH_before anneal	PVA-5wt.%HH_after anneal	Tokuyama® A201
Water Uptake (%)	144±6	40±1	≈40 (Wang et al., 2012)
%Swelling	30±1	15±1	≈9 (50°C) (Duan et al., 2013)
Ionic Conductivity (mS/cm)	7.46±0.57 (70°C)	6.16±0.23 (70°C)	29 (RT) (Merle et al., 2011)
Methanol Permeability (cm^2/s)	$(7.29\pm0.87)\times10^{-7}$ (30°C)	$(7.45\pm0.99)\times10^{-8}$ (30°C)	$(4.44\pm0.02)\times10^{-7}$ (23.5 °C) (Wang et al., 2012)
Selectivity ($S.s/cm^3$)	6.14×10^3 (30°C)	6.00×10^4 (30°C)	6.53×10^4 (≈23.5°C)

TH-2592_156107017

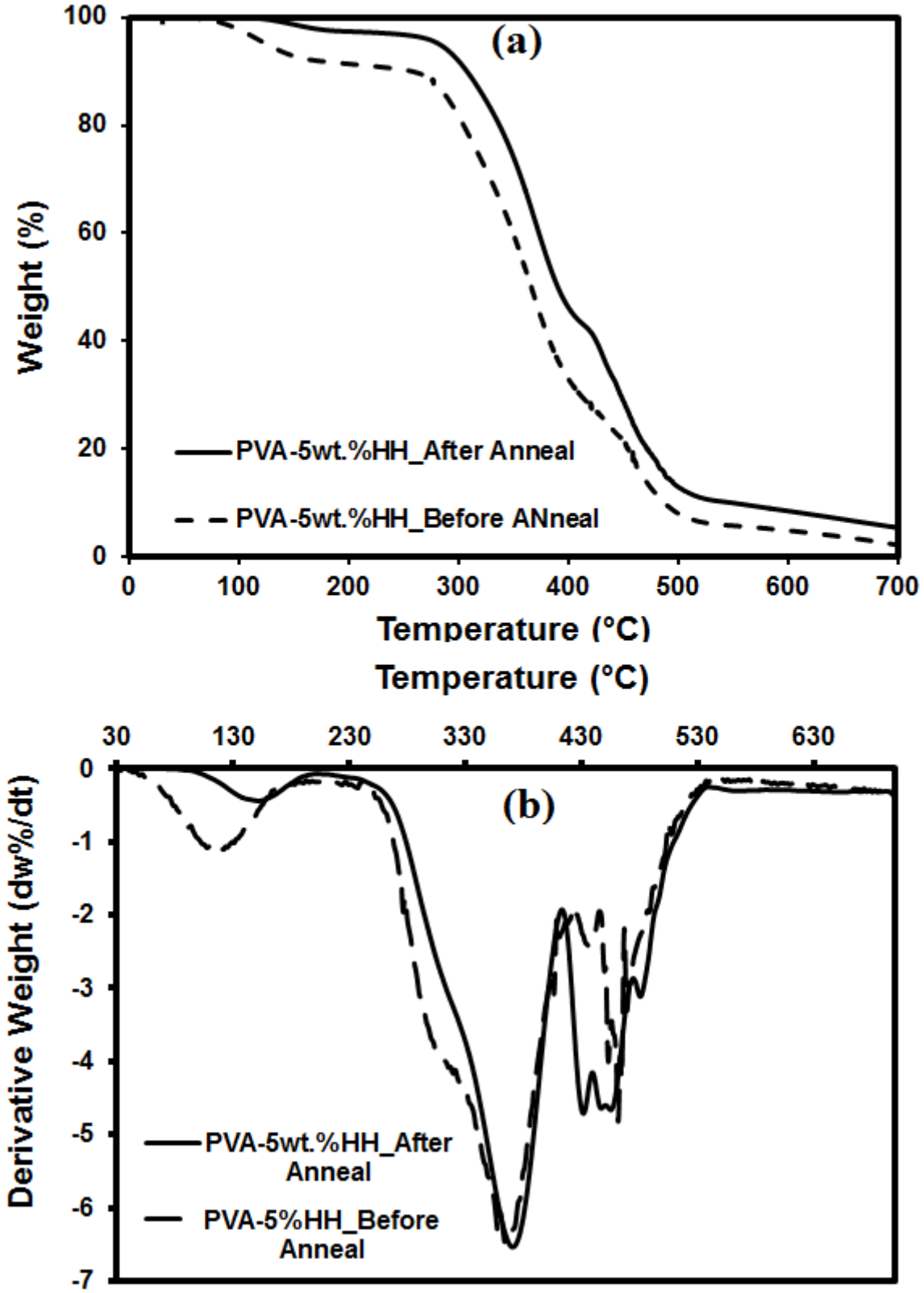

Fig. 3.20 (a) TGA (b) DTG thermographs of PVA-5wt.% hair hydrolysate membrane before and after annealing.

TH-2592_156107017

Increased crystallinity increased the barrier for charge transfer, resulting in reduction in ionic conductivity of the annealed membrane sample by more than 1 mS/cm. At the same time it also improved the methanol barrier property of the sample by reducing the methanol permeability to almost one decimal place, subsequently increasing the selectivity of the membrane from 6.14×10^3 S.s/cm^3 to 6.00×10^4 S.s/cm^3 at 30°C. Annealing had impact on the water uptake and %swelling as well. The water uptake was reduced from 144% to 40%, which is almost 100% reduction in water uptake. While presence of 40 wt.% of water with respect to dried membrane is more than enough for ion conduction, the lower water uptake had a positive effect on %swelling which reduced from 30% to 15% (Table-3.6). As to conclude the effect of annealing on the properties of PVA-5wt.% hair hydrolysate composite membrane, there is only one negative point, that is reduction in ionic conductivity, while all the other properties related to AEMs improved, which includes improvement in thermal, mechanical, thermo-mechanical, water uptake, %swelling, methanol permeability and selectivity. The annealed sample was also tested for the alkaline stability by keeping it in 0.5 M KOH solution for the 10 days. After 10 days the calculated ionic conductivity was found to be 6.09 ± 0.26 mS/ cm at 70°C. It shows very small reduction from the initial ionic conductivity (6.16 ± 0.23), indicating the high stability of the HH based membrane in alkaline medium.

3.5 Conclusions

Hair hydrolysate obtained by simple and green thermal hydrolysis of human hair bio-waste containing 70 wt.% of proteinaceous material has been successfully utilized as ion conductive material to fabricate AEMs for alkaline DMFC. Molecular weight obtained by MALDI-TOF-MS analysis showed two different ranges of molecular weight distribution, one is in lower molecular weight range, having distribution peak in the range of 1-2 KDa,

TH-2592_156107017

while another one was distributed in the range of 7.9-15 KDa. Thus, it contained small amino acid chains to peptides to small size protein chains. FTIR and XRD analysis confirmed the presence of both α-helix and β-sheet structure in the hair hydrolysate. Presence of 27 wt.% of charged amino acids and 19 wt.% of polarizable amino acids in the hair hydrolysate helped in the charge transfer by following hopping kind of mechanism. Further, presence of 7 wt.% arginine in hair hydrolysate, which has a continuous delocalized net positive charge in the guanidino group (the same group which works as anion binding site in red blood cells), making it stable even in high alkaline medium, has also been assumed to play a critical role to provide anion conductivity to the membrane. Hair hydrolysate was used in two different ways to prepare two different types of AEMs. In the first type, we have demonstrated successfully the modification of CNCs by hair hydrolysate and its use in fabrication of CS matrix based AEM. Thus prepared AEM showed improved ionic conductivity, as well as reduced swelling compared to the base CS membrane. The CS based AEMs had mechanical stability issue during methanol permeability tests, at the same time the second type of PVA-hair hydrolysate based membrane showed better performance, so further studies were not carried out on CS based AEM. In the second type of AEMs, hair hydrolysate was directly used in PVA matrix. Hair hydrolysate formed rod and flower shape morphology by aligning its hydrophobic parts inward and hydrophilic parts outward which interacted with hydrophilic PVA matrix. The interaction between hydrophilic sections of both materials improved the thermal stability of the membrane, as with the continuous increase in the loading of hair hydrolysate decreased the weight loss peak due to degradation of the amorphous phase of PVA. Further, the hair hydrolysate crystals formed a channel-like continuous network, which in presence of water and alkaline medium provided a straight path for ion transfer and ion conductivity of around 7.46 mS/cm at 70°C was obtained by 5 wt.% loading of hair hydrolysate in PVA

TH-2592_156107017

matrix. Higher loadings generated more amount of crystals resulting in blockage of the channels and subsequent reduction in ionic conductivity. Thus, 5 wt.% loading was considered to be optimum loading for ionic conductivity. To overcome the issues of high water uptake and swelling, annealing of the 5wt.% hair hydrolysate loaded samples was done at 120°C for 3 hours. The annealing resulted in the improvement of crystallinity of the sample which in turn improved the mechanical, thermal, and thermo-mechanical stability of the membrane. Annealing also resulted in a drastic reduction in water uptake (almost 100%), which helped in reduction of %swelling from 30% to 15%. Increased crystallinity had impact on the barrier properties as well, as ionic conductivity was reduced to 6.16 mS/cm at 70°C due to increased barrier for charge transfer. At the same time methanol permeation was reduced to almost one decimal place, helping in improving the selectivity of the membrane from 6.14×10^3 to 6.00×10^4 at 30°C. The indirect method to check the stability of the membrane by change in ionic conductivity after keeping the sample in KOH solution for 10 days, showed small reduction in conductivity, indicating the high stability of the membrane. Thus, we can conclude that the hair hydrolysate which is a cheap material, obtained from human hair bio-waste can work as anion conductive material and its inclusion in PVA matrix showed promising results to be utilized as anion exchange membrane in alkaline fuel cells. Further, future work on the separation of cationic charged amino acid and peptides form the hair hydrolysate and its use in membrane can enhance the ionic conductivity significantly.

TH-2592_156107017

Chapter 4:

Anion Transport in Human Hair Peptide-based System by Molecular Dynamics Simulation

Graphical Overview

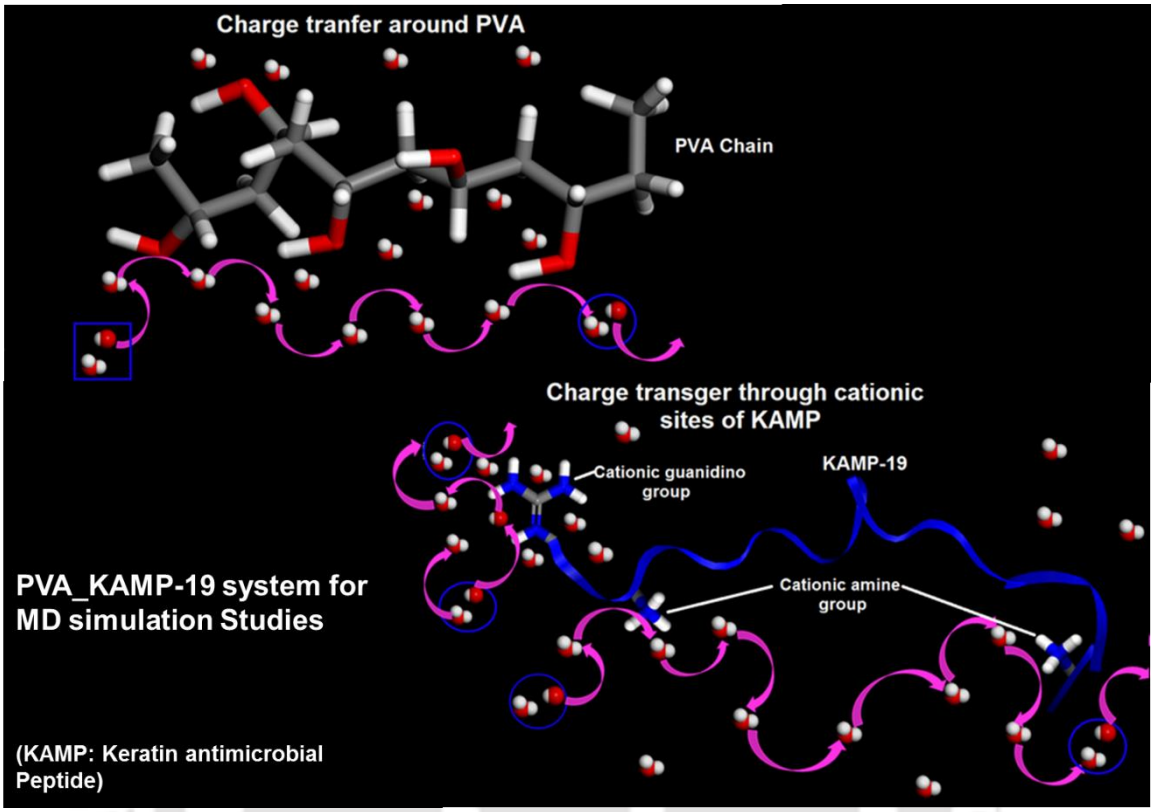

An investigation by molecular dynamics simulation has been carried out to study the possible application of human hair bio-waste derived peptide in anion exchange membrane as a charge carrier. KAMP-19, a keratin-derived antimicrobial peptide, is used as a model OH^- ion charge carrier, having two types of cationic charge transport sites, namely a cationic amine group and a guanidino cation group. Addition of 2.6% of KAMP-19 by weight in a PVA matrix showed an increase in ionic conductivity (of OH^- anions) to almost double the value in the neat PVA matrix. Water plays an important role in charge transport and formation of a low water zone due to hydrophobic sections of peptides when concentration is increased to 5.1 wt.%, resulted in a decrease in ionic conductivity. With further increase in the concentration of KAMP-19, the presence of a larger number of -

Publication (under preparation):

- Gaur, S. S., Katiyar, V., Kumar, A., Molecular dynamics simulation studies on human hair derived peptide for its possible application in anion exchange membrane and investigation on the role of guanidino group in charge transfer.

TH-2592_156107017

charge transfer sites close to each other resulted in increase of ionic conductivity. Methanol diffusion followed the trend of OH^- conductivity for the different wt.% samples, indicating that methanol diffusion is governed by electro-osmotic drag. Electro-osmotic drag reduces the methanol diffusion by dragging it back to anode side with charged ions. Water, ammonium cation and guanidino group cation play an important role in the transport of OH^- which happened through Hopping or Grotthuss mechanism. Hopping of OH^- from one water molecule to another in water channels around hydrophilic PVA chain occured by formation of $H_3O_2^-$ ion through hydrogen-bonded association followed by breaking back to H_2O and OH^-. The transport of OH^- around ammonium cation happened by the same mechanism in which OH^- hopped through water molecules coordinated with ammonium cation by hydrogen bonding. In the guanidino groups, the OH^- transport happened by direct hopping of OH^- from one site to another without formation of any intermediate, resulting in faster transport. So, the presence of functional groups such as the guandino group, which are known to be stable even in highly alkaline medium due to charge delocalization, makes bio-waste materials like human hair keratin a suitable material to be utilized in anion exchange membranes.

4.1 Introduction

Alkaline fuel cell technology is receiving significant attention over acidic type due to the possibility to replace noble metal catalysts by low-cost metal catalyst (Ryu et al., 2019). In general, as reported in literature, OH− ion transfer has been assumed to follow similar kind of mechanism in water as well as in anion exchange membranes (AEMs) used in alkaline fuel cells as proton transport in cation exchange membranes (CEMs) (Lee & Rasaiah, 2011; Miyake & Rolandi, 2015; Tuckerman et al., 1995a; Tuckerman et al., 1995b; Chen et al., 2016; Jensen et al., 2005). It includes the hopping of OH^- ions (known as Grotthuss

TH-2592_156107017

mechanism) and vehicular mechanism. Vehicular mechanism is a simple diffusion of OH^- ions in the form of $H_3O_2^-$ which is continuously formed and cleave back to H_2O and OH^- ions by proton exchange (Takaba et al., 2017). Grotthuss mechanism involves two types of hopping of OH^-, one through water and other through surface charged sites present in polymer matrix used in AEMs. In hopping within water, oxygen of OH^- forms hydrogen bond with four coplanar water molecules and OH^- takes near perpendicular position to form $(H_9O_5)^-$ complex, which converts to $(H_7O_4)^-$ intermediate complex and reverts back to $(H_9O_5)^-$ (Tuckerman et al., 1995[a]; Tuckerman et al., 1995[b]). Hopping of OH^- is simpler in case of polymer matrix, where OH^- simply hops from one cationic site to another cationic site present in the polymer matrix due to ionic interaction (Chen et al., 2016). Several molecular dynamics (MD) simulation studies on OH^- transfer in AEMs have considered Grotthuss to be main mechanism for charge transfer. Wang et al. (2018) in their MD simulation studies on OH^- transfer in amorphous polynorbornen, considered Grotthuss mechanism and mass diffusion as combined mechanism for charge transfer. Takaba et al. (2017) used poly(arylene ether sulfone ketone)s containing quaternized ammonio-substitutedfluorenyl groups (QPE) as anion exchange polymers to study OH^- transfer by MD simulation. They also observed that the hydroxide ion diffuses by hopping between ammonium groups present. Similarly, Chen et al. (2016) also evaluated hydroxide ion transport in AEMs and found significant contribution of both Grotthuss and vehicular mechanism in charge transfer. Zhang et al. (2019) also showed the importance of Grotthuss mechanism for OH^- diffusion in AEMs by atomistic-scale simulations.

AEMs used in alkaline fuel cells are primarily based on quaternary ammonium, quaternary phosphonium, imidazolium, guanidinium and piperazinium cationic functionalities (Cheng et al., 2015). Several of these functionalities are present in proteins and its constituent units. Role of proteins as ionic conductor in various biological processes such

TH-2592_156107017

as photosynthesis in plants (Zivcak et al., 2014) and in anion transport in red blood cells (Sterling & Casey, 1999) is very well known. Several reports are available where researchers have tried to replicate the ion/charge transfer capability of proteins (Bradley et al., 2004; Dhar et al., 2019; Ho et al., 2004; Liu et al., 2020). Use of proteins, peptides and amino acids in the area of alkaline fuel cells is hardly reported. Here, we have tried to use a model keratin-derived antimicrobial peptide (KAMP), KAMP-19 with poly(vinyl alcohol) matrix to investigate the hydroxyl ion (OH^-) transport mechanism by molecular dynamics simulation. KAMP-19 consists of two types of charge transfer sites: one cationic guanidino group and one polarizable amine group site, which upon protonation forms protonated amine group cation. Guanidino group is known to be the anion binding site in erythrocyte protein responsible for anion transfer in red blood cells (Knauf, 1979). It also has advantage of charge delocalization which can help in easy charge transfer and provide stability to the guanidino group cation, even in highly alkaline medium (Xu et al., 2017). Several research studies have utilized guanidinium-based polymers to prepare AEMs, where superior ionic conductivity and membrane stability in alkaline medium compared to the commercially available AEMs have been demonstrated (Sajjad et al., 2014; Lin et al., 2012; Xue et al., 2017; Kim et al., 2011; Chen et al., 2017). Apart from the presence of guanidine group, the choice of KAMP-19 was made based on its source that is the widely available human hair bio-waste. Moreover, in our experimental studies on hair keratin protein extracted subunits (peptides and small size proteins) in AEMs, we have obtained promising results, as reported in last chapter.

TH-2592_156107017

4.2 Theory and Simulation Details

4.2.1 Molecular Dynamics Simulation

Molecular simulation is a process of mimicking a phenomenon occurring at the atomistic or molecular level on a computer. Molecular simulations are becoming an important tool for both understanding polymeric structures and predicting their physical and chemical properties. Molecular simulations are often used to study aspects of a system and obtain details that may not be accessible through experiments. They can be employed as a complementary tool to experimental investigations and can aid in obtaining better insight into the mechanism driving a certain phenomenon. Molecular simulation techniques are broadly classified into two categories: Monte Carlo simulations and molecular dynamics (MD) simulations. MD simulations compute the motion of individual atoms or molecules to describe how positions, velocities and orientations changes with time. MD Simulations solve Newton's equation of motion for a system of N interacting particles.

$$m_i \frac{\partial^2 r_i}{\partial t^2} = F_i, \quad i = 1, 2, 3.....N \tag{4.1}$$

where m_i is the mass of particle i, r_i is its position, t is time and F_i is the total force acting on particle i due to its interaction with all other particles in the system. The forces are the negative derivatives of a potential function V ($r_1, r_2, r_3, ...r_N$) with respect to position.

$$F_i = -\frac{\partial V}{\partial r_i} \tag{4.2}$$

The Newton's equation of motion is solved simultaneously for all the particles in the simulation box in small time steps by generally using the Verlet scheme (Equation (4.3)) to obtain the new position of each atom at each time step.

TH-2592_156107017

$$r_i(t + \Delta t) = 2r_i(t) - r_i(t - \Delta t) + \frac{F_i(t)}{m_i}\Delta t^2 \quad (4.3)$$

In equation (4.3), $r_i(t - \Delta t), r_i(t)$ and $r_i(t + \Delta t)$ are the positions of particle i at times $t - \Delta t$, t and $t + \Delta t$ respectively, Δt is the time step and $F_i(t)$ is the total force acting on particle i at time t. The atomic coordinates of the atoms are written out at regular time intervals to an output file. The coordinates as a function of time represent the trajectory of the system. By averaging over an equilibrium trajectory, many macroscopic properties, such as self-diffusion of gas and vapor in polymers can be extracted from the output file. The diffusivity of a gas in an organic solvent, polymer, or zeolite can be calculated by running an MD simulation and determining the mean square displacement (MSD) of the gas in the material. At long times, if the mean-square-displacement vs time plot becomes linear, the self-diffusion coefficients can be calculated using the Einstein relation (given in section 4.2.3). The movement of penetrants in the host polymer matrix can be qualitatively studied by monitoring the penetrant's displacement from its initial position.

The calculation of forces acting on atoms is critical in any MD simulation. An atom in a system experiences various types of forces from the other atoms in the system, and these forces govern the motion of the atoms. As forces are calculated using the gradient of the potential energy, a reasonably accurate description of the interatomic interactions is important in any MD simulation. The potential energy function should include both bonded and non-bonded interactions. In general, it is written as:

$$E_{total} = E_{bonded} + E_{nonbonded} \quad (4.4)$$

where $E_{bonded} = E_{bond} + E_{angle} + E_{dihedral/torsions}$

and $E_{nonbonded} = E_{electrostatic} + E_{van\ der\ Waals}$

TH-2592_156107017

A representative form of the potential energy function, which includes the primary bonded and non-bonded interactions, is given by (Andrew, 2001):

$$E(r^N) = \sum_{bonds} \frac{k_i}{2}(l_i - l_{i,0})^2 + \sum_{angles} \frac{k_\theta}{2}(\theta_i - \theta_{i,0})^2 + \sum_{torsions} \frac{V_n}{2}(1 + cos(n\omega - \gamma)) + \sum_{i=1}^{N}\sum_{j=i+1}^{N}(4\varepsilon_{ij}[\left(\frac{\sigma_{ij}}{r_{ij}}\right)^{12} - \left(\frac{\sigma_{ij}}{r_{ij}}\right)^{6}] + \frac{q_i q_j}{4\pi\varepsilon_0 r_{ij}}) \quad (4.5)$$

The potential energy is a function of the positions of the N atoms present in the system. The first term on the right hand side of equation (4.5) represents the interaction between two directly bonded atoms by a harmonic potential, where a change in the bond length ($\boldsymbol{l}$) from the equilibrium value increases the energy. Similarly, angle bending term (the second term on the right hand side of equation (4.5)) is the summation of energy terms due to change in the angle between three bonded atoms from the equilibrium value; this term is also often modeled by a harmonic potential. Torsional (or dihedral) interactions involve four consecutively bonded atoms (i.e., three bonds) and account for energy contribution due to bond rotations. Fourth term on the right hand side of equation (4.5) represents the energy contribution by non-bonded interactions, calculated between all pairs of atoms, which are not bonded. First part of the fourth term is the contribution due to van der Waals interactions, usually modeled using the Lennard-Jones potential (as shown in equation (4.5)) and the second part is the energy contribution due to electrostatic interactions, given by Coulomb's law. In equation (4.5), parameters such as k_i, k_θ, V_n, ε_{ij}, σ_{ij} and the partial charges (q_i) are required to calculate the potential energy and forces. A collection of these parameters (and partial charges sometimes) for different types of atoms constitutes a force field. The force on each atom is obtained from the potential energy function and subsequently acceleration can be calculated by dividing with the mass of the atom. Using the atomic accelerations in a numerical integration scheme such as the Verlet scheme, the

TH-2592_156107017

atomic positions at the next time step are obtained. The new positions are used to calculate the updated potential energy, forces and accelerations, which are again used in the Verlet equation. The evolution of atomic position with time is obtained by repeating these calculations a large number of times.

4.2.2 Details of the Simualtion

The structure of KAMP-19 was obtained from RCSB protein data bank and PDB ID is 5KI0 (Lee et al., 2016). KAMP has overall positive charge of three, one due to guanidinium cation and two from protonated amine groups. In the guanidino group, the charge is delocalized between one carbon and three nitrogen atoms; for the molecular dynamics simulations, we considered the positive charge to be distributed (charge distribution was assigned by the force field used) over the guanidino group. Thirty chains of PVA with each chain having a degree of polymerization of 100 (i.e., 100 monomer per polymer chain) were packed in a cubic simulation box for the molecular simulation studies. Four different weight fractions of peptide, i.e. 2.6%, 5.1%, 7.4% and 9.6% were taken with the PVA matrix in the simulation box. Thirty OH^- ions were added, and to balance the charge, appropriate number of K^+ ions were added. To check methanol diffusion in the system -

Table: 4.1 Compositions of simulation cells prepared for different systems.

Sample	PVA	KAMP-19	H_2O	OH^-	K^+	Methanol
PVA-30% H_2O	30	-	2212	30	30	30
PVA-2.6% KAMP-30% H_2O	30	2	2271	30	24	30
PVA-5.1% KAMP-30% H_2O	30	4	2330	30	18	30
PVA-7.4% KAMP-30% H_2O	30	6	2389	30	12	30
PVA-9.6% KAMP-30% H_2O	30	8	2448	30	6	30

TH-2592_156107017

thirty methanol molecules were also added to each system. To compare the OH^- and methanol diffusion with that in the base PVA matrix, a system with pure PVA matrix containing thirty OH^- ions, thirty K^+ ions and thirty methanol molecules was prepared. 30 wt% water (on the basis of dry membrane) was taken in each system. Complete composition of each simulation box is detailed in the Table 4.1 and a representative box is shown in Fig. 4.1 with all the components.

Materials Studio v7.0 software package from BIOVIA 'formerly Accelrys' was used for preparation of all the molecular structures other than the KAMP-19. All the structures were geometry optimized using Forcite module of the Materials Studio. The geometry optimization was done by following the steepest descent algorithm with maximum iteration of 5000. Charges were assigned to each atom by forcefield and the consistent-valence forcefield (CVFF), a classical forcefield was used for the same (Dauber Osguthorpe et al., 1988). CVFF is suitable for all the common amino acids, many organic molecules and hydrocarbons, making it suitable for the current system of analysis. Electrostatic and van der Waals interactions were calculated atom based and cut-off distance for each was kept 15.5 Å. A cubic simulation box was constructed for each system composition (see Table 4.1) by packing the polymer chains and other components in the cubic box using the Amorphous Cell module of Materials Studio. Initial density and temperature of each system were kept at 1 g/cm^3 and 298 K respectively. CVFF force field was used for atom type assignment during simulation box preparation. Electrostatic and van der Waals interactions were calculated with a cut-off distance of 9.5 Å (to decrease the simulation box preparation time cut-off distance was reduced from 15.5 Å to 9.5 Å). Further geometry optimization was carried out on each simulation box using the steepest descent algorithm (with maximum number of iterations = 1000). The same force field as before (i.e., CVFF) was employed for the geometry optimization of the systems. The procedure -

TH-2592_156107017

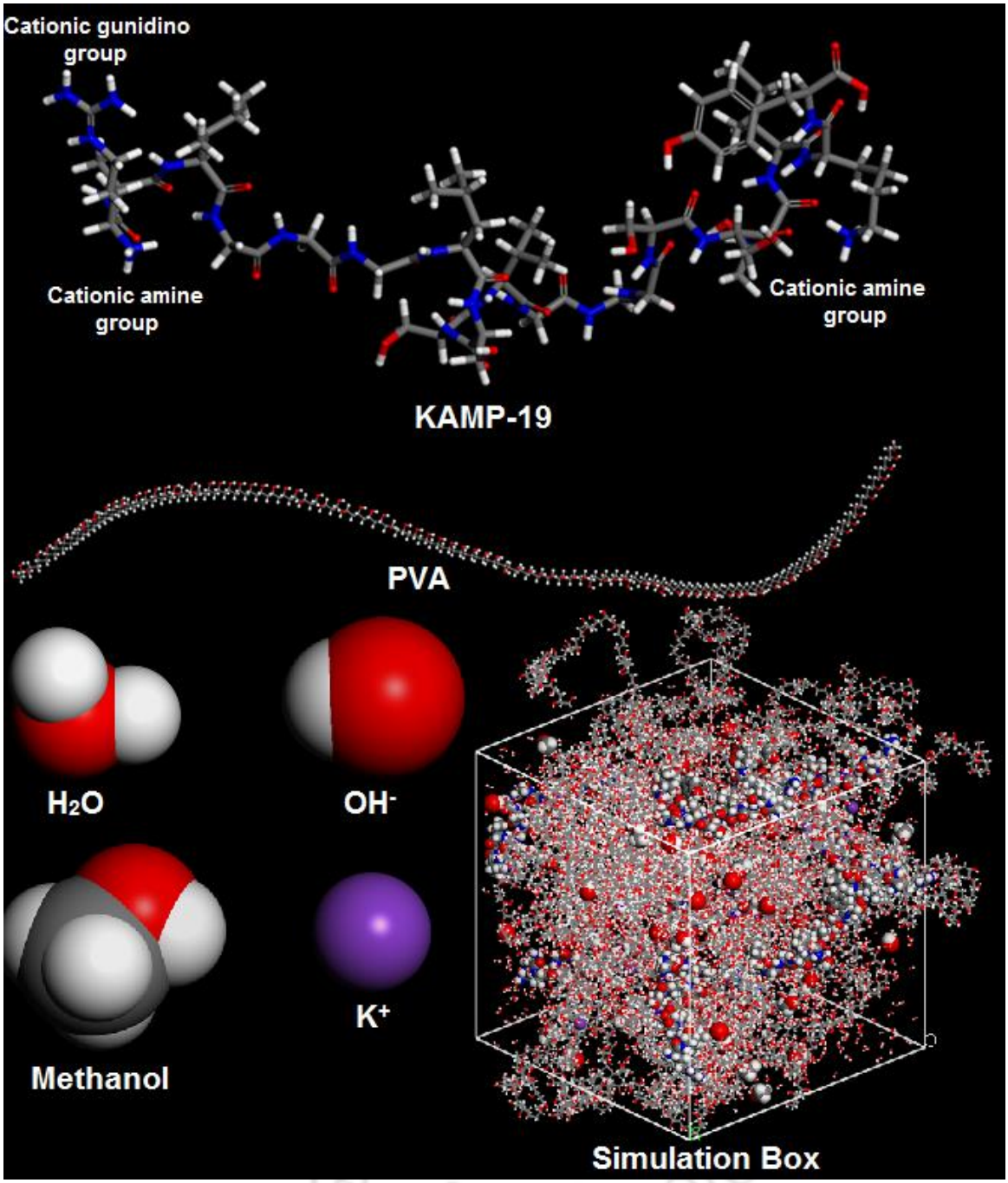

Fig. 4.1 Structure of a representative simulation box with all the components.

TH-2592_156107017

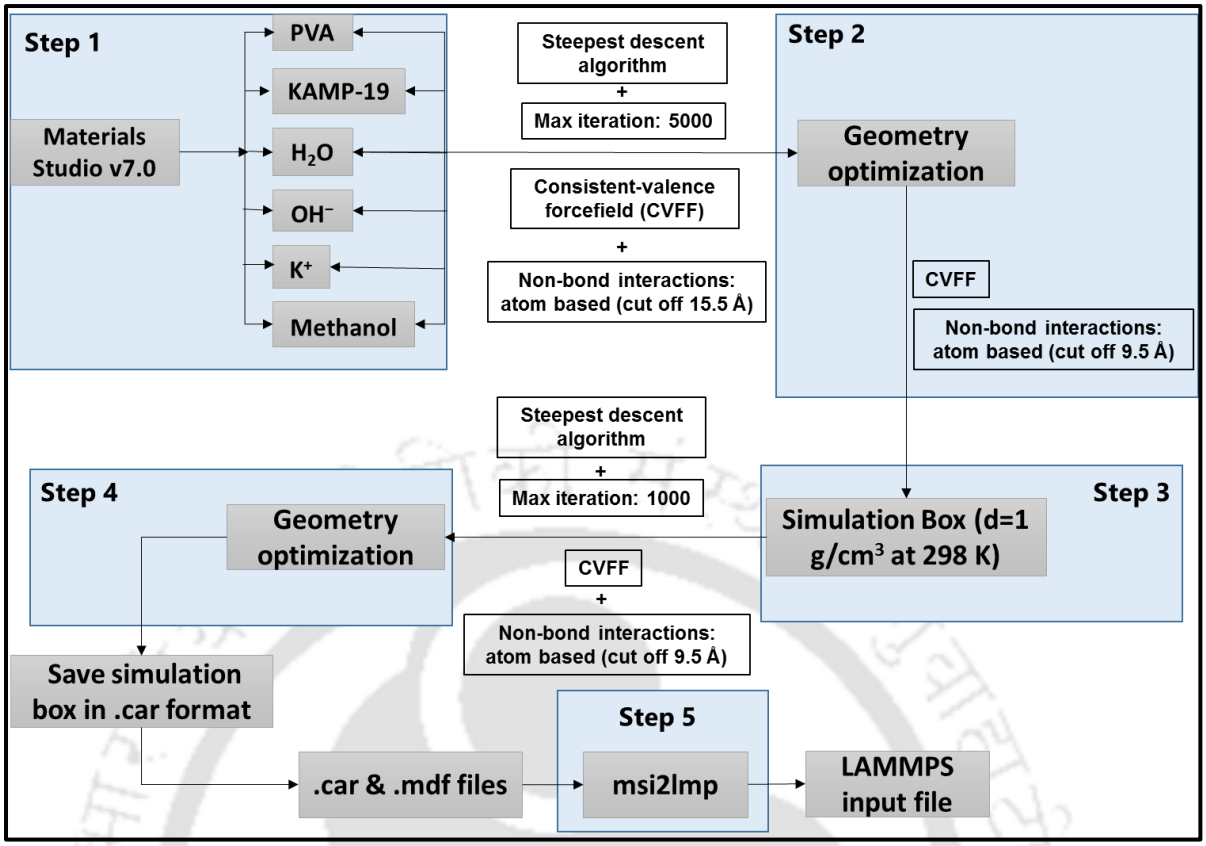

Fig. 4.2 Schematic of simulation box and LAMPPS input preparation.

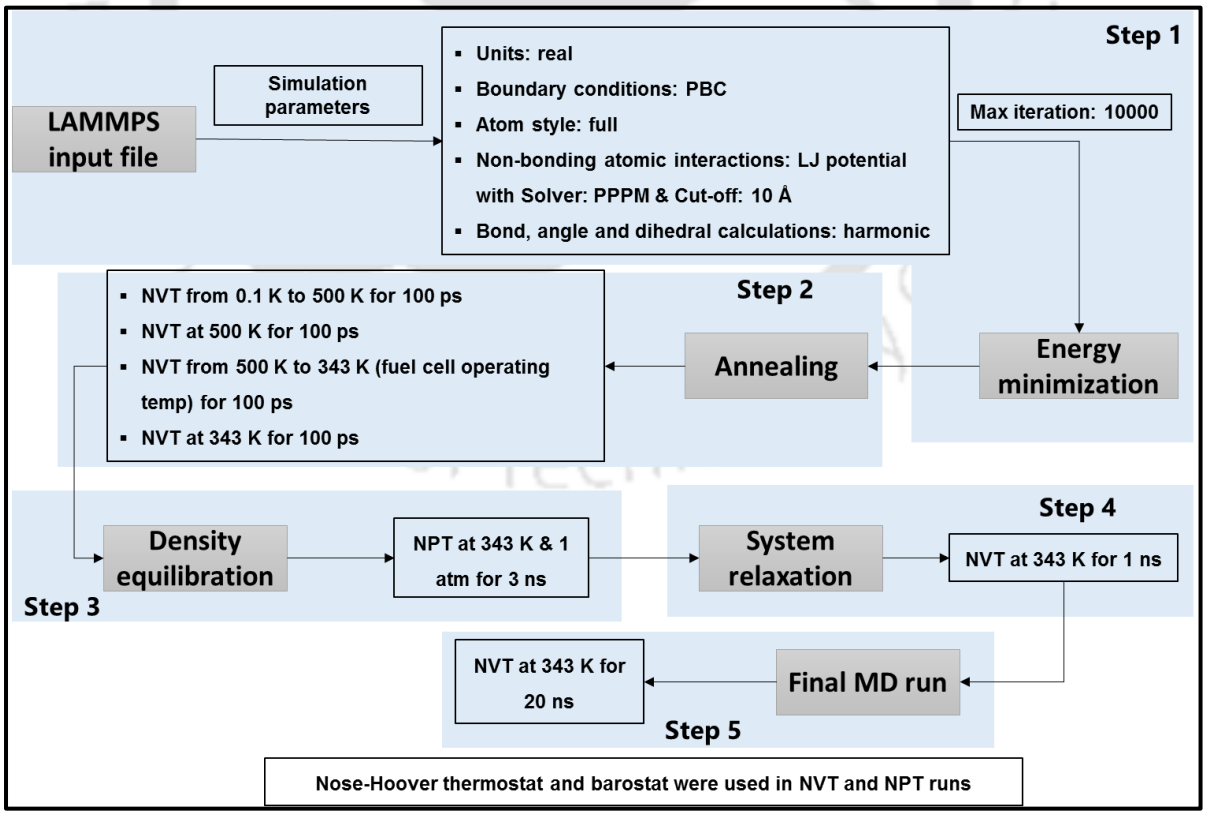

Fig. 4.3 Schematic of MD simulation run procedure for LAMPPS.

TH-2592_156107017

for preparation of simulation box in Materials Studio and input file generation for MD simulation run is shown through schematic in Fig. 4.2.

MD simulations on each system were carried out using the Large-scale Atomic/Molecular Massively Parallel Simulator (LAMMPS) (Plimpton, 1995; Plimpton et al., 2007), which is a molecular dynamics program from Sandia National Laboratories. All LAMMPS simulations were run on PARAM-ISHAN, a 250 Teraflop hybrid High Performance Computing (HPC) cluster at IIT Guwahati. The complete procedure for the MD simulation run using LAMMPS is shown through the schematic in Fig. 4.3. The input data file was prepared by converting the .CAR and .MDF files obtained from simulation box preparation using Materials Studio to LAMMPS data file format by using the msi2lmp plugin available in LAMMPS.

To run the MD simulation using LAMMPS, periodic boundary conditions were used in all three directions. Non-bonded van der Waals interactions were calculated by the Lennard-Jones (LJ) potential with a cutoff at 10 Å. For long-range Coulombic interactions were calculated using the particle-particle particle-mesh (PPPM) solver with a cutoff at 10 Å. The charges and LJ potential parameters for OH^- and K^+ ions were obtained from literature (Vácha, et al., 2008; Zhao et al., 2010) as CVFF does not include the respective atom types. Prior to MD simulation, energy minimization was performed by setting energy and force tolerance to be 1×10^{-5}, maximum number of iterations and the number of total force evaluations to be 10000 each. Thereafter, the temperature of the system was ramped from 0.1 to 500 K in 100 ps using canonical NVT ensemble MD simulation. The system was maintained at 500 K for 100 ps and then cooled to 343 K (≈70°C, the working temperature of AEM fuel cells) in another 100 ps. The system was then further equilibrated at 343 K for 100 ps by running NVT MD simulation. All the systems were generated at an initial

TH-2592_156107017

density of 1 g/cm^3 (using Materials Studio). The density of the system was allowed to evolve to more realistic values by conducting MD simulations in the NPT ensemble at a temperature of 343 K and a pressure of 1 atmospheric for 3 ns. This was followed by another NVT MD simulation at 343 K for 1 ns to further equilibrate the system. Finally, 20 ns of NVT MD simulation was carried out at 343 K and data was recorded at regular interval of 0.1 ps. The time step for each KAMP case was kept at 1 fs, while for without KAMP, for the reference simulation box it was kept 2 fs. LJ-parameter for hydrogen are assaigned (0 0) by forcefield, for the hydrogen of PVA -OH, hydrogen attached to nitrogen in KAMP and hydrogen of water, which may lead to atoms overlapping or uncotroled stretching of bonds, causing error in simulation. Thus, for these three types of hydrogens, manual LJ-parameters were assigned to (0.00001 1.00000). All the bonds having hydrogen were constrained by fix shake command, other than one hydrogen bond in the methanol to avoid the constraint on whole methanol molecule. Nose-Hoover thermostat was used for all the constant NVT MD simulations whereas Nose-Hoover thermostat and Nose-Hoover barostat were used for the constant NPT MD simulations. During the MD run, mean square displacement (MSD) data were recorded for OH^- ions and methanol molecules to calculate their diffusivities, while radial distribution function (RDF) data were recorded to understand the relative distribution of different molecules. RDF calculation for each system was done by taking average of ten different RDF data obtained during the MD run and recoreded in the time interval of each 2 ns. The trajectories of the molecules were visualized through visual molecular dynamics (VMD), a molecular modelling and visualization computer program (Humphrey et al., 1996).

TH-2592_156107017

4.2.3 Calculation of the Diffusivity and Ionic Conductivity

Diffusivities were calculated by using the mean square displacement as shown in equation (4.6) and OH^- conductivity was calculated by using the Nernst–Einstein relation (equation (4.7)) (Müller-Plathe, 1994; Srinophakun & Martkumchan, 2012).

$$D = \frac{1}{6N} \lim_{t\to\infty} \frac{d}{dt} \sum_{j=1}^{n} (r_j(t) - r_j(0))^2 = \frac{1}{6N} \lim_{t\to\infty} \frac{d}{dt} MSD(t) \quad (4.6)$$

$$\sigma_{OH^-} = \frac{Nz^2e^2D_{OH^-}}{VKT} \quad (4.7)$$

In equations (4.6) and (4.7), D is the diffusion coefficient, N is the number of molecules, $r_j(t) - r_j(0)$ is the displacement from time 0 to time t and $MSD(t)$ is the mean square displacement of the species for which diffusion coefficient is calculated. σ_{OH^-} is the conductivity, z is the charge, D_{OH^-} is the diffusion coefficient of OH^- ions, e is the elementary charge, K is the Boltzmann constant, V is the volume of the simulation box and T is the temperature. According to equation (4.6) when the MSD data is plotted against time, in the long time limit, a linear relationship with zero intercept should be obtained. Therefore, the diffusivities were obtained from the slope of the MSD vs time curve by fitting the data with straight lines having zero intercept. Diffusivity calculation was only carried out when the R^2 value for the curve fitting was around 0.9 or higher.

4.3 Results and Discussion

Table 4.2 summarizes the diffusivities of OH^- and methanol, calculated through the MSD data plots. For the case of 5.1 wt.% and 7.4 wt.% KAMP loadings, methanol diffusivity was not calculated through equation (4.1) as the R^2 values for the fit was much less than 0.9, so to make a comparison for methanol self-diffusion, MSD curves for each case are

TH-2592_156107017

shown in Fig. 4.4 (b), as well as methanol MSD values of all the cases are mentioned in Table 4.2. Table 4.2 also lists the density of the each system obtained after NPT run and conductivity data for OH^- obtained from the OH^- diffusivity. MSD of OH^- in Fig. 4.4 (a) as well as the OH^- diffusivity data presented in Table 4.2 show the effect of inclusion of KAMP in the PVA matrix. The diffusivity of the OH^- ions was doubled for PVA with 2.6 wt.% KAMP loading compared to that in neat PVA. The conductivity of OH^- increased from 0.95 mS/cm in pure PVA to 1.59 mS/cm in the PVA-2.6wt.% KAMP sample. Although our simulation results of ionic conductivity show improvement in PVA-KAMP samples compared to the base PVA membrane, when compared with experimental results from the study reported in the previous chapter involving human hair based proteinic materials having guanidinium cations it is lower. At the same time, conductivity results reported for guanidinium based polymers in lieterature for AEMs, as well as simulation results on several AEM membranes, it is much lower. Variation in conditions and effect of the polymer matrix used, as well as morphological properties may have affect on the conductivity data. Sajjad et al. (2015) showed the maximum ionic conductivity of 21 mS/cm for guanidinium based polymer and chitosan blend based AEMs and 11 mS/cm for commercial Tokuyama A201. The same group in their earlier experimental work showed ion conductivity of 80 mS/cm for guanidinium-based polymers with PTFE matrix (Sajjad et al., 2014). Similarly, Lin et al. (2012) also presented ionic conductivity results for guanidinium-based AEMs showing highest ionic conductivity of 71 mS/cm. Takaba et al. (2017) have carried out MD simulations on poly(arylene ether sulfone ketone)s containing quaternized ammonio-substituted fluorenyl AEM and polynorbornene AEM respectively to find out OH^- conductivity and showed maximum ion conductivity to be ≈58 mS/cm and ≈12 mS/cm respectively. There may be several reasons for the lower -

TH-2592_156107017

Table: 4.2 Density, diffusivity and conductivity of OH^-, MSD and diffusivity of methanol for each system.

Sample	Density (g/cm^3)	D_{OH^-} (cm^2/s)	σ_{OH^-} (mS/cm)	MSD_{CH_3OH} ($Å^2$)	D_{CH_3OH} (cm^2/s)
PVA-30% H_2O	1.119	1.52×10^{-6} ($R^2 = 0.87$)	0.95	5690	4.58×10^{-6} ($R^2 = 0.98$)
PVA-2.6% KAMP-30% H_2O	1.126	2.60×10^{-6} ($R^2 = 0.98$)	1.59	8820	8.15×10^{-6} ($R^2 = 0.98$)
PVA-5.1% KAMP-30% H_2O	1.120	2.06×10^{-6} ($R^2 = 0.93$)	1.12	3643	–
PVA-7.4% KAMP-30% H_2O	1.127	2.16×10^{-6} ($R^2 = 0.95$)	1.26	3721	–
PVA-9.6% KAMP-30% H_2O	1.126	2.37×10^{-6} ($R^2 = 0.97$)	1.35	5237	4.91×10^{-6} ($R^2 = 0.98$)

ionic conductivity in the present case. The fixed charge considered on guanidino group in the present case in comparison to the charge delocalization in real experimental conditions may be one of the reasons for lower ionic conductivity. For charge transfer, anions interact with the cation functional groups present in the system and as the cationic charge is continuously moving, the anions will move along with it continually. While at fixed charged the anions may stay for longer time at the site, which depends on the amount of anion carrier present around the cation or fluctuation in energy around it. Another reason could be the lower number charge transfer sites in current case in comparison to the charge transfer sites present in experimental and other simulation studies per unit volume. For lower ionic conductivity in comparison to other simulation reports, stronger ionic interaction could be another reason. The simulation studies mentioned used quaternary ammonium group based AEMs, which have three bulky alkyl groups around the cation, while in the current study both the cation present in KAMP, one on guanidine group and another one on amine group, do not have such bulky groups attached to them, which may-

TH-2592_156107017

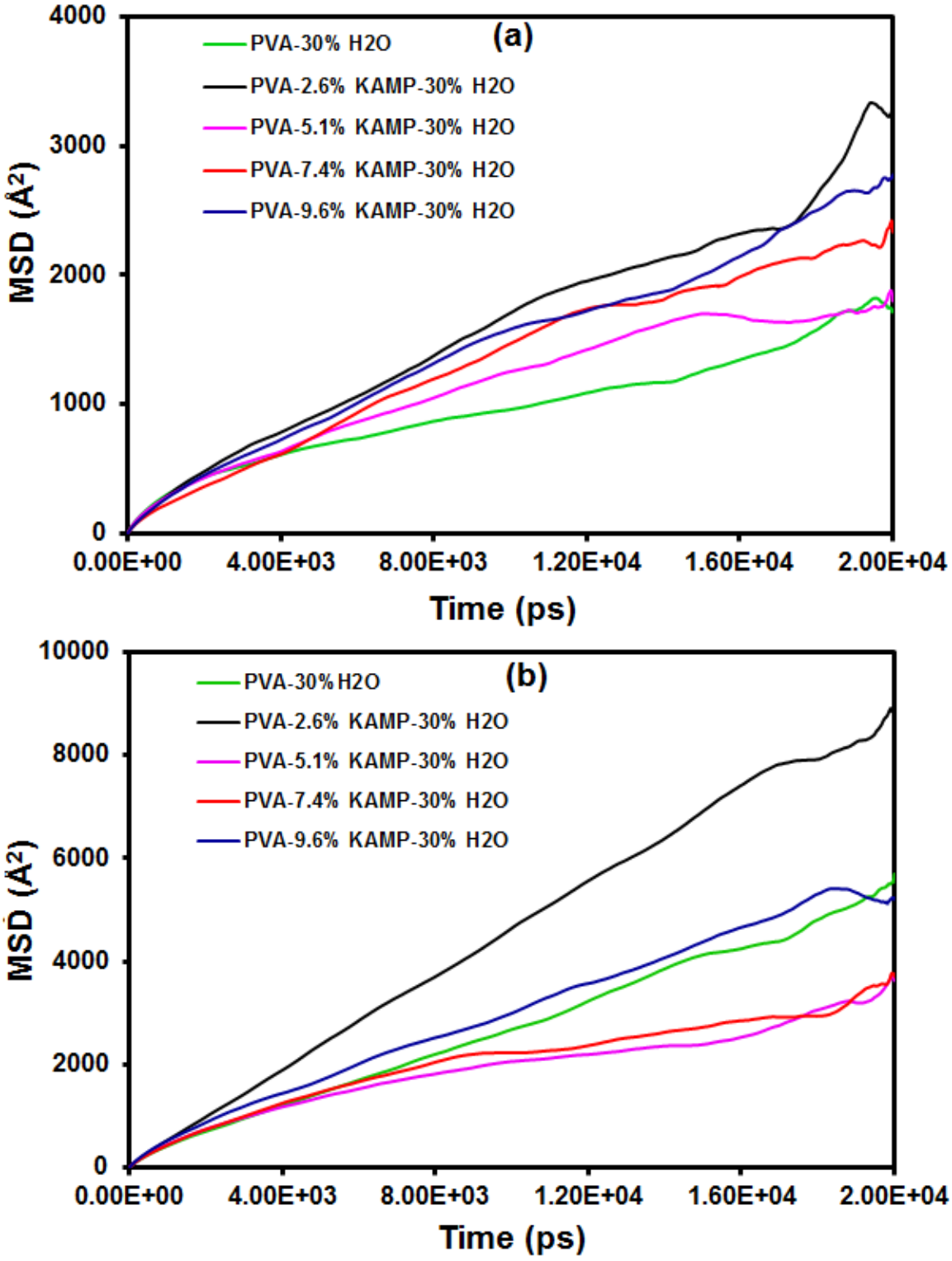

Fig. 4.4 MSD curves of (a) OH^- (b) methanol for all the systems obtained from MD simulation.

TH-2592_156107017

result in stronger ionic interaction between the cation and OH^- anion due to columbic interaction. The columbic interaction between let OH^- ion drift away. Presence of higher amount of water may reduce such strong ionic interactions through the formation of water layer around the cation by hydrogen bonded interactions and at the same time polarized water molecules may work as charge carrier. This was confirmed by running the simulation of 2.6 wt.% KAMP loading in PVA with 50 wt.% water. The conductivity increased to 2.56 mS/cm at 50 wt.% water loading in comparison to 1.59 mS/cm for 30 wt.% water loading.

The results in Table 4.2 for higher loadings of KAMP showed a trend where further increase in loading to 5.1 wt.% decreased the ionic conductivity and thereafter again increased for 7.4 wt.% and 9.6 wt.% loadings. The reason for decrease in ionic conductivity is the formation of a low water content zone. The zone is formed by the hydrophobic sections of KAMP-19 molecules. As reported by Lee et al. (2016) KAMP-19 contains 26% of hydrophobic amino acids, which is at the center area of the peptide structure shown in Fig. 4.1. From the MSD curves in Fig. 4.4 (a), we can see that up to ~3 ns, there is not much difference in the MSD of OH^-, but with time the amount of water molecules near the hydrophobic zone went down resulting in the difference in MSD data for different KAMP loadings. Lower water content around the hydrophobic zone is quite visible in all four PVA-KAMP samples, as shown in Fig. 4.5 through snapshots taken using VMD at 10 ns of the MD run. In Fig. 4.5, only KAMP molecules, water molecules and OH^- ion are shown; polymer molecules have not been shown for clarity. KAMP-19 does not have the typical α-helix or β-sheet structure, it has an extended structure (Lee et al. (2016). In case of 2.6 wt% KAMP sample there are only two KAMP molecules randomly placed in the PVA matrix in the simulation box. So, although there is less water around the hydrophobic part of the peptide, hydrophilic PVA helps in the diffusion of OH^- ions. In the case of 5.1 wt.%-

TH-2592_156107017

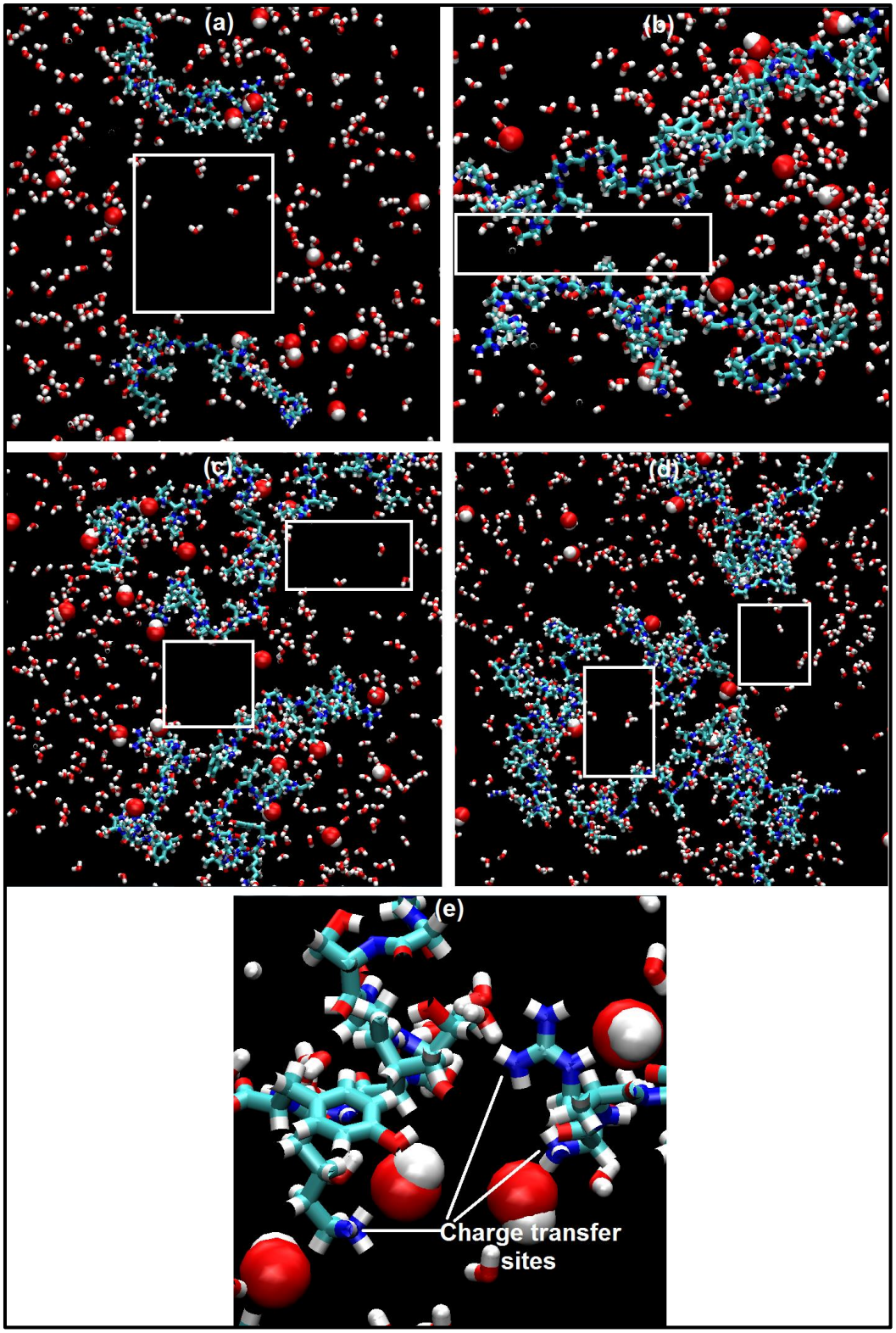

Fig. 4.5 Low water zone boxes in the snapshots at 10 ns for KAMP loading of (a) 2.6wt.% (b) 5.1 wt.%, (c) 7.4 wt.%, (d) 9.6 wt.% (e) Increased number of charge transfer sites in hydrophobic zone in 9.6wt.%.

TH-2592_156107017

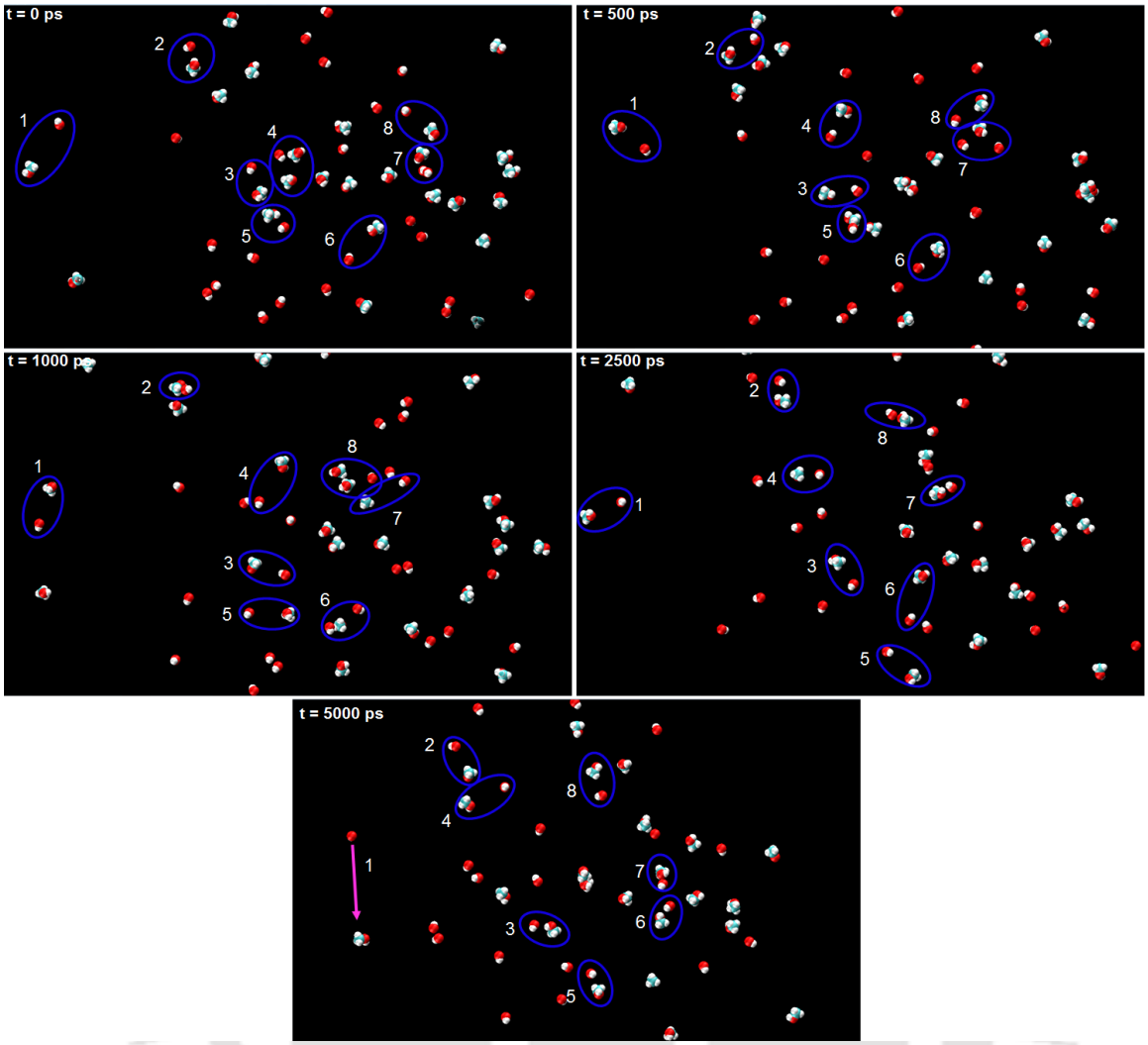

Fig. 4.6 Snapshots of 8 pairs of hydroxyl ion-methanol moving together during MD simulation, showing the effect of electro-osmotic drag of OH^- on methanol.

KAMP sample, four KAMP molecules form a zone of low water molecules; so the diffusion of OH^- trapped in the zone becomes very slow, resulting in the reduction of ionic conductivity. With further increase in the concentration of KAMP, more charge transfer sites are available in the low water zone in close vicinity to each other (Fig. 4.5 (e)), making the diffusion of OH^- faster and thus increasing the ionic conductivity.

From the density data in Table 4.2, we can see that all samples have a density of around 1.12 g/cm^3. From MSD data shown in Fig. 4.4 (b), we can see a large variation in MSD of-

TH-2592_156107017

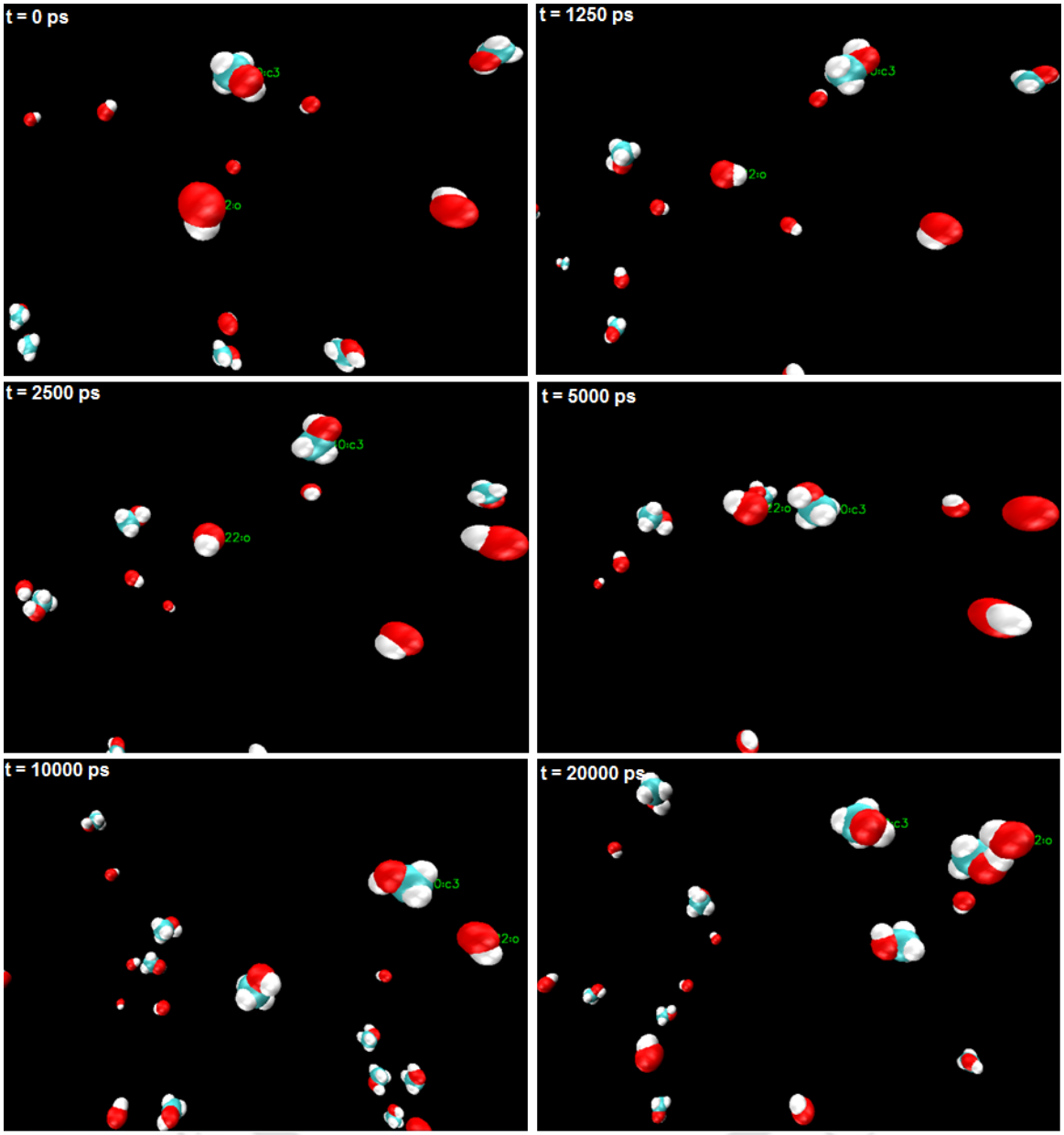

Fig. 4.7 Snapshots of a pair of OH^- ion (O-tagged) and methanol molecules (C-tagged) moving together during the entire duration of the MD simulation run, showing the effect of electro-osmotic drag of OH^- ion on methanol.

methanol between the different samples. As the samples have similar densities, the difference in methanol MSD and diffusivity is due to some other effect. If we observe the data closely from Table 4.2, we can identify a trend in MSD of methanol which follows the ionic conductivity of OH^-. Inclusion of 2.6 wt.% KAMP increased the MSD of methanol

TH-2592_156107017

and with increase in the concentration of KAMP to 5.1 wt.%, the MSD decreased. With further increase in the concentration of KAMP to 7.4 wt.% and 9.6 wt.%, the MSD of methanol gradually increased. This could be attributed to the well-known phenomenon of electro-osmotic drag, where small molecules like water and methanol get dragged with the moving ionic charge. In the case of acidic type of fuel cells, electro-osmotic drag is a big problem, where protons drag the methanol molecules from anode side to cathode side which react on the cathode side, reducing the overall performance of the fuel cell. However, in the case of alkaline fuel cells, this phenomenon is advantageous because OH^- ions move from cathode side to anode side, resisting the diffusion of methanol molecules from anode to cathode and bringing them back to anode side by electro-osmotic drag. The electro-osmotic drag in bulk phase can be visualized through snapshots taken during the MD simulation and shown in Fig. 4.6, where only OH^- ion and methanol molecules are shown for clarity. Fig. 4.6 clearly shows that around 8-pairs of hydroxyl ion–methanol are moving together from time t = 0 ns to t = 5 ns due to electro-osmotic drag. Other than OH^- ion and methanol molecules, Fig. 4.7 shows snapshots of an individual OH^--methanol molecule pair which was tagged and monitored, keeping the other components hidden for clarity. The snapshots taken at different time intervals from time t = 0 ns to t = 20 ns show that the methanol molecule moves around with the OH^- ion during the entire time of MD simulation due to electro-osmotic drag (Fig. 4.7). In addition, the effect of electro-osmotic drag was also confirmed by conducting MD simulation on the 2.6 wt.% KAMP system with reduced number of OH^- ions. In the 2.6 wt.% KAMP system, 24 K^+ ions were removed and out of 30 OH^- ions only 6 OH^- ions were kept in system to balance the positive charge on the KAMP. The MSD of methanol molecules obtained from these MD simulation runs was significantly suppressed. This reduction in MSD indicates a reduction in electro-osmotic drag due to fewer ions available.

TH-2592_156107017

4.3.1 Mechanism of OH^- Transport

To understand the ion transfer mechanism via interaction of OH^- with different sites present in the peptide and PVA. The RDF calculations included all the possible sites of charge interaction in the peptide as shown in Fig. 4.8 and hydroxyl groups of PVA. The distribution of water around these sites was also calculated. Fig. 4.9 shows the RDF of oxygen of OH^- and oxygen of H_2O in all the KAMP systems; all RDFs show a sharp first peak at ~2.9 Å in all the cases. The average coordination values at 2.9 Å for 2.6 wt.%, 5.1 wt.%, 7.4 wt.% and 9.6 wt.% KAMP systems are 1.84, 1.92, 1.58 and 1.59, respectively (Fig. 4.9 (b)). At lower KAMP loadings, where the number of charge transfer sites is low, OH^- is mainly surrounded by water, having higher coordination number. With increase in KAMP concentration, availability of more charged sites attracts more OH^- around them resulting in decrease of coordination number (CN) of water around OH^- at higher KAMP loadings. Coordination values below two for $O_{OH^-} - O_{H_2O}$ around the first peak position suggests that, the OH^- transfer does not follow the typical Grotthuss mechanism proposed in lieterature for OH^- transport in bulk water (Tuckerman et al., 1995[a]; Tuckerman et al., 1995[b]), where OH^- forms four hydrogen bonded and three hydrogen bonded complex species back and forth to charge transfer (mentioned in section 4.1). In this case coordination around the peak RDF value should be in the range of 3-4, as oppose to the below 2 in current case. The coordination values below two suggest that the charge transfer takes place by hydrogen-bonded association between H_2O and OH^-, which further suggests formation of H-bonded $H_3O_2^-$ type ions to carry forward the charge transfer. Here, OH^- interacts with two water molecules: the OH^- forms hydrogen bonds with one water molecule to produce $H_3O_2^-$ ion, and subsequently jumps to the second nearby water molecule. It also indicates that transfer of OH^- takes place by formation of H- bonded -

TH-2592_156107017

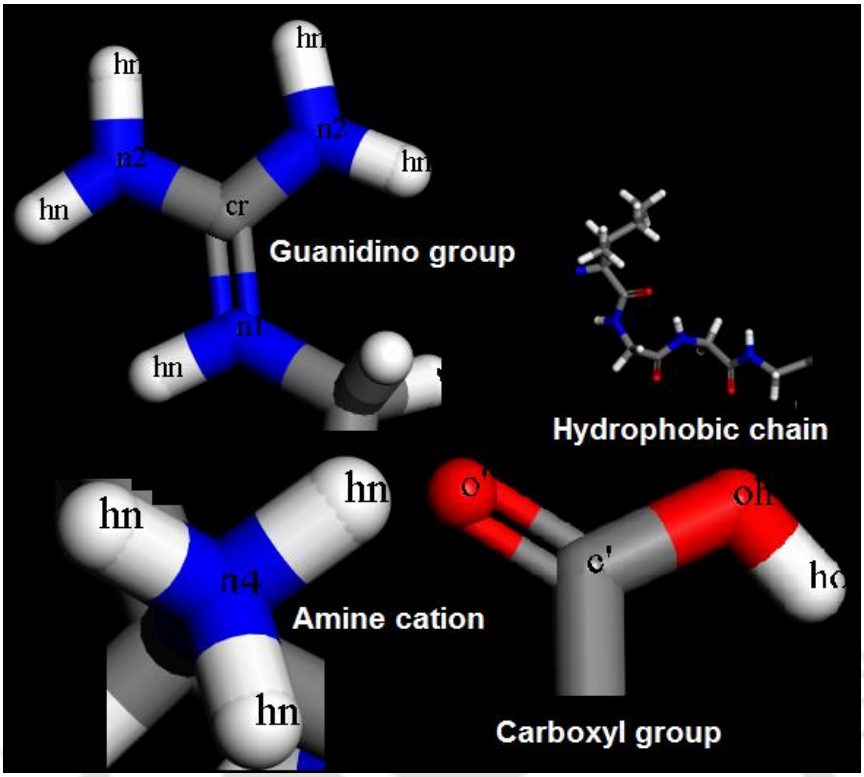

Fig. 4.8 Different functional sites of KAMP-19 considered for RDF calculation with oxygen of OH− and H2O. The atoms names correspond to the CVFF force field and details of each atom type is given in appendix.

$H_3O_2^-$ and its back conversion to H_2O and OH^-. This mechanism can be understood by the snapshots taken during MD run, as shown in Fig. 4.10. First snapshot shows OH^- ion having two H_2O in the surrounding (in blue circle). One H_2O is associated with OH^- ion by H-bonding and the other is in close proximity. After 5 ps as shown in 2nd snapshot, one H_2O molecule moves away, while another comes in close proximity. In the 3rd snapshot after 10 ps (from the first snapshot), the OH^- ion forms H-bonding with the new H_2O molecule, while the old H_2O molecule moves away. At the same time another water molecule approaches the OH^- ion. In the final snapshot after 15 ps, two water can be seen surrounding the OH^- ion, one of which may be H-bonded with it, while the other is in close proximity. The snapshots are taken by hiding the peptides, K^+ and PVA for better view.

TH-2592_156107017

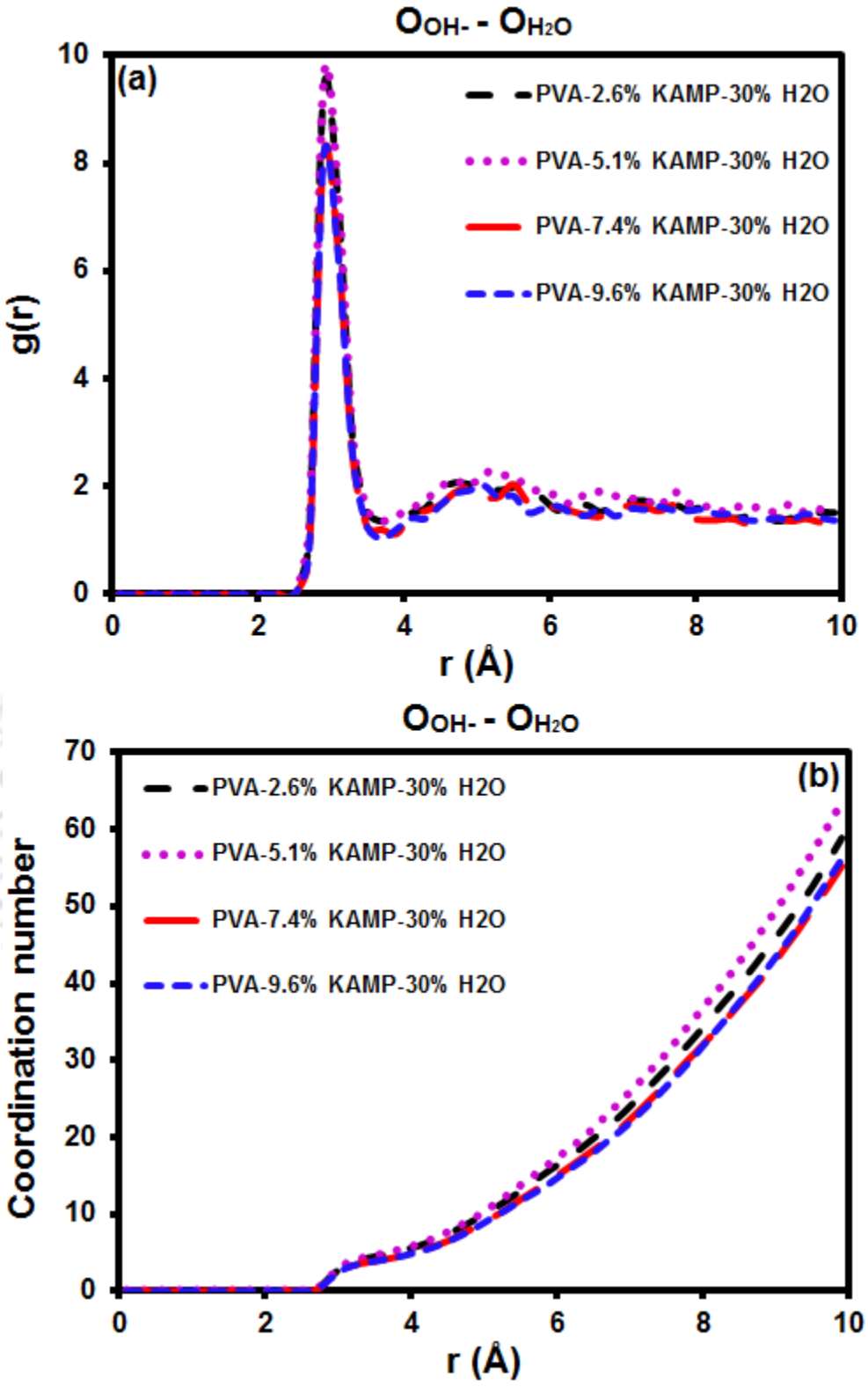

Fig. 4.9 (a) RDF of O_{OH^-} - O_{H_2O} and (b) CN of O_{H_2O} around O_{OH^-} for samples with different KAMP loadings.

TH-2592_156107017

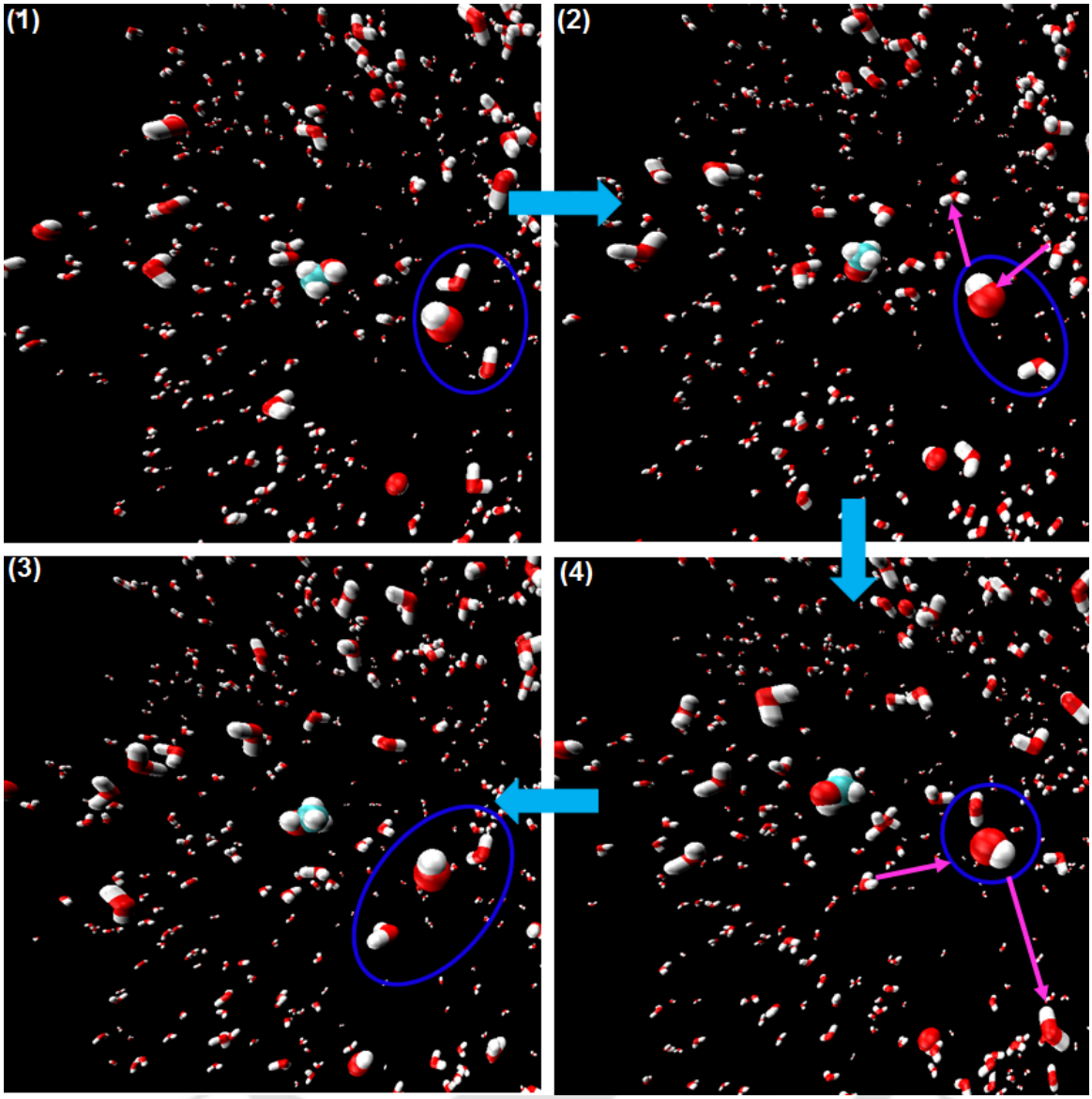

Fig. 4.10 OH^- ion transfer through formation and breaking of H-bond with water.

TH-2592_156107017

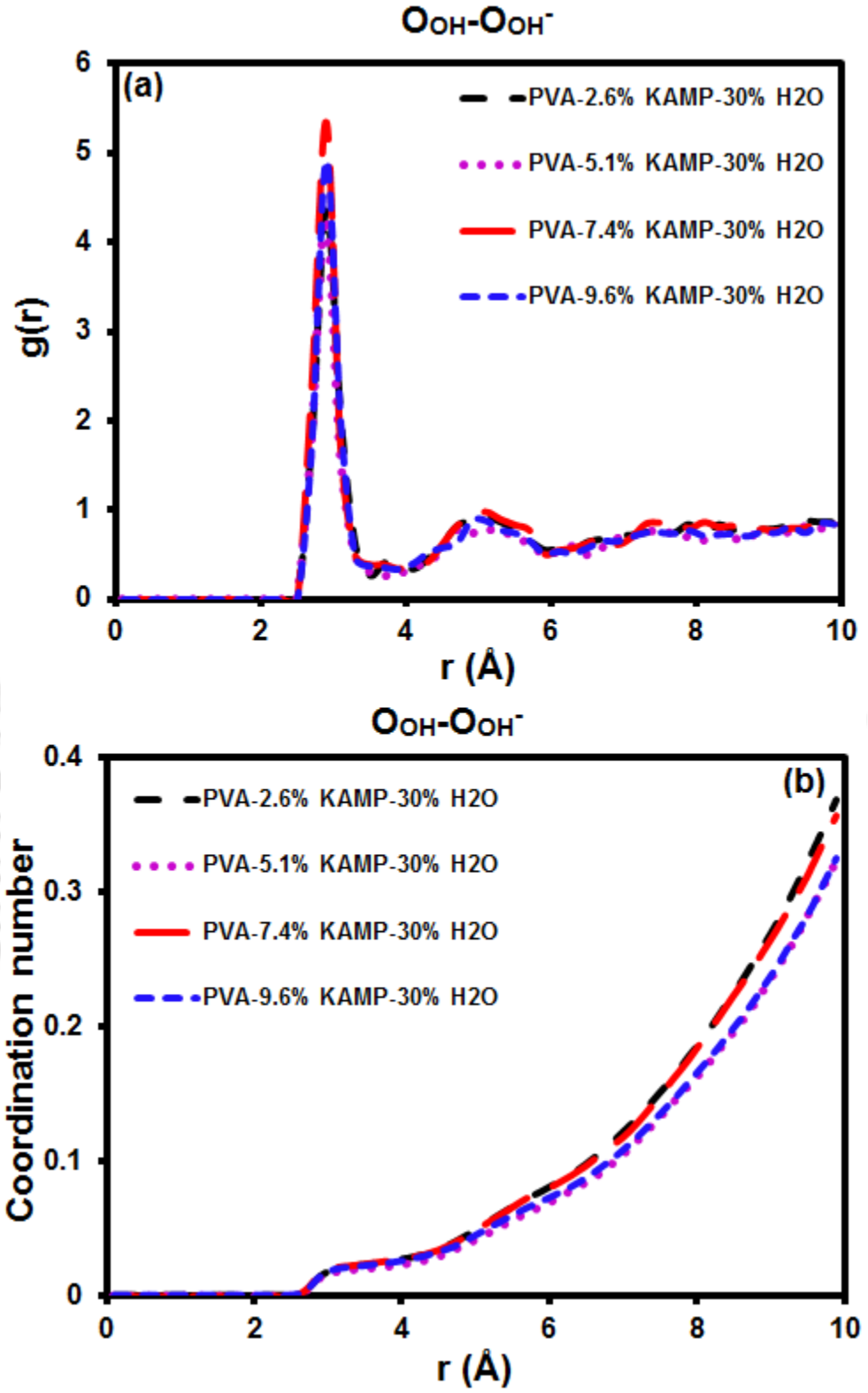

Fig. 4.11 (a) RDF of $O_{OH} - O_{OH^-}$ (b) CN of O_{OH^-} around O_{OH} for samples with different KAMP loadings.

TH-2592_156107017

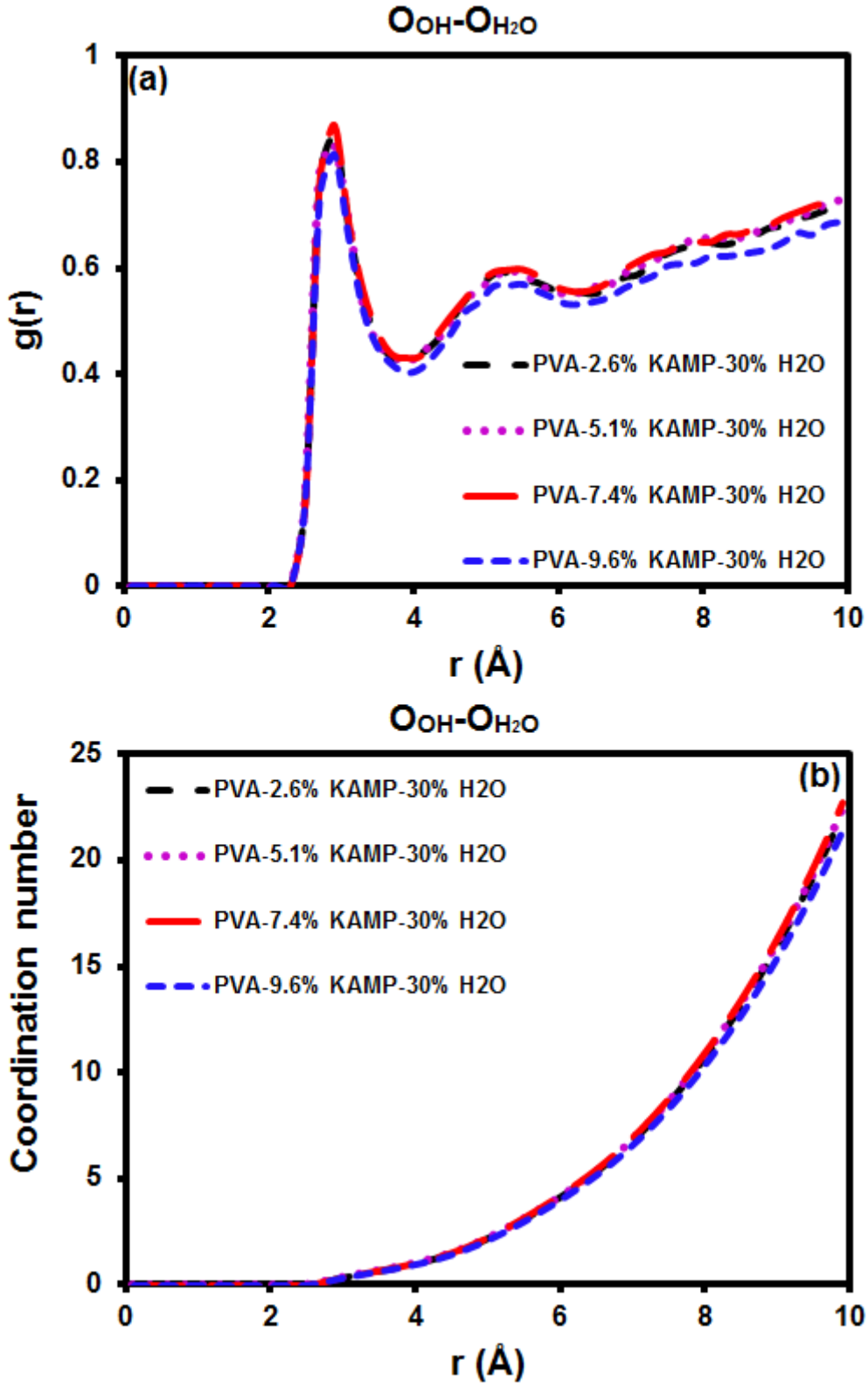

Fig. 4.12 (a) RDF of $O_{OH} - O_{H_2O}$ (b) CN of O_{H_2O} around O_{OH} for samples with different KAMP loadings.

TH-2592_156107017

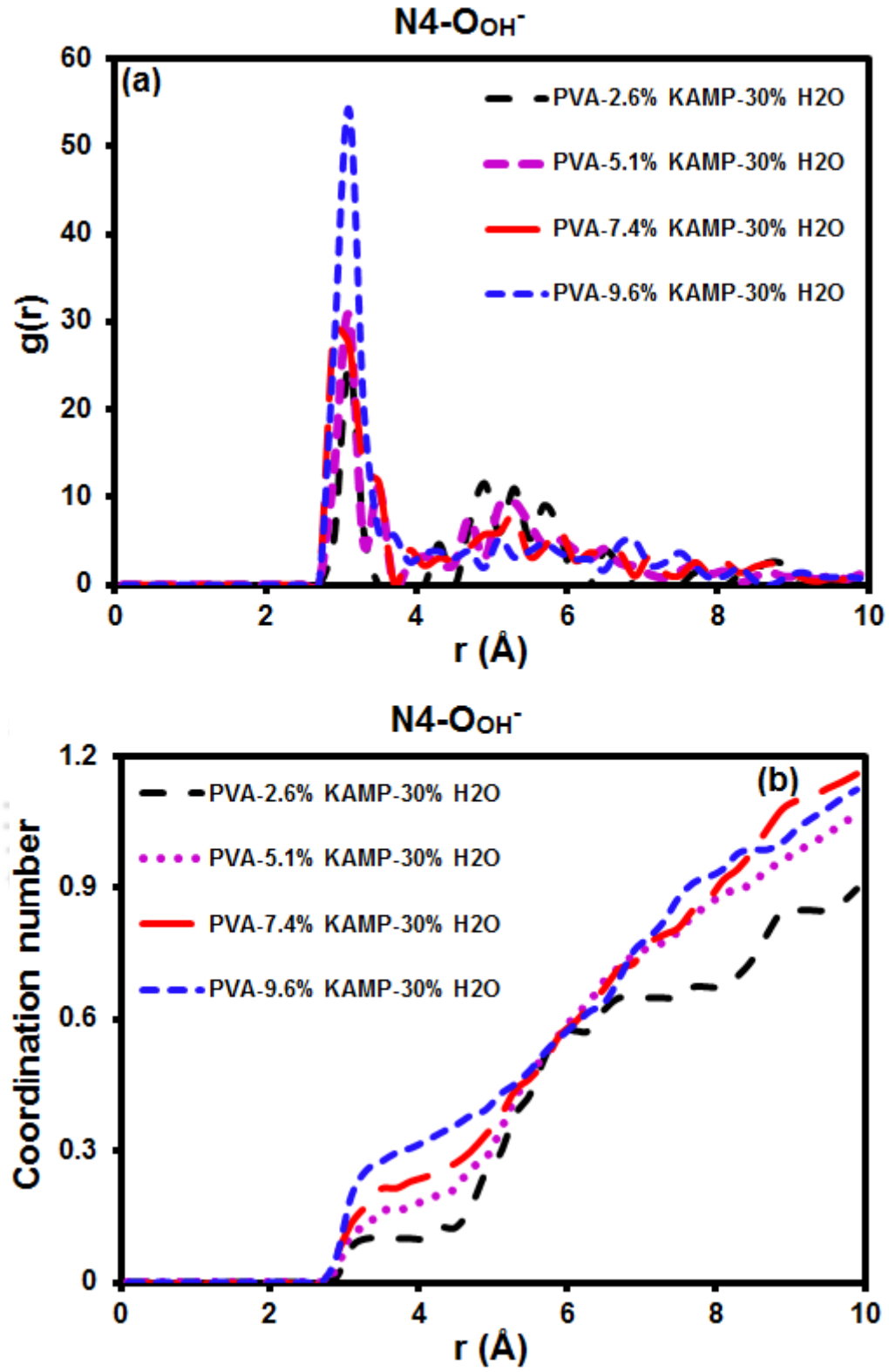

Fig. 4.13 (a) RDF of $N4 - O_{OH^-}$ (b) CN of O_{OH^-} around $N4$ for samples with different KAMP loadings.

TH-2592_156107017

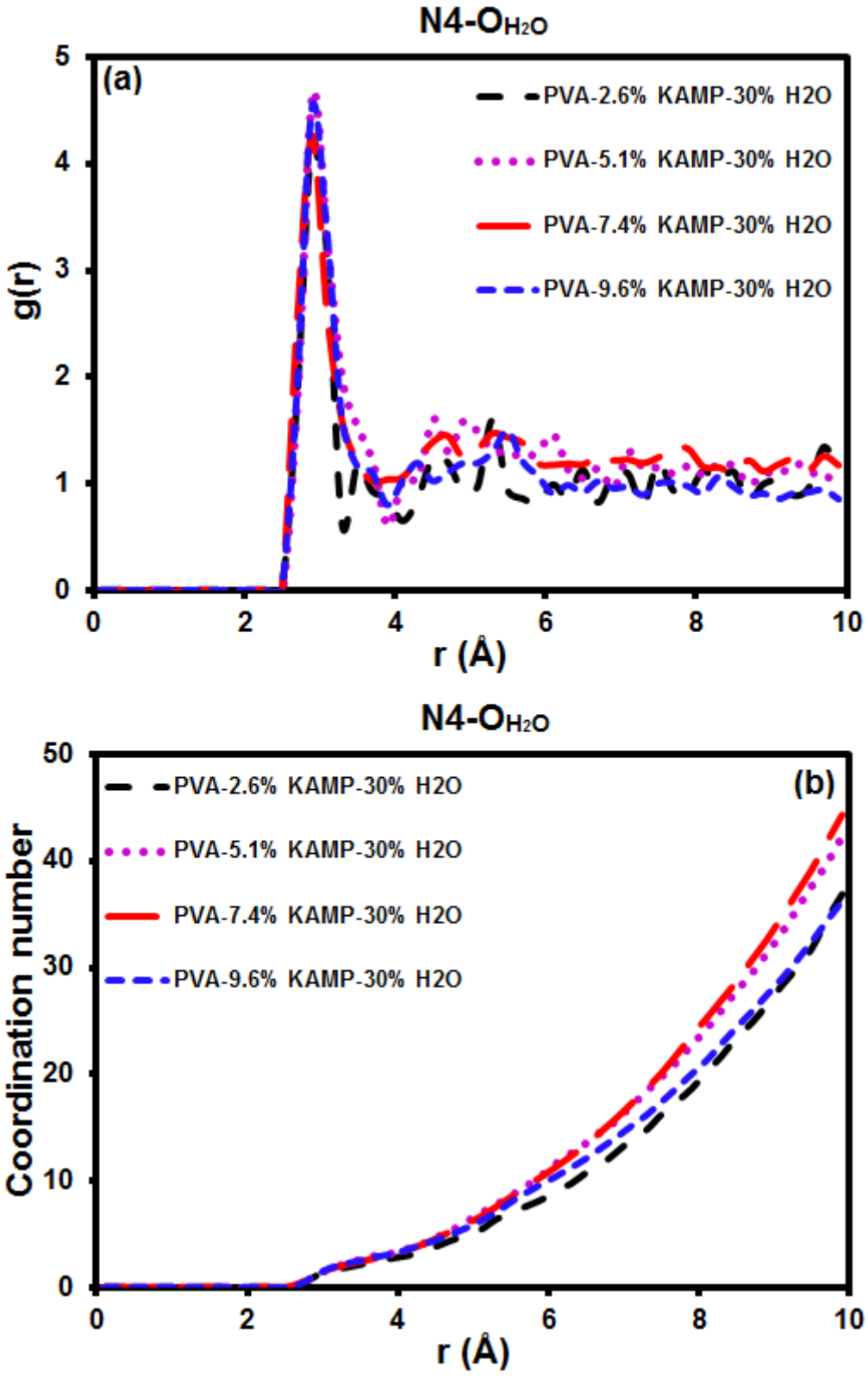

Fig. 4.14 (a) RDF of $N4 - O_{H_2O}$ (b) CN of O_{H_2O}around $N4$ for samples with different KAMP loadings.

TH-2592_156107017

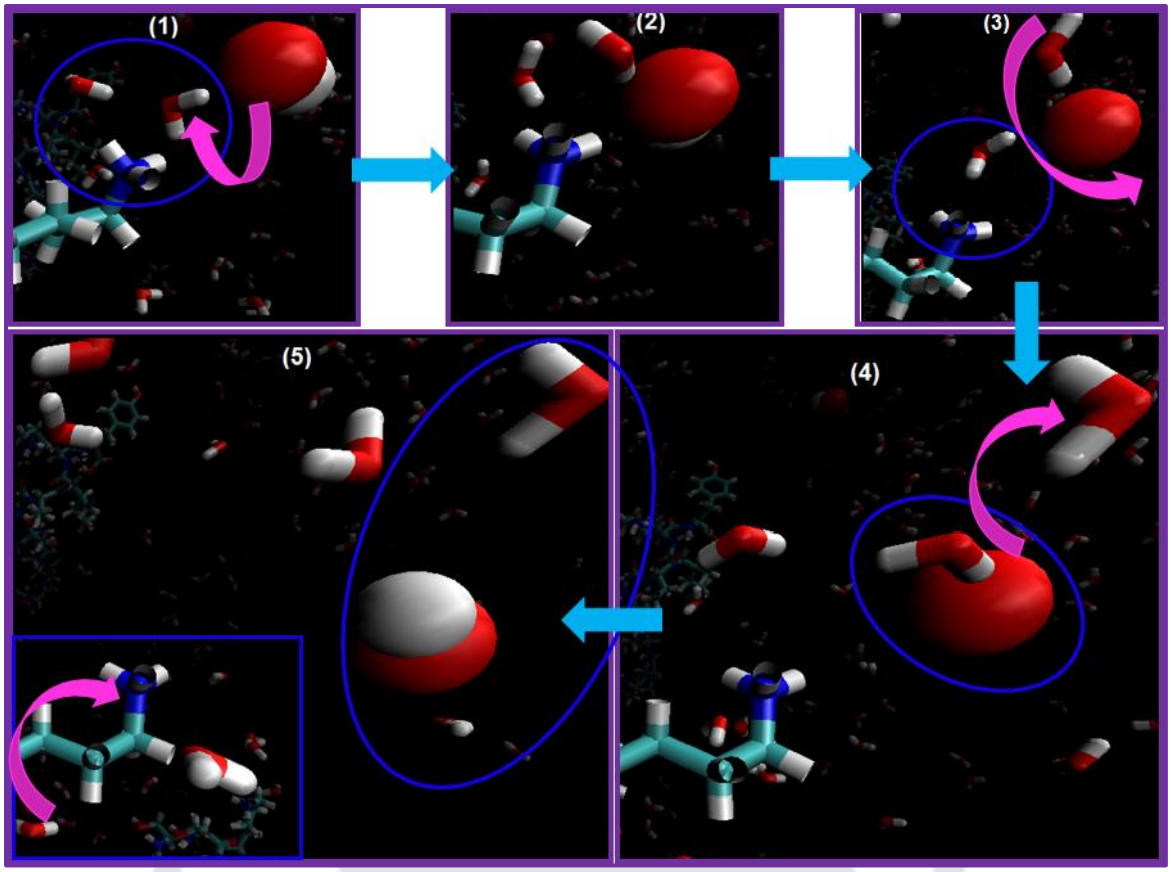

Fig. 4.15 OH^- transfer mechanism at ammonium cation site of peptide.

The role of the hydroxyl (OH) group of PVA in OH^- transfer was evaluated by calculating the RDF between the oxygen atoms of the OH groups of PVA chains and the OH^- ions ($O_{OH} - O_{OH^-}$) (Fig. 4.11) as well as between the oxygen atoms of the OH groups of PVA chains and water ($O_{OH} - O_{H_2O}$) (Fig. 4.12). The RDF of $O_{OH} - O_{OH^-}$ showed (Fig. 4.11 (a)) two different peaks: one major peak at 2.9 Å and the second weaker peak around 5.1 Å corresponding to coordination number of 0.01 for first peak at all the KAMP loadings, and 0.05, 0.04, 0.05 and 0.05 for the second peak at 2.6 wt.%, 5.1 wt.%, 7.4 wt.% and 9.6 wt.% KAMP loadings, respectively (Fig. 4.11 (b)). As the coordination values for OH group of PVA with OH^- ion are very low for each system, it does not contribute significantly to the transfer of OH^-. Fig. 4.12 (a) shows the RDF of $O_{OH} - O_{H_2O}$, having two peaks at similar positions as that of the RDF of $O_{OH} - O_{OH^-}$. The g(r) value below 1

TH-2592_156107017

at both the peak positions suggests that the number density of water in the vicinity of OH groups of PVA is lower than the average density of water in the simulation box. It indicates presence of lower amount of water around the OH groups on average. The coordination number for first peak is around 0.30 for each KAMP system, and 2.39, 2.36, 2.42 and 2.29 at the second peak for the 2.6 wt.%, 5.1 wt.%, 7.4 wt.% and 9.6 wt.% KAMP systems, respectively (Fig. 4.12 (b)). The g(r) peaks value below 1 for water, while g(r) value greater than 1 for OH^- ions around OH of PVA suggests that OH^- has higher density around OH of PVA, but has lower density of water. Due to lower water density around OH, the PVA may not be able to trsasfer the OH^- ions easily, but it has a continuous channel of water molecules away from the hydrogen bonding range, as indicated by coordination values of second peak, which can provide a straight path for OH^- ions transfer. It suggests that without the presence of charge transfer sites also PVA matrix with enough amount of hydration, can transfer the OH^- due formation of water channels. The conuctivty value of 0.95 mS/ cm, shown in Table 4.2 for the PVA system confirms the same. However, the rate of OH^- transport will be slower compared to systems having charge transfer sites.

Fig. 4.13 (a) and Fig. 4.14 (a) show the RDFs of $N4 - O_{OH^-}$ and $N4 - O_{H_2O}$ respectively. N4 is the nitrogen of ammonium cation in the peptide. Except for the 9.6 wt.% KAMP system, RDFs of $N4 - O_{OH^-}$ show two different peaks, one at ~3.1 Å and a second broad peak centred at around 5.3 Å. The coordination values for $N4 - O_{OH^-}$ at the first peak position are 0.08, 0.11, 0.14 and 0.20 for 2.6 wt.%, 5.1 wt.%, 7.4 wt.% and 9.6 wt.% KAMP systems, respectively and at the second peak position are 0.38, 0.42 and 0.44 for 2.6 wt.%, 5.1 wt.% and 7.4 wt.% KAMP systems, respectively (Fig. 4.13 (b)). The coordination values show that ammonium cation does not have strong interaction with OH^- as at the lower RDF peak, the coordination numbers are low. At the same time, the coordination number of OH^- around the ammonium cation increases with increase in the KAMP

TH-2592_156107017

concentration, indicating improved interaction of ammonium cation with OH^- at higher KAMP loadings. The RDF data appears to suggest that ammonium cation does not directly interact with the OH^- ions, but instead forms hydrogen bonds with surrounding water molecules which provide sites for OH^- ion transfer. This can be further verified by the number of water molecules around N4 (see Fig. 4.14 (b)). The coordination numbers of water around the ammonium ion of the peptide at a distance of 3.1 Å (first peak position for the RDF in Fig. 4.14(a)) are 1.69, 1.80, 1.71 and 1.82 for 2.6 wt.%, 5.1 wt.%, 7.4 wt.% and 9.6 wt.% KAMP systems, respectively, indicating that N4 is mainly surrounded by water molecules. The mechanism of OH^- transfer through ammonium cations is further illustrated by representative snapshots of OH^- trajectory around it, as shown in Fig. 4.15. In the first step, both ammonium cation and OH^- have hydrogen bonds formed with one water molecule each and the two water molecules in close proximity to both the ammonium group and the hydroxide anion. The OH^- anion may be associated with the neighbouring water molecules and present in hydrogen bonded form with water ($H_3O_2^-$). In the second step, after 20 ps, OH^- comes close to ammonium cation and in the third step, after 60 ps, due to thermal fluctuations, the water molecule associated with OH^- moves away a little. In the fourth step, after 90 ps, another water molecule comes around it to subsequently take the OH^- forward by forming hydrogen bond with it. This also supports the OH^- transport mechanism proposed earlier in this section, where transfe r of OH^- takes place by continuous formation of $H_3O_2^-$ and its back conversion to H_2O and OH^-. In the fifth step, after 105 ps, the OH^- ion with two water molecules around goes further away, while another water molecule approaches towards the ammonium cation due to electrostatic interaction.

Fig. 4.16 (a) and Fig. 4.17 (a) show the RDF of N1 with oxygen of OH^- and H_2O, respectively. N1 is the cationic site of guanidino group, having one extra proton on it. RDF of $N1 - O_{OH^-}$ showed peak position at 2.9 Å with coordination numbers of 0.88, 0.85, 0.85

TH-2592_156107017

and 0.86 for 2.6 wt.%, 5.1 wt.%, 7.4 wt.% and 9.6 wt.% KAMP system, respectively (Fig. 4.16 (b)). A coordination number of around one at the first peak position means that N1 has approximately one OH^- ion around it, showing direct and strong interaction with OH^-. It also tells that on the gunidino group, OH^- transfers in its original form by jumping from one group to another directly, reducing the time to convert to intermediate species like $H_3O_2^-$ and thus having faster transport. Further, in the real case the charge in gunidino group is delocalized, which may lead to faster transfer of OH^-. Due to both these reasons the experimental study results reported in the previous chapter show higher ionic conductivities. In the current study, where the gunidino groups are far from each other, the OH^- transport may be considered a mix of transfer in water through formation of $H_3O_2^-$ and $H_2O + OH^-$ back and forth, and near the guanidino groups by OH^- jumping from $H_3O_2^-$ to the guanidine cation and then jumping back to nearby water molecule again to form $H_3O_2^-$ to move forward. The snapshots shown in Fig. 4.18 support this description of OH^- transport and further illustrate the mechanism. Step one shows the presence of one OH^- on the guanidino group (in blue circle) and another OH^- with water molecule going away from the guanidino group by possibly forming $H_3O_2^-$ type ion by hydrogen bonding. In the next step, after 30 ps, while the OH^- - H_2O pair moves further away, another water molecule approaches the OH^- of guanidino group. In the third step, after 45 ps, the water molecule leaves the guanidino group with the OH^- in $H_3O_2^-$ form. Second and third steps demonstrate the transfer of OH^- by associating with water and converting to $H_3O_2^-$. In the fourth step, after 90 ps, the OH^- of guanidino group, which moved away with one water molecule brings one more water molecule around to continue the transport in water by possibly forming $H_3O_2^-$ and $H_2O + OH^-$ back and forth by H-bonding. The fifith step shows that the OH^- ion has completely moved away from the guanidino cation. The RDF of $N1 - O_{H_2O}$ shown in Fig. 4.17 (a) has a broad, noisy peak around 5.1 Å. The number of water molecules

TH-2592_156107017

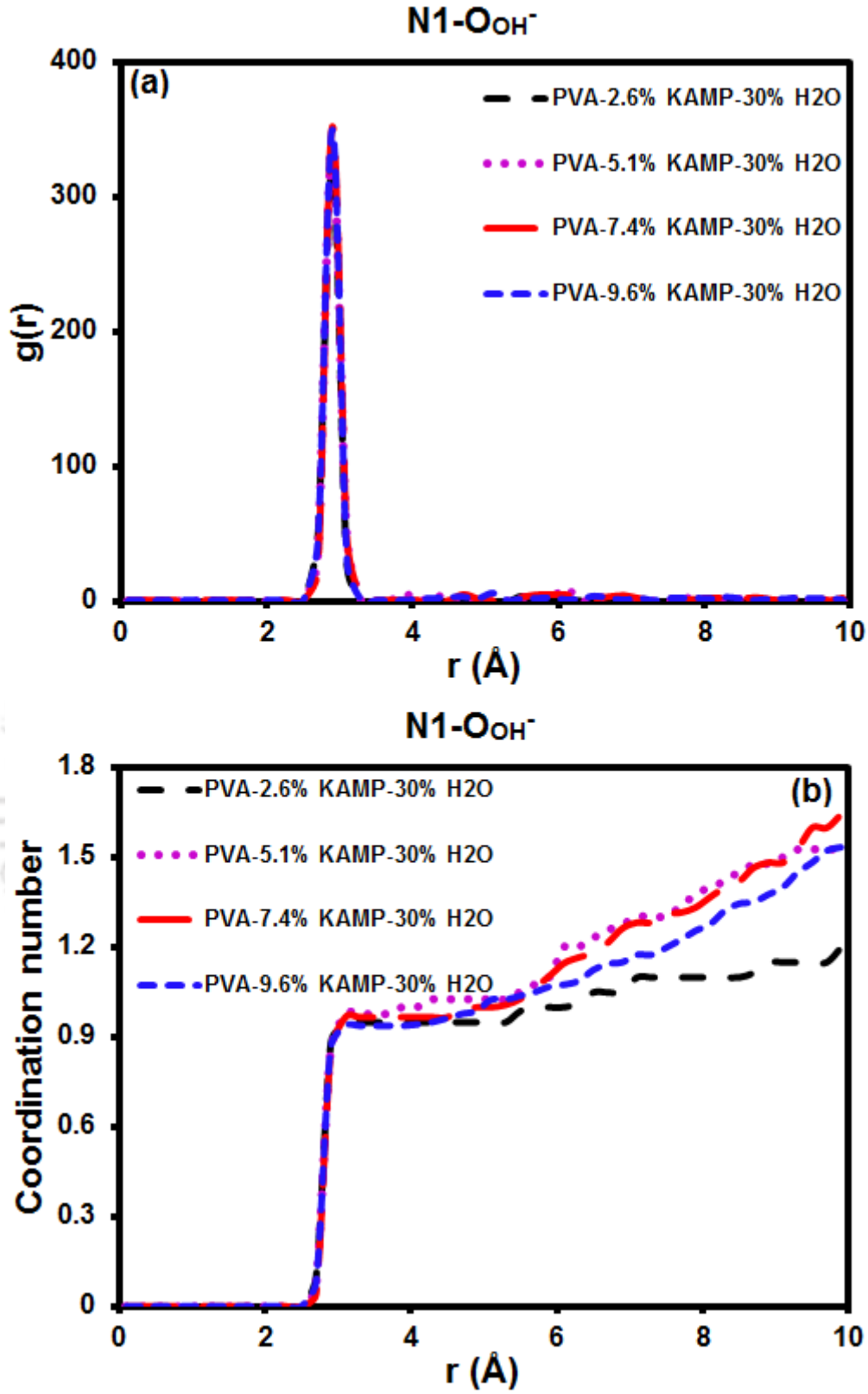

Fig. 4.16 (a) RDF of $N1 - O_{OH^-}$ (b) CN of O_{OH^-} around $N1$ for samples with different KAMP loadings.

TH-2592_156107017

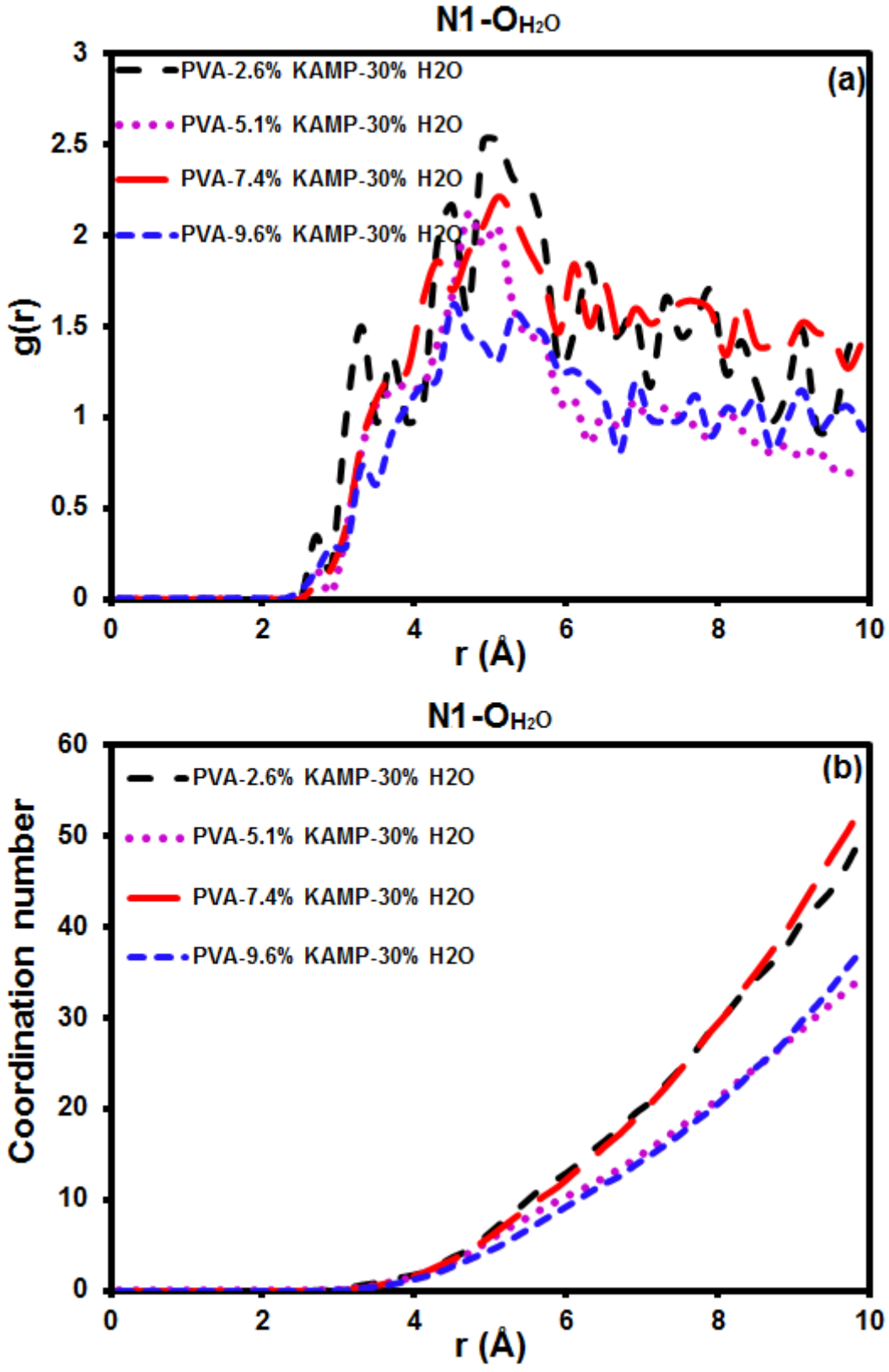

Fig. 4.17 (a) RDF of $N1 - O_{H_2O}$ (b) CN of O_{H_2O} around N1 for samples with different KAMP loadings.

TH-2592_156107017

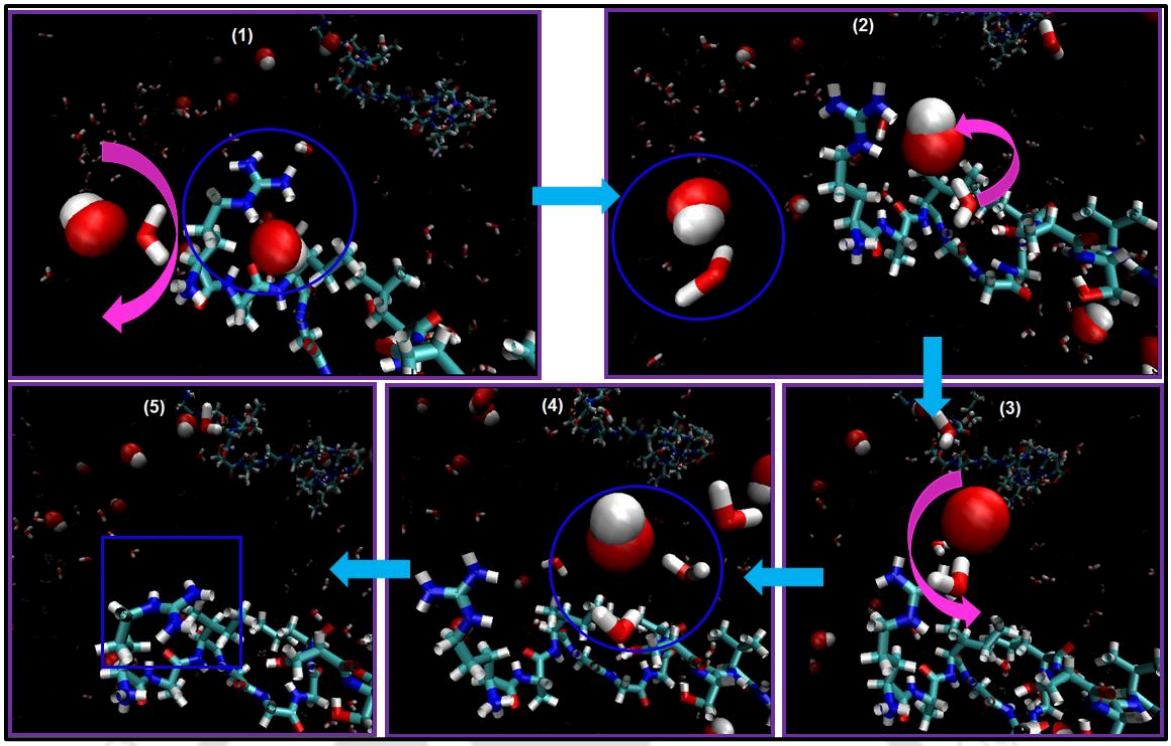

Fig. 4.18 Charge transfer mechanism at guanidino cation site of peptide observed during the MD simulation. The blue circle shows the motion of OH^- ion with increasing time steps. The pink arrows shows the H-bonding interaction between H_2O and OH^- suggesting the formation of $H_3O_2^-$ H-bonded species and its motion. The square box in the final snapshot shows that OH^- ion has completely moved away from the guanidino cation.

present around N1 within a radius of 5.1 Å are 7.20, 6.16, 6.69 and 4.88 for 2.6 wt.%, 5.1 wt.%, 7.4 wt.% and 9.6 wt.% KAMP systems, respectively (Fig. 4.17 (b)). The reduction in coordination number from 7.2 for 2.6 wt.% KAMP system to 4.88 for 9.6 wt.% KAMP system supports the conjecture made earlier in the result and discussion section regarding the reduction in ionic conductivity due to presence of lower amount of water around the peptide due to the formation of a low water zone. The presence of higher number of water molecules around the charged cation reduces the ionic interaction between the -

TH-2592_156107017

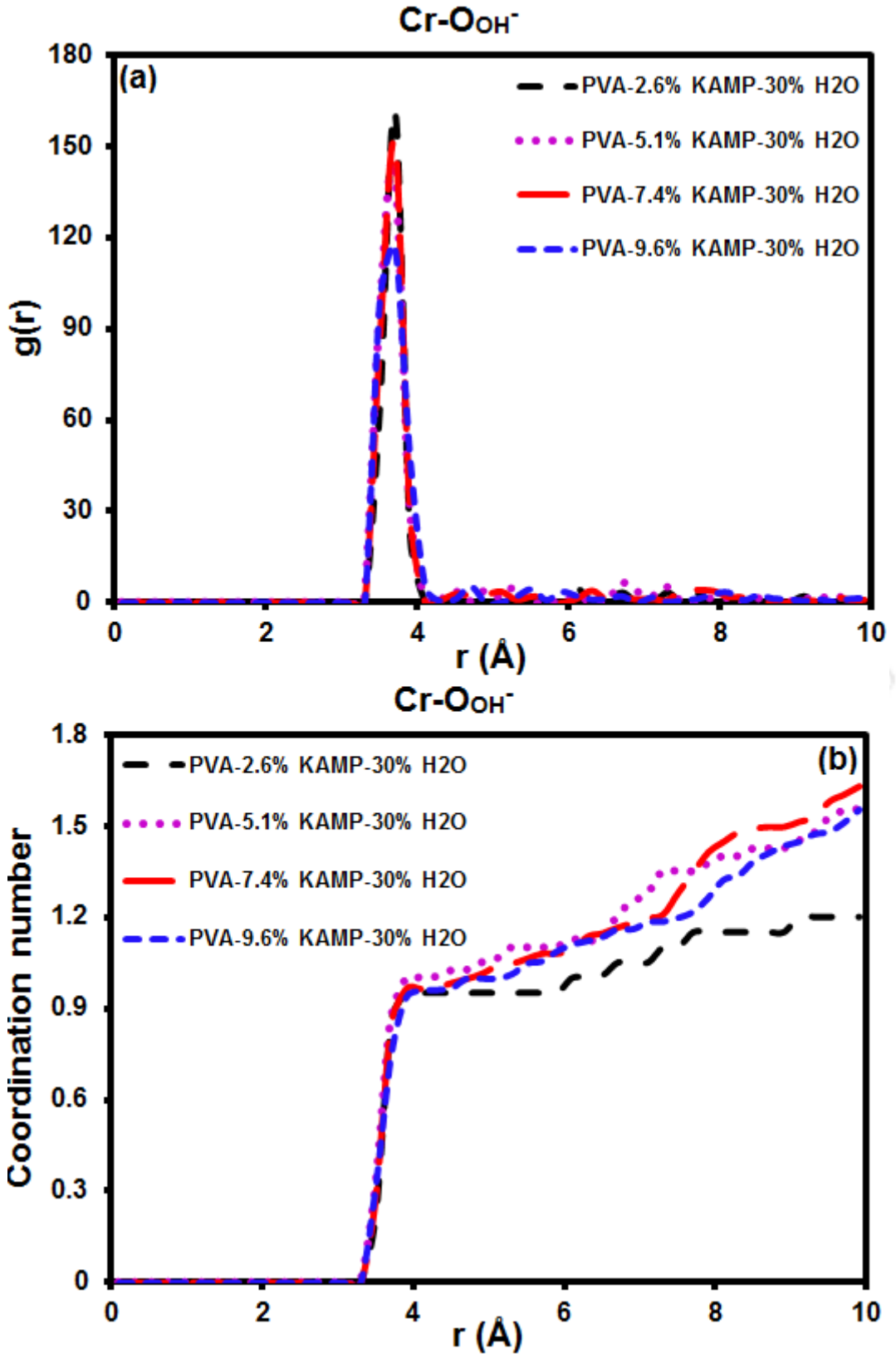

Fig. 4.19 (a) RDF of $Cr - O_{OH^-}$ (b) CN of O_{OH^-} around Cr for samples with different KAMP loadings.

TH-2592_156107017

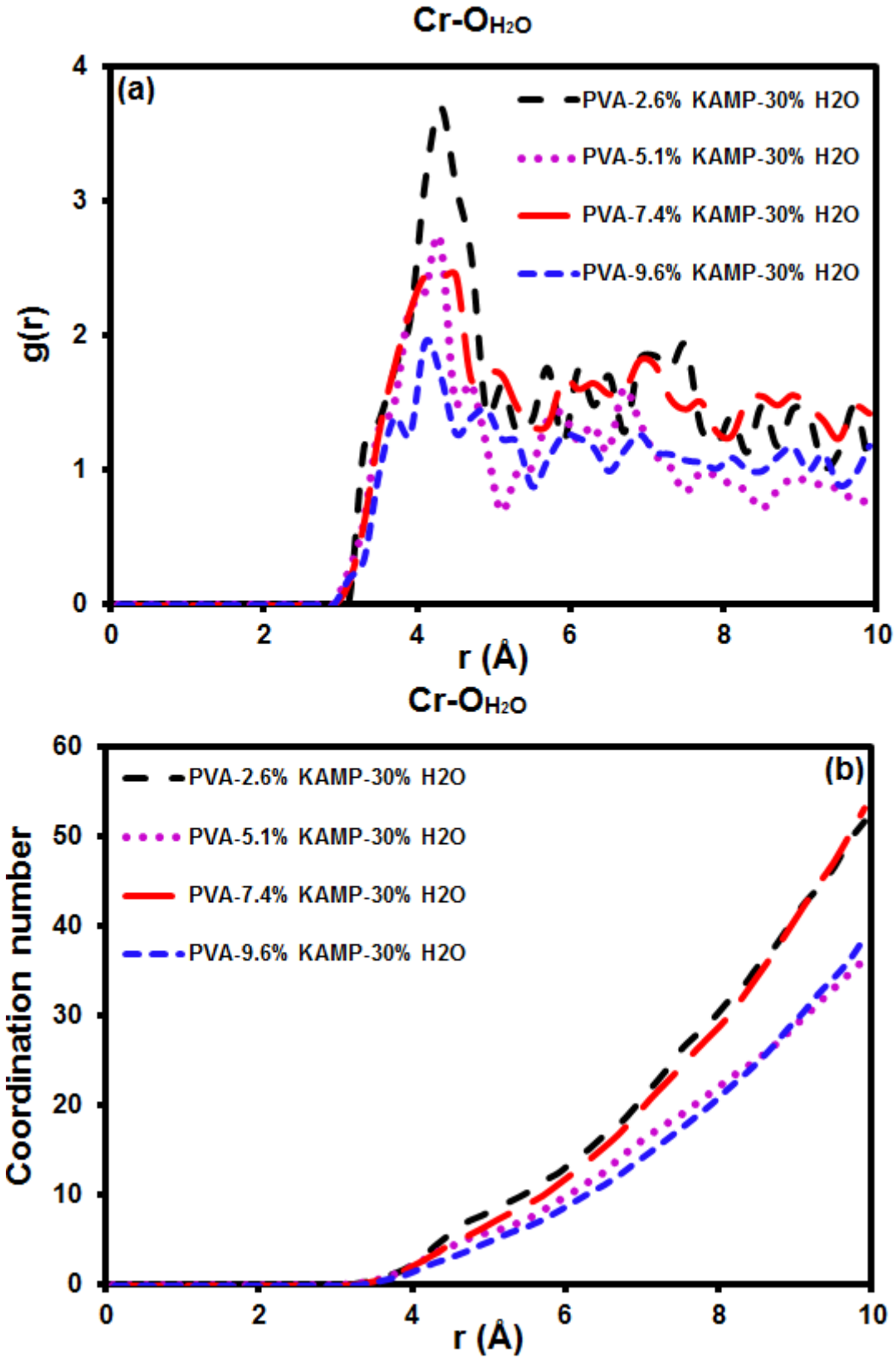

Fig. 4.20 (a) RDF of $Cr - O_{H_2O}$ (b) CN of O_{H_2O} around Cr for samples with different KAMP loadings.

TH-2592_156107017

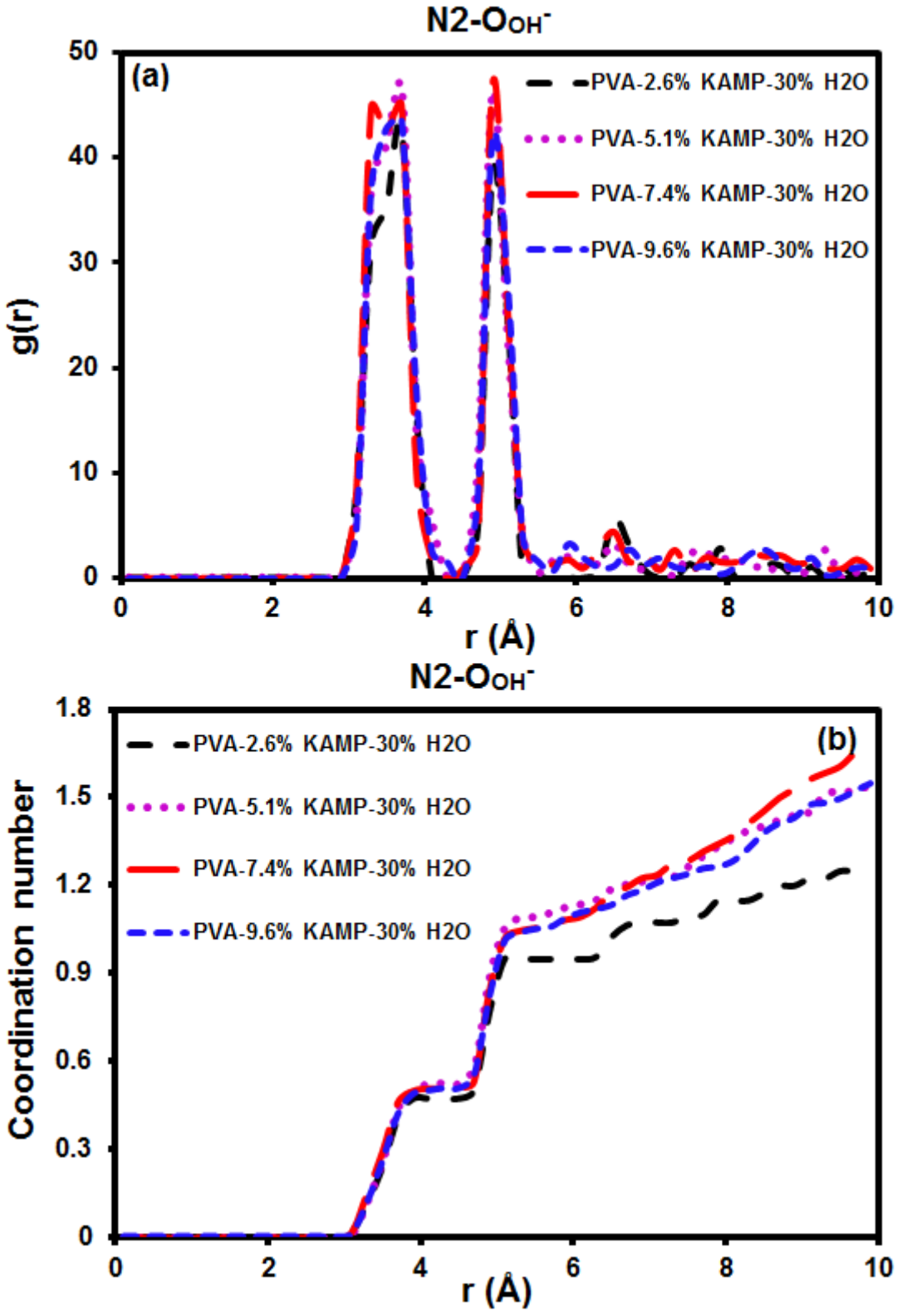

Fig. 4.21 (a) RDF of N2 – O_{OH^-} (b) CN of O_{OH^-} around N2 for samples with different KAMP loadings.

TH-2592_156107017

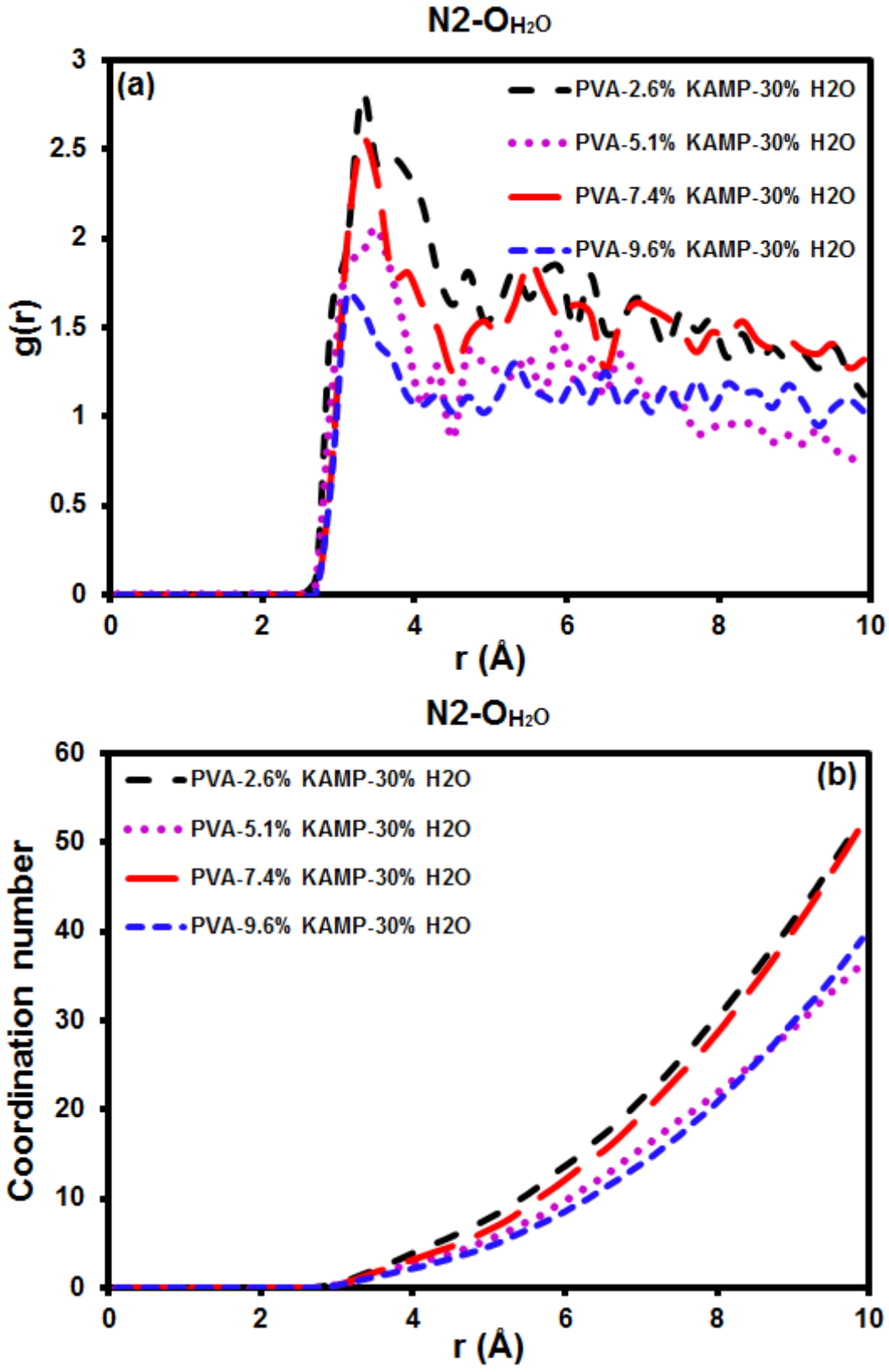

Fig. 4.22 (a) RDF of $N2 - O_{H_2O}$ (b) CN of O_{H_2O} around N2 for samples with different KAMP loadings.

TH-2592_156107017

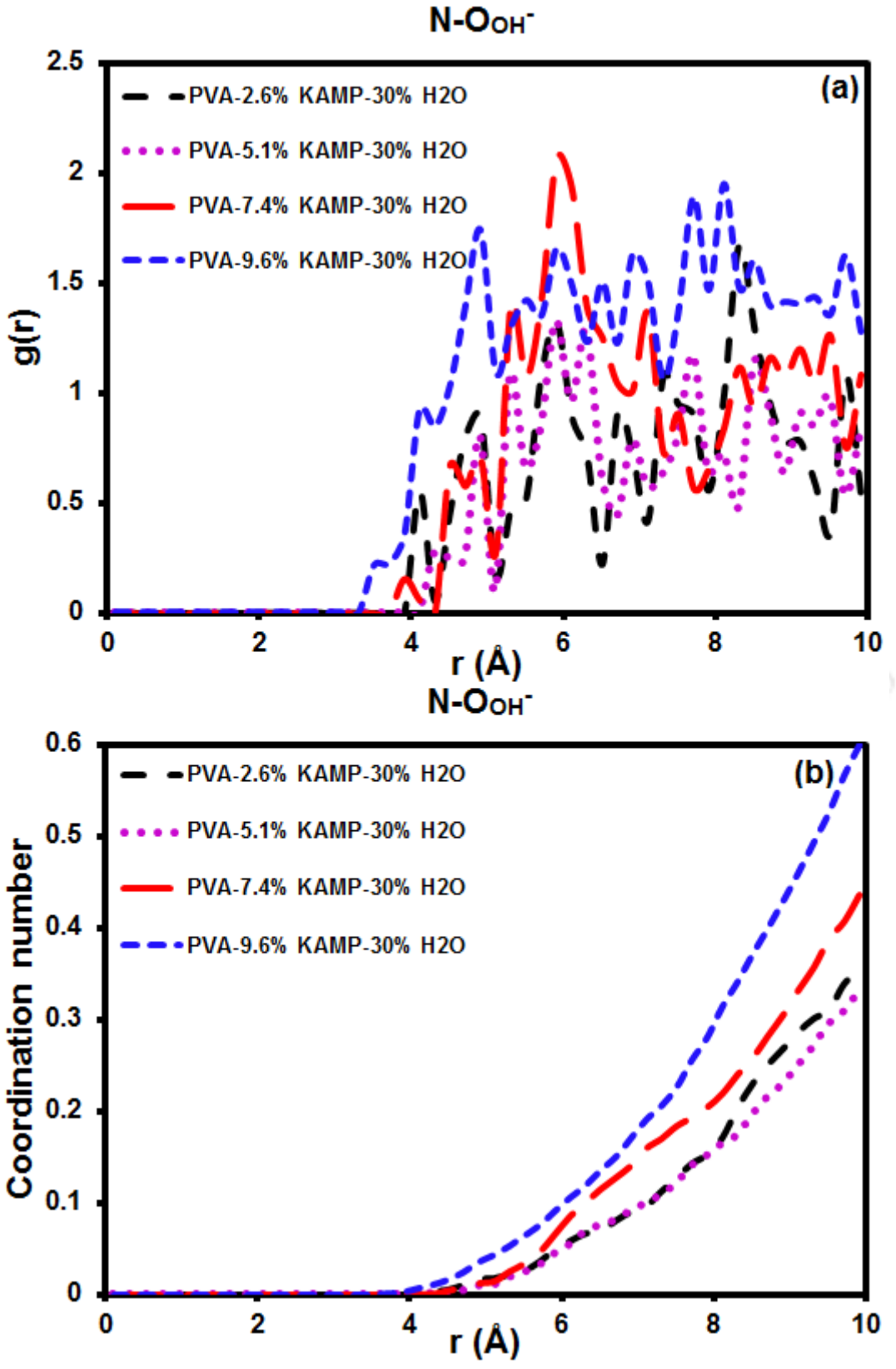

Fig. 4.23 (a) RDF of $N - O_{OH^-}$ (b) CN of O_{OH^-} around N for d samples with different KAMP loadings.

TH-2592_156107017

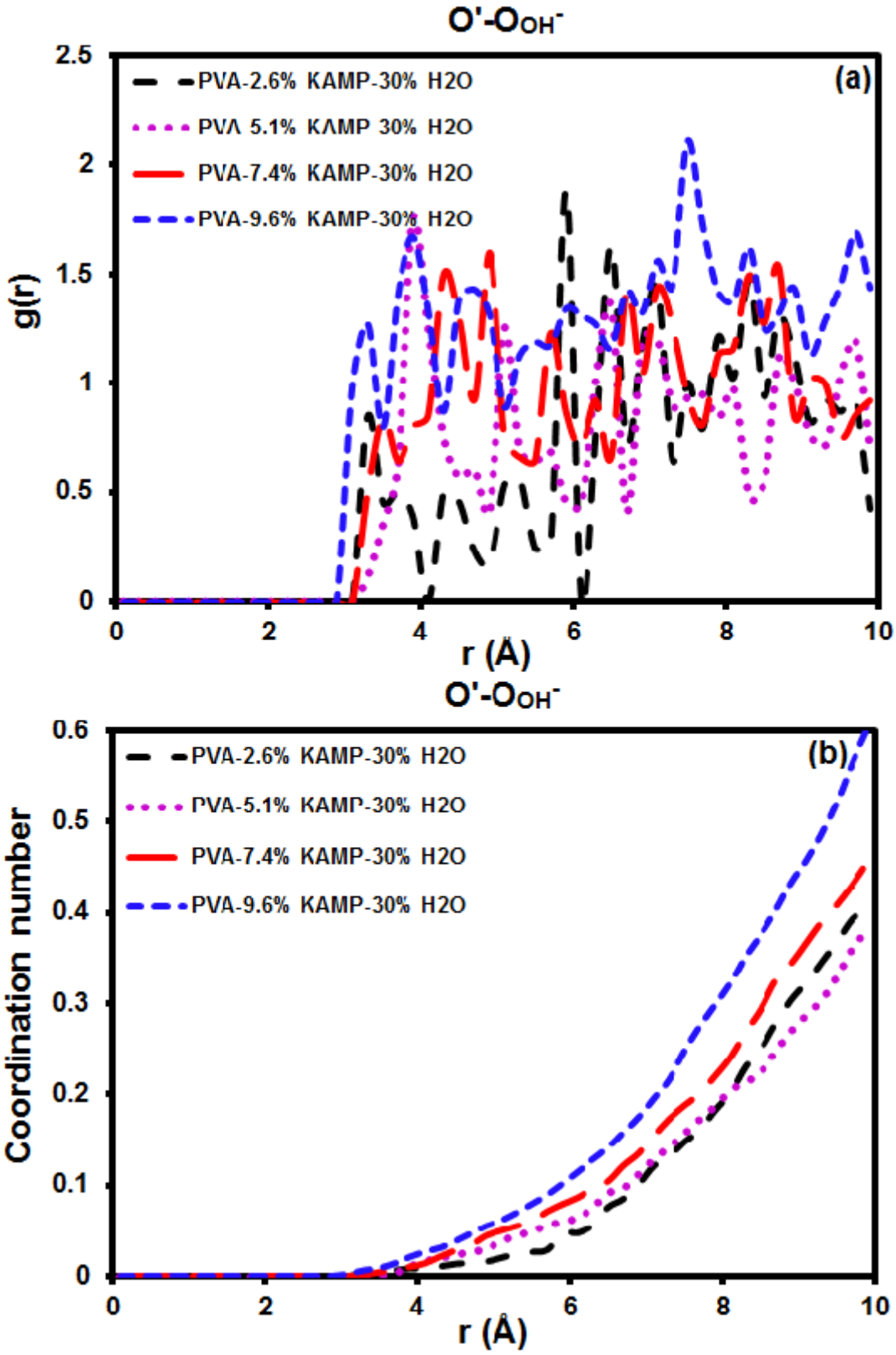

Fig. 4.24 (a) RDF of $O' - O_{OH^-}$ (b) CN of O_{OH^-} around O' for samples with different KAMP loadings.

TH-2592_156107017

OH^- ion and the cationic site, resulting in improved transfer of OH^-. So, 2.6 wt.% KAMP sample has higher ionic conductivity, which reduces in the 5.1 wt.% KAMP system due to reduction in the number of water molecules around the cationic site N1. Increase in ionic conductivity with further increase in KAMP loading can be attributed to the increase in the number of cationic sites, facilitating the transport of OH^- ion from one site to another, even with low number of water molecules around.

Fig. 4.19 (a) and Fig. 4.20 (a) are the RDF of $Cr - O_{OH^-}$ and (b) $Cr - O_{H_2O}$, respectively. Cr represents the central carbon of guanidino group, present next to the cationic N1. Thus, it also shows similar range of coordination numbers with OH^- for all the KAMP systems (Fig. 4.19 (b)) s the N1 site, but has the first RDF peak at a higher distance of 3.7 Å due to weaker ionic interaction with OH^-. The first peak of the $Cr - O_{H_2O}$ RDF is observed at a lower radius of 4.3 Å (Fig. 4.20 (a)) compared to that of the RDF of $N1 - O_{H_2O}$ (Fig. 4.17(a)). Thus, the central carbon atom of the guanidino group has water molecules closer to it than the N1 atom and follows the same trend of water coordination numbers with increasing KAMP loading (4.46, 3.6, 3.62 and 2.61 for 2.6 wt.%, 5.1 wt.%, 7.4 wt.% and 9.6 wt.% KAMP system, respectively) (see Fig. 4.20 (b)) as N1 with water.

The RDF of $N2 - O_{OH^-}$ showed two peaks (Fig. 4.21 (a)), one at 3.7 Å with coordination number in the range of 0.40–0 .45 and the second at 4.9 Å with coordination number in the range of 0.77–0.89 (Fig. 4.21 (b)). N2 represents the two nitrogen atoms of guanidino group (see Fig. 4.8) and presence of two peaks implies that both N2 have the same OH^- around, which is associated with the N1 site. While one N2 is nearer to the guanidino OH^- showing first peak at 3.7 Å, the second N2 further away from the OH^- shows the peak at 4.9 Å. As the two N2 share one OH^- among them, the coordination numbers at 3.7 Å are almost half of the coordination numbers at 4.9 Å. The coordination values of N2 with water

TH-2592_156107017

(Fig. 4.22 (b)) are 1.36, 1.02, 1.14 and 0.85 for 2.6 wt.%, 5.1 wt.%, 7.4 wt.% and 9.6 wt.% KAMP system, respectively, at the distance corresponding to the first peak of the RDF (Fig. 4.22 (a)). To understand the interaction of hydrophobic sites with OH^-, RDFs of nitrogen of amide linkage and oxygen of carboxyl group present in the hydrophobic chain were calculated with the oxygen of OH^- along with the respective coordination numbers, as shown in Fig. 4.23 and Fig. 4.24, respectively. The RDFs for both clearly showed that there is no significant interaction of these sites with OH^- as no well-defined peak in the RDF was observed.

Fig. 4.25 summarizes the proposed transport mechanism of OH^- in all the PVA-KAMP systems. Around PVA, OH^- shows higher density compared to the simulation box, but lower avialbility of water in the H-bond range indicates that may not help much in charge transfer. But, the continuous channels formed by water molecules away from the H-bond range around OH groups, help in OH^- transfer by formation of $H_3O_2^-$ and $H_2O + OH^-$ back and forth through H-bonding. In the peptides, the mechanism of OH^- transfer around the ammonium cations is the same. However, the ammonium groups of the peptides have better interaction with OH^-, providing a more selective transfer site in comparison to the OH groups of the PVA chains. Guanidino group of the peptide is the main site for OH^- transport which has very good interaction with OH^-. Transfer of OH^- at the guanidine group appears to be taking place in its original form without formation of an intermediate like $H_3O_2^-$. If guanidino groups are present in close vicinity to each other, charge transfer will be faster as the time required for the formation of intermediate species will be saved. However, in the systems studied here, guanidino groups are not in close proximity to carry forward OH^- directly. Therefore, the transport of OH^- over the guanidine sites is mediated by water molecules through the formation of $H_3O_2^-$ and $H_2O + OH^-$ back and forth. Thus, we can -

TH-2592_156107017

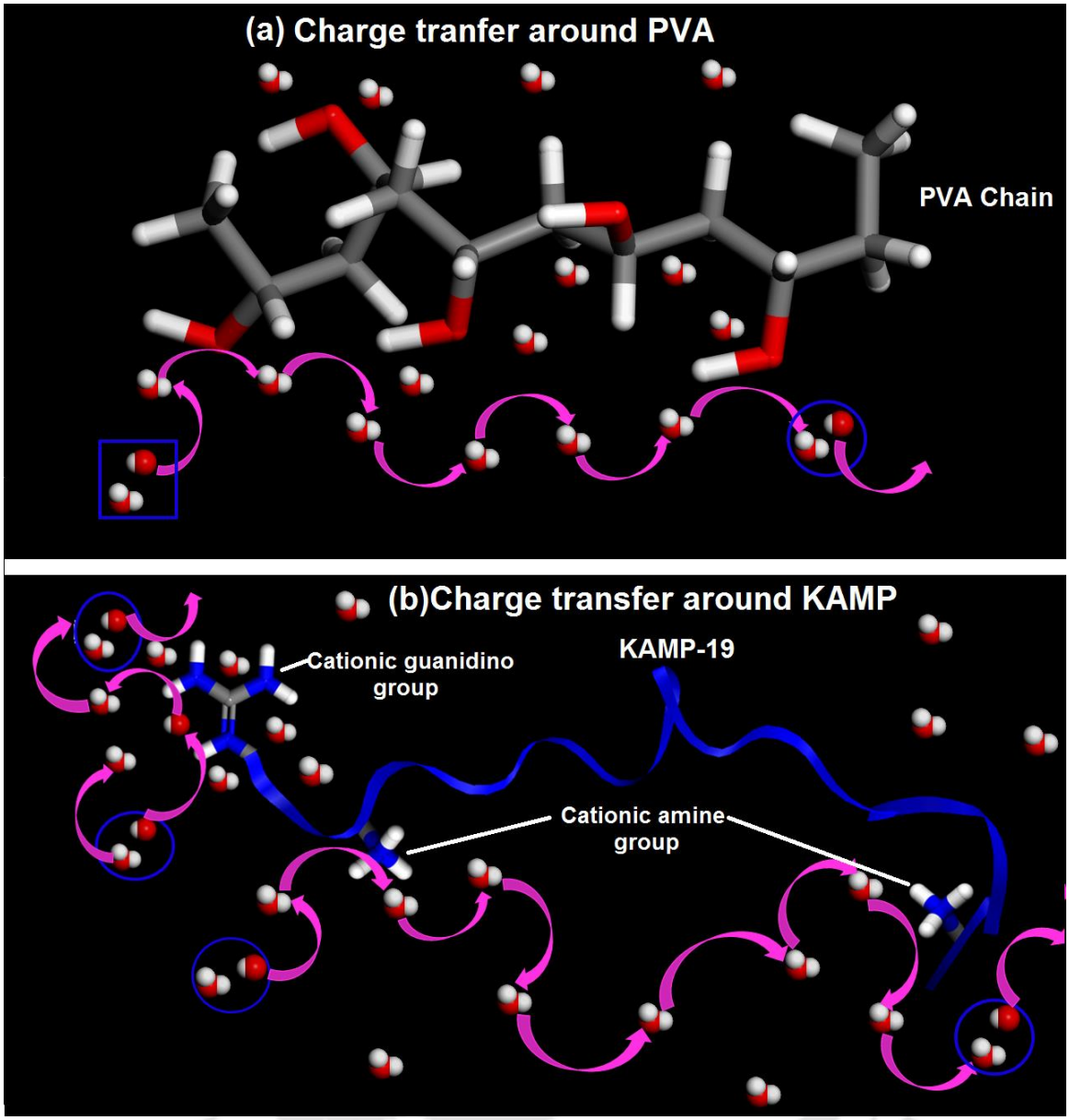

Fig. 4.25 Schematic representation of the proposed OH^- transfer mechanism in the PVA-KAMP system (a) around PVA chains, and (b) around cationic sites of KAMP.

conclude that in the systems studied in the present work, OH^- transfer takes place by hopping or Grotthuss mechanism. There are two types of hopping: in the water phase around PVA chains and around ammonium cation of the peptides, water to water hopping of OH^- takes place, whereas around the guanidino groups of the peptides, OH^- hops from water molecule to guanidino cation and then hops back to another water molecule.

TH-2592_156107017

4.4 Conclusion

A model hair keratein-derived antimicrobial peptide KAMP-19 was taken, having two amine and one guanidino group cations, with PVA matrix for MD simulation studies of OH^- transport. It was observed that inclusion of 2.6 wt.% KAMP-19 in PVA matrix almost doubled the ionic conductivity. Further increase in the peptide concentration to 5.1 wt.% resulted in decrease in the ionic conductivity, which can be attributed to the formation of a low water zone around peptide due to hydrophobic sections of peptide molecules. On further increase in the loading of KAMP to 7.4 wt.% and 9.6 wt.%, the ionic conductivity improved again. Increase in the number of charge transfer sites in close vicinity due to increase in peptide concentration was the main reason behind improvement in the ionic conductivity at higher KAMP loadings. The MSD data of methanol followed a trend similar to that of ionic conductivity for the different systems, indicating that methanol diffusion is governed by electro-osmotic drag. Electro-osmotic drag is helpful in reduction of methanol permeation from anode to cathode as it gets dragged back to anode side with charged ions. The RDF calculations showed the importance of water for charge transfer as the 2.6 wt.% KAMP system despite having fewest charge transfer sites, showed highest ionic conductivity due to the presence of more water molecules around the main charge transfer site of guanidino group cation. Investigation of the OH^- transport mechanism in the systems studied showed three different types of sites that facilitate the movement of OH^- ions. The transport of OH^- takes place by hopping of OH^- from one site to other by Grotthuss mechanism. Near the PVA chains, the water channels help in the movement of OH^- ions by the formation of $H_3O_2^-$ and H_2O back and forth, where OH^- hops from one water molecule to another forming $H_3O_2^-$ ions and converting back to water. Around the ammonium cationic sites on the peptides, the OH^- transport follows the same mechanism

TH-2592_156107017

as that of OH^- in the water channels by hopping from one water molecule near the amine group to another water molecule. The transport of OH^- around the guanidino group present in the peptides follows a slightly different mechanism. On guanidino group cations, OH^- hops in its original form, instead of forming an intermediate. The OH^- ion from the hydrogen-bonded water-OH^- pair (i.e., the $H_3O_2^-$ ion) jumps on the guanidino cation. This OH^- either can jump directly to the next guanidino cation, if there is one present in close proximity. Otherwise, the OH^- jumps back to another water molecule near the guanidino group to form $H_3O_2^-$ and moves by hopping over water molecules. The strong interaction of the guanidino group with OH^- and the transfer of OH^- without formation of intermediate results in faster movement. Having several number of water molecules around the guanidino group helps in reducing the strong electrostatic interaction between the OH^- ion and the guanidine group thus facilitating the movement of OH^-. In addition to the advantages shown here by simulation studies, guanidino group has the advantage of charge delocalization, which makes charge transfer even faster and makes the cation present on it stable in highly alkaline mediums. Thus, we can conclude that bio-waste like human hair-derived proteins or peptides having arginine amino acids in its structure, which has guanidino group, can be utilized for faster transport of OH^- ions in anion exchange membranes.

TH-2592_156107017

Chapter 5:

Stable CNC-Clay Supported Pt/Pd Catalyst for Methanol Oxidation in Alkaline Medium

Graphical Overview

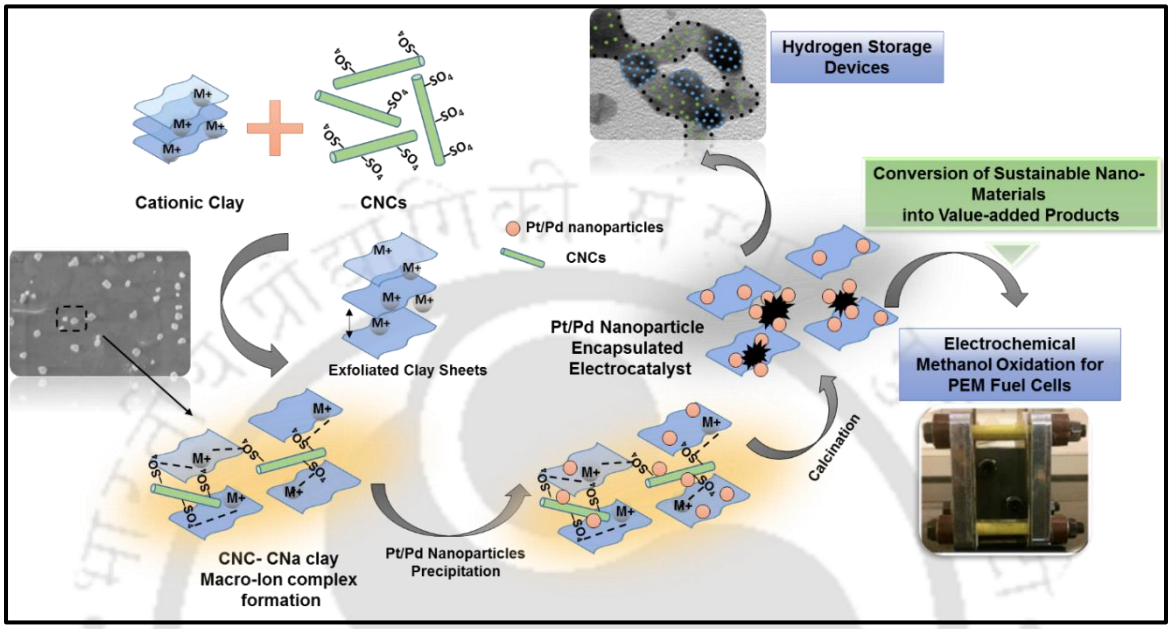

Nanogels are well known for their ability to encapsulate metal nanoparticles. However, only few reports exist on the application of such metal nanoparticle-loaded nanogels as electrocatalyst. Here, the formation of a self-assembled macroion nanogel-based complex using sustainable nanomaterials cellulose nanocrystals (CNCs) and Closite-Na$^+$ (CNa$^+$) montmorillonite (Mt) clay and its functional application as catalyst support for methanol oxidation in alkaline medium is reported. Physico-chemical and morphological investigations of the nanogel showed the formation of micro-nano particles, suggesting the presence of good ionic interactions. Prepared complex was utilized to host catalytically active platinum and palladium nanoparticles. On calcination, Pt/Pd-loaded nanogels showed good activity towards methanol oxidation in alkaline medium with high stability. Further, based on linear sweep voltammetry, it was proposed that for the current-

Publication:

- Gaur, S. S., Dhar, P., Sakurai, S., Kumar, A., & Katiyar, V. (2019). Cellulose nanocrystal/clay based macroion nanogel as support for stable platinum catalyst for electrochemical oxidation of methanol in alkaline medium. *Applied Clay Science*, 182, 105277.

system reported here, reaction intermediates formed in methanol oxidation during the cyclic voltammetry analysis get removed from the catalyst surface during the forward scan, instead of the reverse scan. The proposed hypothesis was further supported by impedance analysis and the potential range for removal of intermediates was determined, which was found to be 0.1 V – 0.2 V in alkaline medium during the forward scan. TEM images of the calcined Pt/Pd complexes have shown formation of carbon sheets covered Pt/Pd nanoparticles on the cationic CNa+ clay sheets, which makes them a material suitable for hydrogen adsorption. The Pt/Pd metal loaded calcined complexes have shown hydrogen adsorption values 3.52 mmol/g and 4.95 mmol/g, respectively at 0°C and 20 bar pressure. Thus, it has been successfully demonstrated that such catalytic nanoparticle-encapsulated complexes have good electrochemical activity and good hydrogen storage capability.

5.1 Introduction

Nanogels, as defined in the literature, are generally hydrogels formed in three dimensions, at the nanoscale size by crosslinking of swellable polymer network with capacity to hold high amount of water, without dissolving in it (Soni et al., 2016). The formation of nanogels is a complex phenomenon, which is generally governed by covalent linkages or multi-layered ionic bonding resulting in crosslinks or polyelectrolyte complexes. Nanogels are known to be good host material for encapsulating molecules and releasing them back in stimulated conditions. Hence, they have emerged as promising candidates for drug delivery systems. Capability of such nanogels to host metal nanoparticles is also quite well known. However, application of such nanogels with encapsulated metal nanoparticles for electrocatalysis has been seldom reported. Nanogels are suitable material for electrochemical reactions, as in presence of liquid fuel they can swell to increase the surface area available for electrochemical reaction. The other possible advantage of nanogel is that

TH-2592_156107017

they may hinder the electrochemical corrosion of electrocatalyst by keeping the metal nanocatalyst in the core. In the case of commercial carbon-supported metal catalyst, during electrochemical reaction, catalyst gets removed due to corrosion of carbon. Keeping in mind the possible advantages of nanogels, synthesis of Pt encapsulated nanogel-based electrocatalyst by using raw CNa^+ montmorillonite (Mt) and cellulose-derived cellulose nanocrystals has been carried out.

Clays have been attractive material for various applications, such as in oil and gas industries as drilling fluids, friction reducing agents, in fabrication of flame retardant polymeric nanocomposites, drug delivery vehicles, cosmetics, adsorbents, ion exchangers and catalytic applications (Joshi et al., 2009; Patel et al., 2006; Adams, 1987). Raw Mt have the general formula $(Na/Ca)_{0.33}(Al/Mg)_2(Si_4O_{10})(OH)_2 \cdot nH_2O$ and are composed of monovalent or divalent cations which are known to tune the ion exchange capacity of the clays (Anthony et al., 2011). Presence of these cations makes Mt suitable for applications where anionic adsorption and transfer is required. In electrochemical sensors and electrochemical reactions, few reports are available for the utilization of clays in material development (Ramasubbu et al., 2000; Mousty, 2004; Charradi et al., 2009; Montilla et al., 2002; Shi et al., 1989). The oxidation of alcohols on Pt/Pd catalyst follows the reaction pathway (1), (2), (3), (4), as reported in the literature (Ozoemena, 2016; Zadick et al., 2015; Qin et al., 2010).

$$Pt/Pd + RCH_2OH \rightarrow Pt/Pd - (RCH_2OH)_{ads} \quad (5.1)$$

$$Pt/Pd - (RCH_2OH)_{ads} + 3OH^- \rightarrow Pt/Pd - (RCO)_{ads} + 3H_2O + 3e^- \quad (5.2)$$

$$Pt/Pd - (RCO)_{ads} + Pt/Pd - OH_{ads} \rightarrow Pt/Pd - (RCOOH) + Pt/Pd[\text{Rate dt. step}] \quad (5.3)$$

$$RCOOH + OH^- \rightarrow RCOO^- + H_2O \quad (5.4)$$

TH-2592_156107017

The reaction between adsorbed alcohol and adsorbed hydroxyl ion on the catalyst surface is the rate-determining step. In such case, the presence of adsorbed hydroxyl groups is a critical parameter to control the reaction and that is where the cationic Mt can play a role to improve the adsorption of hydroxyl group. The reaction mechanism given by path (5.1), (5.2), (5.3) and (5.4) has also been considered in the current study, for the system reported here and analyzed by linear sweep voltammetry (LSV) to investigate the role of hydroxyl groups in oxidation reaction, as well as the role of reaction intermediates produced during methanol oxidation. Clays have the major drawback of low electron conductivity, which can be overcome by utilizing a carbon source along with the clay for catalyst support. Montilla et al. (2002) have reported Mt based carbon-ceramic composites loaded with platinum and its application for electro-oxidation of methanol in acidic medium. Similarly, Hu (1999) has carried out electrochemical reduction of oxygen on a carbon paste electrode modified with sodium Mt-methyl viologen, which has shown enhanced current density in an air-saturated phosphate buffer solution.

Clay as support for electrocatalyst, in alcohol electro-oxidation may affect the reaction kinetics positively. Commercially available carbon-supported platinum electrocatalyst has very low stability in alkaline medium (three times higher loss of electrochemical surface area compared to acidic medium) (Zadick et al., 2015). The instability may be caused by formation of oxides, which results in corrosion of carbon surface. Incorporation of metal oxides is one of the possible solutions, by which stability and activity of Pt-based electrocatalysts can be enhanced greatly (Shen and Xu, 2006; Xu et al., 2010). Metal oxides increase the amount of adsorbed hydroxyl ions, which helps improve the activity and stability of Pt-based catalysts. In this study an alternative to metal oxides has been utilized, which is natural CNa^+ Mt clay, having capability to enhance the adsorption of hydroxyl ion significantly. So, here CNa^+ Mt and cellulose nanocrystal has been used to prepare a

TH-2592_156107017

nanogel (here onwards CNa-CNC gel) as support for the Pt/Pd catalysts and calcined it to prepare clay-carbon supported electrocatalysts. The presence of sulfate groups in CNCs (produced by sulfuric acid hydrolysis) helps in ionic interaction with cationic Mt sheets and nanogel formation. The CNa^+ Mt and CNC macroion complex-based nanogel is prepared by exfoliation of clay sheets by ultra-sonication and binding of these clay sheets by CNCs through ionic interaction without using any crosslinking agent. Such macroionic nanogels have been utilized in applications such as drug delivery (Wang and Roman, 2011) and catalysis (Zeng et al., 2016). The performance of electrocatalyst for electrochemical oxidation of methanol in alkaline medium has been investigated. CNCs are primarily used as carbon source, which subsequently, provides conductive porous carbon material (upon calcination) to enhance the active surface area and conductivity of the catalyst. Several reports (Ravindranathan et al., 1990; Dubey et al., 2015; Shetti et al., 2018) exist where Mt has been used to support the metal nanoparticles. In the present work, the CNa^+ Mt along with CNCs in the CNa-CNC gel has been used as Pt/Pd support. In such case, corrosion of carbon is not expected to affect the performance of electrocatalyst significantly during the electrochemical reaction.

5.2 Materials and Methods

5.2.1 Materials

Mt cloisite Na^+ clay was procured from Southern Clay Products, Inc. Sodium hydroxide (NaOH) (>97 wt.%), sodium hypochlorite (4 wt.%), hydrogen peroxide (30 wt.%) and sulfuric acid (>99 wt.%) (all analytical grade) required for extraction of cellulose and subsequently for acid hydrolysis were received from SISCO Research Laboratories (SRL Chemicals, India). Platinum chloride ($PtCl_2$), palladium chloride ($PdCl_2$), methanol (HPLC

TH-2592_156107017

grade) and hydrochloric acid (35% A.R.) were purchased from HiMedia Laboratories Pvt. Ltd., India. Sodium borohydride ($NaBH_4$) was purchased from SRL Chemicals, India.

5.2.2 Formation of Macroion-nanogel Complex between the CNCs and CNa^+ clay

Fabrication process of CNCs, utilized for nanogel formation has already been discussed in chapter-2. Three different weight fractions 1:1, 1:2 and 2:1 of CNC-CNa^+ clay were taken in three different plastic sample containers with Millipore water and were kept under sonication in a probe ultrasonic homogenizer at 50% amplitude (BioLogic Inc., Model-3000MP, 0-300W, 230V, 50Hz, 4A) for 1 hour. After sonication, the CNC-CNa^+ 2:1 weight ratio, formed a clear, nice thick gel, which after drying formed CNa-CNC gel films. The other two combinations also formed gel, which were less viscous than 2:1 ratio CNa-CNC. Due to layer charge contribution by CNa^+, CNCs binds with the exfoliated clay sheets. Higher CNC content results in better binding of clay sheets and thicker gel. Therefore, 2:1 weight ratio was taken as optimized gel combination and the dried gel films were used for Pt loading and further investigations.

5.2.3 Fabrication of the Platinum/ Palladium Nanoparticles Encapsulated Macrion-nanogels

Dried CNa-CNC gel film was taken and dispersed in Millipore water by sonication for 5 min in probe ultrasonic homogenizer. $PtCl_2$/$PdCl_2$ was dissolved in 10ml Millipore water by adding 100 µl HCl in it and stirring at 80°C. $PtCl_2$/$PdCl_2$ solution was mixed with dispersed CNa-CNC solution by stirring at 80°C and 500 rpm for 30 min, resulting in a solution with $PtCl_2$/$PdCl_2$ to CNa-CNC mass ratio of 2:5. Under the same conditions, excess amount of $NaBH_4$ solution was added drop by drop to the solution for reduction of

TH-2592_156107017

$PtCl_2/PdCl_2$ to Pt/Pd and the stirring was continued for 6 h. After 6 h the final solution was washed three times using methanol to remove the excessive amount of $NaBH_4$ and unreduced salts by centrifugation at 5000 rpm. The precipitate was first dried in hot air oven at 60°C and after that it was calcined in muffle furnace at 400°C for 3 h. The prepared calcined Pt/Pd loaded material, abbreviated as Pt-CNa-CNC/ Pd-CNa-CNC henceforth, was used as catalyst for electrochemical oxidation of methanol in alkaline medium and H_2 adsorption studies were also carried out.

5.3 Characterization

5.3.1 FTIR Spectroscopy, Crystal Structure and Surface Morphology

It is well understood that due to the presence of sulfonyl group in CNCs (introduced during sulfuric acid hydrolysis) and cations in CNa^+ clay, both of them have ion exchange capability and will surely have ionic interaction between them. Further to verify the interaction, Fourier transform infrared (FTIR) spectrophotometer (PerkinElmer Frontier FTIR model) was used. The FTIR analysis was carried out using dispersed sample in KBr pellet (keeping sample to KBr ratio ≈1:100) and the amount of each sample was kept equal so that intensity of peaks can be compared. The spectrum was monitored in the wavenumber range 4000–400 cm^{-1}. Change in the crystal structure of CNa^+ clay and CNCs in CNa-CNC gel were studied by using X-ray diffraction (XRD) (a Bruker D8 advance system with Cu-K_α radiation as X-ray source.) technique for 2θ angles in the range of 1–35°. The crystal structures of calcined Pt-CNa-CNC/ Pd-CNa-CNC were investigated by XRD (a Rigaku TTRAX, Seifert XRD 3003 T/T model) in the 2θ range 5-80° with Cu-K_α radiation (λ= 0.1541 nm) as X-ray source. Surface morphology of prepared macroion-nanogel was analyzed by field emission scanning electron microscope (FESEM) (a SUPRA

TH-2592_156107017

Ultra high resolution FESEM system from Carl Zeiss, India). Morphology of Pt-CNa-CNC/ Pd-CNa-CNC was analyzed by FESEM as well as by transmission electron microscopy (TEM) (a JEOL JEM 2100 TEM system).

5.3.2 Surface Area, XPS and Compositional Analysis of Pt/Pd in Calcined Electrocatalysts

Surface area analysis was carried out on a Quantachrome surface area analyzer (Autosorb-IQ MP) by the Brunauer–Emmett–Teller (BET) method, which works on the basis of nitrogen adsorption-desorption technique. Before analysis degassing of the samples was done at 200°C for 3 h and the analysis was done at 77 K. XPS analysis was carried out on JEOL-JPS-9010MC/SP system by using MgK_{α} X-ray source for confirmation of CNC's conversion to graphitic carbon. Carbon C1s reflection at 285.0 eV was taken as reference and all the spectra were corrected on the basis of this reference. The compositional analysis of the Pt/Pd nanoparticles in the calcined Pt-CNa-CNC and Pd-CNa-CNC was done through elemental mapping. Hydrogen adsorption studies of Pt-CNa-CNC/ Pd-CNa-CNC were carried out on high pressure gas adsorption analyzer (iSorb-HP model from Quantachrome) in the pressure range 0-20 bar at 0°C. Before the analysis, samples were degassed at 150°C for 30 min under the inert gas flow.

5.3.3 Electrochemical Performance, Methanol Oxidation Studies, Linear Sweep Voltammetry (LSV) and Electrochemical Impedance Spectroscopy (EIS) Analysis

Electrochemical studies were carried out on Autolab PGSTAT204 model from Metrohm India Ltd. The samples were prepared by ink formation of Pt-CNa-CNC/ Pd-CNa-CNC electrocatalysts and coating the ink on 1 cm^2 area of carbon paper. Briefly, 10 mg Pt-CNa-

TH-2592_156107017

CNC/ Pd-CNa-CNC, 25 µl of 5 wt.% Nafion perfluorinarted resin solution (Sigma–Aldrich, USA), 100-200 µl of water and 1ml of isopropyl alcohol were taken in small glass beaker and sonicated until a fine ink was achieved. The prepared ink was coated on Toray carbon paper (purchased from Sainergy Fuel Cell India Private Limited) by painting brush and the carbon paper was then dried at 100°C for 2 h. 0.5 M KOH solution was used as electrolyte for the electrochemical investigations. For methanol oxidation, 0.5M methanol was taken along with the 0.5M KOH solution in three-electrode electrochemical cell. The electrochemical cell was purged with nitrogen gas for 20-30 minutes before all the electrochemical analyses. All the electrochemical analyses were done against Ag/AgCl reference electrode, Pt counter electrode and Pt-CNa-CNC/ Pd-CNa-CNC coated carbon paper as working electrode. To understand the formation of intermediates and methanol oxidation LSV was carried out for Pt-CNa-CNC catalyst in the voltage range 0.3 V to −1.0 V at a scan rate of 100 mV/s using the fresh system of 0.5 M KOH and 0.5 M MeOH solution. Electrochemical active surface area and specific activity of each catalyst were calculated by IUPAC oxide reduction method (Trasatti & Petrii, 1991). EIS analysis was carried out in the 0.5 M KOH and 0.5 M methanol solution at different applied potential in the range −1.0 V to 0.3 V for the fresh Pt-CNa-CNC catalyst coated on carbon paper.

5.4 Results and Discussion

5.4.1 Physico-Chemical Properties of the Fabricated Macro-Ion Nanogels

The characteristic bands of CNCs and CNa^+ clay can be observed in the IR spectra, shown in Fig. 5.1 C–H, C=O and C–C stretching bands around 2901, 1635 and 1433 cm^{-1} respectively and band due to the glycosidic ether bond at 1114 cm^{-1} are the characteristics bands of CNCs. Hydroxyl stretching and bending bands in the range 3200–3700 cm^{-1} and

TH-2592_156107017

1600–1700 cm^{-1}, and Si–O, Al–O and Mg–O bands around 1043, 523, 470 cm^{-1} respectively can be observed in the IR spectra of CNa^{+} clay. These characteristic bands of CNCs and CNa^{+} clay are present in the IR spectra of CNa–CNC gel, which signifies that both clay and CNCs are intact with each other. The increase in the intensity of the Si–O stretching and Al–O, Mg–O bands along with the broadness of Al–O and Mg–O bands clearly indicate good interaction between CNCs and CNa^{+} clay.

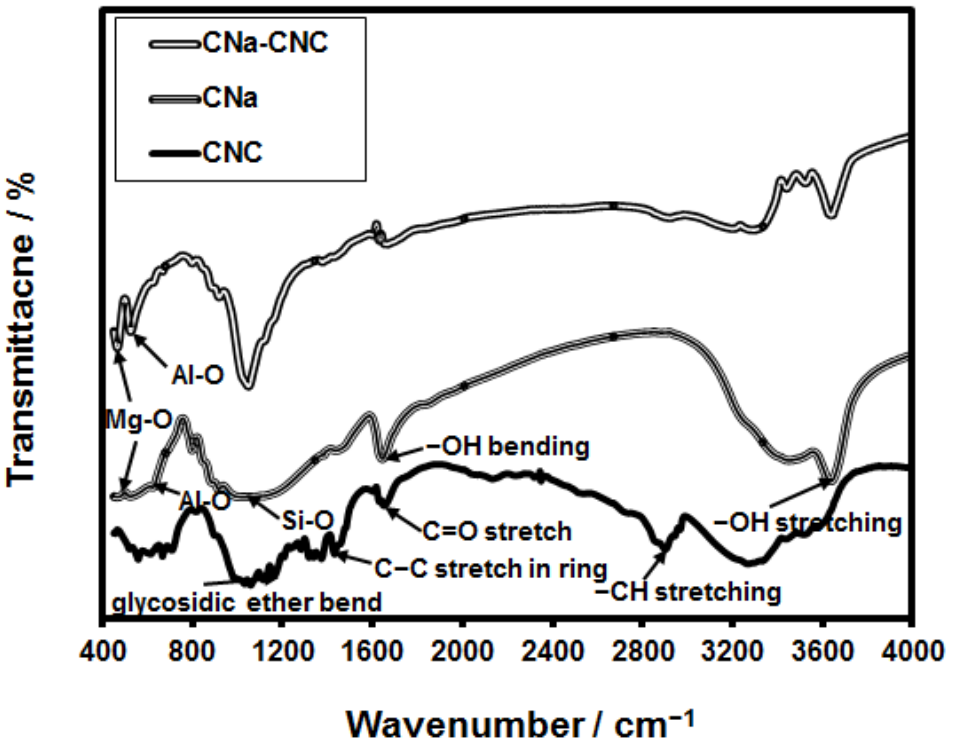

Fig. 5.1 FTIR spectra of CNC, CNa^{+} clay and gel formed by CNa-CNC.

TH-2592_156107017

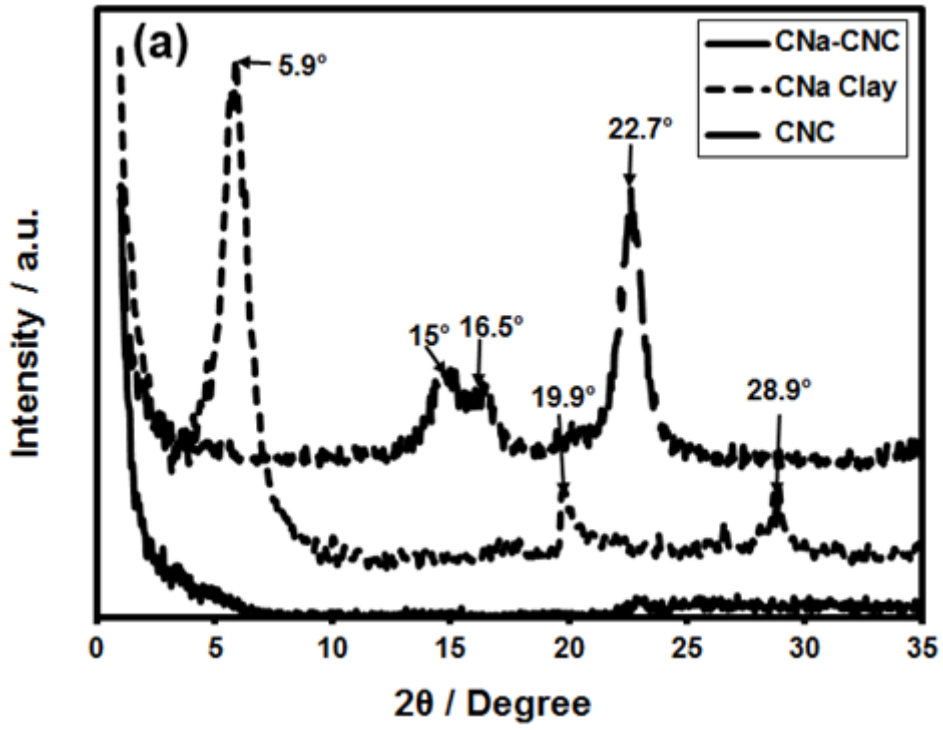

Fig. 5.2 XRD spectra of CNC, CNa^+ clay and gel formed by CNa-CNC.

Change in the crystal structure of CNa^+ clay due to the addition of CNC in CNa-CNC gel can be clearly observed from Fig. 5.2. CNa^+ clay crystal reflections at 5.9° and 19.9° and CNC reflections at 15°, 16.5° and 22.7° have disappeared in the CNa-CNC gel. This indicates the exfoliation of CNa^+ clay sheets and binding of these sheets by randomly oriented CNCs. Fig. 5.3 (a) & (b) are the XRD micrographs of calcined Pt-CNa-CNC and Pd-CNa-CNC, respectively, which show the polycrystalline nature of both Pt and Pd in respective Pt/Pd loaded materials. In Fig. 5.3 (b), along with the polycrystalline peaks of Pd, polycrystalline peaks of PdO also can be clearly observed. It has been reported that, such polycrystalline PdO containing catalysts show high catalytic activity towards electrochemical oxidation of methanol (Lin et al., 2014). PdO is known to contribute towards dissociative hydrogen adsorption to improve the hydrogen adsorption (Martin et al., 2013).

TH-2592_156107017

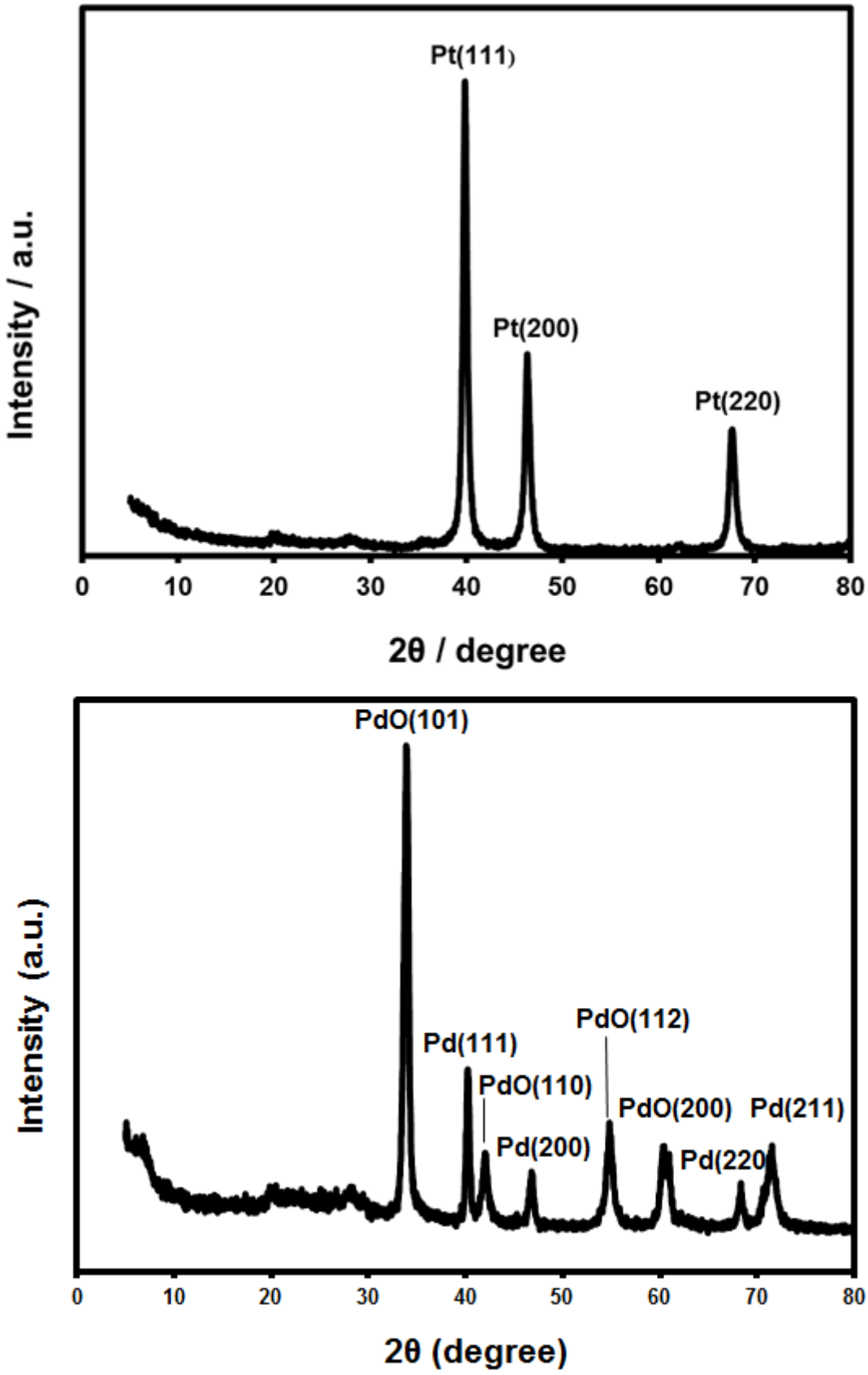

Fig. 5.3 XRD spectra of (a) calcined Pt-CNa-CNC and (b) calcined Pd-CNa-CNC.

TH-2592_156107017

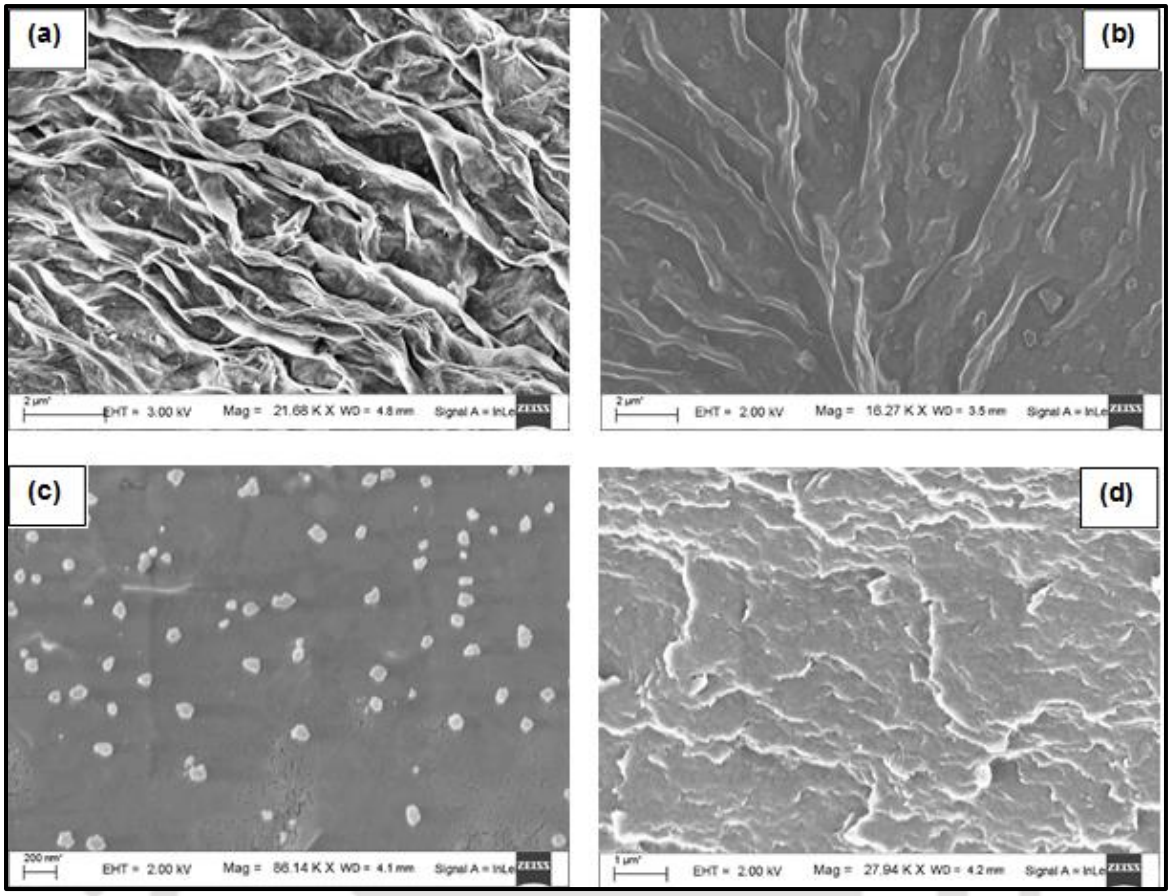

Fig. 5.4 FESEM images of (a) CNa^+ clay, (b) sonicated CNa^+ clay film surface, (c) CNa-CNC gel film surface and (d) CNa-CNC gel film crosssection.

5.4.2 Surface Morphology

Interaction between CNa^+ clay and CNCs can be further confirmed by FESEM images, as shown in Fig. 5.4. Fig. 5.4 (a) shows the FESEM image of CNa^+ clay, which has layered structure. After sonication the CNa^+ clay film surface has shrinking layered morphology with micro-nano size particles on it, which have formed due to rupture of clay sheets in to small particles by ultra-sonication (Fig. 5.4 (b)). But sonication of CNa^+ with CNCs is resulted in a nice gel, which after drying forms smooth surface (Fig. 5.4 (c) & (d)), due to ionic interaction between clay and CNC. Even after the thermochemical reaction of Pt/Pd loading on the CNa-CNC gel film, this interaction remains between CNC and clay, which

TH-2592_156107017

can be clearly seen from highlighted part in Fig. 5.5 (a) & (b), as exfoliated randomly distributed clay sheets are still bound by CNCs. The formation of nano particles due to rupturing of clay sheets, is clearly visible in the case of CNa-CNC gel film (Fig. 5.4 (c)).

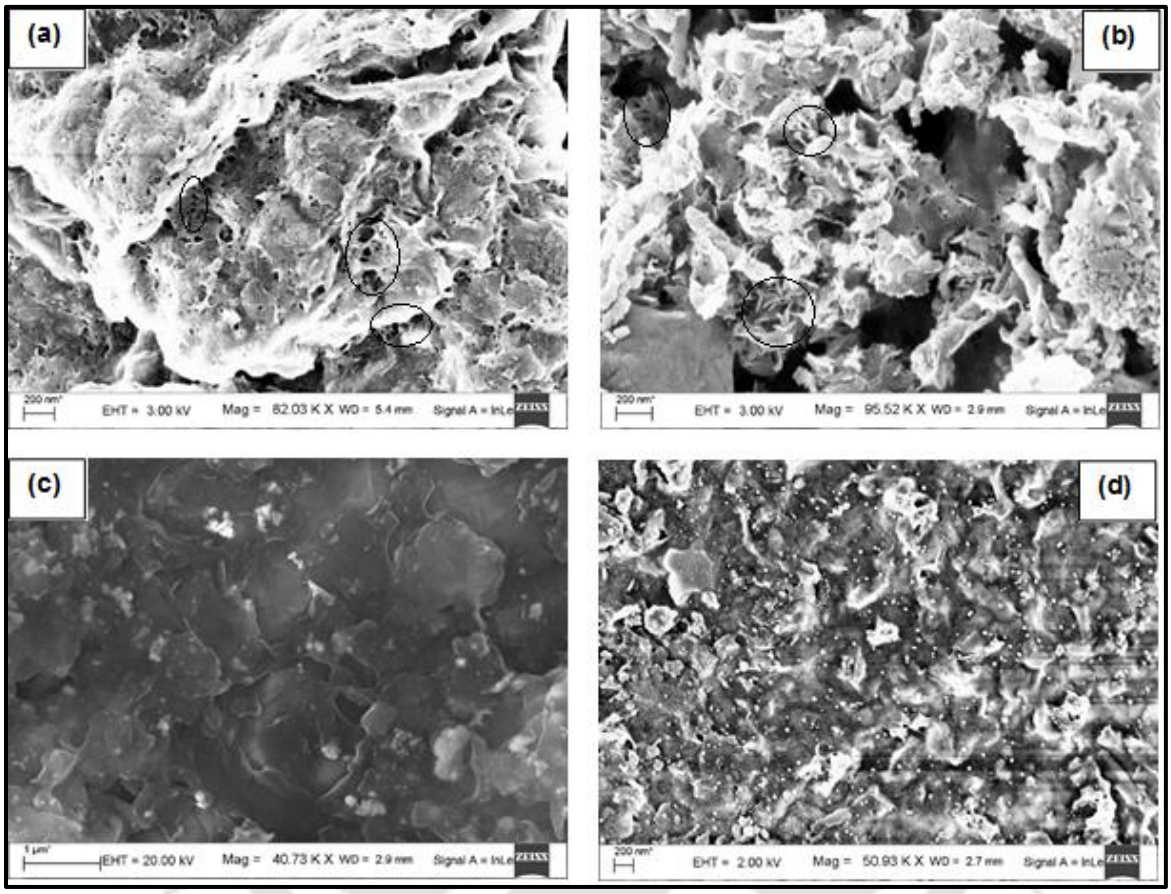

Fig. 5.5 FESEM images of (a) un-calcined Pt-CNa-CNC, (b) un-calcined Pd-CNa-CNC, (c) calcined Pt-CNa-CNC (d) calcined Pd-CNa-CNC catalyst.

The morphology of calcined Pt-CNa-CNC and Pd-CNa-CNC catalysts and distribution of Pt and Pd nanoparticles in it, can be visualize from FESEM images shown in Fig. 5.5 (c) & (d) and from TEM images shown in Fig. 5.6 (a) & (b). Fig. 5.5 (c) & (d) show the clear distribution of nanoparticles in catalyst material, along with some bunch of nanoparticles forming agglomerates. Further inspection by TEM micrographs in (Fig. 5.6 (a) & (b)) show that, these nanoparticles are supported on clay as well as on carbon layers, which have

TH-2592_156107017

covered the metal nanoparticles. The sheets shown in TEM micrographs are of clay, over which the dark particles are of carbon and within the dark carbon particles the black particles are of Pt/Pd. The particle diameter of the dispersed Pt and Pd nanoparticles is in the range of 5.5–7 nm (measured from TEM micrograph by using ImageJ software). At the same time there are bunch of agglomerates of Pt/Pd nanoparticles measuring in the range ≈50–200 nm.

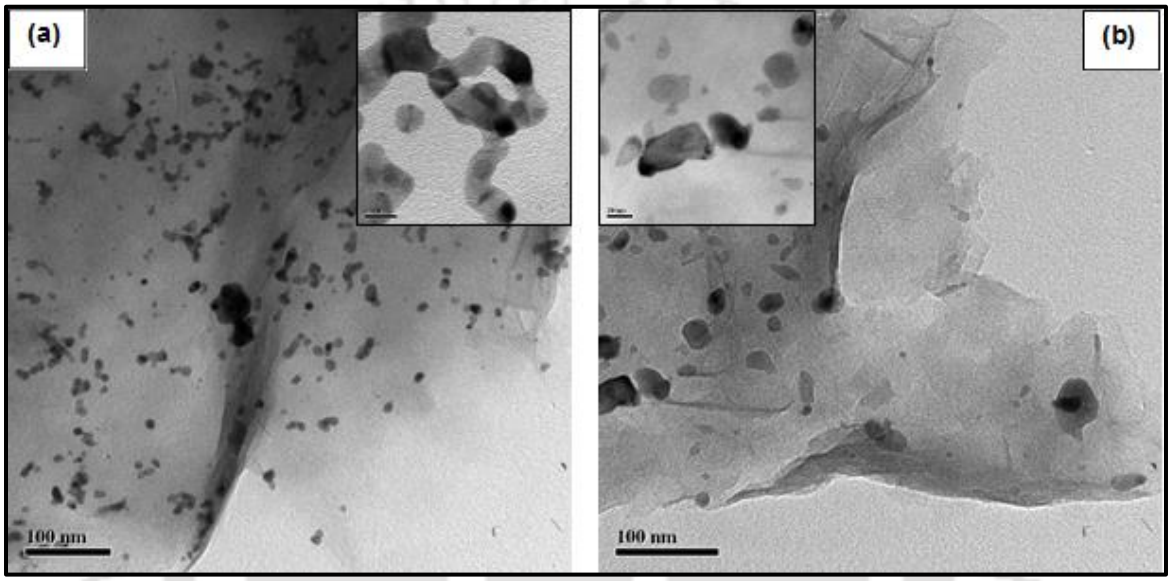

Fig. 5.6 TEM images of calcined (a) Pt-CNa-CNC and (b) Pd-CNa-CNC (in inset magnified images of carbon covered Pt/Pd nanoparticles).

5.4.3 XPS and Compositional Analysis of Pt/Pd in the Calcined Electrocatalysts

Mt clays have low electron conduction due to non-uniform distribution of charges, which necessitates a complimentary support material for Pt/Pd catalysts to provide good electron conduction in electrochemical reaction system. As mentioned in the introduction section, CNCs used in the prepared support gel system were calcined to form carbon to provide electron conductivity. Formation and presence of carbon in Pt-CNa-CNC and Pd-CNa-

TH-2592_156107017

CNC was confirmed by XPS analysis. The result of calcination of Pt/Pd-loaded nanogel can be clearly seen from the XPS spectra of Pt-CNa-CNC and Pd-CNa-CNC (Fig. 5.7 (a) & (b)), where the major reflection observed in both cases is for carbon at ≈285.0 eV, which makes the catalyst support electron conductive. A small C-O reflection has been observed in both the spectra, which is due to oxidation of carbon during calcination in normal atmosphere. Analysis of Pt/Pd present in Pt-CNa-CNC and Pd-CNa-CNC by XPS did not show any reflection, which indicates that Pt/Pd nanoparticles are primarily distributed between the clay sheets and in the porous channels of the carbon, formed due to calcination of CNCs (as shown in TEM micrograph in Fig. 5.6 (a) & (b)). Therefore, the compositional quantification was performed by elemental. The Pt/Pd loading in respective electrocatalysts was found in the range of ≈14–16 wt.%.

5.4.4 Electrochemical Performance and Methanol Oxidation Studies

The Pt and Pd loading on carbon paper for catalyst test of Pt-CNa-CNC and Pd-CNa-CNC were ≈1.14 mg/cm^2 and ≈1.05 mg/cm^2, respectively. Fig. 5.8 (a) & (b) show the cyclic voltammograms of calcined Pt-CNa-CNC and Pd-CNa-CNC catalyst respectively in alkaline medium (0.5M KOH solution), which represents the polycrystalline nature of Pt/Pd. As described in literature (Will, 1965; Yi et al., 2011), the peak shown in lower anodic region, in forward scan corresponds to the adsorbed –OH on Pt/Pd, while the peak at higher anodic potential corresponds to the Pt/Pd oxide formation. The large peak in cathodic scan represents the conversion of Pt/Pd oxides back to Pt/Pd. This oxide reduction peak was used for calculation of electrochemical active surface area and as reported in literature the charge for per unit surface area of Pt and Pd single crystal were taken to be 420 μC/cm2 and 405 μC/cm2, respectively (Trasatti & Petrii, 1991; Gajjala & Palathedath, 2018). The active surface area was found to be ≈67 cm^2/mg and ≈50 m^2/mg -

TH-2592_156107017

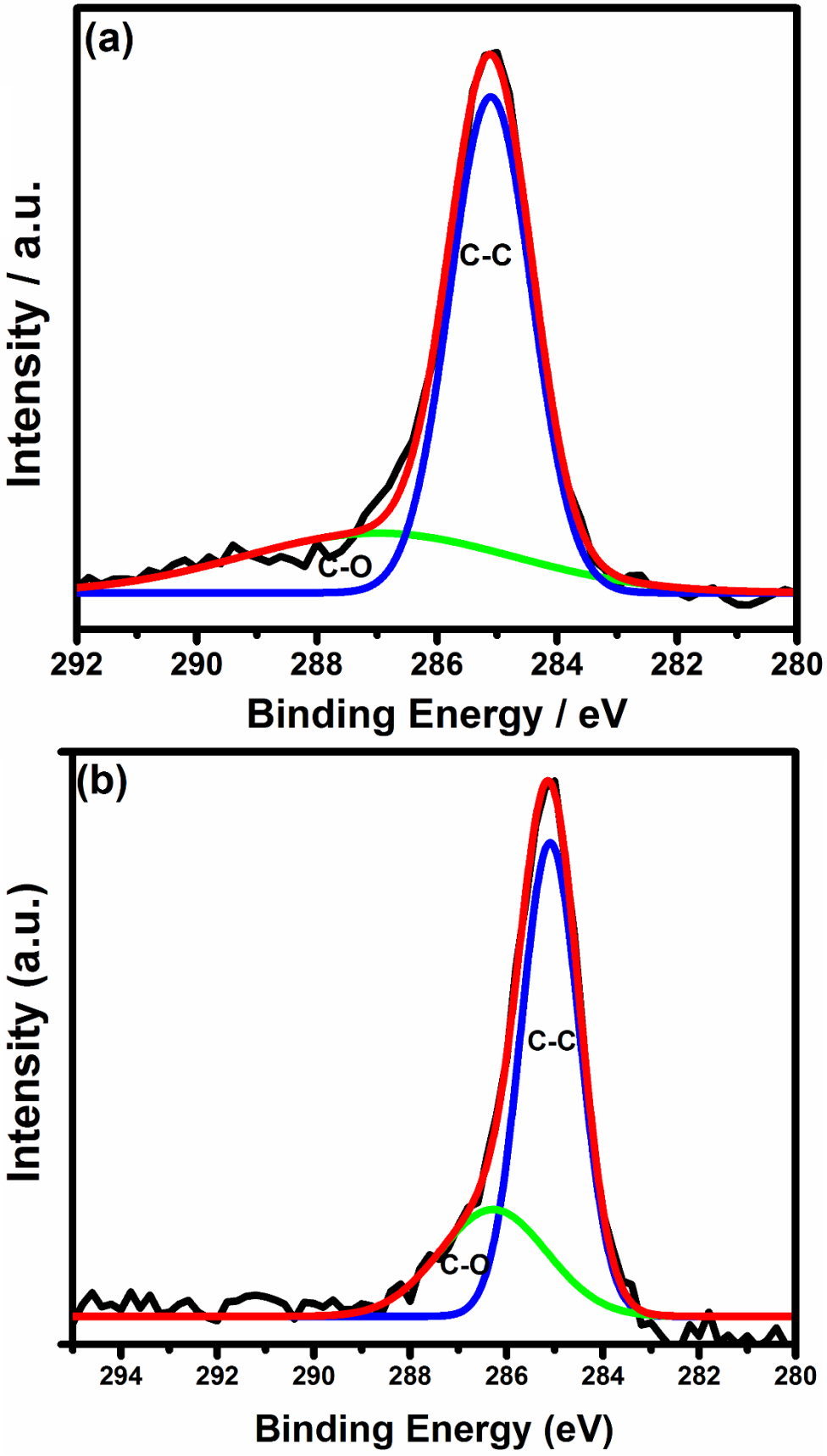

Fig. 5.7 XPS carbon 1s spectra of (a) Pt-CNa-CNC (b) Pd-CNa-CNC.

TH-2592_156107017

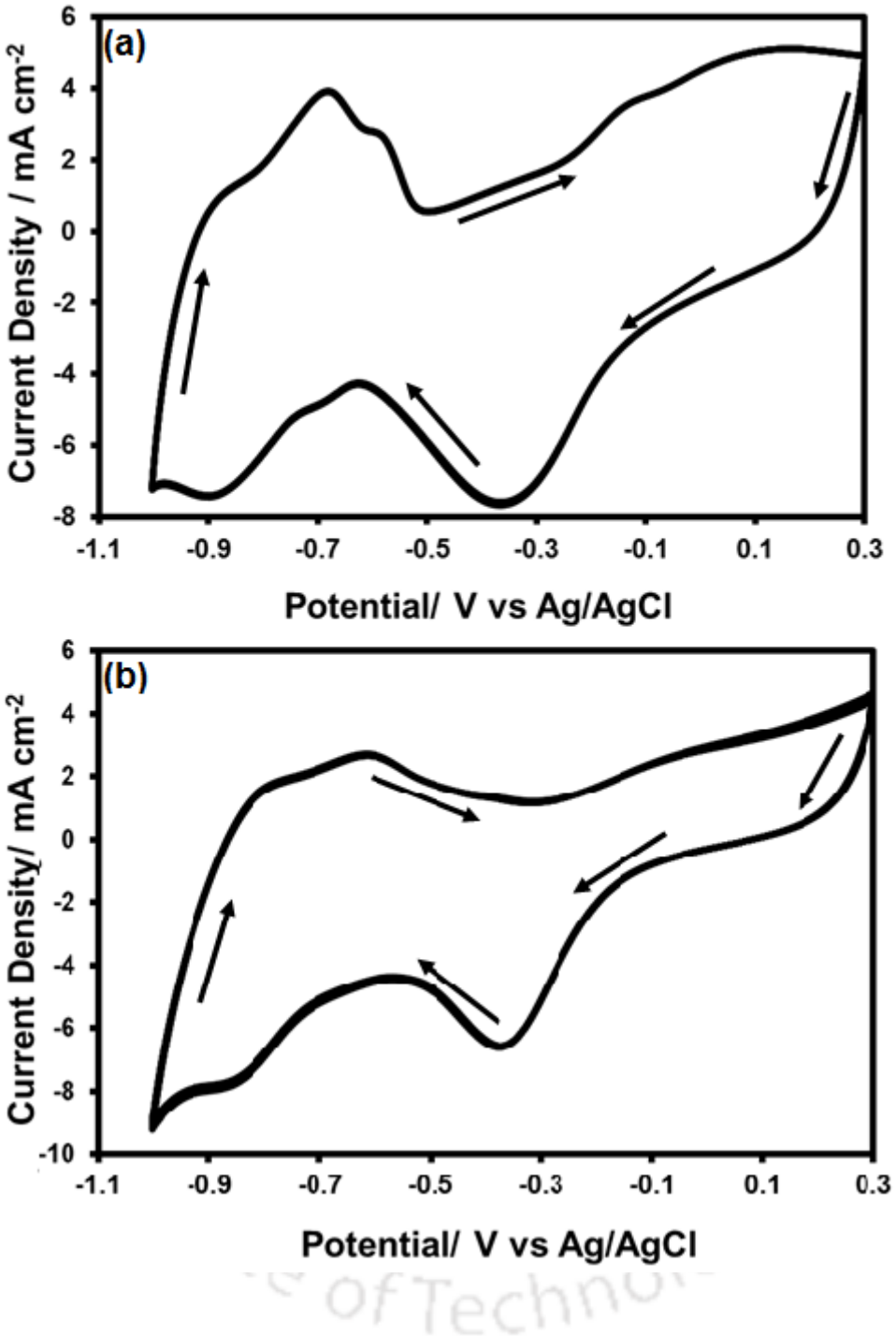

Fig. 5.8 Cyclic voltammograms of calcined (a) Pt-CNa-CNC (b) Pd-CNa-CNC in 0.5M KOH solution at 100mV/s scan rate.

for Pt-CNa-CNC and Pd-CNa-CNC catalyst respectively. The electrochemical surface area is lower than the reported value for Pt-C catalyst (135 cm^2/mg) by CO stripping method (Watt-Smith et al., 2008). Having Pt/Pd catalyst nanoparticles in interspaces of the nanogel-

TH-2592_156107017

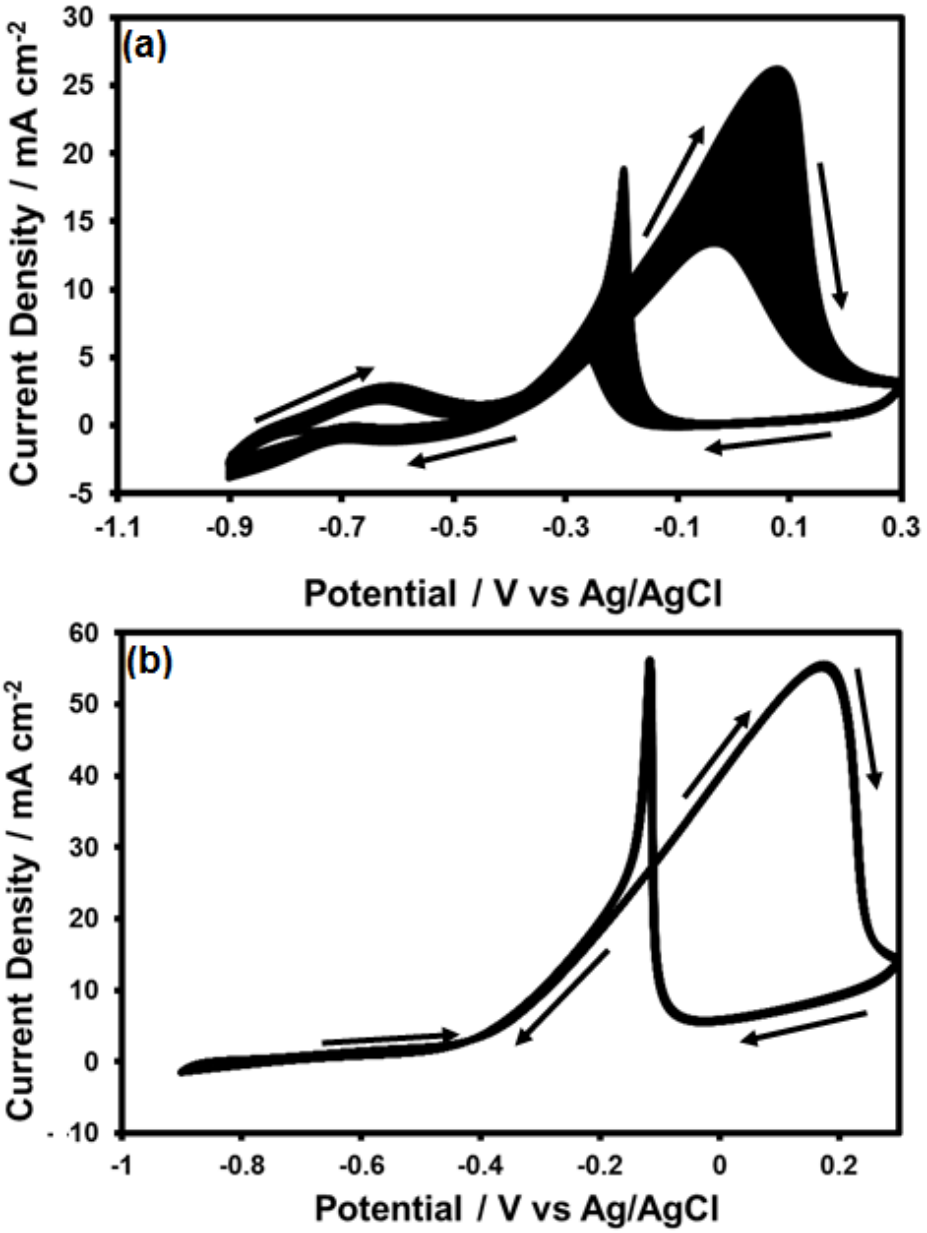

Fig. 5.9 Cyclic voltammogram of the prepared calcined Pt-CNa-CNC catalyst in 0.5M KOH and 0.5M methanol at 100mV/s scan rate (a) for initial 50 cycles (b) after 1000 cycles.

is may be the reason for lower electrochemical surface area in the case of both the catalysts. Fig. 5.9 (a) & (b) show the electrocatalytic activity of prepared calcined Pt-CNa-CNC catalyst towards oxidation of methanol in alkaline medium. As reported in literature (Qin et al., 2010; Yi et al., 2011; Tripkovic et al., 1996; Pandey and Lakshminarayanan, 2009) for methanol oxidation in alkaline medium on Pt electrocatlyst, the large and clear -

TH-2592_156107017

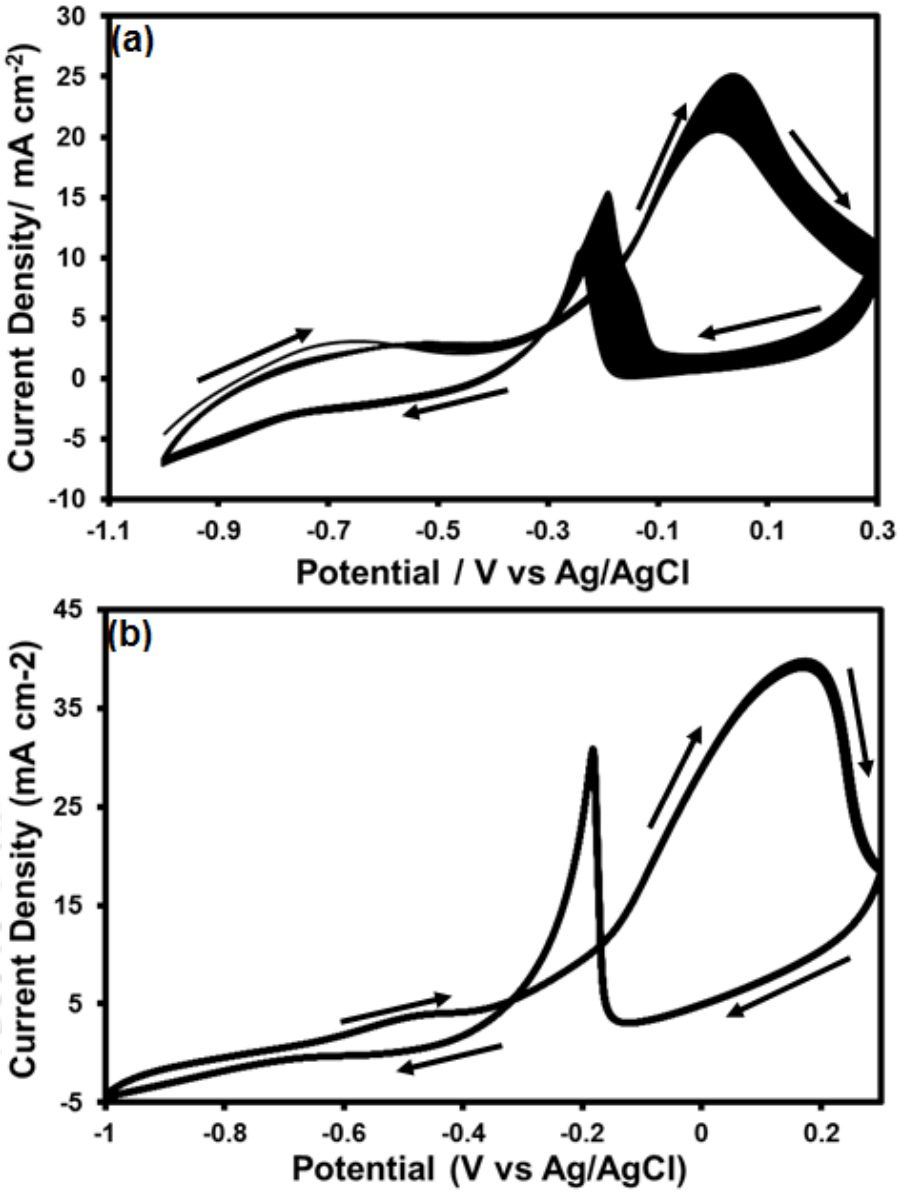

Fig. 5.10 CV of the prepared calcined Pt-CNa-CNC catalyst in 0.5M KOH and 0.5M methanol at 100mV/s scan rate (a) for initial 50 cycles (b) after 1000 cycles.

oxidation peak in-cyclic voltammograms in anodic scan occurs due to methanol oxidation. In the reverse scan, the sharp oxidation peak is assumed to occur due to the removal of carbonaceous species, which form during the forward reaction. However, as mentioned by Zhang et al. (2011), there is no evidence available for the peak observed in the reverse scan is due to removal of these species. As shown in Fig. 5.10 (a) & (b), calcined Pd-CNa-CNC electrocatalyst follows the exactly same trend as of the calcined Pt-CNa-CNc electrocatalyst. The most notable observation made in both of the calcined Pt-CNa-CNC -

TH-2592_156107017

Table: 5.1 Stability of the various electrocatalysts in alkaline medium reported in literature.

Catalyst	% Reduction in current density	Reference
Pd_1Nb_1/C	≈45% (after 1000 CV cycles)	Souza et al., 2018
Pd/Au/C 90:10	≈70% (after chronoamperometry test for 1200 s at a constant potential of −0.2 V)	Zhao et al., 2011
Ni–Al LDHf/G	≈60% (after chronoamperometry test for 1000 s at a constant potential of at 0.55 V)	Wang et al., 2011
Pd	≈90% (after chronoamperometry test for 1800 s at a constant potential of at −0.4 V)	Ye et al., 2007
Pd/C	≈27% (after 3000CV cycles)	Xu et al., 2010
Pt/C	57% (in ECSA) After accelerated test 150 CV cycles at 100 mV/sec in alkaline sol	Zadick et al., 2015
Pd/C	35% (in ECSA) After accelerated test and 150 CV cycles at 100 mV/sec in alkaline sol	Zadick et al., 2015
Pd_3Au/C	≈26% (after 3000CV cycles)	Xu et al., 2010
Pt-CNa-CNC	≈13% (after 1000 CV cycles)	This study
Pd-CNa-CNC	≈5% (after 4000 CV cycles)	This study

and Pd-CNa-CNC electrocatalyst reactions, is their high stability in alkaline medium. The calcined Pt-CNa-CNC shows peak current density for methanol oxidation ≈26 mA/cm^2 for running 50 cycles, which reached to maximum current density of ≈55 mA/cm^2 and remained almost constant even up to 1000 cycles. Similarly, for Pd-CNa-CNC for running 50 cycles, it showed maximum peak current density of ≈25 mA/cm^2, which increased to ≈40 mA/cm^2 and remain stable even after 1000 cycles. Pt based electrocatalyst showed better performance for methanol oxidation than Pd based electrocatalyst. The specific

TH-2592_156107017

activity of Pt-CNa-CNC catalyst was found to be around 0.82 mA/cm^2 and for the Pd-CNa-CNC catalyst it was around 0.80 mA/cm^2.

Increase in the current density for both the catalysts from the 50th cycle to up to certain number of CV cycles can be explained by the swelling behavior of the support material in the presence of methanol fuel solution and subsequently reaching to catalyst present in interfaces of clay sheets present in the gel. Similar phenomena has been observed for Pt-C catalyst, as it takes time for the methanol fuel to reach to the pores of catalyst support and get reacted faster. The swelling of calcined CNC-Clay gel-supported Pt catalyst will result in continuous increase of surface area for electrochemical reaction as well as provide more sites for –OH adsorption, which will subsequently result in continuous increase in current density until the support material reaches maximum swelling. Table 5.1 shows the stability results carried out by long CV runs. The Pd based electrocatalyst showed much better stability compare to the Pt based electrocatalyst as well as several other catalysts, including commercial Pt-C and Pd-C catalysts. The stable nature of the catalysts can be attributed to the presence of clay material, which may help in the adsorption of –OH and participate in electrochemical reaction, and subsequently hinder the corrosion of carbon support during the reaction by carbonate formation (Lafforgue et al., 2018).

5.4.5 LSV Investigation for the Role of –OH and Reaction Intermediates in Methanol Oxidation

The critical role of adsorbed –OH in the electrochemical oxidation of alcohols in alkaline medium is well stablished. Tripkovic et al. (1996) have shown that the catalytic activity depends on the alkaline solution. Comparing NaOH, $NaHCO_3$ and Na_2CO_3, they found the highest activity in NaOH solution, which signifies the importance of the presence of –OH. As mentioned in the previous section, no evidence is observed for the strong adsorption of

TH-2592_156107017

the reaction intermediates formed during the forward scan, on the catalyst surface. So the intermediates formed during the forward reaction may get dissolved in the bulk solution (if mass transfer is not the limiting factor) and the peak observed during the reverse scan may not be partially or completely due to the removal of the intermediates from the catalyst surface. To further understand the role of the presence of –OH and to check the theory of the presence of anodic peak in reverse scan due to removal of intermediates, LSV test has been carried out in 0.5M KOH and 0.5M methanol solution by choosing the range of reverse scan of methanol oxidation cycle (0.3 V – -1 V).

The LSV scans were done with the fresh solution, which means that other than methanol, no other species is present to undergo electrochemical oxidation reaction. In Fig. 5.11, from the 1st LSV scan, no visible peak corresponding to the reduction of Pt oxides can be observed. At the lower potential as –OH gets adsorbed, Pt oxides forms, and from the 2nd LSV scan to 7th LSV scan, the peaks for the reduction of Pt oxides can be clearly seen. This reduction peak initiates around the same potential where the initiation of Pt oxides reduction in KOH solution happens. From the 8th LSV scan, small anodic peak is observed. As no intermediate species is present, this peak must be due to methanol oxidation. The anodic peak appeared in the 8th scan, which indicates that the adsorption of methanol is slow on the catalyst surface; however, when it gets adsorbed it starts reacting with the – OH. As more amount of methanol adsorbs, its oxidation peak becomes more prominent and Pt oxides reduction peak disappears (9th and 10th LSV scan), consuming the oxygen species (–OH) through the path shown in reactions (2) and (3) (in the introduction section). The anodic peak replaced the Pt oxide reduction peak, at the same time, it initiates at the similar potential where Pt oxides reduction initiated during first seven cycles and with the increasing number of scans slowly shifts toward the initial potential of Pt oxides reduction. As the reaction is assumed to follow path (2) and (3), the formation of intermediates will

TH-2592_156107017

take place. Fig. 5.12 shows two cycles of CV of the Pt-CNa-CNC after running the 10 LSV scans (shown in Fig. 5.11), starting from 0.3 V to negative potential direction. The anodic peak observed in the reverse cycle has a shift towards lower potential in the 2nd cycle, without much change in the intensity. The shift in the peak from 1st cycle to 2nd cycle indicates that the reaction intermediates formed during the reverse scan are being consumed during the forward cycle. The reaction intermediates create resistance for methanol oxidation. The position of the peak for the reduction of Pt oxides may not change, but the methanol will have free sites to adsorb on Pt as soon as reduction of Pt oxides starts. As the intermediates are being consumed in the forward scan, there will be less resistance for methanol adsorption and its subsequent reaction with adsorbed –OH, which results in the shift of peak potential towards the initial potential point of Pt oxides reduction.

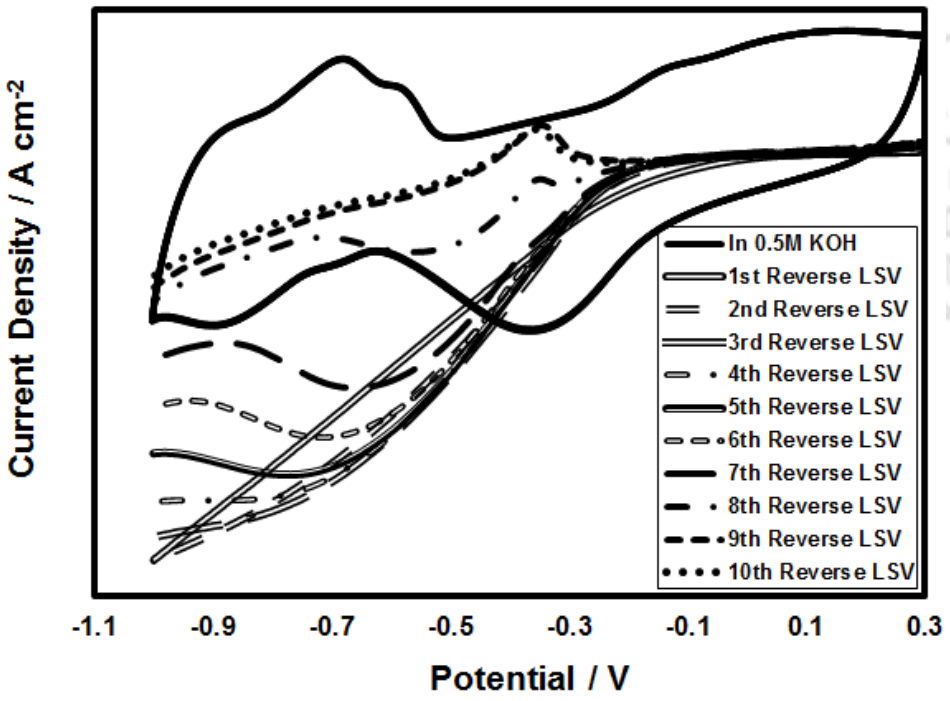

Fig. 5.11 Linear scan voltammetry (LSV) scans of calcined Pt-CNa-CNC in 0.5M KOH and 0.5M methanol solution at 100mV/s scan rate and their comparison with cyclic voltammetry of it in 0.5M KOH solution.

TH-2592_156107017

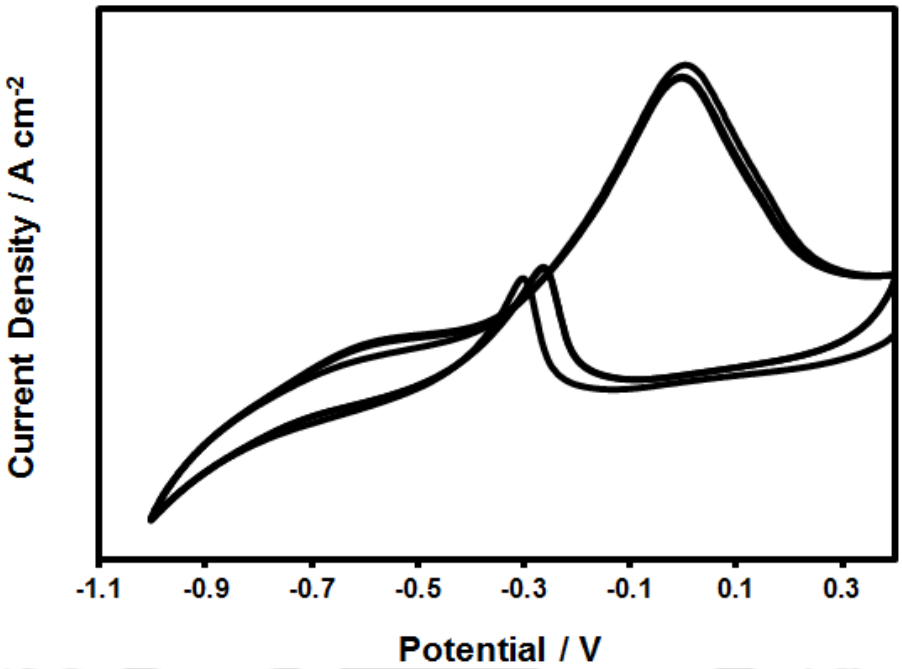

Fig. 5.12 After running 10 LSV scans, two CV cycles of calcined Pt-CNa-CNC catalyst in 0.5M KOH and 0.5M methanol at 100mV/s scan rate, starting the cycle from 0.3 V to reverse direction.

From the above discussion, we can hypothesize two points: first, the reaction intermediates formed during the reverse scan do not participate in the reaction during reverse scan, but they are being consumed in the forward cycle. Second, the methanol will react with the – OH as soon as it is available, during the reverse scan. As hypothesized here, the intermediates are being consumed in the forward cycle, and methanol will adsorb on the free sites of catalyst as soon as the reduction of Pt oxides starts. At the same time, easily available –OH on the support material will react with the methanol resulting in the shift of reverse scan peak potential with increasing CV cycles, towards initiation potential of Pt oxides reduction. So, the amount of adsorbed –OH present in the support material will also play a role in the reverse cycle reaction. Fig. 5.9 (a) also supports this hypothesis, where it can be seen that with the increasing number of CV cycles, the reverse cycle anodic peak shifts to lower potential reaching towards the initiation potential of Pt oxides reduction. As

TH-2592_156107017

there is no other parallel reaction taking place in the reverse cycle, it can be observed very sharp peak after 1000 cycles (shown in Fig 5.9 (b)). In the forward scan, several parallel reactions may be taking place, due to the formation of different types of intermediates, along with the methanol oxidation reaction with the newly adsorbed –OH in the lower potential range. Due to this, the forward cycle peak is getting broader with increasing number of cycles (Fig. 5.9 (a)). The peak current density of the forward cycle anodic peak is much higher compared to the reverse cycle anodic peak, which may be attributed to higher amount of –OH adsorbed in the lower potential range of the forward cycle. As the number of cycle's increases and more reduced intermediates are formed, the forward cycle peak current density becomes almost stagnant or start reducing. However, as more adsorbed –OH groups are available during the reverse cycle, the peak current density in the reverse cycle continues to increase and, as shown in Fig. 5.9 (b), it exceeds the peak current density of the forward peak.

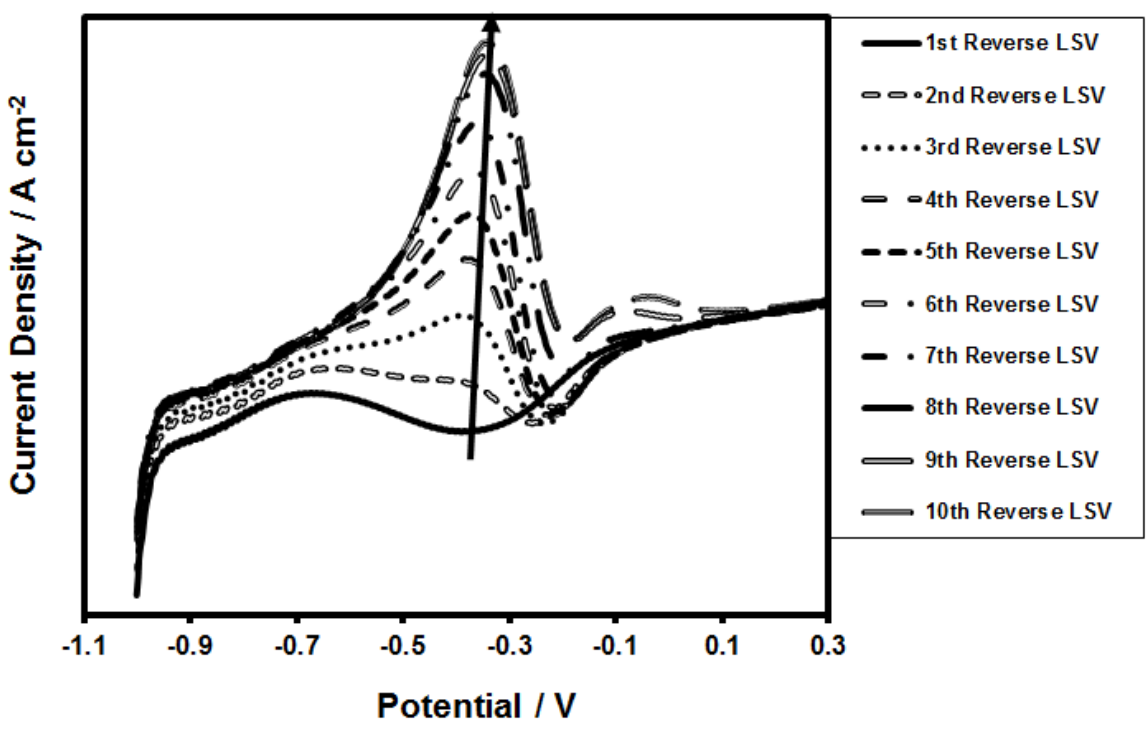

Fig. 5.13 Linear scan voltammetry scans with platinum wire as working electrode in 0.5M KOH and 0.5M methanol solution at 100mV/s scan rate.

TH-2592_156107017

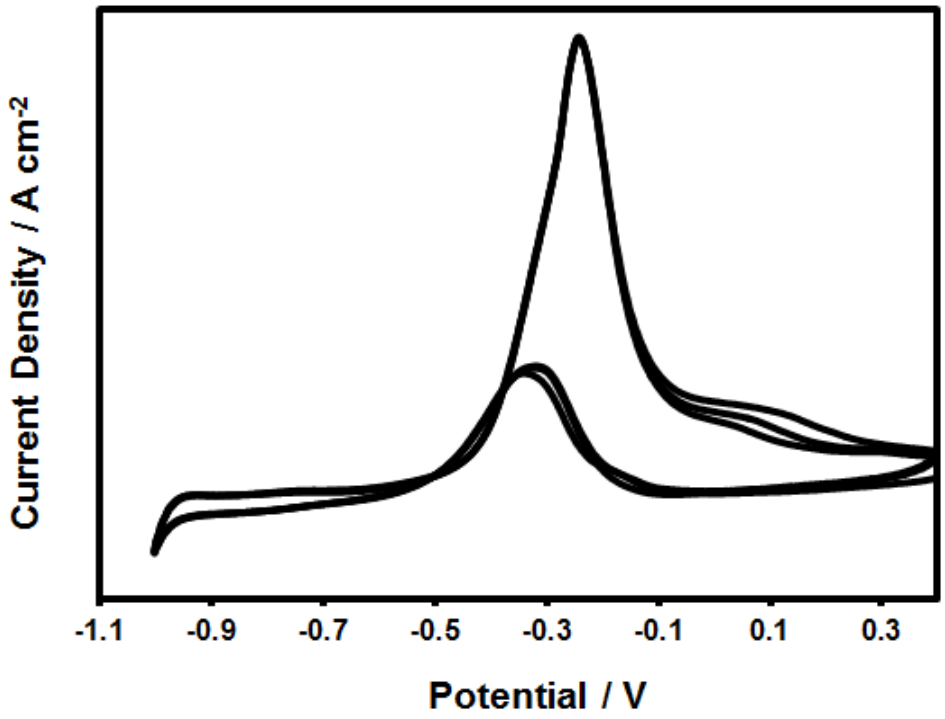

Fig. 5.14 After running 10 LSV scans, three CV cycles of Pt wire in 0.5M KOH and 0.5M methanol at 100mV/s scan rate, starting the cycle from 0.4V to reverse direction.

To make a comparative study of Pt-CNa-CNC, similar LSV scans were done by using Pt wire as working electrode against the Pt counter electrode. From the Fig. 5.13, it can be seen that Pt wire also follows a similar pattern as that of Pt-CNa-CNC in reverse LSV scans. For Pt wire in the 1st LSV scan, the Pt oxides reduction peak can be observed, as it may have already formed oxide layer. From the 2nd LSV scan onwards the anodic peak can be observed and small shift in the peak potential with increasing scans, towards initiation potential of Pt oxides reduction. After the LSV scans, the CV cycles done for Pt-CNa-CNC starting from the 0.3 V to reverse potential direction showed a small shift in the anodic peak to lower potential in reverse cycle from 1st cycle to 2nd cycle (Fig. 5.12). The same analysis was done for the Pt wire, but the jump in the peak potential (shown in Fig. 5.14) is quite insignificant, and the anodic peak broadness present in the forward scan is also less, which indicates that most of the reaction intermediates are dissolved in the bulk solution. It is expected that the formed intermediates get dissolved in the bulk solution, as only the top

TH-2592_156107017

surface of the Pt wire is available for the adsorption of reactive species and as mentioned earlier, there are no reports available which suggest strong adsorption of intermediates on the Pt surface. From the LSV analysis it can be assumed that methanol oxidation follows the reaction mechanism outlined in the introduction section, where the presence of –OH is important and having clay as support may help in the improvement of catalytic activity. Based on the LSV results, it has been hypothesized that the reaction intermediates are consumed in the forward scan anodic cycle and do not take part in the reverse scan anodic peak potential reaction.

5.4.6 Electrochemical Impedance Spectroscopy (EIS) Analysis

As proposed in the previous section, reactive intermediates formed during methanol oxidation are oxidized in the forward anodic cycle. To determine the potential range for the

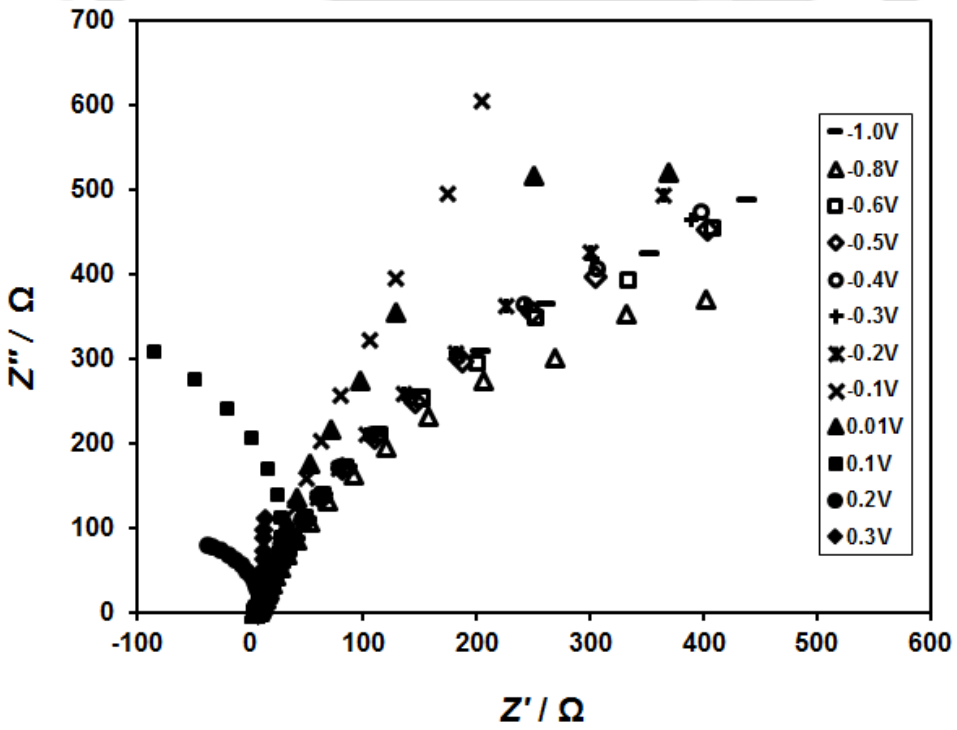

Fig. 5.15 Nyquist plots of calcined Pt-CNa-CNC catalyst at different applied potential in 0.5M KOH and 0.5M methanol.

TH-2592_156107017

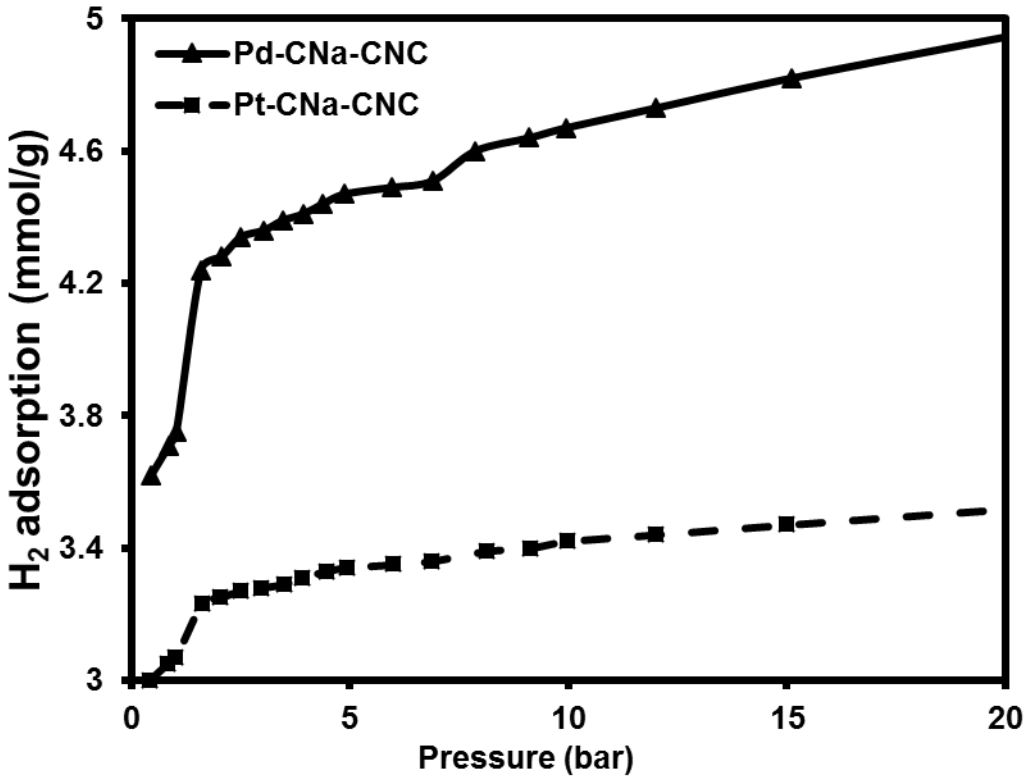

Fig. 5.16 Hydrogen adsorption isotherms for Pt-CNa-CNC and Pd-CNa-CNC.

-oxidation of these intermediates, EIS analysis has been carried out for the Pt-CNa-CNC catalyst in 0.5M KOH and 0.5M methanol solution. During the electrochemical reaction on the catalyst, there will be adsorption of methanol and –OH, oxidation of methanol, production of intermediates and formation of oxides. These processes will take place in different potential ranges and will create certain amount of impedance in that range. However, as Yue et al. (2013) and Hu et al. (2017) have reported, in the potential range where the formed reaction intermediates oxidize and get removed from the catalyst surface, the impedance will become negative due to recovery of catalyst surface. Fig. 5.15 shows the Nyquist plots of Pt-CNa-CNC catalyst in methanol and KOH solution at different applied potentials, and negative impedance for 0.1V and 0.2V can be clearly observed. Nyquist plots shown for various potentials in Fig. 5.15 indicate that removal of intermediates takes place in the potential range 0.1V–0.2V. The results also clarify that the intermediates do not get removed during the reverse part of the CV scan, as negative

TH-2592_156107017

impedance is not observed in the potential range where the anodic peak is observed during reverse cycle. If we correlate this result with the CV curve of Pt-CNa-CNC shown in Fig. 5.9, it can clearly be observed that during the forward scan, with increasing number of cycles, removal of intermediates starts dominating over methanol oxidation and the current density peak starts to shift towards the potential range 0.1V–0.2V. As shown in Fig. 5.9 (b), after 1000 cycles the peak has completely shifted to the range 0.1V–0.2V. The observation made here clearly shows that with increasing number of CV cycles the reaction intermediates start to hinder methanol oxidation in the forward scan and work as poison for the catalyst specifically meant for methanol oxidation.

5.4.7 Surface Area Analysis and Hydrogen Adsorption Studies

Along with electrochemical studies for methanol oxidation, we tried to investigate the application of Pt/Pd based material for hydrogen adsorption, as we show in TEM images that they have small porous nano channels in their morphology. Surface area analysis showed that, Pt-CNa-CNC and Pd-CNa-CNC have low surface area 37.7 m^2/g and 35.5 m^2/g, with total pore volume 0.27cc/g and 0.31 cc/g respectively. As reported in literature (Panella et al., 2005; Will, 1965), hydrogen adsorption on carbon based materials is purely physiosorption type, where else in pure Pt/Pd, hydrogen generally disassociates reversibly to form respective hydrides and revert back to form hydrogen. But in carbon supported Pt/Pd, the site of C–Pt/Pd bond has strong interaction between carbon and Pt/Pd and which results in stronger C–Pt/Pd–H type of interaction with hydrogen and weaker C–Pt/Pd–H_2 type of interaction (López-Corral et al., 2010). So, with larger surface area Pt/Pd loaded carbon materials show higher hydrogen adsorption compared to the pure carbon materials. Therefor in the current investigation, similar system is used for hydrogen adsorption studies, where Pt/Pd is loaded on CNa-CNC gel. Pt/Pd were preferentially

TH-2592_156107017

attached on CNC along with clay sheets and calcination of Pt-CNa-CNC/ Pd-CNa-CNC at 400°C resulted in conversion of CNCs to carbon, which is why the Pt/Pd nanoparticles shown in TEM images are covered by porous carbon layers. Thus, the combination of carbon supported Pt/Pd nanoparticles deposited on cation containing CNa^+ clay sheets results in good hydrogen adsorption material. The calcined Pt-CNa-CNC and Pd-CNa-CNC show hydrogen adsorption values 3.52 mmol/g and 4.95 mmol/g at 0°C and 20 bar pressure, respectively. The adsorption isotherms for hydrogen adsorption on Pt-CNa-CNC and Pd-CNa-CNC are shown in Fig. 5.16.

5.5 Conclusions

The micro-ion complexation-based gel formed in the current investigation is synthesized using bio-derived CNCs and CNa^+ clay biomaterials, by simple, green and scalable approach. Here, catalytically active Pt/Pd nanoparticles have been encapsulated in CNa-CNC gel, resulting in bio-based sustainable materials, which show good performance for applications in energy conversion devices. The prepared Pt/Pd-loaded complexes have shown very good activity towards methanol oxidation in alkaline medium along with significantly high stability. The Pt based catalyst showed better performance for methanol oxidation, while Pd based catalyst showed much better stability in alkaline medium for methanol oxidation. The stability of the electrocatalysts prepared in the current work was also compared with stability of other reported catalysts and commercial Pt-C and Pd-C electrocatalysts and it was found that Pd based electrocatalyst showed much better performance. For both Pt-CNa-CNC and Pd-CNa-CNC, the very common reaction mechanism reported in literature in alkaline medium for methanol oxidation on Pt catalyst (outlined in the Introduction section) have been assumed. Further, the LSV investigation on Pt-CNa-CNC catalyst have shown the critical role of adsorbed –OH on catalyst support,

TH-2592_156107017

and how the clay-based support can have positive impact on catalyst performance. On the basis of LSV analysis, a hypothesis has been made for Pt-CNa-CNC catalyst, that reaction intermediates formed during the methanol oxidation are being removed during the forward CV scan as opposed to the many reports on Pt catalyst, which assume it to happen during reverse scan. This hypothesis was further supported by impedance analysis and the range of potential for the removal of the reaction intermediates was found to be 0.1V–0.2V. The impedance results along with the CV analysis lead to the conclusion that with increasing number of CV cycles, removal of the intermediates starts to dominate over methanol oxidation reaction in the forward scan and the intermediates start to work as poison for the catalyst which is preferentially used for methanol oxidation. It is proposed that during the reverse cathodic scan of CV cycle, only methanol oxidation is taking place, which results in a sharp anodic peak with increasing number of cycles. The reaction is assumed to be following path (2) and (3) given in the reaction mechanism, which can produce several reaction intermediates. Subsequently, the observed forward scan anodic peak in CV cycles results in broader peak, due to parallel oxidation of methanol and removal of intermediates. The porous nature of carbon based Pt/Pd support in the system was also worked to give good hydrogen adsorption capacity to the Pt/Pd based materials, where the hydrogen adsorption capacity was found to be 3.52 mmol/g and 4.95 mmol/g at 0°C and 20 bar pressure, respectively. Thus, from the present study it can be concluded that ionic interactions between CNCs and clays could result in self-assembly, leading to the formation of the micro-nanogel complexes which have good potential to be utilized in energy conversion and storage devices at the commercial scale, providing a novel opportunity in conversion of abundantly available biomass-derived resources to value-added products.

TH-2592_156107017

Chapter 6:

CNC-Clay based Cathode Electrocatalyst for H_2O_2 Reduction in Alkaline medium

Graphical Overview

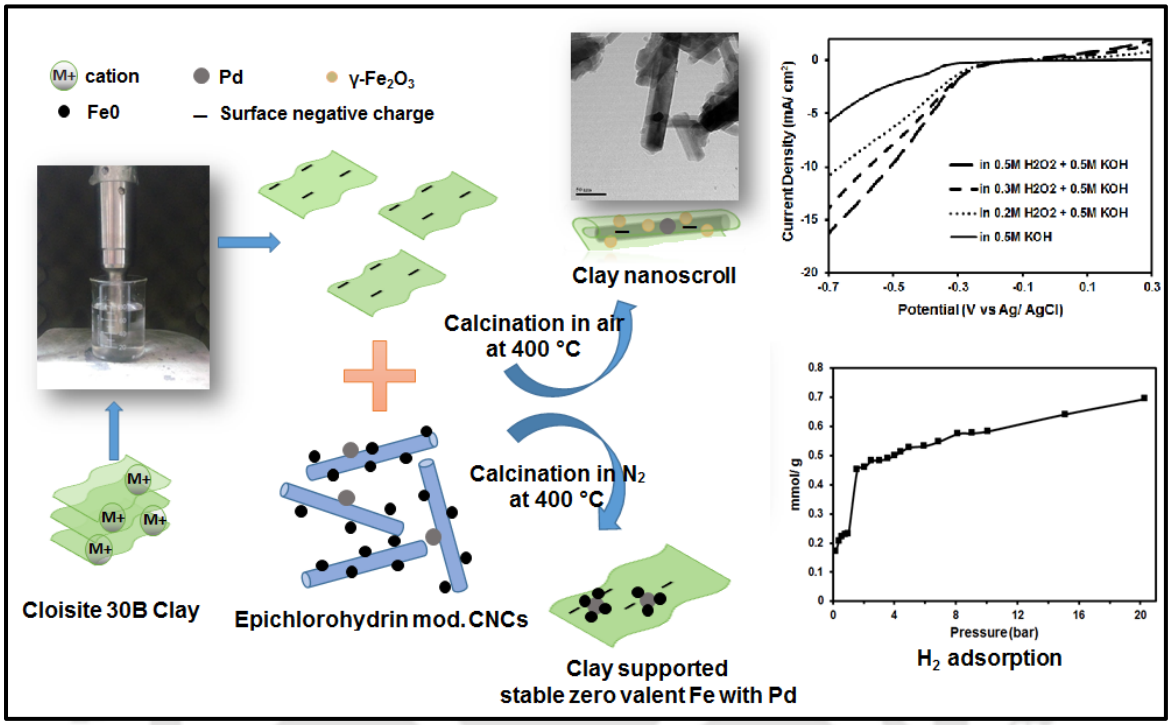

Halloysite are naturally occurring nanotubes which due to unique structural properties have found tremendous applications. Here, we have described the fabrication of cylindrical-shaped clay nanoscrolls similar to natural halloysite nanotubes, first time from 2:1 type montmorillonite, with significantly low amount of palladium and high iron-loaded cellulose nanocrystals used as structural directing agents. Electrostatic interaction between negatively charged surface of clay sheets and γ-Fe_2O_3 resulted in the formation of clay nanoscrolls. The prepared clay nanoscrolls can be used in different application as an alternative of halloysite. In this study, we have utilized the clay nanoscorlls as electrocatalyst for H_2O_2 reduction in alkaline medium which showed current density in the same range as of the commercial Pd-C catalyst with significantly high Pd loading. Along

<u>*Publication:*</u>

- Gaur, S. S., Dhar, P., Narendren, S., Sakurai, S., Kumar, A., & Katiyar, V. (2020). Fabrication and characterization of clay nanoscrolls and stable zerovalent iron using montmorillonite. Applied Clay Science, 193, 105670.

TH-2592_15610717

-with it, we checked the hydrogen adsorption capacity of nanoscrolls, which showed the comparative results reported in the literature for halloysite. Interestingly, change in the calcination environment of the process from normal atmospheric to nitrogen resulted in the formation of stable and ferromagnetic zero-valent iron (ZVI) on the clay support instead of formation of the scrolls. Permanent magnetic nature of ZVI improves induction heating, and thus can be applied in the biomedical field. Thus, a sustainable approach for fabrication of hallyosite nanotubes alternate clay nanoscrolls and stable ZVI has been described here and the role of clay nanoscrolls as the cathode electrocatalyst for reduction of H_2O_2 in alkaline medium is also detailed in the chapter.

6.1 Introduction

2D thin layered structure of graphene nanosheets have found tremendous applications in green and renewable energy technologies, which has inspired the development and investigation of similar 2D layered materials such as, silicene, germanene, phosphorene, hexagonal boron nitride, carbon nitride, layered metal hydroxides, clays, metal-organic frameworks (MOFs) etc. (Wang et al., 2018). Formation of multilayer scrolls from 2D graphene sheets and its advantage of having the properties of both graphene sheets and multiwall carbon nanotubes is very well stablished (Gong et al., 2017; Yu et al., 2017; Tang et al., 2018; Zeng et al., 2012). Different types of clay such as layered double hydroxide (LDH), kaolinite, montmorillonite (Mt), etc. are also formed by the alignment of similar 2D layered sheets bonded by ionic interaction and/or hydrogen bonding, and can be delaminated or exfoliated to prepare clay nanoscrolls for high performance applications. Excellent ion exchange capacity, along with high mechanical and thermal stability of such clays make them suitable for numerous applications in the field of cosmetics, adsorbents, drug delivery, agricultural and environmental, sensors, catalysis, flame retardant materials,

TH-2592_156107017

antimicrobial materials and photoluminescence (Mishra et al., 2018; Rives et al., 2013; Kadwa et al., 2014; Park et al., 2016; Choy et al., 2007; Elmoubarki et al., 2017; Cox et al., 2001). As adsorbents clays have been excellent material, finding application in dye and metal adsorption, adsorption of various organic compounds, adsorption of pesticides, drugs and protein adsorption and adsorption of several toxic gases (Mishra et al., 2018). Thus, the nanoscrolls of such clay materials can find enormous applications in various fields.

Halloysite clay is naturally occurring aluminosilicate clay, which is mostly found in nano size tubular morphology, as well as several different types of morphologies. Halloysite has various advantages over carbon nanotubes and graphene based nanomaterials. Compared to carbon nanotubes and graphene nanoscrolls, halloysite has interesting morphology, where inner layer, outer layer and inter layer spacing, each have different functionalities and provides various different types of sites for modification, which opens the gates for many applications. They can easily be modified as well as they can host a variety of materials. High biocompatibility and low cytotoxicity, extends their application in biomedical area as a good drug carrier material (Yuan et al., 2015). Low cost and its large scale availability is the major advantage of halloysite over the carbon based tubular materials, which can hardly be produced in grams (Yuan et al., 2015). Slow production, non-uniform morphology and presence of impurities are the major issues of halloysite, which is why researchers are trying to prepare nanoscrolls by using kaolinite (Kuroda et al., 2011), which is the base material from which halloysite is formed. Kaolinite has the chemical structure in which $AlO_2(OH)_4$ octahedral sheets and SiO_4 tetrahedral sheets form 1:1 type layered structure. Several techniques have been utilized to prepare kaolinite nanoscrolls, most of which follows exfoliation and subsequently scrolling mechanism. Kuroda et al. (2011) used methoxy modified kaolinite with different guest species for intercalation and solvent directed swelling based one step and two step scroll

TH-2592_156107017

formation techniques. Li et al. (2017) used ultra-sonication assisted liquid exfoliation method along with cetyltrimethylammonium chloride (CTMACl) as intercalation agent to help in formation of nanoscrolls. The same group in their previous study (Liu et al., 2016) used similar mechanism without sonication, to prepare the kaolinite nanoscrolls, where alkyltrimethylammonium salt has been used for intercalation agent to reduce the molecular interaction between clay sheets and methanol is used as swelling agent for exfoliation. Li et al. (2015) earlier reported the scrolling mechanism for kaolinite via intercalation and delamination process and reported that the driving force for kaolinite sheets scrolling is: the size discrepancy of Si–O tetrahedron and Al–O octahedron, while the intercalation agent eliminates the hydrogen bonding between sheets to help in their delamination. Yuan et al. (2013) and Makó et al. (2017) also used CTMACl as intercalation agent and further investigated the effect of intercalation temperature on the morphology and other properties of kaolinite nanoscrolls. Nakagaki et al. (2006) intercalated kaolinite by urea and by the help of ultra-sonication prepared the nanoscrolls, which were further utilized for immobilization of iron porphyrins based oxidation catalysts. As reported in literature that the size discrepancy between tetrahedral and octahedral layers in kaolinite sheet is driving force for kaolinite scroll formation, this concept was utilized by White et al. (2012) and they further increased this size discrepancy by partial substitution of SiO_2 by GeO_2. They found progressive change in the morphology of kaolinite with increasing GeO_2 substitution in sequence of kaolinite nanosheets, spheroidal kaolinite, halloysite nanotubes (kaolinite scrolls). Multiwall nanotubes were formed between 0.1–0.2 mole fractions.

It is known that formation of kaolinite as well as halloysite takes place in nature during long term hydrothermal actions in acidic type of weathering environment containing sulphur dioxide, sulphur vapor, and hydrochloric acid on rocks (Kerr, 1952; Macdonald, 1944; Lovering, 1949). Ryan et al. (2016) studied the sequential

TH-2592_156107017

transformation of smectite (2:1 clay) and kaolinite-smectite to kaolinite and halloysite and suggested that with increasing Al:Si ratio due to leaching of Si in moist environment, the smectite to kaolinite-smectite to halloysite to kaolinite chronosequence of change is thermodynamically favorable. Further, on the basis of very small difference in standard free energy of formation of halloysite and kaolinite and thermodynamically more stable nature of kaolinite, they concluded that hallyositre nanotubes morphology is unstable. Smectite may work as an alternative of kaolinite to prepare halloysite type of nanoscrolls. Smectite is a 2:1 type of clay where one $AlO_2(OH)_4$ octahedral sheet is covered by SiO_4 tetrahedral sheets from both the sides and these negatively charged sheets are bounded by cations like K^+, Na^+, Ca^{2+} etc. The negative charge on the clay sheets arrives from the partial substitution of Al in octahedral by Fe/Mg/Li and/or Si substitution in tetrahedral sheet by Al (Odom, 1984). Montmorillonite (Mt) is a type of smectite clay having a very high cation exchange capacity (CEC) (0.91 – 1.43 meq/ g (Zartman et al., 2010)) as compared to that of halloysite and kaolinite (0.11 – 0.16 meq/ g (Ryan et al., 2016)), and if it can be converted to scrolls, it may provide better properties. To prepare nanoscroll from Mt clay sheets two different approaches can be applied. In the first approach the Mt 2:1 layer can be converted to 1:1 type of layer, which will have similar structure to that of kaolinite. In the second approach, the similar mechanism which has been reported for kaolinite based scroll formation, intercalation and subsequent delamination can be utilized. The first approach looks unviable as in nature it takes a very long time to convert smectite to kaolinite, so even in very severe environment it may take long time to convert 2:1 type sheets to 1:1 type. At the same time, this conversion will result in decrease in CEC of Mt, along with it, the scroll prepared by it may have the similar properties as of kaolinite. The second approach looks feasible, but still challenging, as if we compare kaolinite structure to that of Mt, kaolinite sheets are connected by each other with hydrogen bonding, while the Mt sheets are

TH-2592_156107017

connected by cations present in the interlayer space. Overcoming the hydrogen bonding interaction by intercalation agent is easier compared to overcoming ionic interaction by intercalation. Another structural problem in Mt is that it contains low amount of interlayer hydroxyl groups compared to that of kaolinite, which reduces the sites of interaction for intercalation agent. But, exfoliation of Mt sheets is not a major obstacle and there are large number of reports available, utilizing different methodology for exfoliation. The major issue would be the driving force, which acts during kaolinite scroll formation may not be dominating enough in the case of 2:1 layered Mt, because the stress generated by structural mismatch between tetrahedral and octahedral in kaolinite can be almost balanced by other side of tetrahedral sheet in the Mt. So, to have higher stress, there should be enough partial substitution of Al in octahedral layer or Si in tetrahedral layer or both. Due to absence of high enough driving force, there are experimental and simulation reports on the curved surface formation in Mt (Fu et al., 2011; Heinz, 2012; Sato et al., 2001), but there is no report before this work on the scrolling of Mt clay. If the stress is not high enough, in that case some external interactive forces may be applied to deform the 2:1 sheet into scroll shape.

The current investigation describes the application of green probe sonication technique which generates very high expanse of localized pressure and temperature due to the cavitation process, for the exfoliation of Mt without the use of any intercalation agent. Moreover, sonication also results in the partial removal of cations present in the clay, resulting in the development of an overall negative charge on the clay surface. Subsequently, ionic interactions can be utilized as the driving force for scrolling. In the present study, iron oxide nanoparticles, produced through calcination of iron and palladium loaded cellulose nanocrystals (Fe-Pd-CNC), have been utilized for this purpose. CNCs, having rod-shaped morphology, act as the template for scrolling, while high iron oxide

TH-2592_156107017

content helps in scrolling. Thus prepared clay nascrolls were investigated for their properties related to H_2O_2 reduction in alkaline medium. Low wt% of palladium is loaded along with iron to check for further application of clay nanoscrolls for hydrogen storage studies. Interestingly the calcination environment also has impact on scrolling. The effect of nitrogen atmosphere on the calcination process and the formation of ZVI have also been studied. Formation of the Mt clay nanoscrolls and highly stable ZVI is discussed in the subsequent sections.

6.2 Materials and Methods

6.2.1 Materials

Quaternary ammonium salt modified natural Mt cloisite-30B (C30B) was obtained from the supplier (Connell Bros. Pvt. Ltd., Mumbai, India). It contained quaternary ammonium salt organic modifier cations for balancing the negative charge of the clay sheets, partially replacing Ca^{2+}/ Na^{+} cations. These modifying cations can be removed during sonication in water by dissolution and during calcination by thermal degradation, giving an overall negative charge to the clay sheets. Sodium hypochlorite (4%), hydrogen peroxide (30%), sodium hydroxide (>97%), sulfuric acid (>99%), palladium chloride ($PdCl_2$) and sodium borohydride ($NaBH_4$) were procured from SISCO Research Laboratories (SRL Chemicals, India). Anhydrous $FeCl_3$ and KOH pellets were purchased from Merck Specialities Private Limited, India. Methanol (99.8%), hydrochloric acid (35%) and epichlorohydrin (ECH) (99%) were obtained from HiMedia Laboratories Pvt. Ltd., India.

TH-2592_156107017

6.2.2 Fabrication of Iron-Palladium Loaded CNCs (Fe-Pd-CNC)

Fabrication process of CNCs has already been discussed in chapter-2 and they have been used for loading of iron and palladium using $NaBH_4$ reducing agent. 1:10 weight ratio of CNC to $FeCl_3$ was used, while 2 wt.% $PdCl_2$ of overall precursor materials (including clay) was used. In terms of weight, 50 mg of CNC, 500 mg of $FeCl_3$, 100 mg of C30B clay and 13 mg of $PdCl_2$ were used. CNCs were first dispersed in 20 ml of water and then $FeCl_3$ was added to it. $PdCl_2$ was dissolved in 10 ml of water by adding 50 µl HCl and later added to the CNC-$FeCl_3$ solution. $NaBH_4$ solution (in excess) was then added dropwise with vigorous stirring and the final solution was kept at 90°C. The reaction was stopped after 2 h and the solution was centrifuged. The precipitate was washed multiple times with methanol to remove unreacted salts. The prepared Fe-Pd-CNCs were then used as the template for the formation of clay nanoscrolls.

6.2.3 Fabrication of Clay Nanoscrolls and ZVI

To prepare clay nanoscrolls, 100 mg of C30B clay was taken in Millipore water and sonicated at 50% amplitude (0-300 W, 230 V, 50 Hz, 4 A) for 4 h using a probe sonicator (BioLogic Inc., Model-3000MP, India). Simultaneously, the prepared Fe-Pd-CNCs were dispersed in 15 ml of ECH with continuous stirring at 90°C for 6 h. The ECH-modified Fe-Pd-CNCs were then centrifuged and washed multiple times with methanol to remove the excessive ECH. ECH modification was done to bind the Fe-Pd-CNCs to the -OH groups present in the edges of C30B sheets. Clay nanoscrolls were then prepared according to the similar but modified method described in previous investigation by Dhar et al. (2018) to prepare graphene nanoscrolls. Sonicated clay was first centrifuged to remove the water and added to ECH modified Fe-Pd-CNCs along with 50 ml of methanol, and stirred at 90°C, under reflux condition for another 6 h. The methanol was then removed by centrifugation

TH-2592_156107017

and the precipitate was dried overnight in a hot air oven at 50°C. Part of the dried material was stored for characterization, prior to calcination and the remaining material was calcined in a muffle furnace at 400°C in normal air contained atmosphere for 3 hours. Same procedure was followed for the preparation of ZVI, by substituting the normal atmospheric air with nitrogen gas during the calcination process.

6.3 Characterization

To know the exfoliation and the crystalline phases present in the final calcined materials, Powder X-ray diffraction (XRD) was carried out in a Rigaku Japan TTRAX III (18 kW rotating anode X-ray source, 50 kV and Cu-K_α radiation source) at 20 °/min scan rate. To verify the crosslinking between metal loaded CNCs and C30B clay sheets, X-ray photoelectron spectroscopy (XPS) analysis was done in a JEOL-JPS-9010MC/SP system with an MgK_α X-ray source. Carbon C1s reflection at 285.0 eV was taken as the reference. Morphological analyses was done using a field emission scanning electron microscope (FESEM) (Model Sigma-300, Zeiss, Germany,) and field emission transmission electron microscope (FETEM) (JEOL JEM 2100F FETEM). High-resolution TEM (HRTEM) and selected area electron diffraction (SAED) patterns were measured with FETEM. Compositional analysis the clay sample in micron size range was carried out with energy dispersive X-ray analysis instrument (EDX) (Oxford Instruments, United Kingdom) attached to FESEM, while the analysis for nanoscrolls was carried out with an EDX attached to FETEM. Surface area analysis was carried out on a Quantachrome surface area analyzer (Autosorb-IQ MP) by Brunauer–Emmett–Teller (BET) method based on nitrogen adsorption-desorption technique. Before analysis degassing of the samples was done at 200°C for 3 hours and the analysis was done at 77 K. Hydrogen adsorption measurement was performed in the pressure range of 0-20 bar at ~273 K using a Quantachrome iSorb-

TH-2592_156107017

HP instrument, after degassing at 200°C for 30 min in the presence of inert gas flow. Magnetic characteristics of the clay scrolls and clay ZVI samples were determined by vibrating sample magnetometer (VSM) (Lakeshore, Model 7410 series) at room temperature. Induction heating test was done using an optical fiber temperature sensor (Optocon AG) by taking 10 mg of the each sample. Copper coil (diameter 5 cm with 3 turns) was used under alternating magnetic field at 250 Hz frequency with a heating system (Easy Heat 224, Ambrell, USA) to carry out the induction heating experiments. The temperature was recorded every 10 seconds till 10 minutes. Electrochemical reduction analysis of H_2O_2 in 0.5 M KOH and different concentration of H_2O_2 solution was done using a cyclic voltammetry (Autolab PGSTAT204 model, Metrohm India Ltd).

Fuel cell performance was evaluated by using clay nanscrolls as cathode electrocatalyst and Pt-Ru/C was used as anode electrocatalyst. Annealed PVA-5wt.%HH membrane samples prepared and reported in the chapter-3 are utilized as electrolyrte in the test. The electrolcatalyst inks were prepared by taking each catalysts in separate small glass beakers and adding 30 µl of 5 wt.% Nafion perfluorinarted resin solution, along with 100 µl of water and 1 ml of isopropyl alcohol in each. Each beaker was sonicated till a fine ink was obtained. The prepared catalyst inks were coated on PTFE treated Toray carbon paper (from Sigma-Aldrich India) and loading of both anode and cathode electrocatalysts was kept at 2 mg/ cm^2. Thus prepared carbon paper diffusion layer supported electrocatlysts were dried at 80°C for 6 h. The membrane electrode assembly (MEA) was prepared by sandwiching the membrane between anode and cathode electrocatalyst loaded carbon papers through hot press method using 100°C temperature and 98 bar pressure for 10 min. The active surface area of the MEA was 6.25 cm^2. It was fitted in a single cell, where anode compartment was fed with 3M methanol + 2M KOH solution at a flow rate of 5 ml/min flow rate, while cathode chamber was fed with 6M H_2O_2 solution at 25 sccm flow rate. The cell temperature

TH-2592_156107017

was fixed at 60°C and a manual fuel cell test station from K-PAS Instronic Engineers India Pvt Ltd was used for recording the cell voltage data.

6.4 Results and Discussion

6.4.1 Crosslinking of Fe-Pd-CNCs to Clay Sheets

Fe-Pd-CNCs acted as the structural directing agents for clay scroll formation, and ECH was used as the crosslinking agent between Fe-Pd-CNCs and C30B clay sheets. Crosslinking of the hydroxyl groups of the CNCs with the hydroxyl groups present on the edges of C30B clay sheets resulted in the formation of a high number of C-O and C-O-C bonds. The crosslinking between CNCs and clay sheets was verified from the XPS carbon 1s spectra (Fig.1). The carbon 1s spectra of CNCs (Fig. 6.1 (a)) showed typical reflections of C-C (285 eV), C-O-C & C-O (286.1 eV), and O-C-O (287.3 eV). The reflection at 288 eV was due to the oxidation of CNC surface and formation of O-C=O type of bond. The carbon 1s spectra of C30B clay (Fig. 6.1 (b)) was generated due to the presence of quaternary ammonium salt modifier. It showed a single reflection of C-C type bond due to long carbon tallow present in the modifier, along with a small reflection for C-N type bond. The XPS spectra of Fe-Pd-CNC grafted C30B in uncalcined form (Fig. 6.1 (c)) verified the crosslinking by ECH, as the reflections for C-C type of bonds as well as C-O-C type of bonds were more dominant compared to the CNCs. Further, the crosslinking of Fe-Pd-CNCs on C30B clay sheet edges could be visualized from FESEM image shown in Fig. 6.2 (b).

TH-2592_156107017

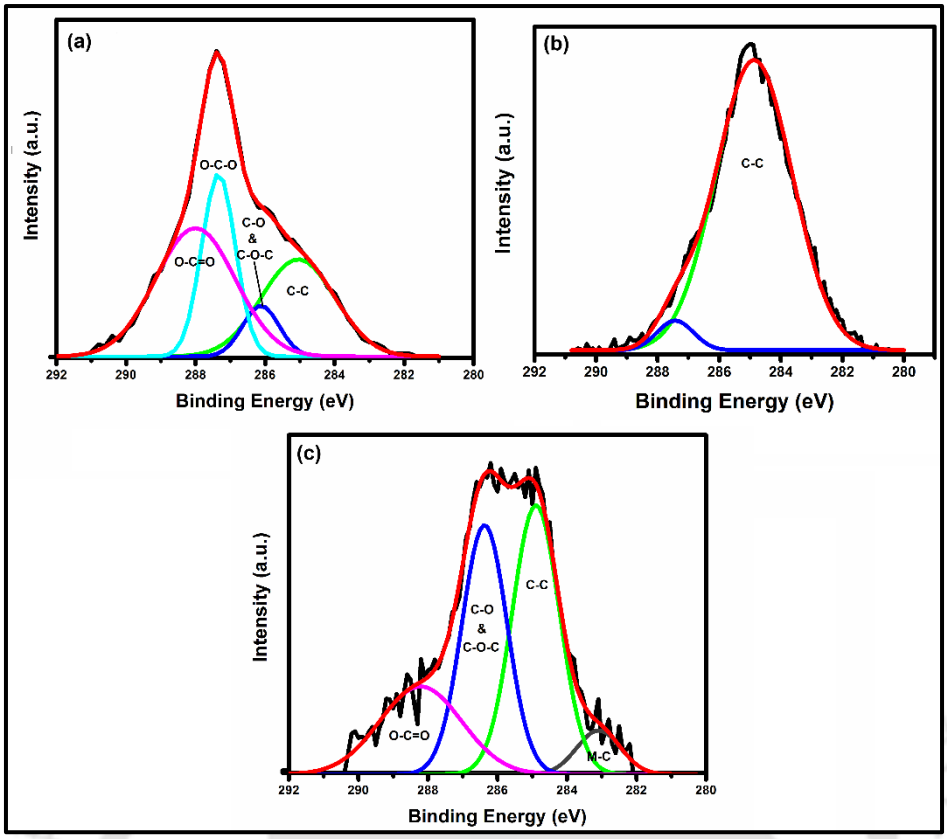

Fig. 6.1 XPS spectra of (a) CNCs (b) C30B clay (c) uncalcined Fe-Pd-CNC grafted C30B.

6.4.2 Morphology

For the fabrication of cylindrical nanoscrolls, Fe-Pd-CNCs having rod shape morphology were required. FESEM micrograph shown in Fig. 6.2 (a) confirmed that even after loading of Fe and Pd, CNCs retained their rod shaped morphology. Epichlorohydrin (ECH) is well known reagent which helps in the crosslinking of hydroxyl functional groups. ECH thus, helped in the binding of –OH groups present in the CNCs with the –OH groups present on the edges of the clay (Fig. 6.2 (b)). Formation of cylindrical clay nanoscrolls by the calcination of Fe-Pd-CNCs grafted C30B clay in an oxygen environment (normal atmosphere) could be verified from Fig. 6.2 (d). The porous morphology of clay nanoscrolls could be visualized from the inset image shown in Fig. 6.2 (d). TEM micrograph (Fig. 6.2 (e)) further confirmed the porous nature of clay nanoscrolls.

TH-2592_156107017

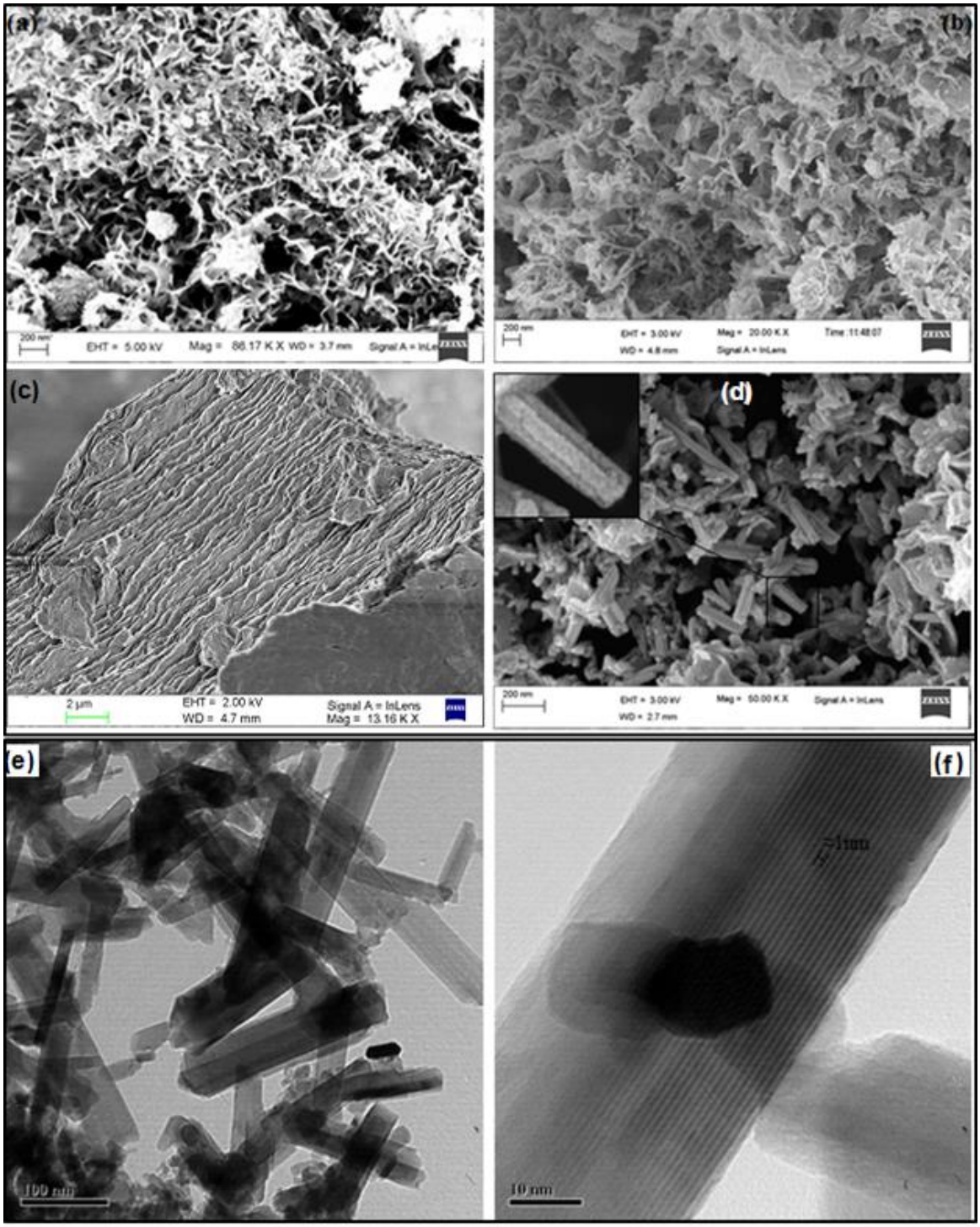

Fig. 6.2 FESEM images of (a) Fe-Pd-CNC (b) Fe-Pd-CNC grafted on C30B clay (c) pristine C30B clay before sonication and any modification (d) nanoscrolls formed by the calcination of Fe-Pd-CNC grafted C30B clay (in inset: enlarged porous morphology of clay scrolls) and TEM images of (e) & (f) C30B clay nanoscrolls.

TH-2592_156107017

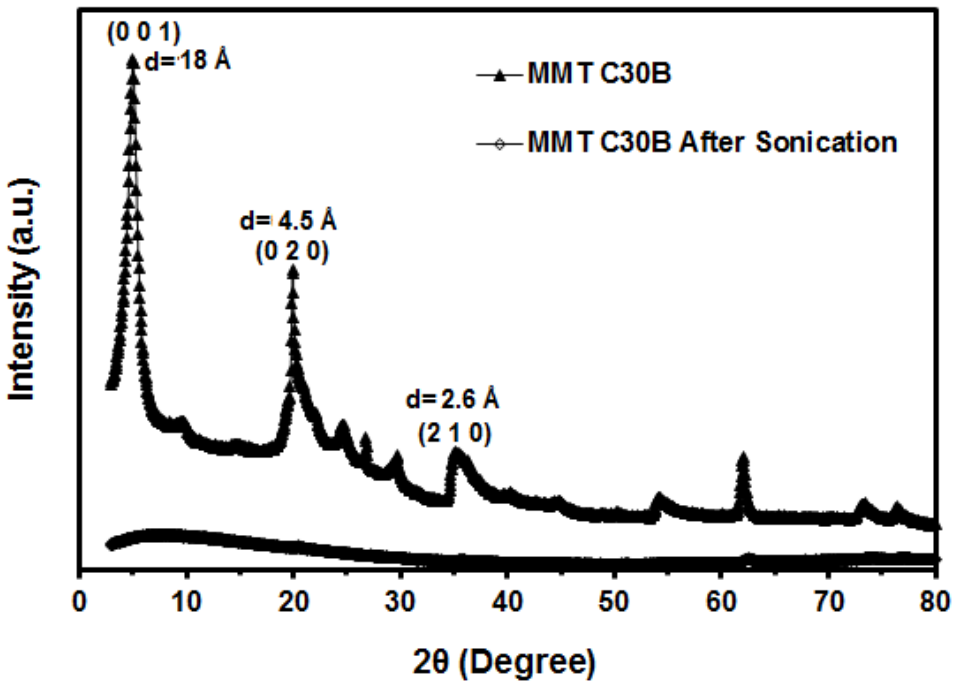

Fig. 6.3 XRD curve of C30B clay before and after sonication.

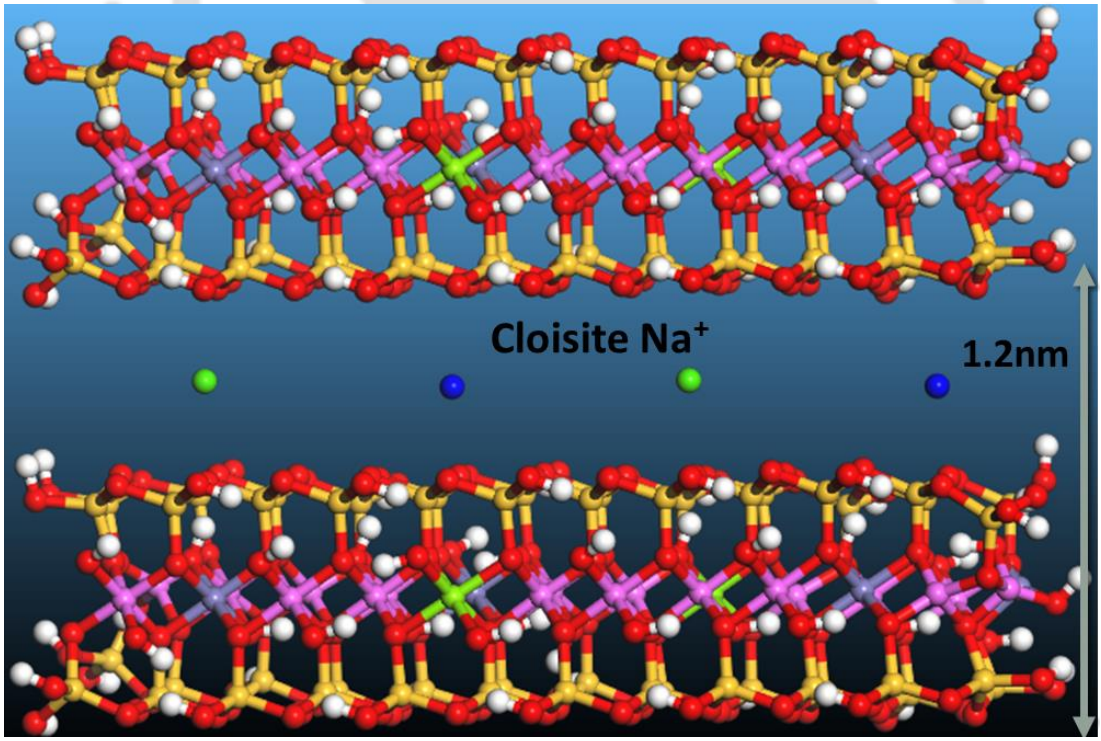

Fig. 6.4 Structure of cloisite-Na^+clay.

TH-2592_156107017

Fig. 6.2 (f) depicted a rare clay sheet which retained its crystalline nature even after sonication and formed scroll. But most of the sheets lost their crystallinity, which is evident from the XRD of sonicated C30B clay (Fig. 6.3), as most of the crystalline reflections had disappeared after sonication. d-value of the C30B clay before calcination was ≈18 Å (Fig. 6.3), while unmodified cloisite-Na^+ clay has a d-value ≈12 Å (Fig. 6.4) (Nazir et al., 2016). Fig. 6.2 (f) shows that the d-value is ≈10 Å, which is even lower than the unmodified Na^+ cation containing clay. This confirmed the removal of interlayer binding cations during the processing and an increase in the overall negative charge on the clay sheet surface.

Processing parameters have an effect on the morphology of Fe-Pd-CNCs, and since it acted as the structure directing agent for the scroll formation, morphology of the clay nanoscrolls also changed subsequently. Reaction time and reaction procedure for metal salt reduction to fabricate Fe-Pd-CNC have a significant effect on the morphology of Fe-Pd-CNC. Higher reaction time results in the caterpillar type of morphology (reported in our previous works (Dhar et al., 2016; Dhar et al. 2018)). Caterpillar kind of morphology results in the formation of similar shape of clay nanoscrolls (Fig. 6.5). Thus, it is clear that the Fe-Pd-CNCs work as structure directing agents. The sonication time too has an effect on the morphology of the scrolls. While shorter sonication time (2 h) resulted in incomplete dissociation of clay sheets and improper scroll formation (Fig. 6.6 (a)), higher sonication time (6 h) resulted in weathered or tampered scrolls (Fig. 6.6 (b)). Calcination of Fe-Pd-CNCs grafted clay sheets in nitrogen atmosphere does not result in the formation of nanoscrolls, but stable ZVI. The morphology of ZVI containing C30B sheets (Fig. 6.7 (a) & (b)) was very similar to Fe-Pd-CNC grafted C30B sheets before calcination. Thus, it could be concluded that clay edges were more active than the clay surface and even after calcination of CNCs, the metal particles remained attached to the edges of the clay sheets, as reported in the literature (Newton et al., 2017; Tournassat et al., 2016). The -

TH-2592_156107017

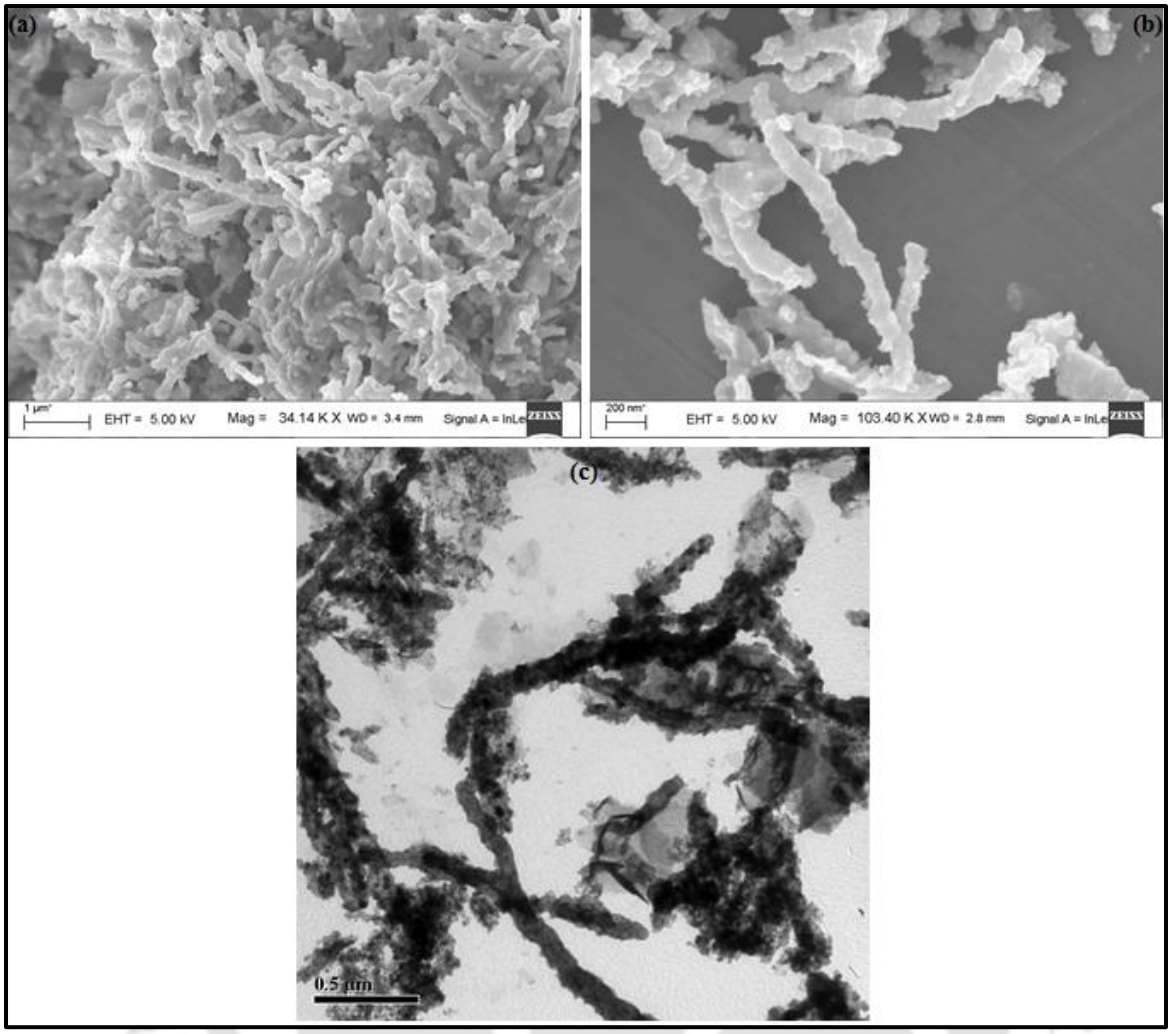

Fig. 6.5 (a) & (b) FESEM images and (c) TEM image of caterpillar shape nanoscrolls.

approximate size of the metal nanoparticles attached on the clay sheet edges was calculated to be approximately 20 nm from the FESEM image (Fig. 6.7 (b)), but the TEM image (Fig. 6.7 (c)) confirmed that except few, most of the metal particles were less than 10 nm in diameter. SAED pattern shown in Fig. 6.7 (d) showed the d-value as 2.02 Å, corresponding to the 2θ value of 44.8°, which confirmed the presence of ZVI nanoparticles on the clay sheets. Presence of γ-Fe_2O_3 could also be seen from the SAED pattern as well as from the XRD graph (Fig. 6.10 (b)). Due to the low content of γ-Fe_2O_3, no scroll formation was observed for the calcined material in the nitrogen atmosphere through FESEM micrographs, but some non-uniform scrolls could be observed in the TEM micrograph

TH-2592_156107017

(Fig. 6.8), which indicated the significant role of γ-Fe_2O_3 for scroll formation, as even low content of γ-Fe_2O_3 could lead to scroll formation.

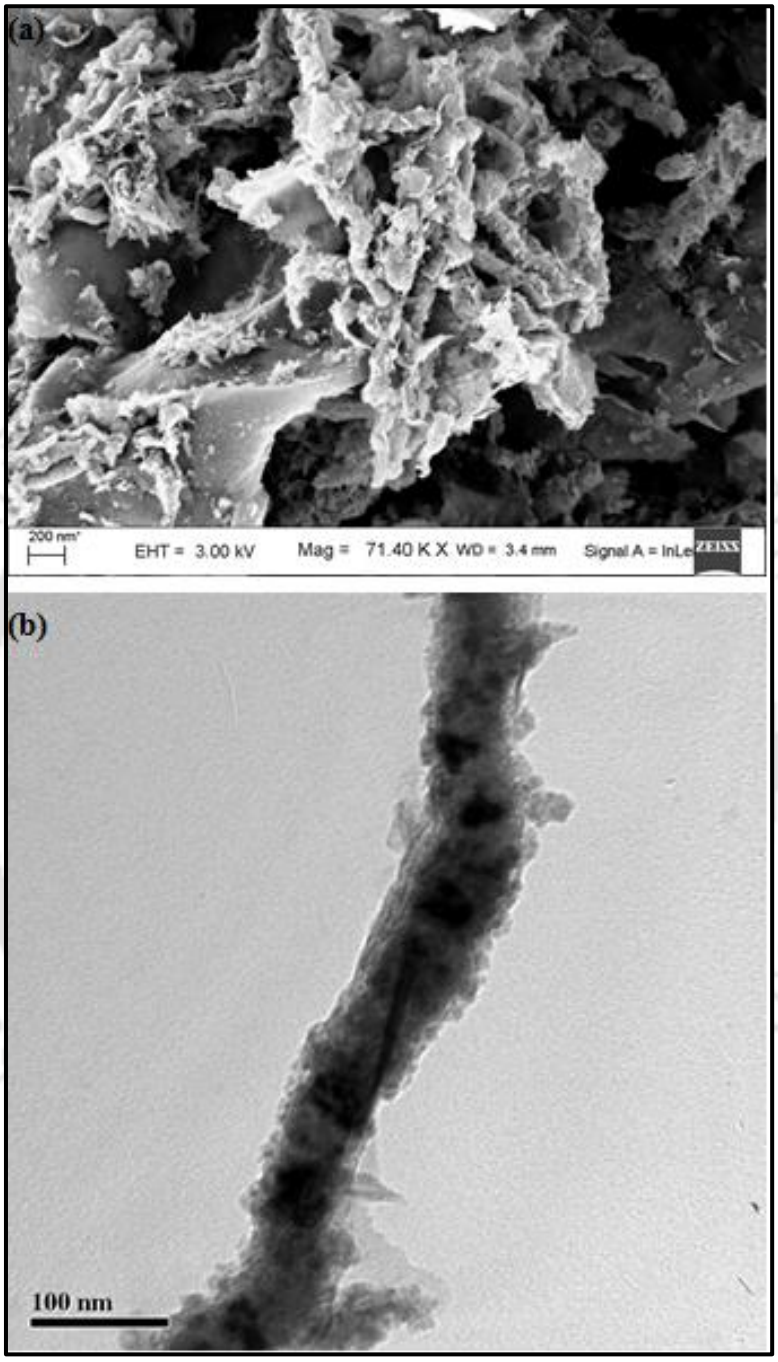

Fig. 6.6 (a) FESEM micrograph of improper scrolls formed due to low sonication time (b) TEM micrograph of tampered type scrolls formed due to more sonication time.

TH-2592_156107017

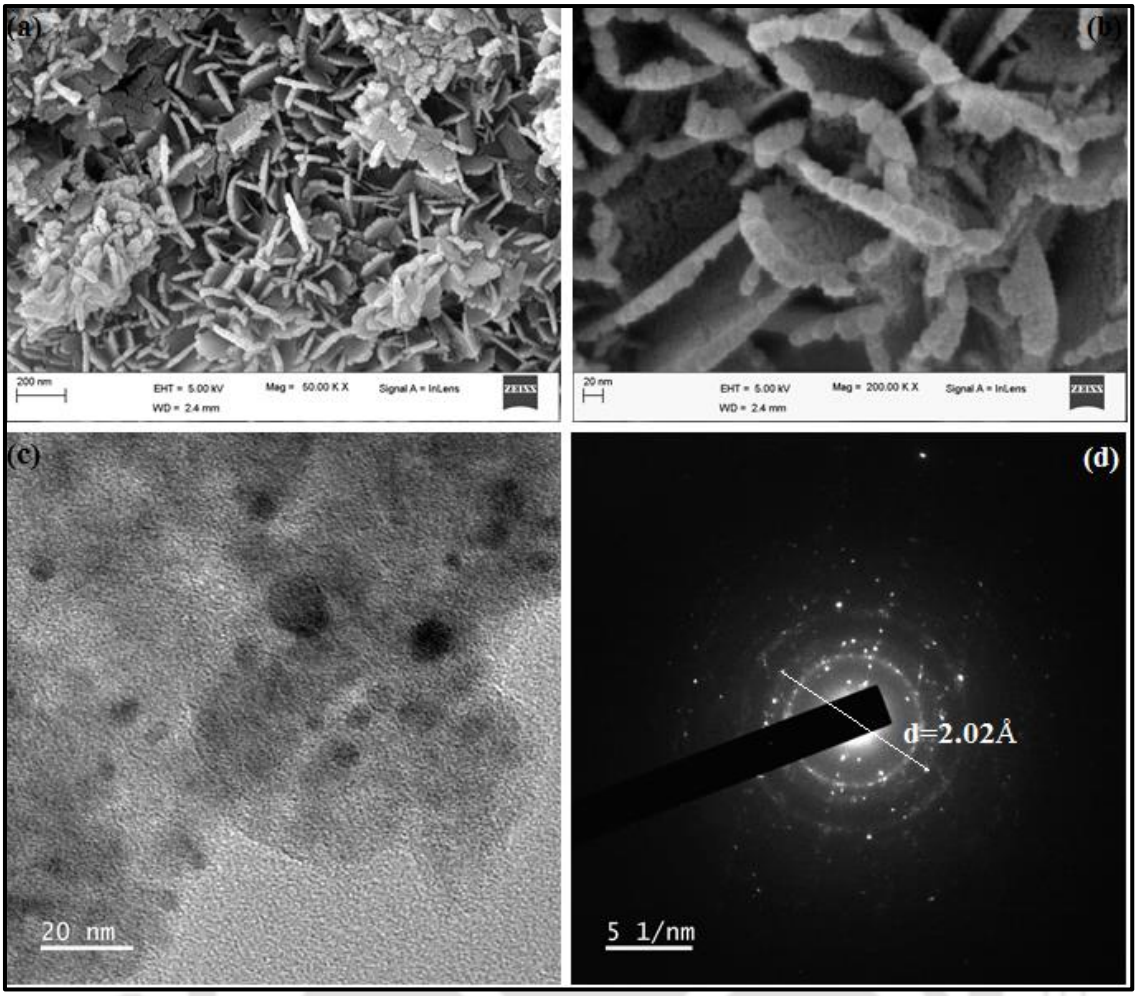

Fig. 6.7 (a) & (b) FESEM images, (c) TEM image and (d) SAED pattern of ZVI containing clay sheets.

6.4.3 X-ray Diffraction Analysis and Magnetic Properties

XRD micrograph of C30B clay shown in Fig. 6.3 displays all the different crystal planes present in the clay. The reflection at 2θ value 4.9° is due to the basal spacing between two layers, which is as mentioned in the morphology section is around 18 Å and represents the layered structure of C30B clay. Where else, the reflections at 2θ value 19.9° and 35° indicates the lattice planes within the clay sheet and corresponds to the d value of 4.5 Å and 2.6 Å, respectively (Bartel et al., 2017). The missing reflection for basal plane at d-spacing 18 Å in the XRD of sonicated clay (Fig. 6.3) confirmed the complete exfoliation -

TH-2592_156107017

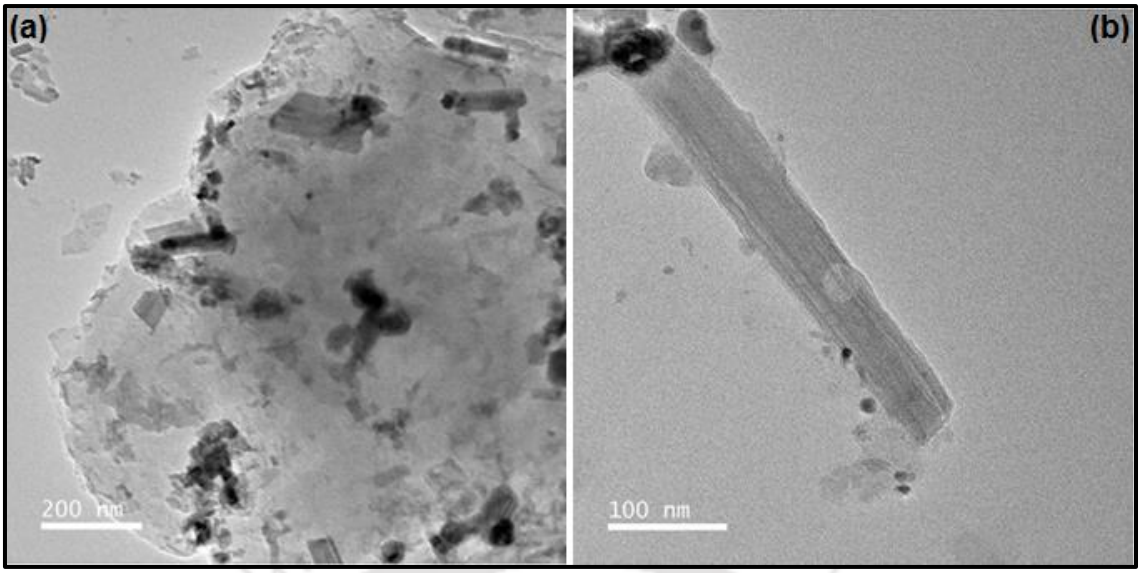

Fig. 6.8 Small amount of non-uniform scrolls formed during the nitrogen atmosphere calcination of Fe-Pd-CNC grafted C30B clay material due to low content of γ - Fe_2O_3.

of C30B clay sheets. At the same time, the reflections for lattice planes within the layer too are missing from the sonicated XRD graph, indicating the disruption of crystalline arrangements of clay sheets. Thus, exfoliated clay sheets were available for interaction with Fe-Pd-CNC and subsequent scrolling. Calcination of Fe-Pd-CNC grafted clay sheets in normal oxygen containing atmosphere resulted in the formation of γ-Fe_2O_3 form of iron oxide, as evident by the formation of dark brown powder (Fig. 6.9) after calcination and also from the XRD micrograph shown in Fig. 6.10 (a). Reflections of different crystalline forms of palladium as well as presence of small amount of ZVI could also be seen in the calcined sample (Fig. 6.10 (a)). But the ZVI reflection was observed at a slightly lower d-spacing (1.98 Å) as compared to the ZVI reflection reported in the literature (d-spacing 2.02 Å) (Li et al., 2012, Dhar et al., 2015). The shift in the ZVI reflection could be attributed to alloy formation. XRD micrograph (Fig. 6.10 (b)) showed the effect of nitrogen atmosphere, which suppressed the formation of γ-Fe_2O_3. Interestingly no reflection shift

TH-2592_156107017

was observed for ZVI in the nitrogen atmosphere calcined material, but the reflections of palladium present at d-spacing 2.24 Å and 1.94 Å in the normal atmosphere calcined material were shifted to lower d-spacing of 2.20 Å and 1.92 Å, respectively. This type of reflection shift for palladium has been reported and attributed to the formation of Pd-Fe alloy (Wang et al., 2012; Gavidia et al., 2017). High stability of the ZVI could be observed from the XRD data (Fig. 6.11), which showed that the absence of inert atmosphere during salt reduction and keeping ZVI in normal atmosphere after fabrication, did not affect its stability much, even after 130 days.

Formation of ZVI during salt reduction in normal atmosphere could be confirmed by Fig. 6.12, which showed the XRD curves of C30B scrolls prepared by using only iron loaded CNCs (Fe-CNCs), by calcination in normal oxygen containing atmosphere and before calcination of the Fe-CNC grafted C30B clay. The Fe-CNC grafted C30B clay before calcination showed the presence of ZVI in XRD curve (Fig. 6.12), without a shift in the ZVI reflection. Due to calcination at high temperature ZVI started to convert into γ - Fe_2O_3 and there was a shift in the reflection of ZVI (Fig. 6.10 (a)) which could be attributed to the alloy formation between ZVI and γ-Fe_2O_3 (having ZVI in core and γ-Fe_2O_3 in the shell). The ZVI reflection in calcined Fe-CNC grafted C30B clay (Fig. 6.12) could not be observed due to complete oxidation of ZVI. While in the nitrogen atmosphere, in the absence of oxygen very little amount of ZVI converted to oxide and rest formed an alloy with palladium. The alloy formation provided ZVI high stability, so that it did not convert to oxides on storage in normal atmosphere, even after 130 days.

TH-2592_156107017

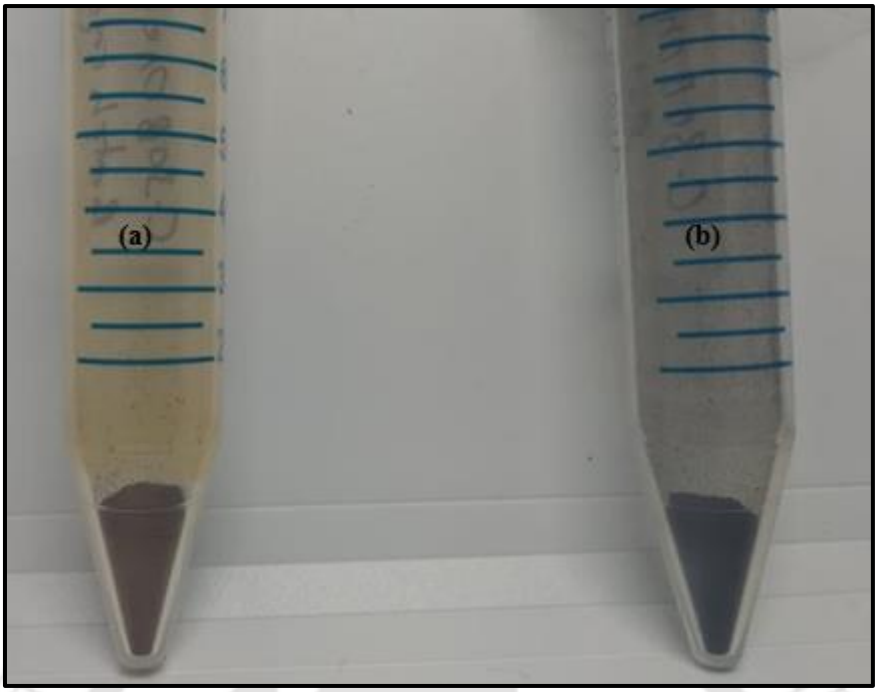

Fig. 6.9 Image of calcined Fe-Pd-CNC grafted clay (a) in normal (oxygen contained) atmosphere (b) in nitrogen atmosphere.

Different forms of iron and its oxides are known to behave differently in the presence of magnetic field. In the present study, it can be clearly seen from the hysteresis loops of both the scrolls and the ZVI containing samples (Fig. 6.13) that they behave ferromagnetically, showing coercivity and retentivity. ZVI contained C30B clay sample had a higher saturation magnetization (37.59 emu/g) as compared to the γ-Fe_2O_3 containing C30B scroll sample (8.45 emu/g), since it had high amount of metallic Fe(0) form. While the coercivity and retentivity values for the C30B scrolls was quite less (34.40 Oe and 1.08 emu/g respectively), the C30B supported ZVI sample had much high coercivity and retentivity (516.86 Oe and 7.29 emu/g respectively) values. High values of coercivity and retentivity of C30B supported ZVI sample showed that it had the nature of forming permanent magnetism, while the higher area of hysteresis loop signified that the energy loss would be higher during the reversal of the magnetic field. The higher energy loss can be utilized for

TH-2592_156107017

induction heating, while the permanent magnetism can help C30B supported ZVI in their easy recovery from different solution phases.

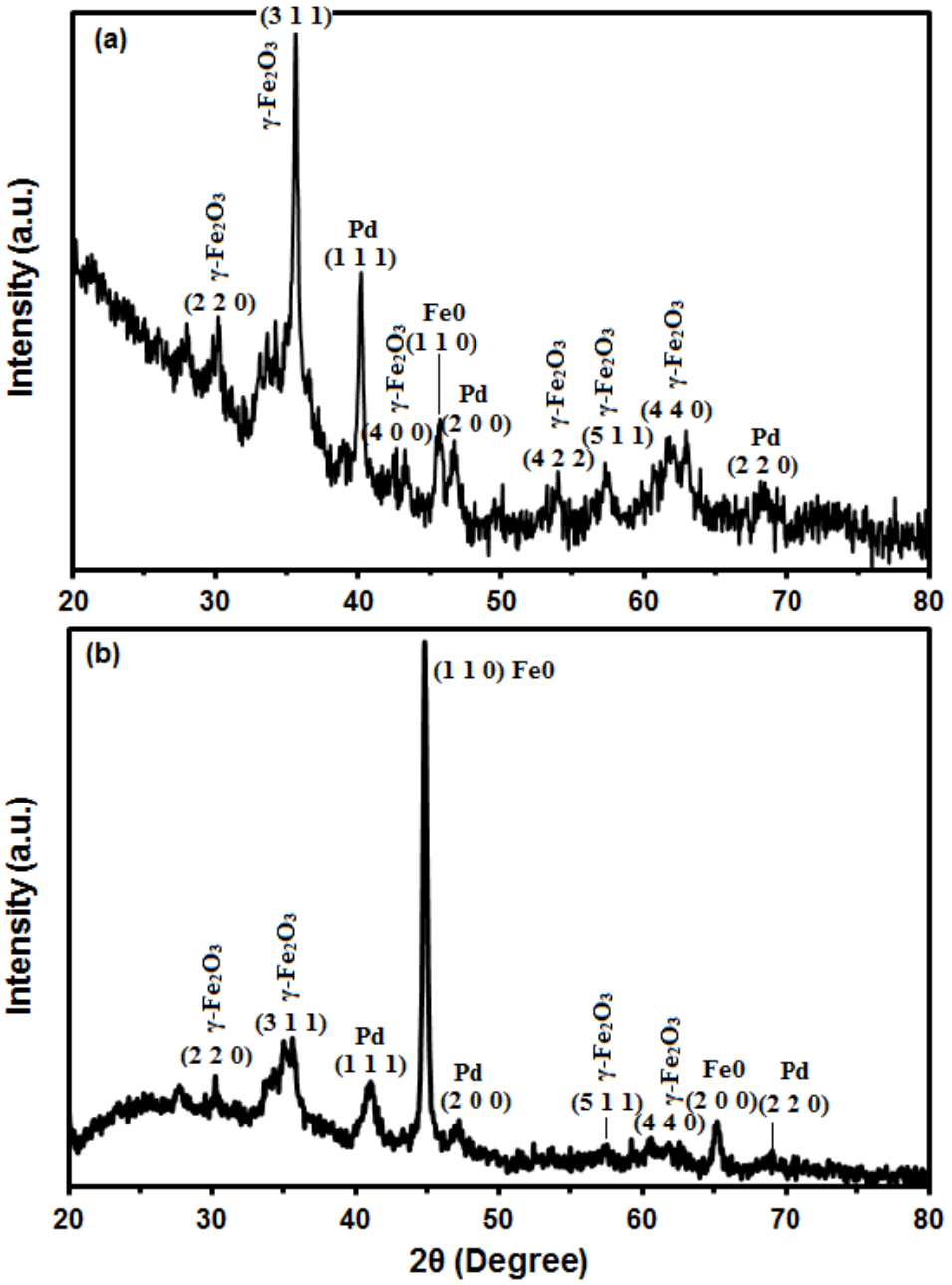

Fig. 6.10 XRD curve of (a) C30B clay nanoscrolls and (b) clay supported Pd and stable ZVI nanoparticles.

TH-2592_156107017

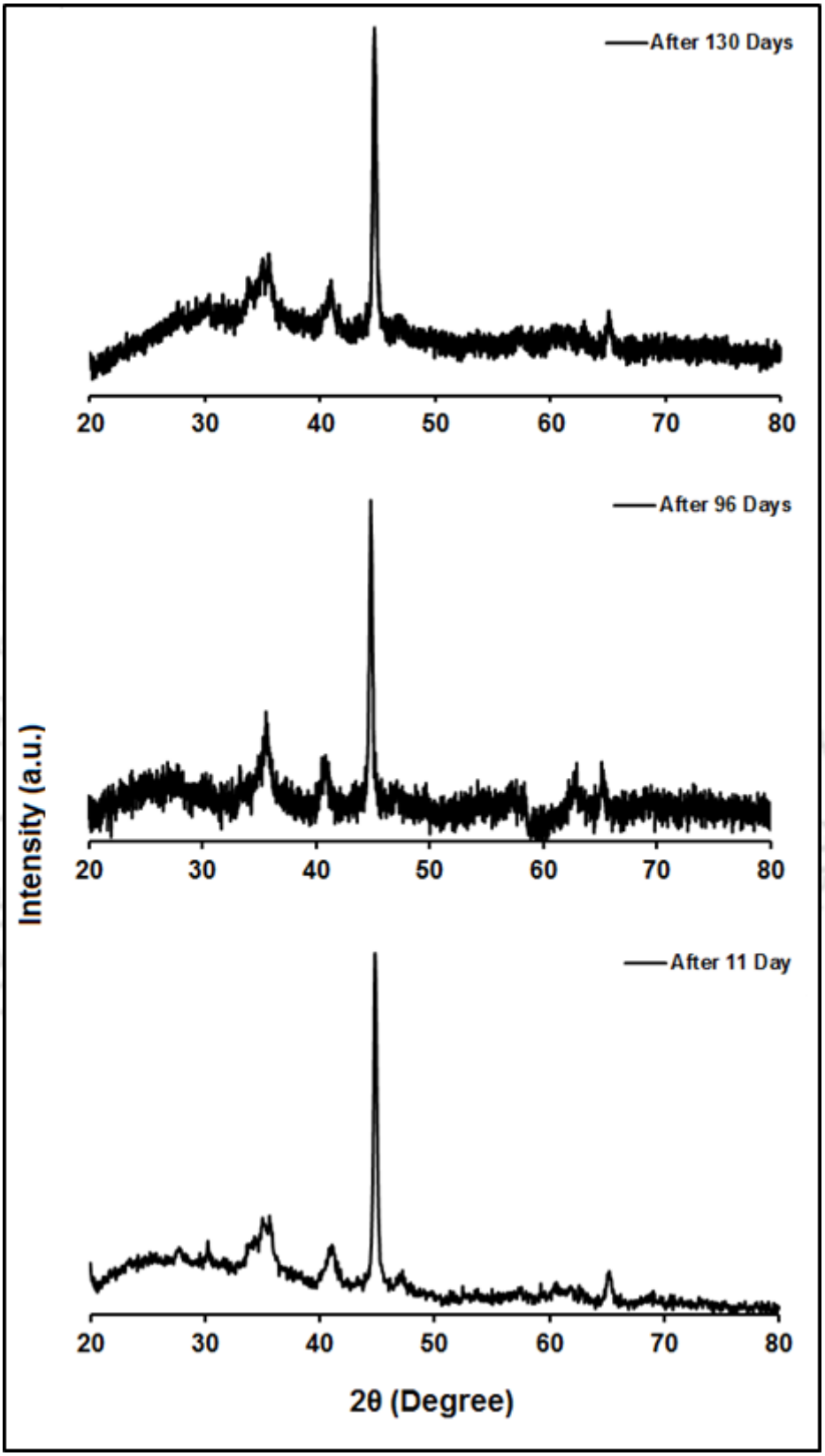

Fig. 6.11 XRD curves of Pd and stable ZVI on clay after specific number of days of synthesis.

TH-2592_156107017

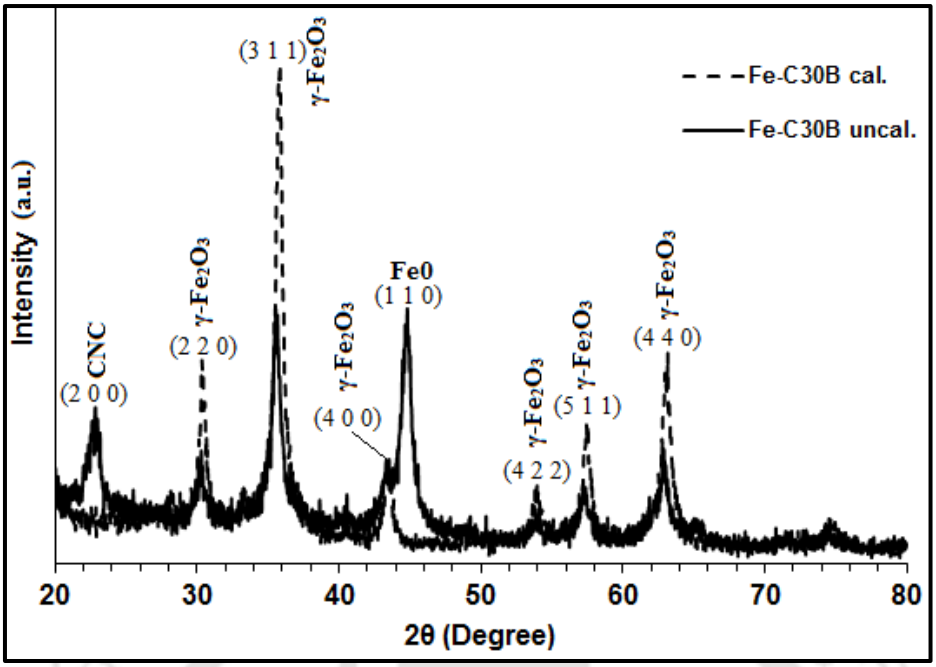

Fig. 6.12 XRD micrographs of C30B scrolls, prepared from Fe-CNC (without palladium loading) by calcination (Fe-C30B cal.) and Fe-CNC graft C30B clay before calcination (Fe-C30B un-calcination).

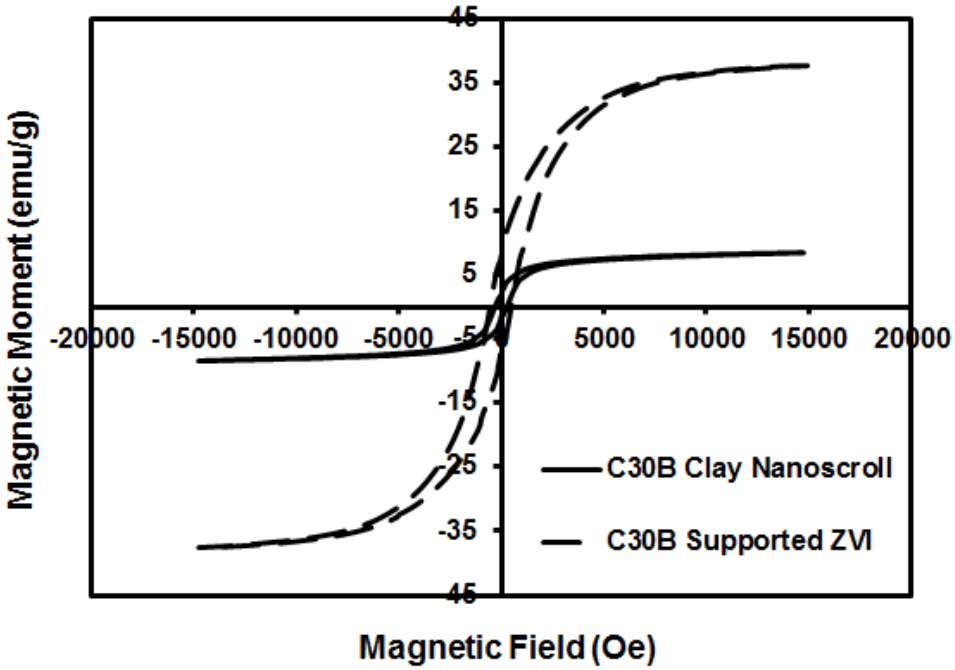

Fig. 6.13 Magnetic hysteresis loops of C30B clay nanoscrolls and C30B supported ZVI.

TH-2592_156107017

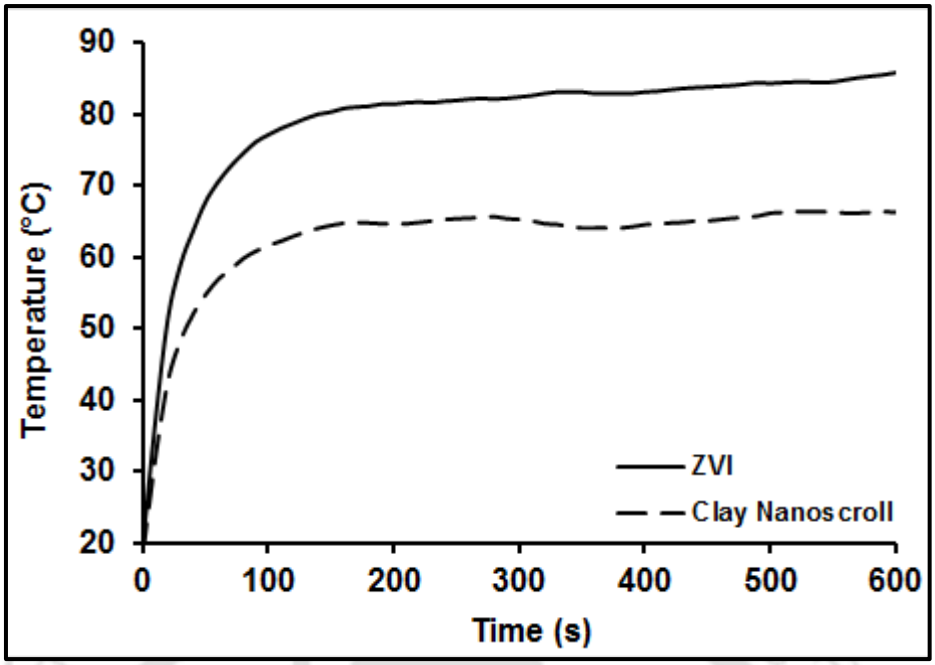

Fig. 6.14 Time-temperature curve for the induction heating of clay nanscroll and ZVI samples.

The effect of magnetic properties of ZVI on induction heating in comparison to clay nanoscroll could be observed from Fig. 6.14, where it could be observed that while the clay nanscroll was able to reach ≈65°C temperature, ZVI reached up-to ≈85°C with the same amount of material. Thus, it can be concluded that C30B supported ZVI has many possibilities of utilization in biomedical applications as well as environmental remediation applications.

6.4.4 Composition Analysis

EDX spectra of C30B clay (Fig. 6.15) showed high carbon content due to the presence of modifier. C30B is a 2:1 type clay, so the ratio of Si:Al is expected to be 2:1. Little lower content of Al and the presence of Fe and Mg showed that some amount of Al had been substituted by Fe and Mg in octahedral $AlO_2(OH)_4$ sheets. While small amount of Ca^{+2} and Na^+ cations were also detected in the C30B clay. Presence of nitrogen due to quaternary

TH-2592_156107017

ammonium salt modifier could not be detected. Fig. 6.16 shows the EDX spectra and elemental mapping of a clay nanoscroll. The spectra showed reduced carbon content, which signified that the organic modifier had been removed during prior processing by sonication and calcination. The carbon present in the sample was mainly from CNCs after calcination. Elements such as Al, Mg, Ca and Na present in the EDX spectra of C30B clay (Fig. 6.15), were missing from the spectra. From the absence of Ca^{+2} and Na^{+} cations and the removal of organic cation modifier, it could be easily assumed that the overall net negative charge on the clay sheets had been increased. Al and Mg could not be detected, as they were present in the middle layer of 2:1 type clay sheet and due to scrolling, Si and O present on the surface of SiO_4 layer could only be detected. The top layer was formed by tetrahedral SiO_4, which could be verified from the elemental mapping of clay scroll shown in Fig. 6.17, where Si was excluded from the mapping. This resulted in the blank boundaries of the clay scroll and showing that the top surface was tetrahedral SiO_4 sheet. Pd content on the surface was detected to be very low (0.05 wt%). The amount of Pd present inside the clay scroll might be higher than that of the surface, but still it would be overall very low as compared to the other elements, as a very low percentage of precursor $PdCl_2$ salt was taken during the synthesis.

6.4.5 Mechanism of Scroll Formation

Number of research articles are available on graphene nanoscroll formation, utilizing the magnetic nature of iron oxide nanoparticles. The work done by Sharifi et al. (2013) nicely explains the role of magnetic nature of γ-Fe_2O_3 nanoparticles in the formation of graphene nanoscrolls. But in the current investigation of C30B clay nanoscrolls, magnetic properties of the metal nanoparticles were not the driving force for scrolling, as scrolling was not observed in the case of higher magnetic material having ZVI nanoparticles. The clay sheets

TH-2592_156107017

in the C30B clay had an overall negative charge due to the substitution in tetrahedral and octahedral sheets, which was balanced by the cations and the cationic modifier. Removal of charge balancing cations and modifier resulted in charge imbalance and the exfoliated clay sheets got a net negative charge.

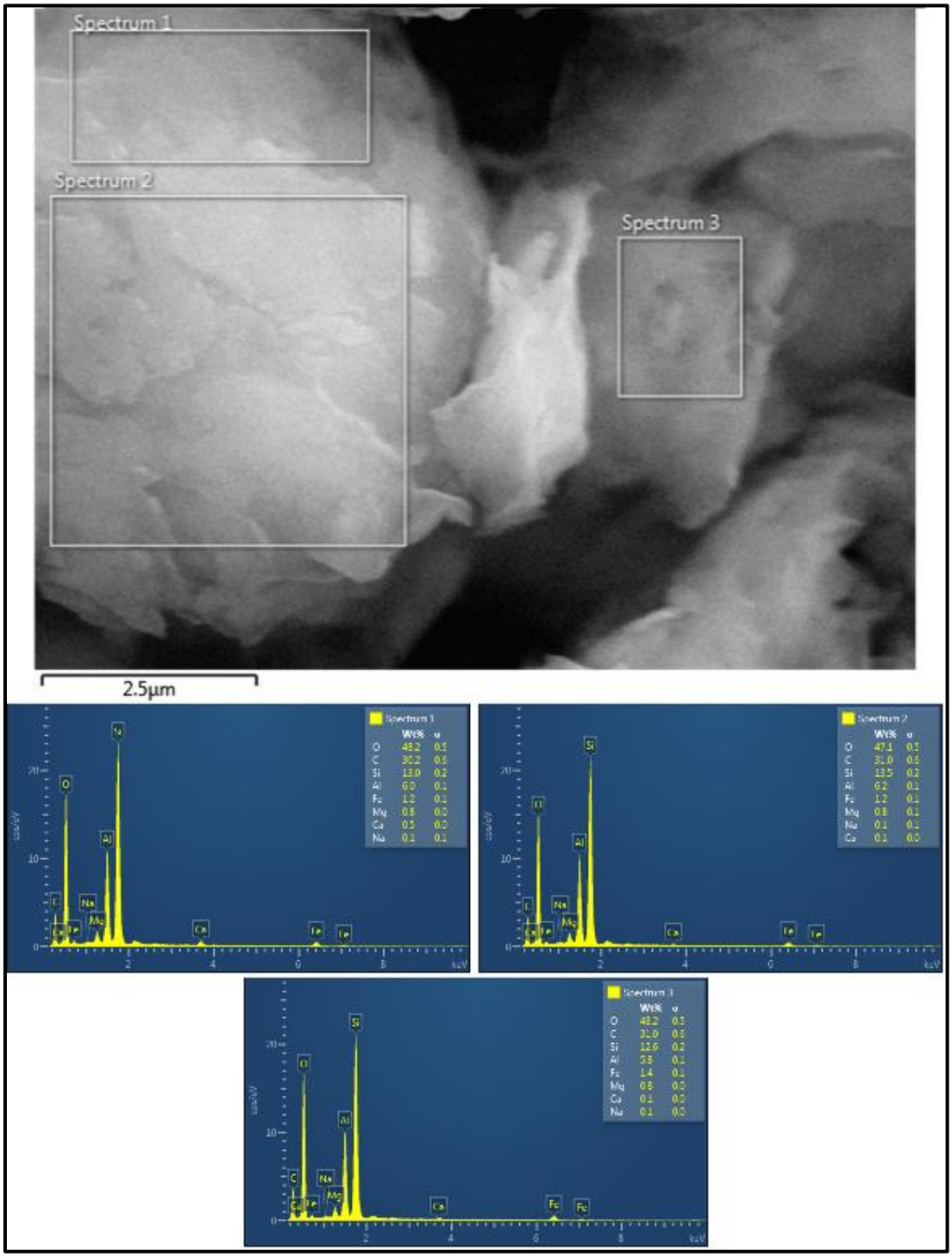

Fig. 6.15 EDX spectra of C30B clay.

TH-2592_156107017

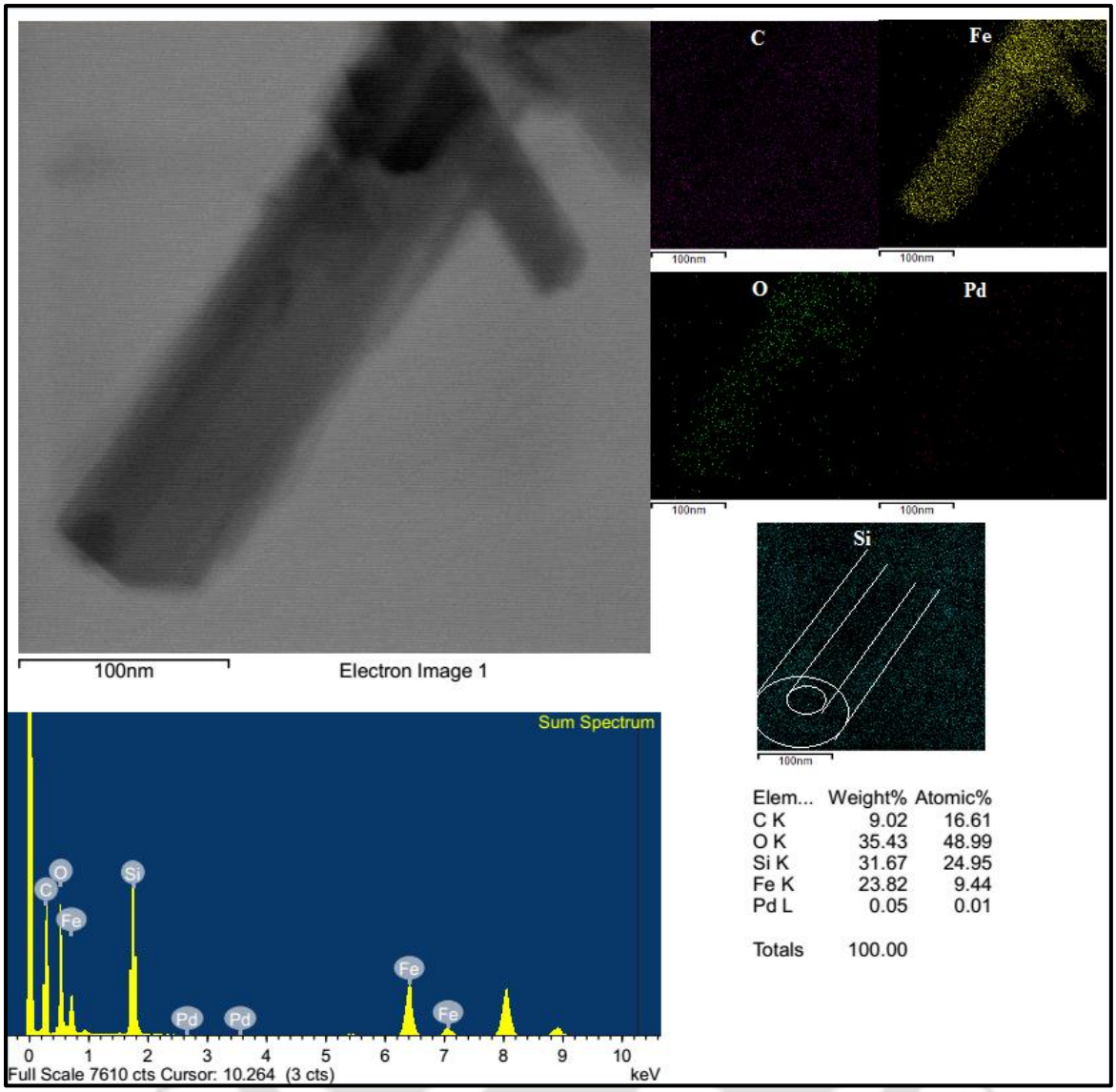

Fig. 6.16 EDX spectra and elemental mapping of clay nanoscrolls.

So, if a cylindrical structure directing agent, having a net positive charge could be introduced, the clay sheets could wrap up around it to form cylindrical nanoscrolls, which actually happened in the current study. γ-Fe_2O_3 nanoparticles present in the clay nanoscrolls provided electrostatic charge to have electrostatic interaction with clay sheets and subsequently form the scrolls. Reports by Nikumbh, et al. (1991) stated that there is loss of oxygen during thermal formation of γ-Fe_2O_3, which gives it positive charge. This positive charge can be compensated by converting some of Fe^{+3} of γ-Fe_2O_3 to Fe^{+2} form of oxide.

TH-2592_156107017

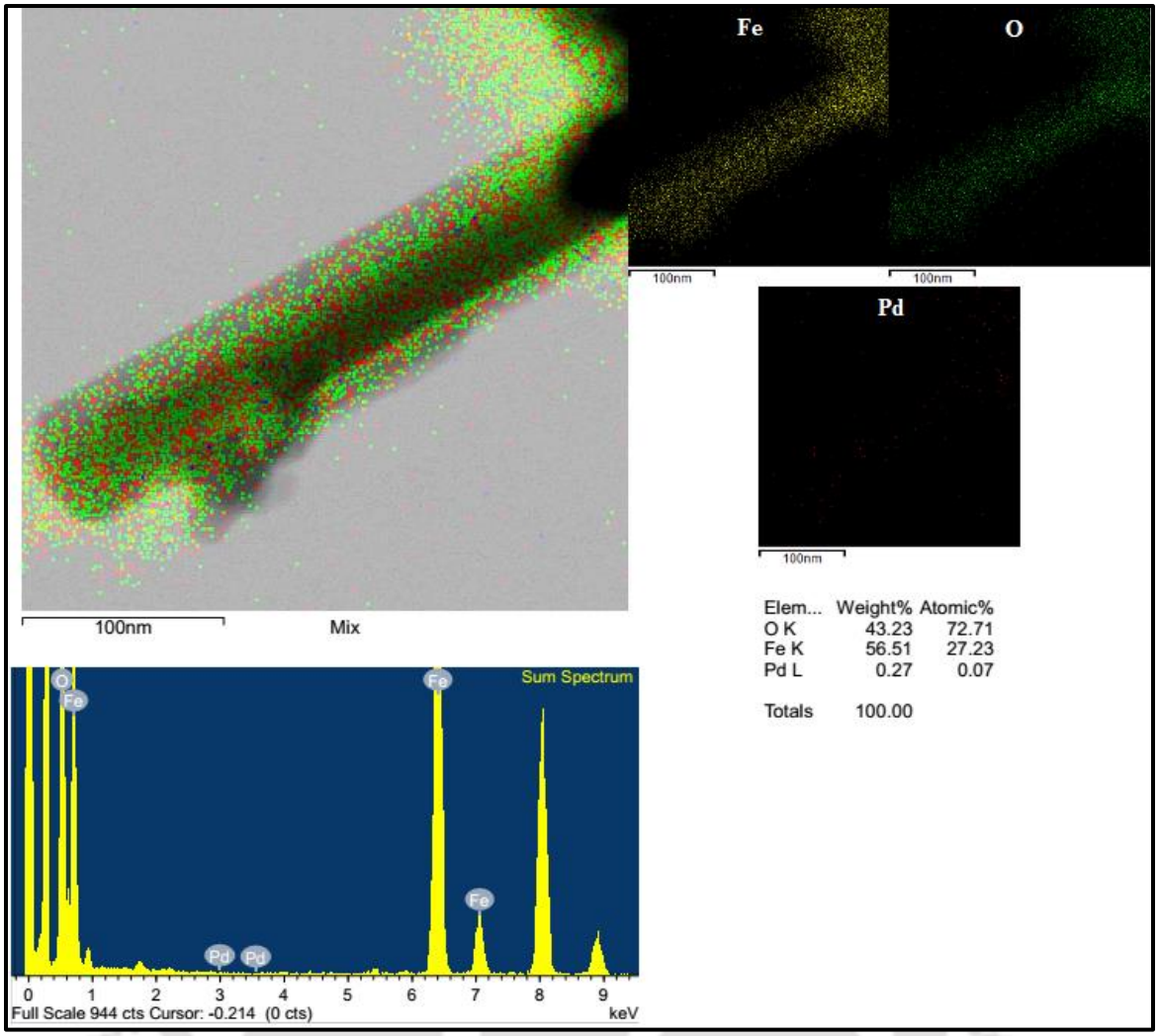

Fig. 6.17 EDX spectra and mapping of Fe, Pd and O on clay nanoscrolls.

But in the present study, negatively charged clay sheets were already present which could compensate the charge misbalance and simultaneously form scroll by electrostatic charge interaction. The electrostatic interaction can be direct charge to charge as well there could be possibility of formation of dipoles in the γ-Fe_2O_3 due to the presence of negatively charged surface and these dipoles could also electrostatically interact with the negatively charged clay sheets. As mentioned due to removal of oxygen γ-Fe_2O_3 contains iron cations and cationic vacancies in its structure (Grau-Crespo et al., 2010; Takei & Chiba, 1966; Wu et al., 2010), so it is possible to form dipole in γ-Fe_2O_3. Talapin et al. (2007) have described such dipolar interactions of nonlocal dipoles in several nanoparticles including

TH-2592_156107017

γ-Fe_2O_3. There are reports of such dipole interaction resulting in different morphology also (Wang et al., 2017; Layek et al., 2010). Moreover, the ferromagnetic nature of γ-Fe_2O_3 present in the clay scrolls could be correlated to the dipole interaction. Super paramagnetic behavior of γ-Fe_2O_3 nanoparticles has been reported in a large number of researches. But, γ-Fe_2O_3 present in the clay nanoscrolls exhibited ferromagnetic nature, which could be due to the strong dipole interaction of γ-Fe_2O_3 with clay sheets, restricting the magnetic moment and resulting in permanent magnetism.

6.4.6 Hydrogen Peroxide Reduction on Clay Nanoscroll in Alkaline Medium

Here, we have shown the use of clay nanoscrolls as electrocatalyst for hydrogen peroxide reduction in alkaline medium and thus can be used as cathode electrocatalyst in alkaline DMFCs. Fig. 6.18 (a) shows the current density-potential curve for H_2O_2 reduction in alkaline medium. From Fig. 6.18 (a) it could be observed that the addition of H_2O_2 resulted in sharp increase in the current density below -0.2 V, due to current generation from H_2O_2 reduction, in addition to the OH^- ions present in the solution. Effect of H_2O_2 concentration could also be clearly seen from the Fig. 6.18 (a) as current density increased continuously with an increase in the concentration of H_2O_2. With lower loading of palladium, the clay nanoscrolls show the similar performance for H_2O_2 reduction as reported for the higher palladium content electrocatalysts (Momeni & Nabipour, 2015; Cao et al., 2008). As well as Fig. 6.18 (b) also shows its better performance compare to the commercial Pd-C catalyst. From the Fig. 6.18 (b) it can be observed that clay scrolls show the same performance (CD ≈140 mA/cm2) with ≈0.003 mg Pd as the commercial 10 wt.% Pd-C shows with ≈0.35 mg Pd loading. Thus, the palladium loaded clay nanoscrolls are a superior candidate for the electrocatalyst in electrochemical reduction of H_2O_2 in alkaline medium.

TH-2592_156107017

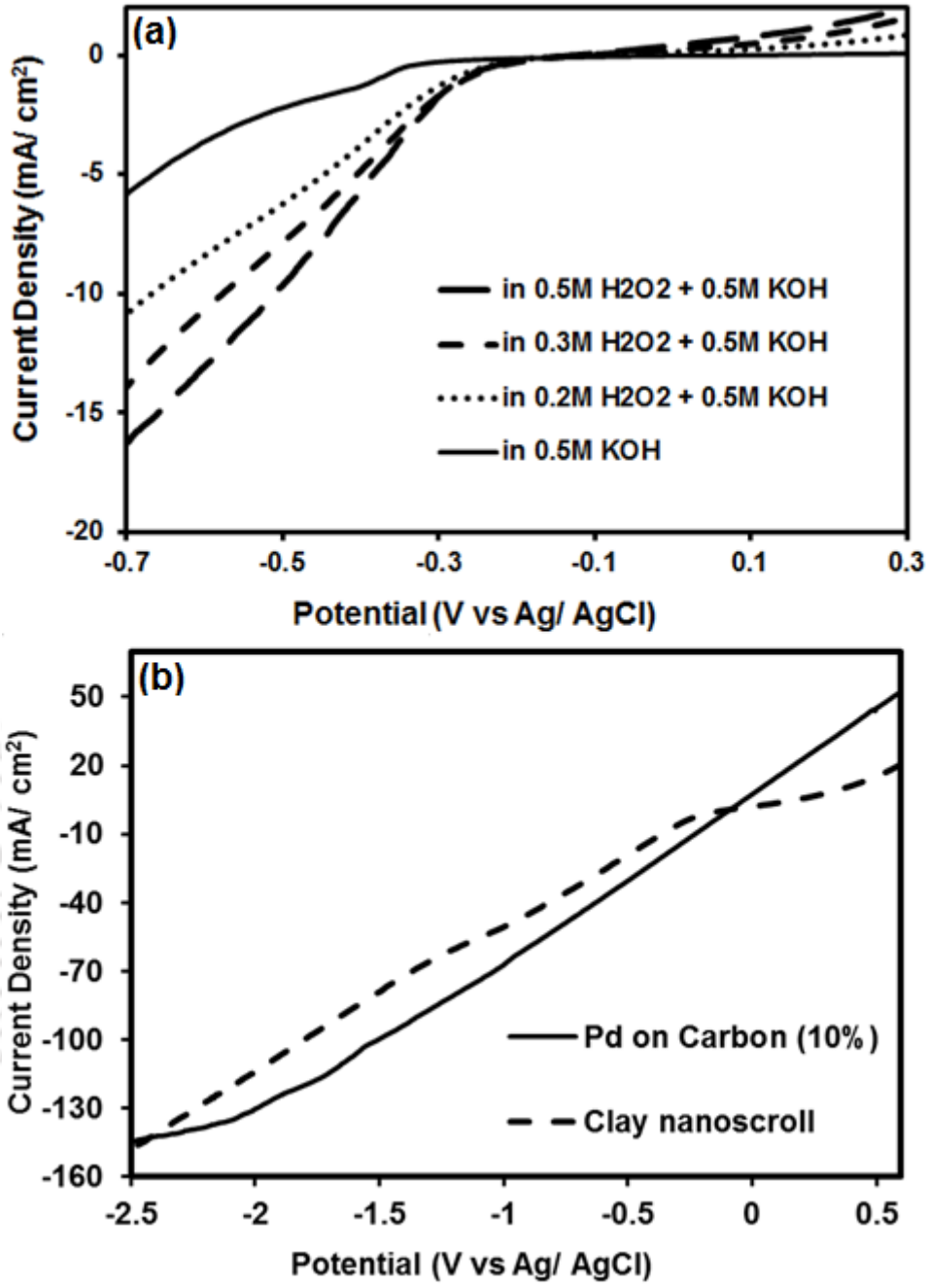

Fig. 6.18 (a) Current density potential curve for H_2O_2 reduction in 0.5M KOH solution with different H_2O_2 concentrations on clay nanoscrolls (b) comparison of current density of clay scrolls with commercial Pd-C catalyst in 0.5M KOH and 0.5 M H_2O_2 solution.

TH-2592_156107017

6.4.7 Fuel Cell Performance

Performance of the clay nanoscrolls as cathode electrocatalyst for H_2O_2 reduction along with PVA-HH based membrane for alkaline DMFCs was obtained through single cell analysis. Due to its stable nature and better ionic conductivity, annealed PVA-5wt% HH membrane was used for analysis and the results obtained for it are shown here through the polarization curve and power density curve in Fig. 6.19. The open circuit voltage (OCV) of the single cell was observed to be around 0.77 V. The effect of activation losses, ohmic losses and mass transport losses is clearly visible in the polarization curve. Maximum power density was observed to be around ≈33.8 mW/cm^2 at the current density of 96 mA/cm^2 for 3M methanol + 2M KOH solution and 6M H_2O_2 as oxidant in 2M KOH solution. The fuel cell performance results obtained for the clay nanoscroll electrocatalyst and annealed membrane sample clearly shows their applicability for alkaline DMFC.

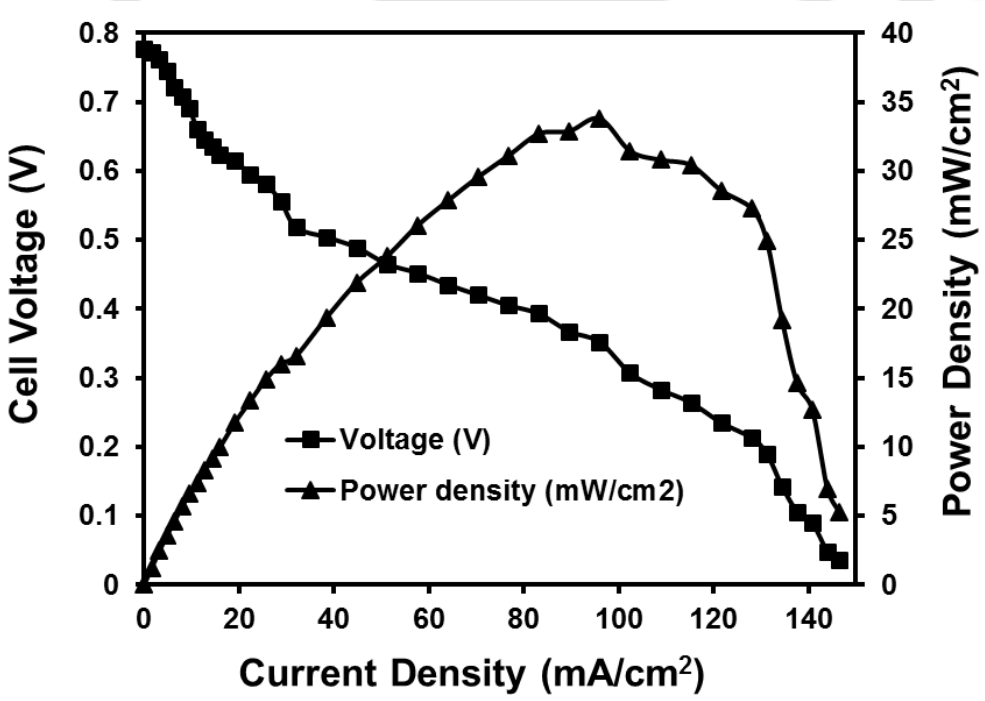

Fig. 6.19 Alkaline DMFC performance of the clay nanoscorlls by polarization curve and power density curve.

TH-2592_156107017

Theoretical OCV of alkaline methanol-H_2O_2 based fuel cell for direct 2-electron path is quite high, but generally H_2O_2 reduces by indirect 4-electron path and thus, the theoretical potential becomes lower (Cao et al., 2008). So, the OCV of the methanol-H_2O_2 system is just slightly higher (0.77 V) compared to the OCV reported for the methanol-O_2 system (0.74 V) in the manuscript.

6.4.8 Hydrogen Adsorption Study

Fig. 6.19 shows the adsorption isotherm of hydrogen at 273 K temperature with varying pressure. The prepared C30B clay nanoscrolls showed good hydrogen adsorption (≈0.14 wt%) at 273 K and 20 bar pressure. The BET surface area obtained for clay nanoscrolls (≈47 m^2/g) is more than 2 times higher than the surface area of C30B clay (≈18 m^2/g). Thus, hydrogen storage capacity of clay nanoscrolls could be attributed to their higher surface area, morphology and the presence of palladium nanoparticles inside it -

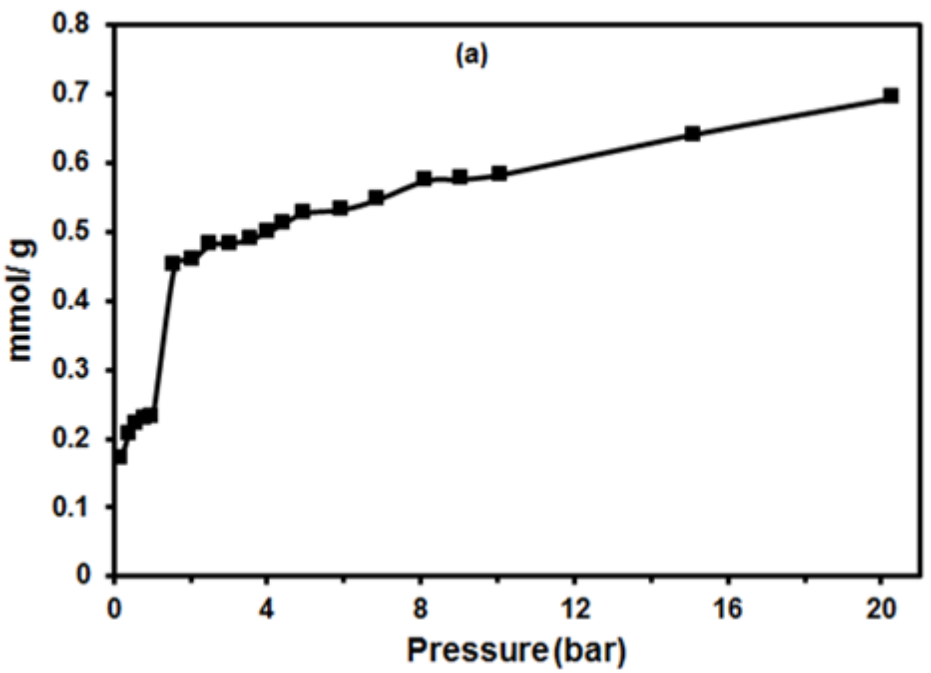

Fig. 6.20 Hydrogen adsorption isotherm of clay nanoscrolls.

TH-2592_156107017

which dissociates H_2 into H atoms through spill over mechanism, resulting in chemisorption of H_2 (Psofogiannakis & Froudakis, 2011). The presence of dipoles of γ- Fe_2O_3 nanoparticles also helped in the physisorption of hydrogen and the cylindrical morphology helped in its entrapment. It was observed that even though the palladium content in clay nanoscrolls was lower than 1 wt%, but it showed hydrogen adsorption capacity in the same range (≈0.16 wt%) as of around 1 wt% palladium loaded graphene nanoscrolls, as reported by Dhar et al., 2018.

Table: 6.1 Hydrogen adsorption capacity of various clay based materials.

Material	**Hydrogen adsorption condition**	**Hydrogen adsorption (wt%)**	**Reference**
Titanosilicate-sepiolite	25°C and 40 bar	0.02	Carvajal et al., 2019
NaMt	25°C and ≈1 bar	0.005	Bouazizi et al., 2019
NaMt-H20-Cu	25°C and ≈1 bar	0.054	Bouazizi et al., 2019
NaMt-H20-Pd	25°C and ≈1 bar	0.046	Bouazizi et al., 2019
Carbon-Mt	25°C and 200 bar	≈0.2	García et al., 2013
Carbon-sepiolite	25°C and 200 bar	≈0.4	García et al., 2013
Halloysite (HNT1, HNT2, HNT3, HNT4, HNT5)*	−196°C and 1 bar	0.01–0.10	Ramadass et al., 2019
Halloysite	25°C and 30 bar	0.436	Jin et al., 2014
C30B Mt nanoscrolls	0°C and 20 bar	0.14	This study

**HNT1, HNT2, HNT3, HNT4 and HNT5 are halloysite obtained from five different locations.*

TH-2592_156107017

It could be concluded that the combined effect of the morphology of nanoscrolls, presence of the palladium nanoparticles and dipole moment provided the clay nanoscrolls with good hydrogen storage capacity. Table 6.1 shows the comparison of hydrogen adsorption capacity of clay nanoscrolls reported in the current study with hydrogen adsorption capacity of halloysite nanotubes and other clay materials reported in the recent reports. The hydrogen adsorption capacity of clay nanoscrolls is comparable with the halloysite nanotubes, which indicates that the scroll fabricated in current study are able to mimic the halloysite nanotubes.

6.5 Conclusions

The chapter summarizes a novel process for fabrication of clay nanoscrolls first time using 2:1 type Mt (C30B clay), which can be a suitable alternate of halloysite nanotubes. In addition, highly stable clay supported ZVI could also be synthesized by the same process by just changing the calcination environment to nitrogen. Fe-Pd-CNCs acted as the structural directing agent in this study, providing a template for scroll formation, while electrostatic interaction had been the driving force for scroll formation, in which charge deficiency resulting due to the removal of oxygen from γ-Fe_2O_3 structure plays a role by creating positively charged holes. Similarly, formation of a core shell type of alloy between Pd and Fe has been considered as a reason for the formation of stable ZVI. Moreover, C30B supported ZVI, having permanent magnetism can help in induction heating and thus can be utilized in various biomedical applications. At the same time, ZVI, known for high catalytically activity, could also be utilized in various applications including environmental remediation. The clay nanoscrolls obtained in the current study have hydrogen storage capacity in the range of halloysite nanotubes reported in the recent literature, which confirms that prepared nanoscrolls are able to mimic the halloysite nanotubes. The prepared

TH-2592_156107017

clay nanoscrolls were mainly utilized for H_2O_2 reduction in alkaline medium and it showed good electrochemical perofrmencve for H_2O_2 reduction in alkaline medium with lower palladium content. The current density obtained by clay nanoscrolls for H_2O_2 reduction was in the same range with significantly high Pd loaded commercial Pd-C catalyst. Thus, the clay nanoscrolls are suitable electrocatalyst for H_2O_2 reduction in alkaline medium. In summary, we are able to fabricate clay nanscrolls, an alternate of halloysite nanotubes by sustainable method using cellulose nanocrystals and cloisite 30B clay, which are able to mimic the halloysite nanotubes and at the same time with similar method we are able to fabricate stable ZVI nanoparticles.

TH-2592_156107017

Chapter 7:
Conclusions and Future Scope

7.1 Conclusions

The objective of the current work was to develop a new set of materials for alkaline DMFCs which are synthesized by using bio-based materials and can address some of the problems associated with the existing materials used in alkaline DMFCs. Here, we have derived bio-based ion conductive materials from different resources including bio-wastes, which includes different types of CNCs and human hair hydrolysate based ion conductive material. CNCs showed there applicability as ion conductive materials, while the human hair based ion conductive material utilized the nature of amino acids present in the structural unit of keratinic protein. The cationic functionalities present in the amino acids worked as the charge transfer sites when the hair hydrolysate was utilized in anion exchange membrane. To understand how these cationic functionalities help in charge transfer, MD simulation studies were carried out by taking a model sample peptide having the cationic functionalities present in the hair hydrolysate material. On the basis of MD simulation studies, a mechanism of charge transfer was proposed for the AEMs having such ion conductive materials. To have stable electrocatalyst and catalyst support, montmorillonite clay based support in combination with CNCs was utilized, which demonstrated its applicability as stable catalyst support in alkaline medium. As explained in the chapter-1, the major reason for catalyst performance reduction in presence of H_2O_2 is attack of H_2O_2 on the carbon support at the active sites. The attack of H_2O_2 and oxidation of carbon support is proposed to happen mainly by two pathways: first is by direct oxidation of carbon support

TH-2592_156107017

by H_2O_2 and second is formation of highly active hydroxyl radicals and its attack on carbon support (Schulenburg et al., 2003; Lefèvre & Dodelet, 2003). To prevent the degradation of catalyst by H_2O_2 attack modified montmorillonite clay was used as support material for Pd-Fe catalyst by encapsulating them inside the scroll formed by the clay. The major conclusions drawn from the current research are summarized below pointwise:

- In the primary work, it was demonstrated that CNCs having different acidic functionalities, exhibit different properties, which are controlled by CNC morphologies. CNCs based solid polymer electrolyte membranes for DMFCs had good thermo-mechanical stability and very low swelling characteristics with improved methanol barrier properties. The comparative study made with different CNCs as ion conductive nanofiller showed that the properties such as water uptake, swelling behavior and ionic conductivity of the base PVA membrane were positively impacted by CNCs. PVA-CS-HNO_3 CNC nanocomposite membrane has superior thermo-mechanical stability, higher water uptake, very low swelling in moisture environment and higher ionic conductivity compared to the PVA-CS-HCl-CNC and PVA-CS-H_2SO_4-CNC nanocomposite membranes. Thus, it was demonstrated that CNCs can work as ion conductive and with suitable morphology and further modification with charge transfer functionalities can significantly improve their applicability in polymer electrolyte membranes.
- Human hair bio-waste was utilized to have an ion conductive material. The hair hydrolysate obtained by simple and green thermal hydrolysis of human hair bio-waste containing 70 wt.% of proteinaceous material was successfully utilized as ion conductive material to fabricate AEMs for alkaline DMFC. Presence of 27 wt.% of charged amino acids and 19 wt.% of polarizable amino acids in the hair hydrolysate helped in the charge transfer. Presence of 7 wt.% arginine in hair hydrolysate, which

TH-2592_156107017

has a continuous delocalized net positive charge in the guanidino group, making it stable even in high alkaline medium, played a critical role to provide anion conductivity to the membrane. The hair hydrolysate was utilized to successfully modify CNCs, which worked as ion conductive material to enhance the conductive properties of CS matrix based AEM. Direct use of hair hydrolysate in PVA matrix formed rod and flower shape morphology by aligning its hydrophobic parts inward and hydrophilic parts outward which interacted with hydrophilic PVA matrix. The hair hydrolysate crystals formed a channel-like continuous network, which in presence of water and alkaline medium provided a straight path for ion transfer. Annealed AEM sample showed improvement in the various properties related to the AEMs with slight decrease in conductvity. Hair hydrolysate based membranes showed their suitability for the alkaline DMFCs with having good stability in alkaline medium.

- MD simulation studies were utilized to demonstrate the charge transfer mechanism in AEMs having charge transfer functionalities similar to hair hydrolysate. A model hair keratein derived antimicrobial peptide KAMP-19 was used with PVA matrix for MD simulation studies. Effect of low water zone formation due to hydrophobic sections of KAMP-19 was observed on ionic conductivities. Methanol diffusion in the system followed the same trend, which confirmed that methanol diffusion is governed by electro-osmotic drag. Lowest KAMP-19 contained sample showed highest conductivity among all the systems due to more number of water molecules around the main charge transfer site of guanidino group cation, showing the importance of water for charge transfer. There were three different source of charge transfer in the system and the charge transfer mainly takes place by hopping of OH^- from one site to other by Grotthuss mechanism. Around PVA the water channels

TH-2592_156107017

work as charge carrier by formation of $H_3O_2^-$ and H_2O back and forth, where OH^- hops from one water molecule to another forming $H_3O_2^-$ ions by H-bonding and converting back to water. Around ammonium cation, it has hydrogen bonded water molecules, while it has better interaction with OH^-, but the charge transfer follows the same mechanism as of OH^- in the water channels by hopping from one water molecule on amine group to another water molecule. The third charge transfer site is guanidino group present in the peptide, which follows a little different mechanism. On guanidino group cation OH^- hops in its original form, instead of forming an intermediate due to strong interaction. From bulk system a $H_3O_2^-$ ion jumps on the cation leaving an OH^- ion on it. This OH^- either can jump directly to the next guanidino cation, if there is one present in close proximity, otherwise it jumps back to another water molecule to form $H_3O_2^-$ by H-bonding and diffuses back to bulk system. Guanidino group having strong interaction with OH^- and transfer of OH^- without formation of intermediate provides faster charge transfer site.

- To have stable nature of electrocatalyst in alkaline medium for methanol oxidation, a micro-ion complexation-based gel was formed using bio-derived CNCs and CNa^+ clay, by simple, green and scalable approach. Catalytically active Pt/Pd nanoparticles have been encapsulated in CNa-CNC gel. The prepared Pt/Pd-loaded complexes have shown very good activity towards methanol oxidation in alkaline medium along with significantly high stability. The Pt based catalyst showed better performance for methanol oxidation, while Pd based catalyst showed much better stability in alkaline medium for methanol oxidation. High stable nature of the prepared catalyst was attributed to the stable nature of clay and possible catalytic participation of metal oxides present in the clay during methanol oxidation. Further,

TH-2592_156107017

LSV investigation on Pt-CNa-CNC catalyst have shown the critical role of adsorbed –OH on catalyst support, and how the clay-based support can have positive impact on catalyst performance. On the basis of LSV analysis, a hypothesis has been made for Pt-CNa-CNC catalyst, that reaction intermediates formed during the methanol oxidation are being removed during the forward CV scan as opposed to the many reports on Pt catalyst, which assume it to happen during reverse scan. This hypothesis was further supported by impedance analysis and the range of potential for the removal of the reaction intermediates was found to be 0.1V–0.2V. The impedance results along with the CV analysis lead to the conclusion that with increasing number of CV cycles, removal of the intermediates starts to dominate over methanol oxidation reaction in the forward scan and the intermediates start to work as poison for the catalyst which is preferentially used for methanol oxidation.

- A novel process for fabrication of clay nanoscrolls first time using 2:1 type Mt (C30B clay), which had catalytically active Pd-Fe nanoparticles encapsulated in it was demonstrated. In addition, highly stable clay supported ZVI could also be synthesized by the same process by just changing the calcination environment to nitrogen. Fe-Pd-CNCs acted as the structural directing agent in this study, providing a template for scroll formation, while electrostatic interaction had been the driving force for scroll formation, in which charge deficiency resulting due to the removal of oxygen from γ-Fe_2O_3 structure plays a role by creating positively charged holes. Similarly, formation of a core shell type of alloy between Pd and Fe has been considered as a reason for the formation of stable ZVI. The prepared clay nanoscrolls were utilized for H_2O_2 reduction in alkaline medium and it showed good electrochemical perofrmencve for H_2O_2 reduction in alkaline medium with significantly low palladium content. The current density obtained by clay

TH-2592_156107017

nanoscrolls for H_2O_2 reduction was in the same range with significantly high Pd loaded commercial Pd/C catalyst.

7.2 Novelty or Technical Problems Addressed

- Fabrication of cheap biopolymers based ion conductive material, which provides stable ion conductive nature to the membranes and can be utilized in alkaline DMFCs.
- Theoretical explanation of ion transfer mechanism in protein based biopolymers having guanidinum based alkaline medium stable charge transfer groups.
- Stable electrocatalyst development for methanol oxidation in alkaline medium using bio-based natural clay material.
- Fabrication of Pd-Fe encapsulated clay nanoscroll electrocatalyst by using first time montmorillonite 2:1 type clay, with significantly low amount of Pd loading, having equivalent performance to commercial Pd-C electrocatalyst for H_2O_2 reduction in alkaline medium.
- Synthesis of montmorillonite clay supported highly stable zero-valent iron having stability of more than 130 days in normal atmosphere.

7.3 Future Scope

- CNCs based materials have high scope for utilizing in DMFCs as ion conductive material. There are reports showing improved properties with much high loading of CNCs with other additives. But, with modification by different charge transfer functionalities, it can much improved electrochemical properties with low loading.

TH-2592_156107017

Such investigations can be carried out in future to further explore CNCs in ion exchange membrane area.

- Hair hydrolysate based ion conductive material is very promising and further separation of cationic part from hair hydrolysate and its investigation with shorter chain peptides for AEMs can be carried out in future.

- Excessive crystallization of the hair hydrolysate is also a problem, which reduces the available charge transfer sites as well as increases the resistance for ion permeation, so studies on reducing the crystallinity such that methanol permeation should not increase, can be carried out in future.

- The hair hydrolysate contains anionic amino acids also and thus can be utilized in proton exchange membrane fabrication. Thus, use of hair hydrolysate to investigate its electrochemical properties for cation exchange membrane can be carried out in future.

- Theoretical investigation through reactive forecefields on PVA based crosslinked system can give the better understanding of intermediate species formation during OH^- ions transfer and further charge transfer mechanism in proteins/ peptides/ amino acids based AEMs

- The active surface area and conductivity of the electrocatalyst prepared for methanol oxidation has to be further improved as it has good stability, but shows lower performance compared to commercial electrocatalysts in alkaline medium.

TH-2592_156107017

Appendix

Lennard-Jones Potential Parameter for MD Simulation

Atom type	ε (Kcal mol^{-1})	r^0(Å)	q(e)
PVA			
h (bonded to carbon)	0.0380000011	2.4499714540	0.100000
c2 (carbon of CH_2OH bonded to carbon (end group))	0.0389999952	3.8754094636	-0.170000
c2 (Sp3 carbon, bonded to two carbons and 2 H's)	0.0389999952	3.8754094636	-0.200000
c1 (carbon of CHOH bonded to two carbons)	0.0389999952	3.8754094636	-0.070000
Oh	0.2280000124	2.8597848722	-0.380000
Ho	0.000010000000	1.0000000000	0.350000
Ammonium cation			
n4 (nitrogen of ammonium cation)	0.1669999743	3.5012320066	-0.500000
hn (bonded to n4)	0.000010000000	1.0000000000	0.360000
Guanidino cation			
n1 (nitrogen double bonded to guanidino carbon)	0.1669999743	3.5012320066	-0.100000
hn (bonded to n1)	0.000010000000	1.0000000000	0.500000
cr (guanidino carbon)	0.1479999981	3.6170487995	0.500000
n2 (two nitrogen atoms bonded to guanidino carbon by single bond)	0.1669999743	3.5012320066	-0.560000
hn (of n2)	0.000010000000	1.0000000000	0.280000

TH-2592_156107017

Atom type	ε (Kcal mol^{-1})	r^0(Å)	q(e)
Remaining KAMP			
c2 (bonded to n1)	0.0389999952	3.8754094636	-0.100000
h (bonded to carbon)	0.0380000011	2.4499714540	0.100000
c2 (Sp3 carbon, bonded to two carbons and 2 H's)	0.0389999952	3.8754094636	-0.200000
ca (amino acid alpha carbon attached to n4)	0.0389999952	3.8754094636	0.320000
c' (C=O)	0.1479999981	3.6170487995	0.380000
o' (C=O)	0.2280000124	2.8597848722	-0.380000
n (nitrogen of amine in peptide chain)	0.1669999743	3.5012320066	-0.500000
hn (bonded to n)	0.000010000000	1.0000000000	0.280000
ca (amino acid alpha carbon attached to n)	0.0389999952	3.8754094636	0.120000
c3 (Sp3 carbon in methyl (CH3) group)	0.0389999952	3.8754094636	-0.300000
cg (Sp3 alpha carbon in glycine)	0.0389999952	3.8754094636	0.020000
c1 (Sp3 carbon bonded to 1 H and 3 carbon atoms)	0.0389999952	3.8754094636	-0.100000
c2 (carbon of CH_2OH bonded to carbon)	0.0389999952	3.8754094636	-0.170000
oh (oxygen of hydroxyl group)	0.2280000124	2.8597848722	-0.380000
ho (hydrogen of hydroxyl group)	0.000010000000	1.0000000000	0.350000
Cp (Sp2 aromatic carbon, partial double bonds))	0.1479999981	3.6170487995	-0.100000
Cp (Sp2 aromatic carbon, partial double bonds and bonded with one hydroxyl group)	0.1479999981	3.6170487995	0.030000

TH-2592_156107017

Atom type	ε (Kcal mol^{-1})	r^0(Å)	q(e)
Cp (Sp2 aromatic carbon, partial double bonds and bonded to aliphatic carbon)	0.1479999981	3.6170487995	0.000000
Methanol			
c3 (methanol carbon)	0.0389999952	3.8754094636	-0.270000
h (bonded to carbon)	0.0380000011	2.4499714540	0.100000
oh (oxygen of hydroxyl group)	0.2280000124	2.8597848722	-0.380000
ho (hydrogen of hydroxyl group)	0.000010000000	1.0000000000	0.350000
Water			
o*	0.1554164124	3.1655200879	-0.820000
h*	0.000010000000	1.0000000000	0.410000
OH^- ion			
O	0.1496175900	3.8400000000	-1.350000
ho (hydrogen of hydroxyl ion)	0.000010000000	1.0000000000	0.350000
K^+ ion			
K	0.7441000000	4.8858000000	1.0000

OH^- LJ-parameters and ionic charge data were taken from Vácha et al. (2008) and K^+ LJ-parameters were taken from Zhao et al. (2010). Rest of the bonded parameters were taken from consistent valence force field (CVFF) (Dauber-Osguthorpe et al., 1988).

TH-2592_156107017

Research Outcome

Research articles published/ under publication/ under preparation:

1. Gaur, S. S., Dhar, P., Sonowal, A., Sharma, A., Kumar, A., & Katiyar, V. (2017). Thermo-mechanically stable sustainable polymer based solid electrolyte membranes for direct methanol fuel cell applications. *Journal of Membrane Science*, 526, 348-354.

2. Gaur, S. S., Dhar, P., Sakurai, S., Kumar, A., & Katiyar, V. (2019). Cellulose nanocrystal/clay based macroion nanogel as support for stable platinum catalyst for electrochemical oxidation of methanol in alkaline medium. *Applied Clay Science*, 182, 105277.

3. Gaur, S. S., Dhar, P., Narendren, S., Sakurai, S., Kumar, A., & Katiyar, V. (2020). Fabrication and characterization of clay nanoscrolls and stable zerovalent iron using montmorillonite. *Applied Clay Science*, 193, 105670.

4. Gaur, S. S., Dhar, P., Wani, K. M., Srivastava, M., Sakurai, S., Kumar, A., & Katiyar, V. (2021). Ion transfer channel network formed by flower and rod shape crystals of hair hydrolysate in poly (vinyl alcohol) matrix and its application as anion exchange membrane in fuel cells. Journal of Colloid and Interface Science, 587, 214-228.

5. Gaur, S. S., Katiyar, V. & Kumar, A., Molecular dynamics simulation studies on human hair derived peptide for its possible application in anion exchange membrane and investigation on the role of guanidino group in charge transfer (under preparation).

TH-2592_156107017

Contribution in research articles during PhD tenure in similar areas:

1. Dhar, P., Gaur, S. S., Kumar, A., & Katiyar, V. (2018). Cellulose nanocrystal templated graphene nanoscrolls for high performance supercapacitors and hydrogen storage: an experimental and molecular simulation study. *Scientific reports*, 8(1), 1-15.

2. Dhar, P., Gaur, S.S., Soundararajan, N., Gupta, A., Bhasney, S.M., Milli, M., Kumar, A. and Katiyar, V., (2017). Reactive extrusion of polylactic acid/cellulose nanocrystal films for food packaging applications: influence of filler type on thermomechanical, rheological, and barrier properties. *Industrial & Engineering Chemistry Research*, 56(16), 4718-4735.

3. Kashyap, D., Gaur, S. S., & Kanagaraj, S. (2020). Development of hybrid shape memory polyurethane composites for endovascular applications. *Materials Today Communications*, 22, 100751.

4. Dhar, P., Narendren, S., Gaur, S. S., Sharma, S., Kumar, A., & Katiyar, V. (2020). Self-propelled cellulose nanocrystal based catalytic nanomotors for targeted hyperthermia and pollutant remediation applications. International Journal of Biological Macromolecules.

5. Pal, A. K., Bhattacharjee, S. K., Gaur, S. S., Pal, A., & Katiyar, V. (2018). Chemomechanical, morphological, and rheological studies of chitosan-graft-lactic acid oligomer reinforced poly (lactic acid) bionanocomposite films. *Journal of Applied Polymer Science*, 135(3), 45546.

TH-2592_156107017

Book Chapters:

1. Surendra Singh Gaur, Tabli Ghosh and Vimal Katiyar, 2017, book chapter titled as General Materials Properties Required for Food-Packaging Applications in book Bio-based Plastics for Food Packaging Applications. (Smithers Rapra, ISBN: 9781910242582).
2. Prodyut Dhar, Surendra Singh Gaur, Tabli Ghosh, Vimal Katiyar, book chapter entitled Nanocellulose: Material Development, Characterization and Testing Protocols in book entitled Cellulose Nanocrystals: An Emerging Nanocellulose for Numerous Chemical Processes. (Walter de Gruyter GmbH (Under Production)).

Conference proceedings:

1. Surendra Singh Gaur, Prodyut Dhar, Amit Kumar and Vimal Katiyar, Cellulose nanocrystals as proton conductive filler and its composite membrane for DMFC. In Abstracts of Papers of the American Chemical Society (Vol. 257). 1155 16TH ST, NW, Washington, DC 20036 USA: Amer Chemical Soc., (2019, March).
2. Surendra Singh Gaur, Prodyut Dhar, Amrita Sonowal, Akanksha Sharma, Amit Kumar and Vimal Katiyar, Application of Cellulose Nanocrystals as Ionic Conductor for Fabrication of Solid Electrolyte Membrane for Direct methanol Fuel Cells, SPSI-MACRO-2018, December 19th – 22nd , 2018.
3. Surendra Singh Gaur, Prodyut Dhar, Amrita Sonowal, Akanksha Sharma, Amit Kumar, and Vimal Katiyar, Fabrication of poly(vinyl chloride)-chitosan-cellulose nanocrystals based solid electrolyte membrane for direct methanol fuel cells: a sustainable approach, International Conference on Polymer Sci. and Tech., MACRO 2017, Jan. 8-11, 2017.

TH-2592_156107017

4. Surendra Singh Gaur, Prodyut Dhar, Amit Kumar and Vimal Katiyar, Application of Cellulose Nanocrystals as Ionic Conductor for Fabrication of Solid Electrolyte Membrane for Direct Methanol Fuel Cells, International Symposium on Sustainable Polymers & National Symposium on Chemistry Education for Sustainable Engineering, August 23-25, 2019, IIT Guwahati.
5. Surendra Singh Gaur, Prodyut Dhar, Amit Kumar and Vimal Katiyar, Study of PVA/ PSSA/ Chitosan/ Closite-30B Clay Based Polyelectrolyte Composite Membrane for Direct Methanol Fuel Cell Application, CHEMCON 2015, IIT Guwahati, Guwahati, Assam, Dec. 27–30, 2015.
6. Amit Kumar, Surendra Singh Gaur, Arooshi Bajaj, Molecular simulation studies on nanocomposites of biodegradable polymers and biobased fillers, 4th IITG-KIT Joint Symposium, ASP-19, 15th Oct., 2019, KIT, Japan.
7. Prodyut Dhar, Surendra Singh Gaur, Amit Kumar and Vimal Katiyar, Cellulose nanocrystals and closite-Na plus clay micro-nano complex formation and its application in drug delivery studies. In Abstracts of Papers of the American Chemical Society (Vol. 251). 1155 16TH ST, NW, Washington, DC 20036 USA: Amer Chemical Soc. (2016, March).
8. Prodyut Dhar, Surendra Singh Gaur, Amit Kumar and Vimal Katiyar, Sustainable approach towards the fabrication of tunable graphene nanoscrolls and its application for energy storage. In Abstracts of Papers of the American Chemical Society (Vol. 257). 1155 16TH ST, NW, Washington, DC 20036 USA: Amer Chemical Soc. (2019, March).
9. Bhanupriya Das, Surendra Singh Gaur, Chin Tsan Wang and Vimal Katiyar, Bio derived ionic conductor based polyelectrolyte membrane for microbial fuel cells,

TH-2592_156107017

The International Conference on Sustainable Energy and Green Technology (SEGT 2019), Dec. 11-14, 2019, Bangkok, Thailand.

TH-2592_156107017

References

Abitbol, T., Johnstone, T., Quinn, T. M. and Gray, D. G., "Reinforcement with cellulose nanocrystals of poly (vinyl alcohol) hydrogels prepared by cyclic freezing and thawing," *Soft Matter*, **7**(6), 2373-2379 (2011).

Adams, J. M., "Synthetic organic chemistry using pillared, cation-exchanged and acid-treated montmorillonite catalysts—A review," *Applied Clay Science*, **2**(4), 309-342 (1987).

Adžić, R. R., Avramov-Ivić, M. L. and Tripković, A. V., "Structural effects in electrocatalysis: oxidation of formaldehyde on gold and platinum single crystal electrodes in alkaline solution," *Electrochimica acta*, **29**(10), 1353-1357 (1984).

Agel, E., Bouet, J. and Fauvarque, J. F., "Characterization and use of anionic membranes for alkaline fuel cells," *Journal of Power Sources*, **101**(2), 267-274 (2001).

Ahmadi, T. S., Wang, Z. L., Green, T. C., Henglein, A. and El-Sayed, M. A., "Shape-controlled synthesis of colloidal platinum nanoparticles," *Science*, **272**(5270), 1924–1925 (1996).

Ahn, T. K., Avenson, T. J., Ballottari, M., Cheng, Y. C., Niyogi, K. K., Bassi, R. and Fleming, G. R., "Architecture of a charge-transfer state regulating light harvesting in a plant antenna protein," *Science*, **320**(5877), 794-797 (2008).

Altmeier, P., "Strongly alkaline anion exchange membranes and process for producing the same," *U.S. Patent 5,746,917*, issued May 5, 1998.

Amin, R. S., Hameed, R. A., El-Khatib, K. M. and Youssef, M. E., "Electrocatalytic activity of nanostructured Ni and Pd–Ni on Vulcan XC-72R carbon black for methanol oxidation in alkaline medium," *International journal of hydrogen energy*, **39**(5), 2026-2041 (2014).

An, H., Pan, L., Cui, H., Li, B., Zhou, D., Zhai, J. and Li, Q., "Synthesis and performance of palladium-based catalysts for methanol and ethanol oxidation in alkaline fuel cells," *Electrochimica Acta*, **102**, 79-87 (2013).

TH-2592_156107017

An, L. and Zhao, T. S., "Performance of an alkaline-acid direct ethanol fuel cell," *International journal of hydrogen energy*, **36**(16), 9994-9999 (2011).

Andrew, M. R., McNicol, B. D., Short, R. T. and Drury, J. S., "Electrolytes for methanol-air fuel cells. I. The performance of methanol electro-oxidation catalysts in sulphuric acid and phosphoric acid electrolytes," *Journal of Applied Electrochemistry*, **7**(2), 153-160 (1977).

Andrew R. L., "Molecular modeling principals and applications," Prentice Hall, Londan (2001).

Anicuta, S. G., Dobre, L., Stroescu, M. and Jipa, I., "Fourier transform infrared (FTIR) spectroscopy for characterization of antimicrobial films containing chitosan," *Analele Universită Ńii din Oradea Fascicula: Ecotoxicologie, Zootehnie şi Tehnologii de Industrie Alimentară*, 1234-1240 (2010).

Anthony, J. W., Bideaux, R. A., Bladh, K. W. and Nichols, M. C., *Handbook of Mineralogy*. Mineralogical Society of America: Vol. II. Silica, Silicates Chantilly, VA, USA (2011).

Arico, A. S., Srinivasan, S. and Antonucci, V., "DMFCs: from fundamental aspects to technology development," *Fuel cells*, **1**(2), 133-161 (2001).

Bagotsky, V. S., *Fuel Cells Problems and Solutions*, John Wiley & Sons, New Jersey (2009).

Banham, D., Ye, S., Pei, K., Ozaki, J. I., Kishimoto, T. and Imashiro, Y., "A review of the stability and durability of non-precious metal catalysts for the oxygen reduction reaction in proton exchange membrane fuel cells," *Journal of Power Sources*, **285**, 334-348 (2015).

Barbir, F., PEM Fuel Cells Theory and Practice, Elsevier Academic Press, MA (2005).

Bartel, M., Remde, H., Bohn, A. and Ganster, J., "Barrier properties of poly (lactic acid)/cloisite 30B composites and their relation between oxygen permeability and relative humidity," *Journal of Applied Polymer Science*, **134**(5), (2017).

TH-2592_156107017

Basri, S., Kamarudin, S. K., Daud, W. R. W. and Yaakub, Z., "Nanocatalyst for direct methanol fuel cell (DMFC)," *International Journal of Hydrogen Energy*, **35**(15), 7957-7970 (2010).

Basu, S., *Recent Trends in Fuel Cell Science and Technology*, Springer Science + Business Media, Inc., NewYork (2007).

Bertini, F., Canetti, M., Patrucco, A. and Zoccola, M., "Wool keratin-polypropylene composites: Properties and thermal degradation," *Polymer degradation and stability*, **98**(5), 980-987 (2013).

Bhat, S. D., Sahu, A. K., George, C., Pitchumani, S., Sridhar, P., Chandrakumar, N., Singh, K .K., Krishna, N. and Shukla, A. K., "Mordenite-incorporated PVA–PSSA membranes as electrolytes for DMFCs," *Journal of membrane science*, **340**(1-2), 73-83 (2009).

Bick, D. S., Kindsmüller, A., Staikov, G., Gunkel, F., Müller, D., Schneller, T., Waser, R. and Valov, I., "Stability and degradation of perovskite electrocatalysts for oxygen evolution reaction," *Electrochimica Acta*, **218**, 156-162 (2016).

Bommarius, A. S., Holzwarth, J. F., Wang, D. I. C. and Hatton, T. A., "Coalescence and solubilizate exchange in a cationic four-component reversed micellar system," *The Journal of Physical Chemistry*, **94**(18), 7232–7239 (1990).

Borkowska, Z., Tymosiak-Zielinska, A. and Shul, G., "Electrooxidation of methanol on polycrystalline and single crystal gold electrodes," *Electrochimica acta*, **49**(8), 1209-1220 (2004).

Borup, R. L., Davey, J. R., Garzon, F. H., Wood, D. L. and Inbody, M. A., "PEM fuel cell electrocatalyst durability measurements," *Journal of Power Sources*, **163**(1), 76-81 (2006).

Bouazizi, N., Ouargli, R., Nousir, S. and Azzouz, A., "Copper and palladium loaded polyol dendrimer–montmorillonite composites as potential adsorbents for CO_2 and H_2," *Journal of Materials Science: Materials in Electronics*, **30**(9), 8182-8190 (2019).

TH-2592_156107017

Bradley, K., Briman, M., Star, A. and Grüner, G., “Charge transfer from adsorbed proteins,” *Nano Letters*, **4**(2), 253-256 (2004).

Burchardt, T., Gouerec, P., Sanchez- Cortezon, E., Karichev, Z. and Miners, J. H., "Alkaline fuel cells: contemporary advancement and limitations," *Fuel*, **81**, 2151-2155 (2002).

Caner, C., Vergano, P. J. and Wiles, J. L., "Chitosan film mechanical and permeation properties as affected by acid, plasticizer, and storage," *Journal of food science*, **63**(6), 1049-1053 (1998).

Cao, D., Chao, J., Sun, L. and Wang, G., "Catalytic behavior of Co3O4 in electroreduction of H_2O_2," *Journal of Power Sources*, **179**(1), 87-91 (2008).

Cao, D., Sun, L., Wang, G., Lv, Y. and Zhang, M., “Kinetics of hydrogen peroxide electroreduction on Pd nanoparticles in acidic medium,” *Journal of Electroanalytical Chemistry*, **621**(1), 31-37 (2008).

Charradi, K., Forano, C., Prevot, V., Ben Haj Amara, A. and Mousty, C., “Direct electron transfer and enhanced electrocatalytic activity of hemoglobin at iron-rich clay modified electrodes,” *Langmuir*, **25**(17), 10376-10383 (2009).

Chempath, S., Boncella, J. M., Pratt, L. R., Henson, N. and Pivovar, B. S., "Density functional theory study of degradation of tetraalkylammonium hydroxides," *The Journal of Physical Chemistry C*, **114**(27), 11977-11983 (2010).

Chen, C., Tse, Y. L. S., Lindberg, G. E., Knight, C. and Voth, G. A., “Hydroxide solvation and transport in anion exchange membranes,” *Journal of the American Chemical Society*, **138**(3), 991-1000 (2016).

Chen, H. Y., Kao, C. L. and Hsu, S. C., "Proton transfer in guanine− cytosine radical anion embedded in B-form DNA," *Journal of the American Chemical Society*, **131**(43), 15930-15938 (2009).

TH-2592_156107017

Chen, Y., Tao, Y., Wang, J., Yang, S., Cheng, S., Wei, H. and Ding, Y., “Comb-shaped guanidinium functionalized poly (ether sulfone) s for anion exchange membranes: Effects of the spacer types and lengths,” *Journal of Polymer Science Part A: Polymer Chemistry*, **55**(8), 1313-1321 (2017).

Cheng, J., He, G. and Zhang, F., “A mini-review on anion exchange membranes for fuel cell applications: stability issue and addressing strategies,” *International Journal of Hydrogen Energy*, **40**(23), 7348-7360 (2015).

Chiellini, E., Corti, A., D'Antone, S. and Solaro, R., "Biodegradation of poly (vinyl alcohol) based materials," *Progress in Polymer Science*, **28**(6), 963-1014 (2003).

Choy, J. H., Choi, S. J., Oh, J. M. and Park, T., “Clay minerals and layered double hydroxides for novel biological applications,” *Applied Clay Science*, **36**(1-3), 122-132 (2007).

Clark, T. J., Robertson, N. J., Kostalik IV, H. A., Lobkovsky, E. B., Mutolo, P. F., Abruna, H. D. and Coates, G. W., "A ring-opening metathesis polymerization route to alkaline anion exchange membranes: development of hydroxide-conducting thin films from an ammonium-functionalized monomer," *Journal of the American Chemical Society*, **131**(36) 12888-12889 (2009).

Cope, A. C. and Mehta, A. S., "Mechanism of the Hofmann elimination reaction: an ylide intermediate in the pyrolysis of a highly branched quaternary hydroxide," *Journal of the American Chemical Society*, **85**(13), 1949-1952 (1963).

Cope, A. C. and Trumbull, E. R., "*Olefins from Amines: The Hofmann Elimination Reaction and Amine Oxide Pyrolysis in Organic Reactions*," RE Krieger Publication: Huntington, NY, USA (1975).

Cox, M., Rus-Romero, J. R. and Sheriff, T. S., “The application of montmorillonite clays impregnated with organic extractants for the removal of metals from aqueous solution: Part I. The preparation of clays impregnated with di-(2-ethylhexyl) phosphoric acid and their use for the removal of copper (II),” *Chemical Engineering Journal*, **84**(2), 107-113 (2001).

TH-2592_156107017

Danks, T. N., Slade, R. C. and Varcoe, J. R., "Comparison of PVDF-and FEP-based radiation-grafted alkaline anion-exchange membranes for use in low temperature portable DMFCs," *Journal of Materials Chemistry*, **12**(12), 3371-3373 (2002).

Danwanichakul, P. and Sirikhajornnam, P., "An investigation of chitosan-grafted-poly (vinyl alcohol) as an electrolyte membrane," *Journal of Chemistry*, **2013** (2012).

Dauber-Osguthorpe, P., Roberts, V. A., Osguthorpe, D. J., Wolff, J., Genest, M. and Hagler, A. T., "Structure and energetics of ligand binding to proteins: Escherichia coli dihydrofolate reductase-trimethoprim, a drug-receptor system," *Proteins: Structure, Function, and Bioinformatics*, **4**(1), 31-47 (1988).

Deshpande, K., Mukasyan, A. and Varma, A., "High throughput evaluation of perovskite-based anode catalysts for direct methanol fuel cells," *Journal of power sources*, **158**(1), 60-68 (2006).

Dhar, P., Bhasney, S. M., Kumar, A. and Katiyar, V. , "Acid functionalized cellulose nanocrystals and its effect on mechanical, thermal, crystallization and surfaces properties of poly (lactic acid) bionanocomposites films: A comprehensive study," *Polymer*, **101**, 75-92 (2016).

Dhar, P., Gaur, S. S., Kumar, A. and Katiyar, V., "Cellulose nanocrystal templated graphene nanoscrolls for high performance supercapacitors and hydrogen storage: an experimental and molecular simulation study," *Scientific reports*, **8**(1), 1-15 (2018).

Dhar, P., Kumar, A. and Katiyar, V., "Fabrication of cellulose nanocrystal supported stable Fe(0) nanoparticles: a sustainable catalyst for dye reduction, organic conversion and chemo-magnetic propulsion," *Cellulose*, **22**(6), 3755-3771 (2015).

Dhar, P., Kumar, A. and Katiyar, V., "Magnetic cellulose nanocrystal based anisotropic polylactic acid nanocomposite films: influence on electrical, magnetic, thermal, and mechanical properties," *ACS applied materials & interfaces*, **8**(28), 18393-18409 (2016).

Dhar, P., Phiri, J., Szilvay, G. R., Westerholm-Parvinen, A., Maloney, T. and Laaksonen, P., "Genetically Engineered Proteins based Nacre-like Nanocomposites with Superior

TH-2592_156107017

Mechanical and Electrochemical Performance," *Journal of Materials Chemistry A*, **8**(2), 656-669 (2019).

Dhar, P., Tarafder, D., Kumar, A. and Katiyar, V., "Effect of cellulose nanocrystal polymorphs on mechanical, barrier and thermal properties of poly (lactic acid) based bionanocomposites," RSC Advances, **5**(74), 60426-60440 (2015).

Dinesh, B., Squillaci, M. A., Ménard-Moyon, C., Samorì, P. and Bianco, A., "Self-assembly of diphenylalanine backbone homologues and their combination with functionalized carbon nanotubes," *Nanoscale*, **7**(38), 15873-15879 (2015).

Duan, Q., Ge, S. and Wang, C. Y., "Water uptake, ionic conductivity and swelling properties of anion-exchange membrane," *Journal of Power Sources*, **243**, 773-778 (2013).

Dubey, N., Sharma, P. and Kumar, A., "Clay-supported Cu (II) catalyst: An efficient, heterogeneous, and recyclable catalyst for synthesis of 1, 4-disubstituted 1, 2, 3-triazoles from alloxan-derived terminal alkyne and substituted azides using click chemistry," *Synthetic Communications*, **45**(22), 2608-2626 (2015).

El Miri, N., Abdelouahdi, K., Zahouily, M., Fihri, A., Barakat, A., Solhy, A. and El Achaby, M., "Bio-nanocomposite films based on cellulose nanocrystals filled polyvinyl alcohol/chitosan polymer blend," *Journal of Applied Polymer Science*, **132**(22), (2015).

Elmoubarki, R., Mahjoubi, F. Z., Elhalil, A., Tounsadi, H., Abdennouri, M., Sadiq, M. H., Qourzal, S., Zouhri, A. and Barka, N., "Ni/Fe and Mg/Fe layered double hydroxides and their calcined derivatives: preparation, characterization and application on textile dyes removal," *Journal of Materials Research and Technology*, **6**(3), 271-283 (2017).

El-Shafei, A. A., "Electrocatalytic oxidation of methanol at a nickel hydroxide/glassy carbon modified electrode in alkaline medium," *Journal of Electroanalytical Chemistry*, **471**(2), 89-95 (1999).

Fauvarque, J. F., Guinot, S., Bouzir, N., Salmon, E. and Penneau, J. F., "Alkaline poly (ethylene oxide) solid polymer electrolytes. Application to nickel secondary batteries," *Electrochimica Acta*, **40**(13-14), 2449-2453 (1995).

TH-2592_156107017

Feketeföldi, B., Cermenek, B., Spirk, C., Schenk, A., Grimmer, C., Bodner, M., Koller, M., Ribitsch, V. and Hacker, V., "Chitosan-based anion exchange membranes for direct ethanol fuel cells," *Journal of Membrane Science & Technology*, **6**(1), 1000145 (2016).

Ferreira, P. J., Shao-Horn, Y., Morgan, D., Makharia, R., Kocha, S. and Gasteiger, H. A., "Instability of Pt/ C electrocatalysts in proton exchange membrane fuel cells: a mechanistic investigation," *Journal of the Electrochemical Society*, **152**(11), A2256 (2005).

Filipkowska, U. and Jóźwiak, T., "Application of chemically-cross-linked chitosan for the removal of Reactive Black 5 and Reactive Yellow 84 dyes from aqueous solutions," *Journal of Polymer Engineering*, **33**(8), 735-747 (2013).

Fischer, W. N., Loo, D. D., Koch, W., Ludewig, U., Boorer, K. J., Tegeder, M., Rentsch, D., Wright, E. M. and Frommer, W. B., "Low and high affinity amino acid H^+-cotransporters for cellular import of neutral and charged amino acids," *The Plant Journal*, **29**(6), 717-731 (2002).

Fort, C. I., Cotet, L. C., Danciu, V., Turdean, G. L. and Popescu, I. C., "Iron doped carbon aerogel–New electrode material for electrocatalytic reduction of H_2O_2," *Materials Chemistry and Physics*, **138**(2-3), 893-898 (2013).

Frano, B., *PEM fuel cells: theory and practice*, Academic, Burlington, (2005), p. 17-31.

Fu, Y. T., Zartman, G. D., Yoonessi, M., Drummy, L. F. and Heinz, H., "Bending of layered silicates on the nanometer scale: mechanism, stored energy, and curvature limits," *The Journal of Physical Chemistry C*, **115**(45), 22292-22300 (2011).

Gajjala, R. K. R. and Palathedath, S. K., "Cu@ Pd core-shell nanostructures for highly sensitive and selective amperometric analysis of histamine," *Biosensors and Bioelectronics*, **102**, 242-246 (2018).

García-Cruz, L., Casado-Coterillo, C., Iniesta, J., Montiel, V. and Irabien, Á., "Preparation and characterization of novel chitosan-based mixed matrix membranes resistant in alkaline media," *Journal of Applied Polymer Science*, **132**(29), (2015).

TH-2592_156107017

Gaur, S. S., Dhar, P., Kumar, A. and Katiyar, V. , "Prospects of poly (vinyl alcohol)/ Chitosan/poly (styrene sulfonic acid) and montmorillonite Cloisite® 30B clay composite membrane for direct methanol fuel cells," *Journal of renewable and sustainable energy*, **6**(5), 053135 (2014).

Gaur, S. S., Dhar, P., Sonowal, A., Sharma, A., Kumar, A. and Katiyar, V., "Thermo-mechanically stable sustainable polymer based solid electrolyte membranes for direct methanol fuel cell applications," *Journal of Membrane Science*, **526**, 348-354 (2017).

Gojković, S. L., Gupta, S. and Savinell, R. F., "Heat-treated iron (III) tetramethoxyphenyl porphyrin chloride supported on high-area carbon as an electrocatalyst for oxygen reduction: Part II. Kinetics of oxygen reduction," *Journal of Electroanalytical Chemistry*, **462**(1), 63-72 (1999).

Gong, C., Zhao, S., Tsen, W. C., Hu, F., Zhong, F., Zhang, B., Liu, H., Zheng, G., Qin, C. and Wen, S., "Hierarchical layered double hydroxide coated carbon nanotube modified quaternized chitosan/polyvinyl alcohol for alkaline direct methanol fuel cells," *Journal of Power Sources*, **441**, 227176 (2019).

Gong, Z., Shi, J., Zhang, B. and Zhang, J., "Graphene nano scrolls responding to superlow friction of amorphous carbon," *Carbon*, **116**, 310-317 (2017).

Goodenough, J. B., Hamnett, A., Kennedy, B. J., Manoharan, R. and Weeks, S. A., "Porous carbon anodes for the direct methanol fuel cell—I. The role of the reduction method for carbon supported platinum electrodes," *Electrochimica Acta*, **35**(1), 199-207 (1990).

Grau-Crespo, R., Al-Baitai, A. Y., Saadoune, I. and De Leeuw, N. H., "Vacancy ordering and electronic structure of γ-Fe_2O_3 (maghemite): a theoretical investigation," *Journal of Physics: Condensed Matter*, **22**(25), 255401 (2010).

Grew, K. N. and Chiu, W. K. S., "A dusty fluid model for predicting hydroxyl anion conductivity in alkaline anion exchange membranes," *Journal of the Electrochemical Society*, **157**(3), B327–B337 (2010).

TH-2592_156107017

Grew, K. N. and Chiu, W. K., "A dusty fluid model for predicting hydroxyl anion conductivity in alkaline anion exchange membranes," *Journal of the electrochemical Society*, **157**(3), B327-B337 (2010).

Gu, S., Cai, R., Luo, T., Chen, Z., Sun, M., Liu, Y., He, G. and Yan, Y., "A soluble and highly conductive ionomer for high-performance hydroxide exchange membrane fuel cells," *Angewandte Chemie*, **121**(35), 6621-6624 (2009).

Gülzow, E. and Schulze, M., "Long-term operation of AFC electrodes with CO2 containing gases," *Journal of Power Sources*, **127**(1-2), 243-251 (2004).

Gyenge, E. L. and Oloman, C. W., "Electrosynthesis of hydrogen peroxide in acidic solutions by mediated oxygen reduction in a three-phase (aqueous/organic/gaseous) system Part I: Emulsion structure, electrode kinetics and batch electrolysis," *Journal of applied electrochemistry*, **33**(8), 655-663 (2003).

Halima, N. B., "Poly (vinyl alcohol): review of its promising applications and insights into biodegradation," *RSC advances*, **6**(46), 39823-39832 (2016).

Handbook, Fuel Cell. "EG&G technical services." Inc., Albuquerque, NM, DOE/NETL-2004/1206 (2004), p. 1-10.

Heinz, H., “Clay minerals for nanocomposites and biotechnology: surface modification, dynamics and responses to stimuli,” *Clay Minerals*, **47**(2), 205-230 (2012).

Henry, G. D. and Sykes, B. D., "Determination of the rotational dynamics and pH dependence of the hydrogen exchange rates of the arginine guanidino group using NMR spectroscopy," *Journal of biomolecular NMR*, **6**(1), 59-66 (1995).

Herranz, J., Jaouen, F., Lefèvre, M., Kramm, U. I., Proietti, E., Dodelet, J. P., Bogdanoff, P., Fiechter, S., Abs-Wurmbach, I., Bertrand, P. and Arruda, T. M., "Unveiling N-protonation and anion-binding effects on Fe/N/C catalysts for O2 reduction in proton-exchange-membrane fuel cells," *The Journal of Physical Chemistry C*, **115**(32), 16087-16097 (2011).

TH-2592_156107017

Ho, D., Chu, B., Lee, H. and Montemagno, C. D., “Protein-driven energy transduction across polymeric biomembranes,” *Nanotechnology*, **15**(8), 1084 (2004).

Hong, J. H., Li, D. and Wang, H., “Weak-base anion exchange membranes by amination of chlorinated polypropylene with polyethyleneimine at low temperatures,” *Journal of Membrane Science*, **318**, 441–444 (2008).

Hoogers G., *Fuel Cell Technology Handbook*, CRC Press LLC, Boca Raton (2003), p. 173-204.

Hu, S., “Electrocatalytic reduction of molecular oxygen on a sodium montmorillonite-methyl viologen carbon paste chemically modified electrode,” *Journal of Electroanalytical Chemistry*, **463**(2), 253-257 (1999).

Hu, S., Wang, B., Ju, H., Jiang, L., Ma, Y. and Fan, Y., “Photo-assisted electrocatalytic methanol oxidation based on an efficient 1D-TiO_2 nanorods arrays support electrode,” *Journal of the Taiwan Institute of Chemical Engineers*, **80**, 533-539 (2017).

Huissoud, A. and Tissot, P., "Electrochemical reduction of 2-ethyl-9, 10-anthraquinone (EAQ) and mediated formation of hydrogen peroxide in a two-phase medium Part II: Production of alkaline hydrogen peroxide by the intermediate electroreduction of EAQ in a flow-by porous electrode in two-phase liquid–liquid flow," *Journal of applied electrochemistry*, **29**(1), 17-25 (1999).

Humphrey, W., Dalke, A. and Schulten, K., “VMD: visuval molecular dynamics,” *Journal of molecular graphics*, **14**(1), 33-38, 1996.

Ingole, P. G., Thakare, N. R., Kim, K., Bajaj, H. C., Singh, K. and Lee, H., "Preparation, characterization and performance evaluation of separation of alcohol using crosslinked membrane materials," *New Journal of Chemistry*, **37**(12), 4018-4024 (2013).

Jang, S. C., Tsen, W. C., Chuang, F. S. and Gong, C., "Simultaneously enhanced hydroxide conductivity and mechanical properties of quaternized chitosan/functionalized carbon nanotubes composite anion exchange membranes," *International Journal of Hydrogen Energy*, **44**(33), 18134-18144 (2019).

TH-2592_156107017

Jensen, M. Ø., Röthlisberger, U. and Rovira, C., “Hydroxide and proton migration in aquaporins,” *Biophysical journal*, **89**(3), 1744-1759 (2005).

Jiang, X., Sun, Y., Zhang, H. and Hou, L., "Preparation and characterization of quaternized poly (vinyl alcohol)/chitosan/MoS_2 composite anion exchange membranes with high selectivity," *Carbohydrate polymers*, **180**, 96-103 (2018).

Jiao, K. and Li, X., “Water transport in polymer electrolyte membrane fuel cells,” *Progress in Energy and Combustion Science*, **37**(3), 221-291 (2011).

Jin, J., Zhang, Y., Ouyang, J. and Yang, H., “Halloysite nanotubes as hydrogen storage materials,” *Physics and Chemistry of Minerals*, **41**(5), 323-331 (2014).

Joshi, G. V., Patel, H. A., Kevadiya, B. D. and Bajaj, H. C., “Montmorillonite intercalated with vitamin B1 as drug carrier,” *Applied Clay Science*, **45**(4), 248-253 (2009).

Kadwa, E., Bala, M. D. and Friedrich, H. B., “Characterisation and application of montmorillonite-supported Fe Schiff base complexes as catalysts for the oxidation of n-octane,” *Applied Clay Science*, **95**, 340-347 (2014).

Karim, N. A. and Kamarudin, S. K., "An overview on non-platinum cathode catalysts for direct methanol fuel cell," *Applied energy*, **103**, 212-220 (2013).

Kerr, P. F.,” Formation and occurrence of clay minerals,” *Clays and clay minerals*, **1**(1), 19-32 (1952).

Khoshtariya, D. E., Wei, J., Liu, H., Yue, H. and Waldeck, D. H., "Charge-transfer mechanism for cytochrome c adsorbed on nanometer thick films. Distinguishing frictional control from conformational gating," *Journal of the American Chemical Society*, **125**(25), 7704-7714 (2003).

Kim, D. S., Labouriau, A., Guiver, M. D. and Kim, Y. S., “Guanidinium-functionalized anion exchange polymer electrolytes via activated fluorophenyl-amine reaction,” *Chemistry of Materials*, **23**(17), 3795-3797 (2011).

TH-2592_156107017

Kim, D. S., Yun, T. I., Seo, M. Y., Cho, H. I. and Lee, Y. M., "Preparation of ion-exchange membranes for fuel cell based on crosslinked PVA/PSSA_MA/silica hybrid," *Desalination (Amsterdam)*, **200**(1-3), 634-635 (2006).

Kim, L., Chung, C. G., Sung, Y. W. and Chung, J. S., "Dissolution and migration of platinum after long-term operation of a polymer electrolyte fuel cell under various conditions," *Journal of Power Sources*, **183**(2), 524-532 (2008).

Knauf, P. A., *Current topics in membranes and transport*, Academic Press (1979), p. 249-363.

Kong, J. and Yu, S., "Fourier transform infrared spectroscopic analysis of protein secondary structures," *Acta biochimica et biophysica Sinica*, **39**(8), 549-559 (2007).

Kostalik IV, H. A., Clark, T. J., Robertson, N. J., Mutolo, P. F., Longo, J. M., Abruna, H. D. and Coates, G. W., "Solvent processable tetraalkylammonium-functionalized polyethylene for use as an alkaline anion exchange membrane," *Macromolecules*, **43**(17), 7147-7150 (2010).

Kristiansen, K. A., Potthast, A. and Christensen, B. E., "Periodate oxidation of polysaccharides for modification of chemical and physical properties," *Carbohydrate Research*, **345**(10), 1264-1271 (2010).

Kuroda, Y., Ito, K., Itabashi, K. and Kuroda, K., "One-step exfoliation of kaolinites and their transformation into nanoscrolls," *Langmuir*, **27**(5), 2028-2035 (2011).

Ladewig, B. P., Jiang, S. P. and Yan, Y., *Materials for Low-Temperature Fuel Cells*, Wiley-VCH, Weinheim (2015).

Lafforgue, C., A. Zadick, L. Dubau, F. Maillard, and M. Chatenet, "Selected Review of the Degradation of Pt and Pd-based Carbon-supported Electrocatalysts for Alkaline Fuel Cells: Towards Mechanisms of Degradation," Fuel Cells, **18**(3), 229-238 (2018).

Lan, A. and Mukasyan, A. S., "Perovskite-based catalysts for direct methanol fuel cells," The Journal of Physical Chemistry C, **111**(26), 9573-9582 (2007).

TH-2592_156107017

Layek, S., Pandey, A., Pandey, A. and Verma, H. C., “Synthesis of γ–Fe_2O_3 nanoparticles with crystallographic and magnetic texture,” *International journal of engineering, science and technology*, **2**(8), (2010).

Lee, J. T., Wang, G., Tam, Y. T. and Tam, C., “Membrane-active epithelial keratin 6A fragments (KAMPs) are unique human antimicrobial peptides with a non-αβ structure,” *Frontiers in microbiology*, **7**, 1799 (2016).

Lee, S. H. and Rasaiah, J. C., “Proton transfer and the mobilities of the H^+ and OH^- ions from studies of a dissociating model for water,” *The Journal of chemical physics*, **135**(12), 124505 (2011).

Leem, H. J., Dorbandt, I., Rojas-Chapana, J., Fiechter, S. and Tributsch, H., "Bio-analogue amino acid-based proton-conduction wires for fuel cell membranes," *The Journal of Physical Chemistry C*, **112**(7), 2756-2763 (2008).

Lefèvre, M. and Dodelet, J. P., "Fe-based catalysts for the reduction of oxygen in polymer electrolyte membrane fuel cell conditions: determination of the amount of peroxide released during electroreduction and its influence on the stability of the catalysts," *Electrochimica Acta*, **48**(19), 2749-2760 (2003).

Lewandowski, A., Skorupska, K. and Malinska, J., "Novel poly (vinyl alcohol)–KOH–H2O alkaline polymer electrolyte," *Solid state ionics*, **133**(3-4), 265-271 (2000).

Li, L., Xu, L. and Wang, Y., "Novel proton conducting composite membranes for direct methanol fuel cell," *Materials Letters*, **57**(8), 1406-1410 (2003).

Li, M., Chen, X., Guan, J., Wang, X., Wang, J., Williams, C.T. and Liang, C., “A facile and novel approach to magnetic Fe@SiO_2 and $FeSi_2$@SiO_2 nanoparticles,” *Journal of Materials Chemistry*, **22**(2), 609-616 (2012).

Li, P. C., Liao, G. M., Kumar, S. R., Shih, C. M., Yang, C. C., Wang, D. M. and Lue, S. J., "Fabrication and characterization of chitosan nanoparticle-incorporated quaternized poly (vinyl alcohol) composite membranes as solid electrolytes for direct methanol alkaline fuel cells," *Electrochimica Acta*, **187**, 616-628 (2016).

TH-2592_156107017

Li, X., Liu, Q., Cheng, H. and Komarneni, S., “High-yield production of mesoporous nanoscrolls from kaolinite by ultrasonic assisted exfoliation,” *Microporous and Mesoporous Materials*, **241**, 66-71 (2017).

Li, X., Liu, Q., Cheng, H., Zhang, S. and Frost, R. L., “Mechanism of kaolinite sheets curling via the intercalation and delamination process,” *Journal of colloid and interface science*, **444**, 74-80 (2015).

Lim, B., Jiang, M., Camargo, P. H. C., Cho, E. C., Tao, J., Lu, X., Zhu, Y. and Xia, Y., “Pd-Pt bimetallic nanodendrites with high activity for oxygen reduction,” *Science*, **324**(5932), 1302–1305 (2009).

Lin, J. S., Kumar, S. R., Ma, W. T., Shih, C. M., Teng, L. W., Yang, C. C. and Lue, S. J., "Gradiently distributed iron oxide@ graphene oxide nanofillers in quaternized polyvinyl alcohol composite to enhance alkaline fuel cell power density," *Journal of Membrane Science*, **543**, 28-39 (2017).

Lin, J., Mei, T., Lv, M., Zhang, C. A., Zhao, Z. and Wang, X., “Size-controlled PdO/graphene oxides and their reduction products with high catalytic activity,” *RSC Advances*, **4**(56), 29563-29570 (2014).

Lin, X., Wu, L., Liu, Y., Ong, A. L., Poynton, S. D., Varcoe, J. R. and Xu, T., “Alkali resistant and conductive guanidinium-based anion-exchange membranes for alkaline polymer electrolyte fuel cells,” *Journal of Power Sources*, **217**, 373-380 (2012).

Liu, G., Li, X. and Popov, B., "Stability study of nitrogen-modified carbon composite catalysts for oxygen reduction reaction in polymer electrolyte membrane fuel cells," *ECS Transactions*, **25**(1), 1251 (2009).

Liu, H. and Zhang, J., *Electrocatalysis of direct methanol fuel cells: from fundamentals to applications*. Wiley-Vch, Weinheim (2009) p. 487-521.

Liu, H., Song, C., Zhang, L., Zhang, J., Wang, H. and Wilkinson, D. P., "A review of anode catalysis in the direct methanol fuel cell," *Journal of Power Sources*, **155**(2) 95-110 (2006).

TH-2592_156107017

Liu, J. G., Zhao, T. S., Liang, Z. X. and Chen, R, “Effect of membrane thickness on the performance and efficiency of passive direct methanol fuel cells,” *Journal of Power Sources*, **153**(1), 61-67 (2006).

Liu, L., Li, Q., Dai, J., Wang, H., Jin, B. and Bai, R., "A facile strategy for the synthesis of guanidinium-functionalized polymer as alkaline anion exchange membrane with improved alkaline stability," *Journal of membrane science*, **453**, 52-60 (2014).

Liu, Q., Li, X. and Cheng, H., “Insight into the self-adaptive deformation of kaolinite layers into nanoscrolls,” *Applied Clay Science*, **124**, 175-182 (2016).

Liu, X., Gao, H., Ward, J.E., Liu, X., Yin, B., Fu, T., Chen, J., Lovley, D.R. and Yao, J., “Power generation from ambient humidity using protein nanowires,” *Nature*, **578**(7796), 550-554 (2020).

Liu, Z., Liu, J., Zhang, S. and Su, Z., "Study of operational performance and electrical response on mediator-less microbial fuel cells fed with carbon-and protein-rich substrates," *Biochemical Engineering Journal*, **45**(3), 185-191 (2009).

López-Corral, I., Germán, E., Volpe, M. A., Brizuela, G. P. and Juan, A., “Tight-binding study of hydrogen adsorption on palladium decorated graphene and carbon nanotubes,” *International journal of hydrogen* energy, 35(6), 2377-2384 (2010).

Lovering, T. S., *Rock alteration as a guide to ore: East Tintic district* (Vol. 1), Economic Geology Pub. Co., Utah. (1949).

Lović, J., "The kinetics and mechanism of methanol oxidation on Pt and PtRu catalysts in alkaline and acid media," *Journal of the Serbian Chemical Society*, **72**(7), 709-712 (2007).

Lu, Y., Armentrout, A. A., Li, J., Tekinalp, H. L., Nanda, J. and Ozcan, S., "A cellulose nanocrystal-based composite electrolyte with superior dimensional stability for alkaline fuel cell membranes," *Journal of Materials Chemistry A*, **3**(25), 13350-13356 (2015).

TH-2592_156107017

Luo, Y., Guo, J., Wang, C. and Chu, D., "Quaternized poly (methyl methacrylate-co-butyl acrylate-co-vinylbenzyl chloride) membrane for alkaline fuel cells," *Journal of Power Sources*, **195**(12), 3765-3771 (2010).

Ma, B., Qiao, X., Hou, X., and Yang, Y., "Pure keratin membrane and fibers from chicken feather," *International journal of biological macromolecules*, **89**, 614-621 (2016).

Macdonald, G. A., "Solfataric alteration of rocks at Kilauea volcano," *American Journal of Science*, **242**(9), 496-505 (1944).

Mahato, N., Banerjee, A., Gupta, A., Omar, S. and Balani, K, "Progress in material selection for solid oxide fuel cell technology: A review," *Progress in Materials Science*, **72**, 141-337 (2015).

Mahmoud Nasef, M., El-Hefian, E. A., Saalah, S. and Yahaya, A. H., "Preparation and properties of non-crosslinked and ionically crosslinked chitosan/agar blended hydrogel films," *Journal of Chemistry*, **8**(S1), S409-S419 (2011).

Mahmoud, A. M. A., Elsaghier, A. M. M. and Miyatake, K., "Effect of ammonium groups on the properties of anion conductive membranes based on partially fluorinated aromatic polymers," *RSC advances*, **6**(33), 27862-27870 (2016).

Maiti, J., Kakati, N., Lee, S. H., Jee, S. H., Viswanathan, B. and Yoon, Y. S., "Where do poly (vinyl alcohol) based membranes stand in relation to Nafion® for direct methanol fuel cell applications?," *Journal of Power Sources*, **216**, 48-66 (2012).

Makó, É., Kovács, A., Antal, V. and Kristóf, T., "One-pot exfoliation of kaolinite by solvothermal cointercalation," *Applied Clay Science*, **146**, 131-139 (2017).

Mallick, R. K., Thombre, S. B. and Shrivastava, N. K., "Vapor feed direct methanol fuel cells (DMFCs): A review," *Renewable and Sustainable Energy Reviews*, **56**, 51-74 (2016).

Marković, N. M. and Ross Jr, P. N., "Surface science studies of model fuel cell electrocatalysts," *Surface Science Reports*, **45**(4-6), 117-229 (2002).

TH-2592_156107017

Martin, N. M., Van den Bossche, M., Grönbeck, H., Hakanoglu, C., Gustafson, J., Blomberg, S., Arman, M. A., Antony, A., Rai, R., Asthagiri, A. and Weaver, J. F., "Dissociative adsorption of hydrogen on PdO (101) Studied by HRCLS and DFT," *The Journal of Physical Chemistry C*, **117**(26), 13510-13519 (2013).

Maurya, S., Shin, S. H., Kim, Y. and Moon, S. H., "A review on recent developments of anion exchange membranes for fuel cells and redox flow batteries," *RSC Advances*, **5**(47), 37206-37230 (2015).

Meenakshi, S., Bhat, S. D., Sahu, A. K., Sridhar, P., Pitchumani, S. and Shukla, A. K., "Chitosan-polyvinyl alcohol-sulfonated polyethersulfone mixed-matrix membranes as methanol-barrier electrolytes for DMFCs," *Journal of Applied Polymer Science*, **124**(S1), E73-E82 (2012).

Mehta, V. and Cooper, J. S, "Review and analysis of PEM fuel cell design and manufacturing," *Journal of Power Sources*, **114**(1), 32-53 (2003).

Menefee, E., *Protein Crosslinking*, Springer, Boston, MA (1977), p. 307-327.

Merle, G., Wessling, M. and Nijmeijer, K., "Anion exchange membranes for alkaline fuel cells: A review," *Journal of Membrane Science*, **377**(1-2), 1-35 (2011).

Miley, G. H., Luo, N., Mather, J., Burton, R., Hawkins, G., Gu, L., Byrd, E., Gimlin, R., Shrestha, P. J., Benavides, G. and Laystrom, J., "Direct $NaBH_4/H_2O_2$ fuel cells," *Journal of Power Sources*, **165**(2), 509-516 (2007).

Minteer, S. D., Atanassov, P., Luckarift, H. R. and Johnson, G. R., "New materials for biological fuel cells," *Materials Today*, **15**(4), 166-173 (2012).

Mishra, G., Dash, B. and Pandey, S., "Layered double hydroxides: A brief review from fundamentals to application as evolving biomaterials," *Applied Clay Science*, **153**, 172-186 (2018).

Miyake, T. and Rolandi, M., "Grotthuss mechanisms: from proton transport in proton wires to bioprotonic devices," *Journal of Physics: Condensed Matter*, **28**(2), 023001 (2015).

TH-2592_156107017

Miyanishi, S. and Yamaguchi, T., "Analysis of the degradation mechanism of the polyarylene ether anion-exchange membrane for alkaline fuel cell and water-splitting cell applications," *New Journal of Chemistry*, **41**(16), 8036-8044 (2017).

Miyazaki, K., Sugimura, N., Matsuoka, K., Iriyama, Y., Abe, T., Matsuoka, M. and Ogumi, Z., "Perovskite-type oxides $La_{1-x}Sr_xMnO_3$ for cathode catalysts in direct ethylene glycol alkaline fuel cells," *Journal of power sources*, **178**(2), 683-686 (2008).

Moll, R., Divo, M. and Langbein, L., "The human keratins: biology and pathology," *Histochemistry and cell biology*, **129**(6), 705 (2008).

Momeni, S. and Nabipour, I., "A simple green synthesis of palladium nanoparticles with Sargassum alga and their electrocatalytic activities towards hydrogen peroxide," *Applied biochemistry and biotechnology*, **176**(7), 1937-1949 (2015).

Mond, R., "Umkehr der Anionenpermeabilität der roten Blutkörperchen in eine elektive Durchlässigkeit für Kationen." *Pflüger's Archiv für die gesamte Physiologie des Menschen und der Tiere*, **217**(1), 618-630 (1927).

Montilla, F., Morallon, E., Vázquez, J. L., Alcañiz-Monge, J., Cazorla-Amorós, D. and Linares-Solano, A., "Carbon–ceramic composites from coal tar pitch and clays: application as electrocatalyst support," *Carbon*, **40**(12), 2193-2200 (2002).

Mousty, C., "Sensors and biosensors based on clay-modified electrodes-new trends," *Applied Clay Science*, **27**(3-4), 159-177 (2004).

Müller-Plathe, F., "Permeation of polymers - a computational approach," *Acta Polymerica*, **45**(4), 259-293 (1994).

Murphy, E. J., "The dependence of the conductivity of cellulose, silk and wool on their water content," *Journal of Physics and Chemistry of Solids*, **16**(1-2), 115-122 (1960).

Nakagaki, S., Machado, G. S., Halma, M., dos Santos Marangon, A. A., de Freitas Castro, K. A. D., Mattoso, N. and Wypych, F. "Immobilization of iron porphyrins in tubular kaolinite obtained by an intercalation/delamination procedure," *Journal of Catalysis*, **242**(1), 110-117 (2006).

TH-2592_156107017

Nazir, M. S., Kassim, M. H. M., Mohapatra, L., Gilani, M. A., Raza, M. R. and Majeed, K., *Nanoclay reinforced polymer composites*, Springer, Singapore (2016), p. 35-55.

Newton, A. G., Lee, J. Y. and Kwon, K. D., "Na-Montmorillonite Edge Structure and Surface Complexes: An Atomistic Perspective," *Minerals*, **7**(5), 78 (2017).

Nikumbh, A. K., Sayanekar, P. L. and Chaskar, M. G., "Magnetic and electrical properties of γ-Fe_2O_3 prepared from ferrous malonate dehydrate," *Journal of magnetism and magnetic materials*, **97**(1-3), 119-125 (1991).

Odom, I. E., "Smectite clay minerals: properties and uses. Philosophical Transactions of the Royal Society of London," *Series A, Mathematical and Physical Sciences*, **311**(1517), 391-409 (1984).

Ohmori, T., Nodasaka, Y. and Enyo, M., "Electro-oxidation of methanol on Pt electrodes modified by metal oxides and noble metals," *Journal of electroanalytical chemistry and interfacial electrochemistry*, **281**(1-2), 331-337 (1990).

Ozoemena, K. I., "Nanostructured platinum-free electrocatalysts in alkaline direct alcohol fuel cells: catalyst design, principles and applications," *RSC Advances*, **6**(92), 89523-89550 (2016).

Palani, P. B., Abidin, K. S., Kannan, R., Sivakumar, M., Wang, F. M., Rajashabala, S. and Velraj, G., "Improvement of proton conductivity in nanocomposite polyvinyl alcohol (PVA)/chitosan (CS) blend membranes," *RSC Advances*, **4**(106), 61781-61789 (2014).

Paliteiro, C., Hamnett, A. and Goodenough, J. B., "The electroreduction of oxygen on pyrolytic graphite," *Journal of electroanalytical chemistry and interfacial electrochemistry*, **233**(1-2), 147-159 (1987).

Pan, J., Lu, S., Li, Y., Huang, A., Zhuang, L. and Lu, J., "High-Performance alkaline polymer electrolyte for fuel cell applications," *Advanced Functional Materials*, **20**(2), 312-319 (2010).

TH-2592_156107017

Pandey, R. K. and Lakshminarayanan, V., “Electro-oxidation of formic acid, methanol, and ethanol on electrodeposited Pd-polyaniline nanofiber films in acidic and alkaline medium,” *The Journal of Physical Chemistry C*, **113**(52), 21596-21603 (2009).

Panella, B., Hirscher, M. and Roth, S., “Hydrogen adsorption in different carbon nanostructures,” *Carbon*, **43**(10), 2209-2214 (2005).

Park, J. H., Shin, H. J., Kim, M. H., Kim, J. S., Kang, N., Lee, J. Y., Kim, K. T., Lee, J. I. and Kim, D. D.,” Application of montmorillonite in bentonite as a pharmaceutical excipient in drug delivery systems,” *Journal of Pharmaceutical Investigation*, **46**(4), 363-375 (2016).

Patel, H. A., Somani, R. S., Bajaj, H. C. and Jasra, R. V., “Nanoclays for polymer nanocomposites, paints, inks, greases and cosmetics formulations, drug delivery vehicle and waste water treatment,” *Bulletin of Materials Science*, **29**(2), 133-145 (2006).

Peighambardoust, S. J., Rowshanzamir, S. and Amjadi, M, "Review of the proton exchange membranes for fuel cell applications," *International journal of hydrogen energy*, **35**(17), 9349-9384 (2010).

Perez-Carvajal, J., Aranda, P. and Ruiz-Hitzky, E., “Titanosilicate-sepiolite hybrid nanoarchitectures for hydrogen technologies applications,” *Journal of Solid State Chemistry*, **270**, 287-294 (2019).

Piela, P., Eickes, C., Brosha, E., Garzon, F. and Zelenay, P., "Ruthenium crossover in direct methanol fuel cell with Pt-Ru black anode," *Journal of the Electrochemical Society*, **151**(12), A2053 (2004).

Poux, T., Bonnefont, A., Ryabova, A., Kéranguéven, G., Tsirlina, G. A. and Savinova, E. R., "Electrocatalysis of hydrogen peroxide reactions on perovskite oxides: experiment versus kinetic modeling," *Physical Chemistry Chemical Physics*, **16**(27), 13595-13600 (2014).

Prakash, J. and Joachin, H., "Electrocatalytic activity of ruthenium for oxygen reduction in alkaline solution," *Electrochimica Acta*, **45**(14), 2289-2296 (2000).

TH-2592_156107017

Plimpton, S., Fast parallel algorithms for short-range molecular dynamics," *Journal of computational physics*, **117**(1), 1-19 (1995)

Plimpton, S., Crozier, P. and Thompson, A., "LAMMPS-large-scale atomic/molecular massively parallel simulator," *Sandia National Laboratories*, **18**, 43 (2007).

Psofogiannakis, G. M. and Froudakis, G. E., "Fundamental studies and perceptions on the spillover mechanism for hydrogen storage," *Chemical Communications*, **47**(28), 7933-7943 (2011).

Qin, Y. H., Yang, H. H., Zhang, X. S., Li, P. and Ma, C. A., "Effect of carbon nanofibers microstructure on electrocatalytic activities of Pd electrocatalysts for ethanol oxidation in alkaline medium," *International Journal of Hydrogen Energy*, **35**(15), 7667-7674 (2010).

Rahim, M. A. A., Hameed, R. M. A. and Khalil, M. W, "Nickel as a catalyst for the electro-oxidation of methanol in alkaline medium," *Journal of Power Sources*, **134**, 160-169 (2004).

Ramadass, K., Sathish, C. I., Johns, A., Ruban, S. J., Singh, G., Lakhi, K. S., Almajid, A. M., Belperio, T. and Vinu, A., "Characterization and hydrogen storage performance of halloysite nanotubes," *Journal of nanoscience and nanotechnology*, **19**(12), 7892-7898 (2019).

Ramasubbu, A., Vanangamudi, A., Muthusubramanian, S., Ramachandran, M. S. and Sivasubramanian, S., "Electrocatalytic studies using silver-clay composite-a novel material," *Electrochemistry communications*, **2**(1), 56-64 (2000).

Ramos-Sánchez, G. and Solorza-Feria, O., "Synthesis and characterization of $Pd_{0.5}Ni_xSe_{(0.5-x)}$ electrocatalysts for oxygen reduction reaction in acid media," *International journal of hydrogen energy*, **35**(21), 12105-12110 (2010).

Ravindranathan, P., Malla, P. B., Komarneni, S. and Roy, R., "Preparation of metal supported montmorillonite catalyst: A new approach," *Catalysis Letters*, **6**(3-6), 401-407 (1990).

TH-2592_156107017

Rhim, J. W., Park, H. B., Lee, C. S., Jun, J. H., Kim, D. S. and Lee, Y. M., "Crosslinked poly (vinyl alcohol) membranes containing sulfonic acid group: proton and methanol transport through membranes." *Journal of Membrane Science*, **238**(1-2), 143-151 (2004).

Rivera Gavidia, L. M., Sebastián, D., Pastor, E., Aricò, A. S. and Baglio, V., "Carbon-supported Pd and PdFe alloy catalysts for direct methanol fuel cell cathodes," *Materials*, **10**(6), 580 (2017).

Rives, V., del Arco, M. and Martín, C., "Layered double hydroxides as drug carriers and for controlled release of non-steroidal antiinflammatory drugs (NSAIDs): a review," *Journal of Controlled Release*, **169**(1-2), 28-39 (2013).

Roguska, A., Pisarek, M., Andrzejczuk, M., Dolata, M., Lewandowska, M. and Janik-Czachor, M., "Characterization of a calcium phosphate-TiO_2 nanotube composite layer for biomedical applications," *Materials Science and Engineering: C*, **31**(5), 906-914 (2011).

Román-Martínez, M. C., Cazorla-Amoros, D., Yamashita, H., De Miguel, S. and Scelza, O. A., "XAFS study of dried and reduced PtSn/C catalysts: Nature and structure of the catalytically active phase," *Langmuir*, **16**(3), 1123-1131 (2000).

Ruiz-García, C., Pérez-Carvajal, J., Berenguer-Murcia, A., Darder, M., Aranda, P., Cazorla-Amorós, D. and Ruiz-Hitzky, E., "Clay-supported graphene materials: application to hydrogen storage," *Physical Chemistry Chemical Physics*, **15**(42), 18635-18641 (2013).

Ryan, P. C., Huertas, F. J., Hobbs, F. W. C. and Pincus, L. N., "Kaolinite and halloysite derived from sequential transformation of pedogenic smectite and kaolinite-smectite in a 120ka tropical soil chronosequence," *Clays and Clay Minerals*, **64**(5), 639-667 (2016).

Rynkowska, E., Fatyeyeva, K., Marais, S., Kujawa, J. and Kujawski, W., "Chemically and Thermally Crosslinked PVA-Based Membranes: Effect on Swelling and Transport Behavior," *Polymers*, **11**(11), 1799 (2019).

TH-2592_156107017

Ryu, J., Seo, J. Y., Choi, B. N., Kim, W. J. and Chung, C. H., “Quaternized chitosan-based anion exchange membrane for alkaline direct methanol fuel cells,” *Journal of Industrial and Engineering Chemistry*, **73**, 254-259 (2019).

Sahu, A. K., Selvarani, G., Pitchumani, S., Sridhar, P., Shukla, A. K., Narayanan, N., Banerjee, A. and Chandrakumar, N., "PVA-PSSA membrane with interpenetrating networks and its methanol crossover mitigating effect in DMFCs," *Journal of The Electrochemical Society*, **155**(7), B686-B695 (2008).

Sajjad, S. D., Hong, Y. and Liu, F., "Synthesis of guanidinium-based anion exchange membranes and their stability assessment," *Polymers for advanced technologies*, **25**(1), 108-116 (2014).

Sajjad, S. D., Liu, D., Wei, Z., Sakri, S., Shen, Y., Hong, Y. and Liu, F., “Guanidinium based blend anion exchange membranes for direct methanol alkaline fuel cells (DMAFCs),” *Journal of Power Sources*, **300**, 95-103 (2015).

Sarapuu, A., Vaik, K., Schiffrin, D. J. and Tammeveski, K., "Electrochemical reduction of oxygen on anthraquinone-modified glassy carbon electrodes in alkaline solution," *Journal of Electroanalytical Chemistry*, **541**, 23-29 (2003).

Sarma, L. S., Chen, C. H., Wang, G. R., Hsueh, K. L., Huang, C. P., Sheu, H. S., Liu, D. G., Lee, J. F. and Hwang, B. J., "Investigations of direct methanol fuel cell (DMFC) fading mechanisms," *Journal of Power Sources*, **167**(2), 358-365 (2007).

Sata, T., Tsujimoto, M., Yamaguchi, T. and Matsusaki, K., "Change of anion exchange membranes in an aqueous sodium hydroxide solution at high temperature," *Journal of Membrane Science*, **112**(2), 161-170 (1996).

Sato, H., Yamagishi, A. and Kawamura, K., “Molecular simulation for flexibility of a single clay layer,” *The Journal of Physical Chemistry B*, **105**(33), 7990-7997 (2001).

Schulenburg, H., Stankov, S., Schünemann, V., Radnik, J., Dorbandt, I., Fiechter, S., Bogdanoff, P. and Tributsch, H., "Catalysts for the oxygen reduction from heat-treated iron (III) tetramethoxyphenylporphyrin chloride: structure and stability of active sites," *The Journal of Physical Chemistry B*, **107**(34), 9034-9041 (2003).

TH-2592_156107017

Schulze, M. and Gülzow, E., "Degradation of nickel anodes in alkaline fuel cells," *Journal of Power Sources*, **127**(1-2), 252-263 (2004).

Scott, K., Yu, E., Vlachogiannopoulos, G., Shivare, M. and Duteanu, N., "Performance of a direct methanol alkaline membrane fuel cell," *Journal of Power Sources*, **175**(1), 452-457 (2008).

Shaari, N. and Kamarudin, S. K., "Chitosan and alginate types of bio-membrane in fuel cell application: an overview," *Journal of Power Sources*, **289**, 71-80 (2015).

Sharifi, T., Gracia-Espino, E., Barzegar, H. R., Jia, X., Nitze, F., Hu, G., Nordblad, P., Tai, C. W. and Wågberg, T., "Formation of nitrogen-doped graphene nanoscrolls by adsorption of magnetic γ-Fe_2O_3 nanoparticles," *Nature communications*, **4**(1), 1-9 (2013).

Sharma, S., Gupta, A., Chik, S. M. S., Kee, C. G., Mistry, B. M., Kim, D. H. and Sharma, G., "Characterization of keratin microparticles from feather biomass with potent antioxidant and anticancer activities," *International journal of biological macromolecules*, **104**, 189-196 (2017).

Shekhawat, D., Spivey, J. J. and Berry, D. A., *Fuel Cells: Technologies For Fuel Processing*, Elsevier B.V., Amsterdam (2011), p. 11-27.

Shen, P. K. and Xu, C., "Alcohol oxidation on nanocrystalline oxide Pd/C promoted electrocatalysts," *Electrochemistry Communications*, **8**(1), 184-188 (2006).

Shetti, N. P., Nayak, D. S., Kuchinad, G. T. and Naik, R. R., "Electrochemical behavior of thiosalicylic acid at γ-Fe2O3 nanoparticles and clay composite carbon electrode," *Electrochimica Acta*, **269**, 204-211 (2018).

Shi, C., Rusling, J. F., Wang, Z., Willis, W. S., Winiecki, A. M. and Suib, S. L., "Electrocatalytic reactions in organized assemblies. 6. Electrochemical and spectroscopic studies of catalytic clay micelle electrodes," *Langmuir*, **5**(3), 650-660 (1989).

TH-2592_156107017

Shinoda, K. and Friberg, S., “Microemulsions: colloidal aspects. Advances in Colloid and Interface,” *Science*, **4**(4), 281–300 (1975).

Shobba, T., Mayanna, S. M. and Sequeira, C. A. C., "Preparation and characterization of Co–W alloys as anode materials for methanol fuel cells," *Journal of power sources*, **108**(1-2), 261-264 (2002).

Smitha, B., Sridhar, S. and Khan A. A., "Solid polymer electrolyte membranes for fuel cell applications-a review," *Journal of membrane science*, **259**(1-2), 10-26 (2005).

Soni, K. S., Desale, S. S. and Bronich, T. K., “Nanogels: An overview of properties, biomedical applications and obstacles to clinical translation,” *Journal of Controlled Release*, **240**, 109-126 (2016).

Souza, F. M., Nandenha, J., Batista, B. L., Oliveira, V. H. A., Pinheiro, V. S., Parreira, L. S., Neto, A. O. and Santos, M. C., "PdxNby electrocatalysts for DEFC in alkaline medium: stability, selectivity and mechanism for EOR," *International Journal of Hydrogen Energy*, **43**(9), 4505-4516 (2018).

Souzy, R. and Ameduri, B., "Functional fluoropolymers for fuel cell membranes," *Progress in Polymer Science*, **30**(6), 644-687 (2005).

Srinophakun, T. and Martkumchan, S., “Ionic conductivity in a chitosan membrane for a PEM fuel cell using molecular dynamics simulation,” *Carbohydrate polymers*, **88**(1), 194-200 (2012).

Sterling, D. and Casey, J. R., “Transport activity of AE3 chloride/bicarbonate anion-exchange proteins and their regulation by intracellular pH,” *Biochemical Journal*, **344**(1), 221-229 (1999).

Stuchebrukhov, A. A., "Mechanisms of proton transfer in proteins: localized charge transfer versus delocalized soliton transfer," *Physical Review E*, **79**(3), 031927 (2009).

Sun, Z., Pan, J., Guo, J. and Yan, F., "The alkaline stability of anion exchange membrane for fuel cell applications: the effects of alkaline media," *Advanced Science*, **5**(8), 1800065 (2018).

TH-2592_156107017

Takaba, H., Hisabe, T., Shimizu, T. and Alam, M. K., "Molecular modeling of OH^- transport in poly (arylene ether sulfone ketone)s containing quaternized ammonio-substituted fluorenyl groups as anion exchange membranes," *Journal of Membrane Science*, **522**, 237-244 (2017).

Takei, H. and Chiba, S., "Vacancy ordering in epitaxially-grown single crystals of γ-Fe_2O_3," *Journal of the Physical Society of Japan*, **21**(7), 1255-1263 (1966).

Talapin, D. V., Shevchenko, E. V., Murray, C. B., Titov, A. V. and Kral, P., "Dipole - dipole interactions in nanoparticle superlattices," *Nano letters*, **7**(5), 1213-1219 (2007).

Tang, B., Yun, X., Xiong, Z. and Wang, X., "Formation of Graphene Oxide Nanoscrolls in Organic Solvents: Toward Scalable Device Fabrication," *ACS Applied Nano Materials*, **1**(2), 686-697 (2018).

Taraszewska, J. and Rosłonek, G., "Electrocatalytic oxidation of methanol on a glassy carbon electrode modified by nickel hydroxide formed by ex situ chemical precipitation," Journal of Electroanalytical Chemistry, **364**(1-2), 209-213 (1994).

Taylor, R. J. and Humffray, A. A., "Electrochemical studies on glassy carbon electrodes: II. Oxygen reduction in solutions of high pH (pH> 10)," *Journal of electroanalytical chemistry and interfacial electrochemistry*, **64**(1), 63-84 (1975).

Tehrani, R. M. A. and Ab Ghani, S., "The nanocrystalline nickel with catalytic properties on methanol oxidation in alkaline medium," *Fuel Cells*, **9**(5), 579-587 (2009).

Torres, M. A., Vieira, R. S., Beppu, M. M., Arruda, E. J. and Santana, C. C., "Production of chemically modified chitosan microspheres by a spraying and coagulation method," *Materials Research*, **10**(4), 347-352 (2007).

Toshima, N. and Yonezawa, T., "Bimetallic nanoparticles-novel materials for chemical and physical applications," *New Journal of Chemistry*, **22**(11), 1179–1201 (1998).

Tournassat, C., Davis, J. A., Chiaberge, C., Grangeon, S. and Bourg, I. C., "Modeling the acid–base properties of montmorillonite edge surfaces," *Environmental science & technology*, **50**(24), 13436-13445 (2016).

TH-2592_156107017

Trasatti, S. and Petrii, O. A, “Real surface area measurements in electrochemistry,” *Pure Appl. Chem*, **63**(5), 711-734 (1991).

Tripković, A. V., Popović, K. D., Grgur, B. N., Blizanac, B., Ross, P. N. and Marković, N. M., "Methanol electrooxidation on supported Pt and PtRu catalysts in acid and alkaline solutions," *Electrochimica Acta*, **47**(22-23), 3707-3714 (2002).

Tripković, A. V., Popović, K. D., Momčilović, J. D. and Draić, D. M., “Kinetic and mechanistic study of methanol oxidation on a Pt (111) surface in alkaline media,” *Journal of Electroanalytical Chemistry*, **418**(1-2), 9-20 (1996).

Tripković, A., Popović, K. and Lović, J., "Kinetic study of methanol oxidation on Pt_2Ru_3/C catalyst in the alkaline media," *Journal of the Serbian Chemical Society*, **72**(11), 1095-1101 (2007).

[a]Tuckerman, M., Laasonen, K., Sprik, M. and Parrinello, M., “Ab initio molecular dynamics simulation of the solvation and transport of $H3O^+$ and OH^- ions in water,” *The Journal of Physical Chemistry*, **99**(16), 5749-5752 (1995).

[b]Tuckerman, M., Laasonen, K., Sprik, M. and Parrinello, M., “Ab initio molecular dynamics simulation of the solvation and transport of hydronium and hydroxyl ions in water,” *The Journal of chemical physics*, **103**(1), 150-161 (1995).

Tulloch, J. and Donne, S. W., "Activity of perovskite $La_{1-x}Sr_xMnO_3$ catalysts towards oxygen reduction in alkaline electrolytes," *Journal of Power Sources*, **188**(2), 359-366 (2009).

Vácha, R., Horinek, D., Berkowitz, M. L. and Jungwirth, P., “Hydronium and hydroxide at the interface between water and hydrophobic media,” *Physical Chemistry Chemical Physics*, **10**(32), 4975-4980 (2008).

Van Der Putten, A. M. T. P., Elzing, A., Visscher, W. and Barendrecht, E., "Oxygen reduction on pyrolysed carbon-supported transition metal chelates," *Journal of electroanalytical chemistry and interfacial electrochemistry*, **205**(1-2), 233-244 (1986).

TH-2592_156107017

Van Effen, R. M. and Evans, D. H., "A study of aldehyde oxidation at glassy carbon, mercury, copper, silver, gold and nickel anodes," *Journal of Electroanalytical Chemistry and Interfacial Electrochemistry*, **103**(3), 383-397 (1979).

Varcoe, J. R. and Slade, R. C. T., "An electron-beam-grafted ETFE alkaline anion-exchange membrane in metal cation-free solid-state alkaline fuel cells," *Electrochemistry Communications*, **8**, 839–843 (2006).

Varcoe, J. R., "Investigations of the ex situ ionic conductivities at 30 C of metal-cation-free quaternary ammonium alkaline anion-exchange membranes in static atmospheres of different relative humidities," *Physical Chemistry Chemical Physics*, **9**(12) 1479-1486 (2007).

Varcoe, J. R., Atanassov, P., Dekel, D. R., Herring, A. M., Hickner, M. A., Kohl, P. A., Kucernak, A. R., Mustain, W. E., Nijmeijer, K., Scott, K. and Xu, T., "Anion-exchange membranes in electrochemical energy systems," *Energy & environmental science*, **7**(10), 3135-3191 (2014).

Vijayakumar, V. and Nam, S. Y., "Recent advancements in applications of alkaline anion exchange membranes for polymer electrolyte fuel cells," *Journal of Industrial and Engineering Chemistry*, **70**, 70-86 (2019).

Villa, A. L. V., Aragão, M. R. S., dos Santos, E. P., Mazotto, A. M., Zingali, R. B., de Souza, E. P. and Vermelho, A. B., "Feather keratin hydrolysates obtained from microbial keratinases: effect on hair fiber," *Bmc Biotechnology*, **13**(1), 15 (2013).

Wan, Y., Creber, K. A., Peppley, B. and Bui, V. T., "Ionic conductivity of chitosan membranes," *Polymer*, **44**(4) 1057-1065 (2003).

Wan, Y., Creber, K. A., Peppley, B., Bui, V. T. and Halliop, E., "New solid polymer electrolyte membranes for alkaline fuel cells," *Polymer international*, **54**(1), 5-10 (2005).

Wan, Y., Peppley, B., Creber, K. A., Bui, V. T. and Halliop, E., "Quaternized-chitosan membranes for possible applications in alkaline fuel cells," *Journal of Power Sources*, **185**(1), 183-187 (2008).

TH-2592_156107017

Wan, Y., Peppley, B., Creber, K. A., Bui, V. T. and Halliop, E., "Preliminary evaluation of an alkaline chitosan-based membrane fuel cell," *Journal of Power Sources*, **162**(1), 105-113 (2006).

Wang, C., Hou, Y., Kim, J. and Sun, S., "A general strategy for synthesizing FePt nanowires and nanorods," *Angewandte Chemie: International Edition*, **46**(33), 6333–6335 (2007).

Wang, C., Mo, B., He, Z., Xie, X., Zhao, C.X., Zhang, L., Shao, Q., Guo, X., Wujcik, E.K. and Guo, Z., "Hydroxide ions transportation in polynorbornene anion exchange membrane," *Polymer*, **138**, 363-368 (2018).

Wang, D., Yang, X. H., Tang, R. C. and Yao, F., "Extraction of keratin from rabbit hair by a deep eutectic solvent and its characterization," *Polymers* 10, no. **9**, 993 (2018).

Wang, F., Li, M., Yu, L., Sun, F., Wang, Z., Zhang, L., Zeng, H. and Xu, X., "Corn-like, recoverable γ-Fe_2O_3@SiO_2@TiO_2 photocatalyst induced by magnetic dipole interactions," *Scientific reports*, **7**(1), 1-10 (2017).

Wang, G., Bao, Y., Tian, Y., Xia, J. and Cao, D., "Electrocatalytic activity of perovskite $La_{1-x}Sr_xMnO_3$ towards hydrogen peroxide reduction in alkaline medium," *Journal of Power Sources*, **195**(19), 6463-6467 (2010).

Wang, H. and Roman, M., "Formation and properties of chitosan - cellulose nanocrystal polyelectrolyte macroion complexes for drug delivery applications," *Biomacromolecules*, **12**(5), 1585-1593 (2011).

Wang, H., Ji, S., Wang, W., Linkov, V., Pasupathi, S. and Wang, R., "Pt decorated PdFe/C: extremely high electrocatalytic activity for methanol oxidation," *Int J Electrochem Sci*, **7**, 3390-3398 (2012).

Wang, H., Wu, Y., Yuan, X., Zeng, G., Zhou, J., Wang, X. and Chew, J. W., "Clay-Inspired MXene-Based Electrochemical Devices and Photo-Electrocatalyst: State-of-the-Art Progresses and Challenges," *Advanced Materials*, **30**(12), 1704561 (2018).

TH-2592_156107017

Wang, J. and Wang, L., "Preparation and properties of organic–inorganic alkaline hybrid membranes for direct methanol fuel cell application," *Solid State Ionics*, **255**, 96-103 (2014).

Wang, J. L., Wang, L. L., Feng, R. J. and Zhang, Y., "Synthesis and characterization of novel anion exchange membranes containing bi-imidazolium-based ionic liquid for alkaline fuel cells," *Solid State Ionics*, **278**, 144-151 (2015).

Wang, L., Yi, B. L., Zhang, H. M. and Xing, D. M., "Characteristics of polyethersulfone/sulfonated polyimide blend membrane for proton exchange membrane fuel cell," *The Journal of Physical Chemistry B*, **112**(14), 4270-4275 (2008).

Wang, P., Zhou, Y., Hu, M. and Chen, J., "Well-dispersed NiO nanoparticles supported on nitrogen-doped carbon nanotube for methanol electrocatalytic oxidation in alkaline media," *Applied Surface Science*, **392**, 562-571 (2017).

Wang, X., McClure, J. P., & Fedkiw, P. S., "Transport properties of proton-and hydroxide-exchange membranes for fuel cells." *Electrochimica acta*, **79**, 126-132 (2012).

Wang, Y. J., Qiao, J., Baker, R. and Zhang, J., "Alkaline polymer electrolyte membranes for fuel cell applications," *Chemical Society Reviews*, **42**(13), 5768-5787 (2013).

Wang, Y., Chen, K. S., Mishler, J., Cho, S. C. and Adroher, X. C., "A review of polymer electrolyte membrane fuel cells: technology, applications, and needs on fundamental research," *Applied Energy*, **88** (4), 981-1007 (2011).

Wang, Y., Zhang, D., Peng, W., Liu, L. and Li, M, "Electrocatalytic oxidation of methanol at Ni–Al layered double hydroxide film modified electrode in alkaline medium," *Electrochimica Acta*, **56**(16), 5754-5758 (2011).

Wasmus, S. and Küver, A., "Methanol oxidation and direct methanol fuel cells: a selective review," *Journal of Electroanalytical Chemistry*, **461**(1-2), 14-31 (1999).

TH-2592_156107017

Watanabe, M. A. and Motoo, S., "Electrocatalysis by ad-atoms: Part II. Enhancement of the oxidation of methanol on platinum by ruthenium ad-atoms," *Journal of Electroanalytical Chemistry and Interfacial Electrochemistry*, **60**(3), 267-273 (1975).

Watanabe, S., Fukuta, K. and Yanagi, H., "Determination of carbonate ion in MEA during the alkaline membrane fuel cell (AMFC) operation," *ECS transactions*, **33**(1), 1837 (2010).

Watt-Smith, M. J., Friedrich, J. M., Rigby, S. P., Ralph, T. R. and Walsh, F. C., "Determination of the electrochemically active surface area of Pt/C PEM fuel cell electrodes using different adsorbates," *Journal of Physics D: Applied Physics*, **41**(17), 174004 (2008).

White, R. D., Bavykin, D. V. and Walsh, F. C., "Spontaneous scrolling of kaolinite nanosheets into halloysite nanotubes in an aqueous suspension in the presence of GeO_2," *The Journal of Physical Chemistry C*, **116**(15), 8824-8833 (2012).

Wilkinson, D. P., Zhang, J., Hui, R., Fergus, J. and Li, X., *Proton exchange membrane fuel cells: materials properties and performance*. CRC Press, Boca Raton (20010), p. 107-190.

Will, F. G., "Hydrogen Adsorption on Platinum Single Crystal Electrodes I. Isotherms and Heats of Adsorption," *Journal of the electrochemical society*, **112**(4), 451 (1965).

Willner, I., "Biomaterials for sensors, fuel cells, and circuitry," *Science*, **298**(5602), 2407-2408 (2002).

Wu, G. M., Lin, S. J. and Yang, C. C., "Preparation and characterization of PVA/PAA membranes for solid polymer electrolytes," *Journal of Membrane Science*, **275**(1-2), 127-133 (2006).

Wu, H., Shen, X., Xu, T., Hou, W. and Jiang, Z., "Sulfonated poly (ether ether ketone)/ amino-acid functionalized titania hybrid proton conductive membranes," *Journal of Power Sources*, **213**, 83-92 (2012).

TH-2592_156107017

Wu, Q., Zhang, J. and Sang, S., "Preparation of alkaline solid polymer electrolyte based on PVA–TiO_2–KOH–H_2O and its performance in Zn–Ni battery," *Journal of Physics and Chemistry of Solids*, **69**(11), 2691-2695 (2008).

Wu, W., Xiao, X. H., Zhang, S. F., Peng, T. C., Zhou, J., Ren, F. and Jiang, C. Z., "Synthesis and magnetic properties of maghemite (γ-Fe_2O_3) short-nanotubes," *Nanoscale research letters*, **5**(9), 1474-1479 (2010).

Wu, Y., Wu, C., Yu, F., Xu, T. and Fu, Y., "Free-standing anion-exchange PEO–SiO_2 hybrid membranes," *Journal of Membrane Science*, **307**(1), 28-36 (2008).

www.tokuyama.co.jp

Xing, B. and Savadogo, O., "Hydrogen/oxygen polymer electrolyte membrane fuel cells (PEMFCs) based on alkaline-doped polybenzimidazole (PBI)," *Electrochemistry communications*, **2**(10), 697-702 (2000).

Xiong, L., Kannan, A. M., and Manthiram, A., "Pt–M (M = Fe, Co, Ni and Cu) electrocatalysts synthesized by an aqueous route for proton exchange membrane fuel cells," *Electrochemistry Communications*, **4**(11), 898–903 (2002).

Xiong, Y., Liu, Q. L., Zhang, Q. G. and Zhu, A. M., "Synthesis and characterization of cross-linked quaternized poly (vinyl alcohol)/chitosan composite anion exchange membranes for fuel cells," *Journal of Power Sources*, **183**(2), 447-453 (2008).

Xu, B., Jacobs, M. I., Kostko, O. and Ahmed, M., "Guanidinium Group Remains Protonated in a Strongly Basic Arginine Solution," *ChemPhysChem*, **18**(12), 1503-1506 (2017).

Xu, C., Cheng, L., Shen, P. and Liu, Y., "Methanol and ethanol electrooxidation on Pt and Pd supported on carbon microspheres in alkaline media," *Electrochemistry Communications*, **9**(5), 997-1001 (2007).

Xu, C., kang Shen, P. and Liu, Y., "Ethanol electrooxidation on Pt/C and Pd/C catalysts promoted with oxide," *Journal of Power Sources*, **164**(2), 527-531 (2007).

TH-2592_156107017

Xu, C., Tian, Z. and Shen, P., "Oxide (CeO_2, NiO, Co_3O_4 and Mn_3O_4)-promoted Pd/C electrocatalysts for alcohol electrooxidation in alkaline media," *Electrochimica Acta*, **53**(5), 2610-2618 (2008).

Xu, J. B., Zhao, T. S., Shen, S. Y. and Li, Y. S., "Stabilization of the palladium electrocatalyst with alloyed gold for ethanol oxidation," *International journal of hydrogen energy*, **35**(13), 6490-6500 (2010).

Xu, X., Zhao, G., Wang, H., Li, X., Feng, X., Cheng, B., Shi, L., Kang, W., Zhuang, X. and Yin, Y., "Bio-inspired amino-acid-functionalized cellulose whiskers incorporated into sulfonated polysulfone for proton exchange membrane," *Journal of Power Sources*, **409**, 123-131 (2019).

Xue, B., Dong, X., Li, Y., Zheng, J., Li, S. and Zhang, S., "Synthesis of novel guanidinium-based anion-exchange membranes with controlled microblock structures," *Journal of Membrane Science*, **537**, 151-159 (2017).

Yang, C. C. and Lin, S. J., "Preparation of composite alkaline polymer electrolyte," *Materials Letters*, **57**(4), 873-881 (2002).

Yang, C. C., "Fabrication and characterization of poly (vinyl alcohol)/ montmorillonite/ poly (styrene sulfonic acid) proton-conducting composite membranes for direct methanol fuel cells," *International journal of hydrogen energy*, **36**(7), 4419-4431 (2011).

Yang, C. C., "Polymer Ni–MH battery based on PEO–PVA–KOH polymer electrolyte," *Journal of Power Sources*, **109**(1), 22-31 (2002).

Yang, C. C., "Study of alkaline nanocomposite polymer electrolytes based on PVA–ZrO_2–KOH," *Materials Science and Engineering: B*, **131**(1-3), 256-262 (2006).

Yang, C. C., "Synthesis and characterization of the cross-linked PVA/TiO2 composite polymer membrane for alkaline DMFC," *Journal of Membrane Science*, **288**(1-2), 51-60 (2007).

TH-2592_156107017

Yang, C. C., Chien, W. C. and Li, Y. J., "Direct methanol fuel cell based on poly (vinyl alcohol)/titanium oxide nanotubes/poly (styrene sulfonic acid)(PVA/nt-TiO2/PSSA) composite polymer membrane," *Journal of Power Sources*, **195**(11), 3407-3415 (2010).

Yang, T., "Preliminary study of SPEEK/PVA blend membranes for DMFC applications," *International Journal of Hydrogen Energy*, **33**(22), 6772-6779 (2008).

Yang, Y. F., Zhou, Y. H. and Cha, C. S., "Electrochemical reduction of oxygen on small palladium particles supported on carbon in alkaline solution," *Electrochimica acta*, **40**(16), 2579-2586 (1995).

Yasuda, K., Taniguchi, A., Akita, T., Ioroi, T. and Siroma, Z., "Platinum dissolution and deposition in the polymer electrolyte membrane of a PEM fuel cell as studied by potential cycling," *Physical Chemistry Chemical Physics*, **8**(6), 746-752 (2006).

Ye, J., Liu, J., Xu, C. and Tong, Y., "Electrooxidation of 2-propanol on Pt, Pd and Au in alkaline medium," *Electrochemistry Communications*, **9**(12), 2760-2763 (2007).

Ye, Y. S., Cheng, M. Y., Xie, X. L., Rick, J., Huang, Y. J., Chang, F. C. and Hwang, B. J., "Alkali doped polyvinyl alcohol/graphene electrolyte for direct methanol alkaline fuel cells," *Journal of power sources*, **239**, 424-432 (2013).

Yeager, E., "Dioxygen electrocatalysis: mechanisms in relation to catalyst structure," *Journal of Molecular Catalysis*, **38**(1-2), 5-25 (1986).

Yi, Q., Niu, F. and Sun, L., "Fabrication of novel porous Pd particles and their electroactivity towards ethanol oxidation in alkaline media," *Fuel*, **90**(8), 2617-2623 (2011).

Yu, Y., Li, G., Zhou, S., Chen, X., Lee, H. W. and Yang, W., "Self–adaptive Si/reduced graphene oxide scrolls for high–performance Li–ion battery anodes," *Carbon*, **120**, 397-404 (2017).

Yuan, P., Southon, P. D., Liu, Z., Green, M. E., Hook, J. M., Antill, S. J. and Kepert, C. J., "Functionalization of halloysite clay nanotubes by grafting with γ-

TH-2592_156107017

aminopropyltriethoxysilane," *The Journal of Physical Chemistry C*, **112**(40), 15742-15751 (2008).

Yuan, P., Tan, D. and Annabi-Bergaya, F., "Properties and applications of halloysite nanotubes: recent research advances and future prospects," *Applied Clay Science*, **112**, 75-93 (2015).

Yuan, P., Tan, D., Annabi-Bergaya, F., Yan, W., Liu, D. and Liu, Z., "From platy kaolinite to aluminosilicate nanoroll via one-step delamination of kaolinite: Effect of the temperature of intercalation," *Applied Clay Science*, **83**, 68-76 (2013).

Yuan, Y., Shen, C., Chen, J. and Ren, X., "Synthesis and characterization of cross-linked quaternized chitosan/poly (diallyldimethylammonium chloride) blend anion-exchange membranes," *Ionics*, **24**(4), 1173-1180 (2018).

Yue, R., Zhang, Q., Wang, C., Du, Y., Yang, P. and Xu, J., "Graphene–poly (5-aminoindole) composite film as Pt catalyst support for methanol electrooxidation in alkaline medium," *Electrochimica Acta*, **107**, 292-300 (2013).

Zadick, A., Dubau, L., Sergent, N., Berthomé, G. and Chatenet, M., "Huge instability of Pt/C catalysts in alkaline medium," *ACS Catalysis*, **5**(8), 4819-4824 (2015).

Zaidi, S. M. J. and Matsuura, T., *Polymer Membranes for Fuel Cells*, Springer Science + Business Media, LLC, New York (2009), p. 361-384.

Zartman, G. D., Liu, H., Akdim, B., Pachter, R. and Heinz, H., "Nanoscale tensile, shear, and failure properties of layered silicates as a function of cation density and stress," *The Journal of Physical Chemistry C*, **114**(4), 1763-1772 (2010).

Zeng, F., Kuang, Y., Liu, G., Liu, R., Huang, Z., Fu, C. and Zhou, H., "Supercapacitors based on high-quality graphene scrolls," *Nanoscale*, **4**(13), 3997-4001 (2012).

Zeng, G., Han, J., Dai, B., Liu, X., Li, J., Chen, C., Yang, J. and Sun, D., "Preparation and Characterization of Alkaline Anion Exchange Membrane for Fuel Cells Application," *Journal of Nanotechnology*, **2017**, (2017).

TH-2592_156107017

Zeng, M., Wang, Y., Liu, Q., Yuan, X., Zuo, S., Feng, R., Yang, J., Wang, B., Qi, C. and Lin, Y., “Encaging palladium nanoparticles in chitosan modified montmorillonite for efficient, recyclable catalysts,” *ACS applied materials & interfaces*, **8**(48), 33157-33164 (2016).

Zeng, Q. H., Liu, Q. L., Broadwell, I., Zhu, A. M., Xiong, Y. and Tu, X. P., "Anion exchange membranes based on quaternized polystyrene-block-poly (ethylene-ran-butylene)-block-polystyrene for direct methanol alkaline fuel cells," *Journal of Membrane Science*, **349**(1-2), 237-243 (2010).

Zhai, S., Dai, W., Lin, J., He, S., Zhang, B. and Chen, L., "Enhanced proton conductivity in sulfonated poly (ether ether ketone) membranes by incorporating sodium dodecyl benzene sulfonate," *Polymers*, **11**(2), 203 (2019).

Zhang, J., Li, Y., Li, J., Zhao, Z., Liu, X., Li, Z., Han, Y., Hu, J. and Chen, A., "Isolation and characterization of biofunctional keratin particles extracted from wool wastes," *Powder technology*, **246**, 356-362 (2013).

Zhang, J., *PEM Fuel Cell Electrocatalysts and Catalyst Layers*, Springer-Verlag, London (2008).

Zhang, J., Xie, Z., Zhang, J., Tang, Y., Song, C., Navessin, T., Shi, Z., Song, D., Wang, H., Wilkinson, D. P., Liu, Z. S. and Holdcroft, S., “High temperature PEM fuel cells,” *Journal of Power Sources*, **160**(2), 872-891 (2006).

Zhang, M., Yan, Y., Gong, K., Mao, L., Guo, Z. and Chen, Y., "Electrostatic layer-by-layer assembled carbon nanotube multilayer film and its electrocatalytic activity for O_2 reduction," *Langmuir*, **20**(20), 8781-8785 (2004).

Zhang, W., Dong, D., Bedrov, D. and van Duin, A. C., “Hydroxide transport and chemical degradation in anion exchange membranes: a combined reactive and non-reactive molecular simulation study,” *Journal of materials chemistry A*, **7**(10), 5442-5452 (2019).

TH-2592_156107017

Zhang, Z., Xin, L., Sun, K. and Li, W., “Pd–Ni electrocatalysts for efficient ethanol oxidation reaction in alkaline electrolyte,” *International Journal of Hydrogen Energy*, **36**(20), 12686-12697 (2011).

Zhao, G., Xu, X., Di, Y., Wang, H., Cheng, B., Shi, L., Zhu, Y., Zhuang, X. and Yin, Y., "Amino acid clusters supported by cellulose nanofibers for proton exchange membranes," *Journal of Power Sources*, **438**, 227035 (2019).

Zhao, J., Culligan, P.J., Qiao, Y., Zhou, Q., Li, Y., Tak, M., Park, T. and Chen, X., “Electrolyte solution transport in electropolar nanotubes,” *Journal of Physics: Condensed Matter*, **22**(31), 315301 (2010).

Zhao, Y., Zhan, L., Tian, J., Nie, S. and Ning, Z., "Enhanced electrocatalytic oxidation of methanol on Pd/polypyrrole–graphene in alkaline medium," *Electrochimica Acta*, **56**(5), 1967-1972 (2011).

Zhou, J., Unlu, M., Vega, J. A. and Kohl, P. A., "Anionic polysulfone ionomers and membranes containing fluorenyl groups for anionic fuel cells," *Journal of Power Sources*, **190**(2), 285-292 (2009).

Zhuang, S., Liu, S., Huang, C., Tu, F., Zhang, J. and Li, Y., "Electrocatalytic activity of nanoporous perovskite $La_{1-x}Ca_xCoO_3$ towards hydrogen peroxide reduction in alkaline medium," *Int. J. Electrochem. Sci.*, **7**, 338-344 (2012).

Zivcak, M., Kalaji, H. M., Shao, H. B., Olsovska, K. and Brestic, M., “Photosynthetic proton and electron transport in wheat leaves under prolonged moderate drought stress,” *Journal of Photochemistry and Photobiology B: Biology*, **137**, 107-115 (2014).

Zoccola, M., Aluigi, A., Patrucco, A., Vineis, C., Forlini, F., Locatelli, P., Sacchi, M. C. and Tonin, C., "Microwave-assisted chemical-free hydrolysis of wool keratin," *Textile Research Journal*, **82**(19), 2006-2018 (2012).

TH-2592_156107017